Thermodynamics, Reaction Kinetics, and Microstructure of Alkali-Activated Fly Ash - An experimental and modeling study

Chen, Y.

DOI
10.4233/uuid:5b86bb25-2031-4268-86b2-082f768b5d57

Publication date
2024

Document Version
Final published version

Citation (APA)
Chen, Y. (2024). *Thermodynamics, Reaction Kinetics, and Microstructure of Alkali-Activated Fly Ash - An experimental and modeling study*. [Dissertation (TU Delft), Delft University of Technology]. https://doi.org/10.4233/uuid:5b86bb25-2031-4268-86b2-082f768b5d57

Thermodynamics, Reaction Kinetics, and Microstructure of Alkali-Activated Fly Ash

-An experimental and modeling study

Dissertation

For the purpose of obtaining the degree of doctor
at Delft University of Technology
by the authority of the Rector Magnificus Prof.dr.ir. T.H.J.J. van der Hagen
chair of the Board of Doctorates
to be defended publicly on
Friday 13 December 2024 at 10:00 o'clock

By

Yun CHEN
Born in Guangdong Province, P.R. China

This dissertation has been approved by the promotors

Promotor: Prof. dr. G. Ye

Promotor: Prof. Qijun Yu

Composition of the doctoral committee:

Rector Magnificus	Chairperson
Prof. dr. G. Ye	Delft University of Technology, promotor
Prof. Qijun Yu	South China University of Technology, promotor

Independent Members:

Prof. dr. ir. E. Schlangen	Delft University of Technology
Prof. dr. ir. K. van Breugel	Delft University of Technology
Prof. dr. B. Lothenbach	EMPA, Switzerland
Dr. R. Snellings	KU Leuven, Belgium
Dr. J.S. Dolado	Materials Physics Center, Spain
Dr. ir. B. Šavija	Delft University of Technology, reserve member

Keywords:	Alkali-activated fly ash; N-(C-)A-S-H gel; reaction kinetics; microstructure; molecular dynamics simulation; thermodynamic database; thermodynamic modeling; GeoMicro3D
Printed by:	Ipskamp Printing, The Netherlands
Thesis format by:	*Yun Chen*
Cover design:	*Qi Chen*

ISBN 978-94-6384-679-0

An electronic version of this dissertation is available at

http://repository.tudelft.nl/

To my family

谨以此书献给家人

Table of Contents

List of Symbols

Roman lower case letters

a_i	Ion size	[Å]
a_{nm}	Spherical harmonic expansion coefficient	
b_y	A parameter for common short-range interactions of the charged species	
b^{SC}	Neutron scattering length	[fm]
e_j	Discrete velocity at direction j	
e_s	Lattice speed of sound	
$f_j(x,t), f_j^{eq}((x,t))$	Non-equilibrium and equilibrium particle distribution function at location x at time t and in the direction of the velocity j (j = 0, 1, 2, 3, 4, 5, 6)	
f_x	The ratio of the dissolution rate of element X relative to the dissolution rate of Ca	
f_{Fe}	The ratio of the dissolution rate of Fe relative to the dissolution rate of Al	
m	Mass	[g]
$\Delta n_{X,i}$	Dissolved amount of element X at interface i at one time step	[mol]
l_0	Side length of a lattice cell	[m]
r	Overall dissolution rate	[mol/m^2/s]
r_+	Forward dissolution rate	[mol/m^2/s]
r_{new}, r_{ref}	Rates of dissolution at the Kelvin temperatures T_{new} and T_{ref}, respectively	[mol/m^2/s]
$r_{X,i}$	Dissolution rate of element X at the interface i	[mol/m^2/s]
$r(\theta,\varphi)$	Radial distance	[m]
t_0	Time step	[s]
v_X	Molar fraction of element X in fly ash	
w_j	Weighting factor in the velocity direction j	
z_i	Charge of species i	

Roman capital case letters

A	Kinetic parameter	[m^{-3}·s^{-1}]
A^*	Chemical affinity	[J/mol]
A_y	Electrostatic parameter	
B	Thermodynamic parameter	
B_y	Electrostatic parameter	

C_P^0	Standard heat capacity	[J/mol/K]
$\Delta C_{p,T_0}^0$	Changes in heat capacity of the reaction at T_0	[J/mol/K]
D_p	Ion diffusivity in physical unit	[m^2/s]
E_a	Activation energy of the dissolving element	[J/mol]
F_0	Volume fraction of fly ash in the mixture	
$F_{X,non-steady}$	Non-steady factor for element X	
F_t	Volume fraction of fly ash in the paste at time t	
$\Delta_a G_T^0$	Apparent Gibbs free energy of formation at any temperature T	[kJ/mol]
$\Delta_f G^0$	Gibbs free energy of formation	[kJ/mol]
$\Delta_f G_i^0$	Gibbs free energy of formation of the species i	[kJ/mol]
$\Delta_r G^0$	Gibbs free energy of reaction	[kJ/mol]
$\Delta_f H^0$	Enthalpy of formation	[kJ/mol]
I	Ionic strength	[mol/kg]
IAP	Ion activity product	
J	Nucleation rate	[m^3/s]
K_N	A constant	
K_{sp}	Solubility product	
$K_{sp,T}$	Solubility product at temperature T	
$M_{N(C)ASH}$	Molar mass of a N-(C-)A-S-H end-member	[g/mol]
M_s	Activator modulus	
N	Reaction grade	
N_a	Avogadro's number	
$\frac{NBO}{T}$	Ratio of the non-bridging oxygen atoms to oxygen atoms in tetragonal coordination	
ΔN_X	Dissolved amount of element X at six interfaces at one time step	[mol]
$P_{nm}(cos\theta)$	Legendre polynomial	
$P(\Delta t)$	Nucleation probability at the time interval Δt	
$Q(t)$	Cumulative heat release at time t	[J/g]
$Q_{\max\_exp}$	Maximum heat release	[J/g]
$Q_{\max\_fit}$	Fitting maximum heat release	[J/g]
R	Gas constant	[J/mol/K]
S	Source term	
S_S	Supersaturation index of reaction products	
SSA	Specific surface area	[m^2/g]
S^0	Standard entropy	[J/mol/K]
$S_{T_0}^0$	Standard entropy at 298.15 K	[J/mol/K]
$\Delta S_{T_0}^0$	Changes in entropy of the reaction at T_0	[J/mol/K]
T	Absolute temperature	[K]
V_a	Apparent volume of fly ash	[cm^3]
V_v	Volume of voids in fly ash particle	[cm^3]
V^0	Standard molar volume	[cm^3/mol]
$Y_{nm}(cos\theta)$	Spherical harmonic function	

Greek letters

$\alpha(t)$	Degree of reaction at time t	
β	Shape parameter	
γ_i	Activity coefficient of species i	
δt	Lattice Boltzmann time step	[s]
λ	Time parameter	
ρ_a	Apparent density of fly ash	[g/cm^3]
ρ_r	Real density of fly ash	[g/cm^3]
$\rho_{N(C)ASH}^{SC}$	Scattering length density	[m^{-2}]
$\rho'_{N(C)ASH}$	Predicted density of a N-(C-)A-S-H solid solution member	[g/cm^3]
τ	Relaxation time	[m/m]
φ	Azimuthal angle	
Φ^0	Denotes C_p^0 or S^0	

List of Abbreviations

AAFA	Alkali-activated fly ash
AAMs	Alkali-activated materials
AAS	Alkali-activated slag
ASTM	American Society for Testing and Materials
BET	Brunauer-Emmett-Teller
BSE	Backscattered electron
C-A-S-H	Calcium aluminosilicate hydrate
C-(N-)A-S-H	Calcium (sodium) aluminosilicate hydrate
C-S-H	Calcium silicate hydrate
DTG	Differential thermogravimetric
EDS	Energy dispersive spectroscopy
FTIR	Fourier transform infrared spectroscopy
GEMS	Gibbs energy minimization software
GeoMicro3D	Geopolymer Microstructure three Dimensions model
ICP-OES	Inductively coupled plasma optical emission spectroscopy
LAMMPS	Large-scale atomic/molecular massively parallel simulator
LB	Lattice Boltzmann
MA-OH-LDH	Hydrotalcite-like phase
MAS NMR	Magic angle spinning nuclear magnetic resonance
MD	Molecular dynamics
MIP	Mercury intrusion porosimetry
M-S-H	Magnesium silicate hydrate
N-A-S-H	Sodium aluminosilicate hydrate
N-C-A-S-H	Sodium calcium aluminosilicate hydrate
N-(C-)A-S-H	N-A-S-H and/or N-C-A-S-H
NMR	Nuclear magnetic resonance
OVITO	Open visualization tool
PC	Portland cement
PSD	Particle size distribution
QXRD	Quantitative X-ray diffraction
Reaxff	Reactive force field
SEM	Scanning electron microscopy
TGA	Thermogravimetric analysis
VMD	Visual molecular dynamics
XRD	X-ray diffraction
XRF	X-ray fluorescence

x

Summary

Alkali-activated fly ash (AAFA) is being increasingly acknowledged as an eco-friendly binder free of Portland cement, valued for its low carbon footprint and promising engineering properties. However, the application of AAFA has been limited due to its unstable and uncontrollable engineering properties, which are closely tied to its microstructure. The microstructure of AAFA can be affected by several factors, including the intrinsic properties of fly ash, the types of alkaline activators, the mixture and curing regime. These factors can lead to various reactions, resulting in diverse microstructures, and thus a wide range of engineering properties. A deep understanding of the relationship between these influencing factors and the resulting microstructure is essential to bridge the gap between the mixtures and their corresponding engineering properties. Although the effects of these factors on the microstructure of AAFA have been extensively investigated experimentally, there is currently no numerical model capable of simulating the chemical reactions and microstructural development of AAFA. As a result, the reactions and microstructure, and thus the engineering properties of AAFA, remain unpredictable for a given mixture. Simulating the reactions and microstructural development would enable the customization of mix designs to achieve desired engineering properties, thereby promoting the application of AAFA. Therefore, the aim of this research is to simulate the reaction process and development of the microstructure of AAFA.

Thermodynamic modeling is a robust approach to simulate chemical reactions. However, the main challenge in thermodynamic modeling of AAFA lies in the lack of a thermodynamic database of its primary reaction product, N-(C-)A-S-H gel, which varies in Si/Al and Ca/Al ratios. Developing such a database requires accurate determination of the chemical compositions of N-(C-)A-S-H gels, which is difficult to achieve with conventional experimental techniques. Therefore, this research addresses this challenge by utilizing molecular dynamics simulations to determine the chemical compositions of N-(C-)A-S-H gels. By simulating the polymerization process that mimics actual reactions, the atomic structures of N-(C-)A-S-H gels with various Si/Al and Ca/Al ratios were constructed. According to the simulation results, it is proposed that N-(C-)A-S-H gels with a Si/Al ratio of 1-3 and a Ca/Al ratio of 0-0.5 can represent the chemical compositions of N-(C-)A-S-H gel in a mature AAFA paste.

After determining chemical compositions, synthesis of pure N-(C-)A-S-H gels is the second step to determine their thermodynamic data. However, synthesizing N-(C-)A-S-H gel with a Si/Al≥2 at a high pH (corresponding to the alkalinity range of pore solutions in AAFA paste), posed a double challenge. To address this issue, using a concentrated solution with an initial Si/Al ratio higher than the target is the key. Following this approach, N-(C-)A-S-H gels with a Si/Al ratio of 1-3 and a Ca/Al ratio of 0-0.5 were synthesized successfully and characterized by using XRF, XRD, FTIR, and TGA techniques. Subsequently, the solubility of the synthesized N-(C-)A-S-H gels was measured through a dissolution test. A thermodynamic database of N-(C-)A-S-H gels with various Si/Al and Ca/Al ratios was established for the first time,

encompassing not only the solubility, but also the Gibbs free energy, heat capacity, entropy, enthalpy, and molar volume. This established thermodynamic database is the key to performing thermodynamic modeling to simulate the reactions of AAFA.

Coupled with the reaction kinetics determined by isothermal calorimetry and SEM-EDS analysis, the thermodynamic modeling of AAFA was performed for the first time to investigate the formation of reaction products and the phase assemblage of AAFA over time in GEMS software. The sodium hydroxide-activated system showed a close consistency between the modeling and experimental data regarding phase assemblage and pore solution chemistry, while for the sodium silicate-activated system, the simulated ion concentrations in the pore solution showed discrepancies compared to the experimental results. This discrepancy may be attributed to the high ionic strength in the sodium silicate-activated system, limitations in thermodynamic data of N-(C-)A-S-H gel and thermodynamic modeling approach itself.

To simulate the microstructure of AAFA, GeoMicro3D model, originally designed for alkali-activated slag, was extended to adapt to AAFA. To achieve this, first, the dissolution of fly ash in an alkaline solution was investigated experimentally, from which prediction functions were developed to describe the dissolution rate of Si and Al, accounting for the intrinsic characteristics of fly ash, solution pH, and temperature. The developed functions can accurately predict the dissolution behavior of fly ash, aligning well with the experimental results. Then, the GeoMicro3D model was extended by equipping with the thermodynamic database of N-(C-)A-S-H gels and the prediction functions for the dissolution of fly ash. GeoMicro3D was employed to simulate the reaction process and the 3D microstructural development over time of the sodium hydroxide-activated fly ash paste. The distribution of various phases in a 3D microstructure of AAFA can be captured and visualized over time. The simulated degree of reaction of fly ash and the porosity of AAFA were in good agreement with the corresponding experimental data. Furthermore, GeoMicro3D can well simulate the pore solution chemistry over time, consistent with the experimental results.

To sum up, the reaction and microstructure evolution of AAFA were investigated using multiple simulation techniques in this work. The extended GeoMicro3D model developed in this research paves the way for simulating the microstructure and the pore solution chemistry for any given AAFA mixture. This advancement contributes to a deeper understanding of the relationship between the AAFA mixture and the resulting microstructure. Furthermore, the mechanical properties, transport properties and durability of AAFA can be further evaluated based on the simulated microstructure constructed by using the extended GeoMicro3D. This model enables industries to effectively manage fly ashes of varying qualities and customize AAFA to meet specific engineering requirements. This not only improves the utilization of fly ash but also promotes the sustainability of construction practices.

Samenvatting

Alkali-geactiveerde vliegas (AAFA) wordt steeds meer erkend als een milieuvriendelijke binder zonder Portlandcement, gewaardeerd om zijn lage ecologische voetafdruk en veelbelovende technische eigenschappen. De toepassing van AAFA is echter beperkt vanwege zijn onstabiele en onvoorspelbare technische eigenschappen, die nauw verbonden zijn met zijn microstructuur. De microstructuur van AAFA kan worden beïnvloed door verschillende factoren, waaronder de intrinsieke eigenschappen van vliegas, de soorten alkalische activatoren, het mengsel en het uithardingsregime. Deze factoren kunnen leiden tot verschillende reacties, resulterend in diverse microstructuren en daarmee een breed scala aan technische eigenschappen. Een diepgaand begrip van de relatie tussen deze invloedsfactoren en de resulterende microstructuur is essentieel om de kloof tussen de mengsels en hun bijbehorende technische eigenschappen te overbruggen. Hoewel de effecten van deze factoren op de microstructuur van AAFA uitgebreid experimenteel zijn onderzocht, is er momenteel geen numeriek model beschikbaar dat in staat is de chemische reacties en de microstructurele ontwikkeling van AAFA te simuleren. Hierdoor blijven de reacties en microstructuur, en dus de technische eigenschappen van AAFA, onvoorspelbaar voor een gegeven mengsel. Het simuleren van de reacties en de ontwikkeling van de microstructuur zou de maatwerkontwerpen van mengsels mogelijk maken om gewenste technische eigenschappen te bereiken, waardoor de toepassing van AAFA wordt bevorderd. Daarom is het doel van dit onderzoek om het reactieproces en de ontwikkeling van de microstructuur van AAFA te simuleren.

Thermodynamische modellering is een robuuste benadering voor het simuleren van chemische reacties. De grootste uitdaging bij de thermodynamische modellering van AAFA is echter het ontbreken van een thermodynamische database van het primaire reactieproduct, N-(C-)A-S-H-gel, dat varieert in Si/Al- en Ca/Al-verhoudingen. Het ontwikkelen van een dergelijke database vereist een nauwkeurige bepaling van de chemische samenstellingen van N-(C-)A-S-H-gels, wat moeilijk te bereiken is met conventionele experimentele technieken. Daarom pakt dit onderzoek deze uitdaging aan door gebruik te maken van moleculaire dynamicasimulaties om de chemische samenstellingen van N-(C-)A-S-H-gels te bepalen. Door het polymerisatieproces dat werkelijke reacties nabootst te simuleren, werden de atomaire structuren van N-(C-)A-S-H-gels met verschillende Si/Al- en Ca/Al-verhoudingen geconstrueerd. Volgens de simulatie-resultaten wordt voorgesteld dat N-(C-)A-S-H-gels met een Si/Al-verhouding van 1-3 en een Ca/Al-verhouding van 0-0.5 de chemische samenstellingen van N-(C-)A-S-H-gel in een volwassen AAFA-pasta kunnen vertegenwoordigen.

Na het bepalen van de chemische samenstellingen is de synthese van zuivere N-(C-)A-S-H-gels de tweede stap om hun thermodynamische gegevens te bepalen. Echter, het synthetiseren van N-(C-)A-S-H gel met een Si/Al verhouding ≥ 2 bij een hoge pH (overeenkomend met het alkaliniteitsbereik van de porieoplossingen in AAFA-pasta), vormde een dubbele uitdaging. Om dit probleem aan te pakken, is het gebruik van een

geconcentreerde oplossing met een initiële Si/Al verhouding hoger dan het doel essentieel. Door deze aanpak werden N-(C-)A-S-H gels succesvol gesynthetiseerd met een Si/Al verhouding van 1-3 en een Ca/Al verhouding van 0-0,5, en gekarakteriseerd met behulp van XRF, XRD, FTIR en TGA technieken. Vervolgens werd de oplosbaarheid van de gesynthetiseerde N-(C-)A-S-H gels gemeten door middel van een oplostest. Voor het eerst werd een uitgebreide thermodynamische database van N-(C-)A-S-H gels met verschillende Si/Al en Ca/Al verhoudingen opgesteld, waarbij niet alleen de oplosbaarheid maar ook de Gibbs vrije energie, warmtecapaciteit, entropie, enthalpie en molaire volume werden meegenomen. Deze vastgestelde thermodynamische database vormt de sleutel tot het uitvoeren van thermodynamische modellering om de reacties van AAFA te simuleren.

In combinatie met de reactiekinetiek bepaald door isothermische calorimetrie en SEM-EDS analyse, werd voor het eerst thermodynamische modellering van AAFA uitgevoerd om de vorming van reactieproducten en de fase-assemblage van AAFA in de loop van de tijd te onderzoeken in GEMS-software. Het natriumhydroxide-geactiveerde systeem vertoonde een nauwe consistentie tussen de modellering en experimentele gegevens met betrekking tot fase-assemblage en chemie van de porieoplossing, terwijl voor het natriumsilicaat-geactiveerde systeem de gesimuleerde ion concentraties in de porieoplossing afwijkingen vertoonden ten opzichte van de experimentele resultaten. Deze afwijking kan worden toegeschreven aan de hoge ionsterkte in het natriumsilicaat-geactiveerde systeem, de beperkingen in de thermodynamische gegevens van N-(C-)A-S-H gel en de thermodynamische modelleringsbenadering zelf.

Om de microstructuur van AAFA te simuleren, werd het GeoMicro3D-model, oorspronkelijk ontworpen voor alkali-geactiveerde slak, uitgebreid om aan te passen aan AAFA. Om dit te bereiken, werd eerst het oplossen van vliegas in een alkalische oplossing experimenteel onderzocht, waaruit voorspellingsfuncties werden ontwikkeld om de oplosbaarheidssnelheid van Si en Al te beschrijven, rekening houdend met de intrinsieke kenmerken van vliegas, oplossing pH en temperatuur. De ontwikkelde functies kunnen nauwkeurig het oplosgedrag van vliegas voorspellen, wat goed aansluit bij de experimentele resultaten. Vervolgens werd het GeoMicro3D-model uitgebreid door het uit te rusten met de thermodynamische database van N-(C-)A-S-H gels en de voorspellingsfuncties voor de oplossing van vliegas. GeoMicro3D werd gebruikt om het reactieproces en de driedimensionale microstructurele ontwikkeling in de tijd van het natriumhydroxide-geactiveerde vliegas-pasta te simuleren. De verdeling van verschillende fasen in een driedimensionale microstructuur van AAFA kan in de loop van de tijd worden vastgelegd en gevisualiseerd. De gesimuleerde reactiegraad van vliegas en de porositeit van AAFA waren in goede overeenstemming met de bijbehorende experimentele gegevens. Bovendien kan GeoMicro3D goed de chemie van de porieoplossing in de loop van de tijd simuleren, consistent met de experimentele resultaten.

In deze studie werd de reactie en microstructuur evolutie van AAFA onderzocht met behulp van meerdere simulatietechnieken. Het uitgebreide GeoMicro3D-model dat in dit onderzoek is ontwikkeld, opent de weg naar het simuleren van de microstructuur en de chemie van de porieoplossing voor elke gegeven AAFA-mix. Deze vooruitgang draagt bij aan een dieper inzicht in de relatie tussen de AAFA-mix en de resulterende microstructuur. Bovendien kunnen de mechanische eigenschappen, transporteigenschappen en duurzaamheid van AAFA verder worden geëvalueerd op basis van de gesimuleerde microstructuur die is

geconstrueerd met GeoMicro3D. Daarnaast stelt dit model industrieën in staat om vliegassen van uiteenlopende kwaliteiten effectief te beheren en AAFA aan te passen aan specifieke technische eisen. Dit verbetert niet alleen het gebruik van vliegas, maar bevordert ook de duurzaamheid van bouwpraktijken.

Chapter 1

General Introduction

1.1 Research background

Alkali activation technology has been developed globally for its potential to transform industrial by-products or waste streams into low-cost, low-carbon footprint, and/or high-value products [1]. This technology involves the use of solid aluminosilicate precursors and alkaline activators to produce alkali-activated materials (AAMs) that can serve as alternative binders in construction materials, aside from Portland cement (PC). Among the various precursors utilized in AAMs, coal fly ash (hereafter referred to as fly ash) stands out as a widely employed option, owing to its abundance as a by-product of coal-fired power plants. Despite facing competition from other renewable energy resources, coal-fired power generation remains a mainstream method of electricity production, leading to the substantial generation of fly ash. The annual global production of fly ash has surpassed 700 million tons since 2010 as shown in Figure 1.1, while the global utilization of fly ash is only around 25 % of the total production [2]. The main application of fly ash is as a supplementary cementitious material to replace PC. However, to enhance the utilization of fly ash, research on its use in the production of alkali-activated fly ash (AAFA) has experienced a notable surge in popularity in recent years.

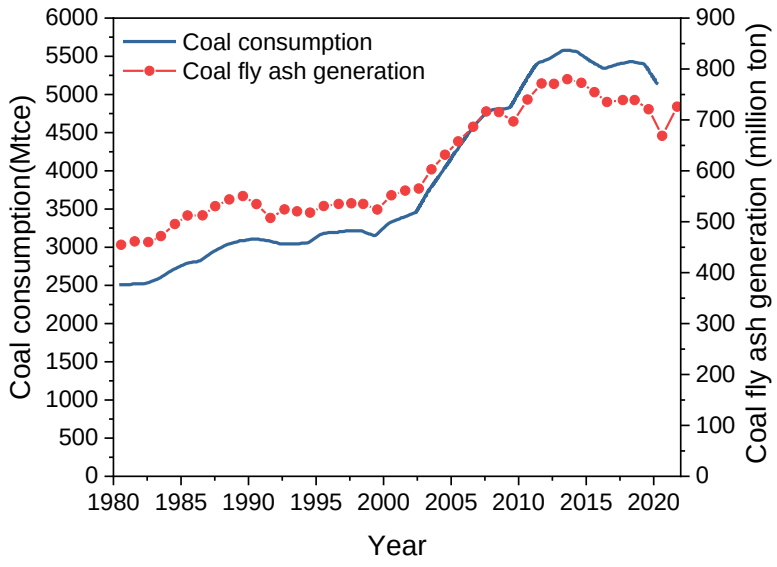

Figure 1.1 Trends in global coal consumption and coal fly ash generation from 1981 to 2021. Data from [2].

AAFA, also known as fly ash-based geopolymer, has become as a prominent alternative to PC after the first report in the 1990s [3,4]. As a cement-free binder, AAFA has much lower embodied energy and CO_2 emission compared with PC [5]. Moreover, given proper mixture design and curing regime, AAFA can even exhibit better engineering properties than PC, e.g. higher mechanical strength [6,7], higher resistance to chemical attacks [8,9], lower shrinkage [10] and better thermal resistance [11,12].

The reaction of fly ash and alkaline activator involves the dissolution of fly ash, gelation, reorganization, polymerization and ends up with a hardened matrix [13]. The microstructure within the AAFA hardened matrix contains four main phases: solid reaction products, unreacted fly ash particles, pore solution, and pores. The main reaction product of AAFA is generally believed to be a sodium aluminosilicate hydrate (N-A-S-H) gel [14,15]. As fly ash contains a certain amount of Ca, Ca could be incorporated into N-A-S-H gel to form sodium calcium aluminosilicate hydrate (N-C-A-S-H) gel [16]. Note that it is different from another term C-(N-)A-S-H gel, the main reaction product in alkali-activated slag (AAS). C-(N-)A-S-H gel refers to that a few Na could be incorporated into the basic structure C-A-S-H gel. In this research, the term N-(C-)A-S-H[1] gel is used to describe the main reaction product of AAFA, representing N-A-S-H gel and/or N-C-A-S-H gel.

The microstructure of AAFA can exhibit significant variability since the reaction between fly ash and alkaline activator is controlled by numerous factors, each of which can vary greatly. First of all, fly ash from different sources across the world shows large variations in terms of chemical composition, reactivity and fineness [17,18]. These could affect not only the dissolution rate of fly ash, but also the amount and type of dissolved species. Second, the types of alkaline activators include sodium/potassium hydroxide, silicate, carbonate, and sulfate. These alkaline activators exhibit variations in pH level and ion types, which can influence not only the dissolution kinetics of fly ash [19,20] but also the types of reaction products [21]. In addition, the mixture of AAFA, e.g. alkaline solution-to-binder ratio, is another influential factor. A higher alkaline solution-to-binder ratio contributed to more reaction products as it provides more hydroxyl ions in contact with fly ash [14]. Last, the curing regime, like temperature and time, also plays an important role in reaction kinetics, types and amount of reaction product [6,22]. With increasing time and thus reaction degree, more and more solid reaction products are formed, leading to the changes in pore solution and pore structure [23,24]. Any changes in these factors can affect the overall reaction, including the dissolution of fly ash and the formation of reaction products. This subsequently affects the microstructure of AAFA, resulting in variations in its engineering properties, e.g. mechanical properties [25,26], volume stability [27] and durability [28]. As a result, the application of AAFA is hindered by its various and unpredictable engineering properties. Prediction of the reaction of AAFA with consideration of the above factors, therefore, is an essential step toward a better understanding of the properties of AAFA.

Thermodynamic modeling provides an opportunity to describe the reaction process and quantitatively predict the reaction products. Recently, the application of thermodynamic

[1] N-(C-)A-S-H refers to NaO-(CaO-)Al_2O_3-SiO_2-H_2O, of which hyphens indicate nonstoichiometric compounds and round brackets stand for possible substituted element.

modeling to cement hydration and AAS reaction has underscored its robustness in unraveling chemical processes and elucidating the effect of different factors on the reaction products and pore solution [29–31]. However, thermodynamic modeling of AAFA materials has rarely been performed. The main reason lies in the scarcity of a thermodynamic database of N-(C-)A-S-H gel. A thermodynamic database mainly contains solubility product, heat capacity, enthalpy, entropy and Gibbs free energy of substances and phases [32]. The challenge in developing this database lies in determining the chemical compositions of N-(C-)A-S-H gel, especially the Si/Al ratio, which is the main variable in N-(C-)A-S-H gel. However, determination of the Si/Al ratio of N-(C-)A-S-H gel in AAFA paste is challenging through experiments due to potential interference from the Si species in the pore solution. These species cannot be separated when measuring the chemical composition of N-(C-)A-S-H gel through experimental techniques, leading to an inaccurate Si/Al ratio determination. Currently, the only existing thermodynamic database of N-(C-)A-S-H gel proposed by Zuo [33] is largely based on the assumption regarding the chemical composition of N-(C-)A-S-H gel, including a fixed Ca/Al ratio of 0.45 and a Si/Al ratio ranging from 1 to 4. Furthermore, the thermodynamic properties of these N-(C-)A-S-H gels were derived from fitting outcomes rather than experimental measurements, leaving the precision of this database uncertain. Although a few research has measured the solubility product of N-A-S-H gel with a Si/Al ratio of 1 and 2 by solubility test [34–36], the solubility products of N-A-S-H gel with a higher Si/Al ratio (>2) and Ca-containing N-C-A-S-H gel remain unexplored.

The microstructure of AAFA can be further simulated over time based on the prediction of the AAFA reaction. While computer-based simulation models have been proposed to simulate the microstructure of PC-based materials [37–39] and AAS [33], analogous models for AAFA are absent. The GeoMicro3D model [40], abbreviated for Geopolymer Microstructure three Dimensions model, has been established by Zuo to describe the microstructure development of AAS systems. GeoMicro3D consists of several simulation modules, with which it can simulate the initial 3D particle packing structure, dissolution of the precursor(s), transportation of ions, nucleation of reaction products and thermodynamic modeling of chemical reactions. However, given the undetermined dissolution kinetics of fly ash and the incapability of thermodynamic modeling of AAFA, GeoMicro3D currently lacks the capability to simulate the microstructure of AAFA.

In summary, predicting the reaction and microstructure of the AAFA is crucial for tailoring mixture designs to achieve diverse performance goals. However, there are no models capable of simulating the reaction and microstructure of the AAFA. In this research, a numerical model will be extended to simulate the chemical reaction process and the microstructure development of AAFA based on the investigation of the chemical compositions of N-(C-)A-S-H gel and thermodynamics modeling of the reaction of AAFA.

1.2 Research aim and objectives

The aim of this research is to simulate the reaction process and development of the microstructure of AAFA paste. To achieve this research aim, the following objectives are set:

- To determine possible ranges of the chemical compositions of the main reaction product, i.e. N-(C-)A-S-H gels.
- To model the evolution of phase assemblage of AAFA quantitatively by establishing a thermodynamic database of N-(C-)A-S-H gels.
- To develop a function to describe the dissolution of fly ash.
- To extend the existing GeoMicro3D model for AAFA.

1.3 Research strategy

According to the aim and objectives of this research, a step-by-step plan is formulated as follows:

First, in light of the limitations associated with determining chemical compositions of N-(C-)A-S-H gels through experimental methods, molecular dynamics simulation was conducted to identify the possible range of chemical compositions of N-(C-)A-S-H gels in terms of Si/Al and Ca/Al ratio. Based on the chemical formulas determined above, N-(C-)A-S-H gels were synthesized using the sol-gel method, and subsequently subjected to a solubility test to measure the concentrations of dissolving ions and calculate the corresponding solubility products. On the basis of solubility products, the thermodynamic properties of N-(C-)A-S-H gels are calculated to supplement the thermodynamic database. Once the thermodynamic database for N-(C-)A-S-H gels was established, the phase assemblages of AAFA were modeled over time using a thermodynamic tool, GEMS [41]. Additionally, the dissolution of fly ash was conducted under different pH values and temperatures to establish a function for its dissolution rate. Equipped with the dissolution kinetic of fly ash and thermodynamic modeling of AAFA, GeoMicro3D was extended to simulate the three-dimensional microstructural development of AAFA paste. Meanwhile, both thermodynamic modeling and numerical simulation results on reaction kinetics, reaction products, pore solution composition and microstructure are validated via experiments.

1.4 Research scope

In this research, AAFA was studied through simulation and experimental methods with the following specifications:

- AAFA in the paste level was studied.
- Low calcium fly ash (Class F according to ASTM C618) was studied.
- Two common alkaline activators, i.e. sodium hydroxide and sodium silicate, were used.
- To study the reaction and microstructure of AAFA, the following typical mixtures were selected: a water/fly ash mass ratio of 0.35, Na_2O content of 9.3 % with respect to fly ash to accelerate the dissolution of fly ash, and a molar modulus of sodium silicate of 0 or 1 to represent sodium hydroxide and sodium silicate activated systems, respectively.
- Curing was in sealed condition at 40 °C or 60 °C up to 28 days in order to study the microstructural development of AAFA. Elevated temperature curing can ensure a hardened matrix at an early age.

1.5 Outline of this research

The structure of this thesis is shown in Figure 1.2. The main content of each chapter is summarized as follows:

Chapter 1 outlines a general introduction, aim, strategy, and scope of this research.

Chapter 2 reviews the reaction mechanism, reaction products and microstructure of AAFA. Different types of models relating to the reaction products and reaction process of AAFA are described. The research gaps based on the literature survey are proposed.

Chapter 3 investigates the nano-nature of N-(C-)A-S-H gels by molecular dynamics simulation. The chemical composition of N-(C-)A-S-H gels is determined and used to guide the synthesis of N-(C-)A-S-H gels in Chapter 4. The structural characteristics of modeled N-(C-)A-S-H gels are also used to validate the synthesized N-(C-)A-S-H gels in Chapter 4.

Chapter 4 establishes a modified synthesis procedure for N-(C-)A-S-H gels with different Si/Al ratios and Ca/Al ratios by studying the effect of different reaction parameters on the obtained N-(C-)A-S-H gels. The chemical composition of N-(C-)A-S-H gel is measured by using X-ray fluorescence analysis (XRF) and thermogravimetric analysis (TGA). The structural information of N-(C-)A-S-H gel is gained from X-ray diffraction (XRD) and Fourier transform infrared spectroscopy (FTIR).

Chapter 5 determines the solubility product of N-(C-)A-S-H gels obtained in Chapter 4 through solubility measurement. In addition, a thermodynamic database is developed for N-(C-)A-S-H gels. This database includes various thermodynamic data of N-(C-)A-S-H gels, such as their heat capacity, enthalpy, entropy, Gibbs free energy and molar volume, along with their solubility product.

Chapter 6 models the phase evolution of AAFA over time using the thermodynamic database developed in Chapter 5. Experimental analysis is conducted on solid phases and aqueous phases of AAFA paste to validate the accuracy of thermodynamic modeling.

Chapter 7 investigates the dissolution rate of fly ash in alkaline solutions at different temperatures. Coupled with thermodynamic modeling in Chapter 6, the GeoMicro3D is extended to model the spatial distribution of unreacted fly ash and reaction products. Experimental results including reaction degree, pore solution compositions and porosity are presented to validate the simulation results obtained from the extended GeoMicro3D.

Chapter 8 gives the conclusions of this research. Some remarks and recommendations for future studies are presented.

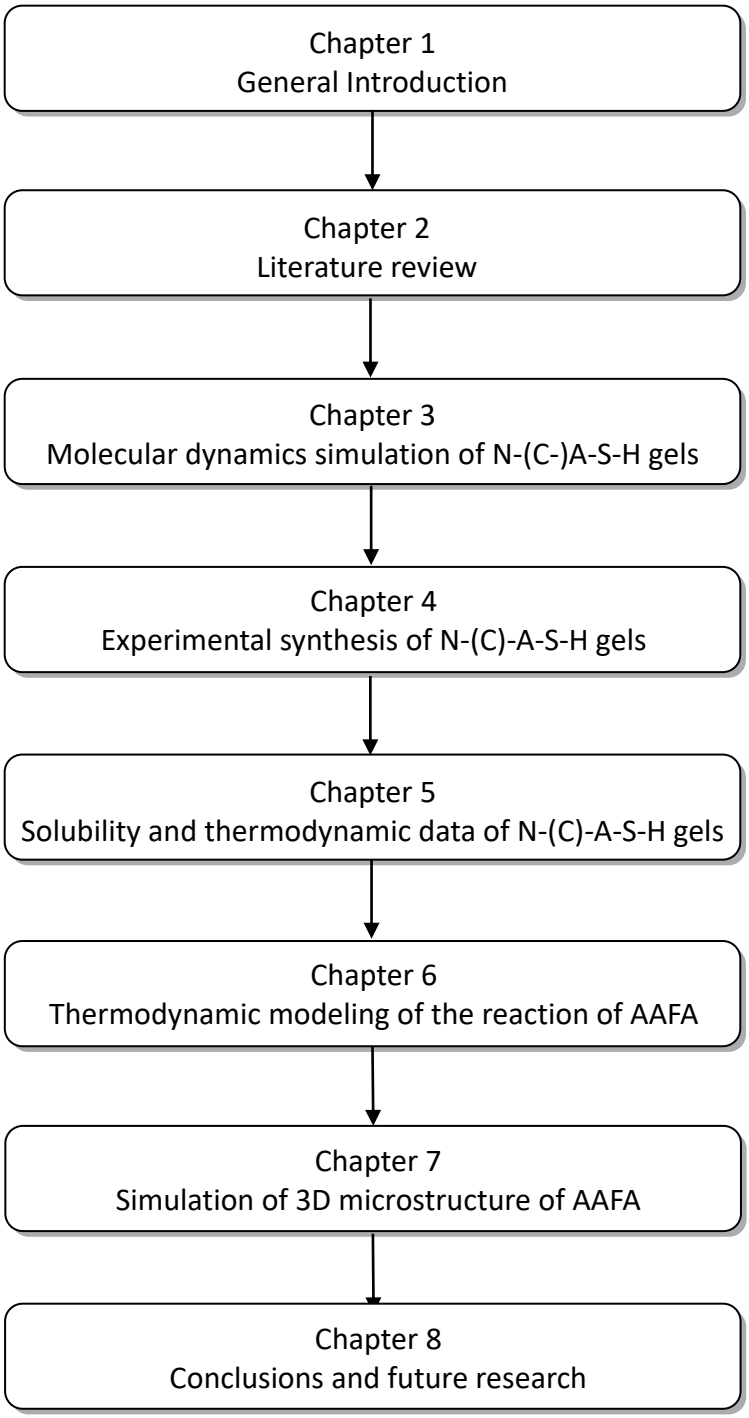

Figure 1.2. Outline of this thesis.

Chapter 2

Literature Review

2.1 Introduction

This chapter provides a brief overview of fundamental chemical and structural characteristics of alkali-activated fly ash (AAFA). First, a general introduction of AAFA is given. Then, experimental studies of AAFA concerning its reaction mechanism, reaction products, pore solution and microstructure are reviewed. Following that, simulation studies of AAFA including molecular dynamics (MD) simulation of the reaction product of AAFA, thermodynamic modeling of AAFA reaction, and a numerical model (GeoMicro3D) for microstructure simulation are reviewed. Based on the literature survey, the research gaps of this research are outlined in the end.

2.2 General introduction of AAFA

Alkali-activated materials (AAMs) can be classified into high-calcium system and low-calcium system according to the calcium content of the precursor [1]. Alkali-activated slag (AAS) is a prevalent high-calcium AAM, with its main reaction product being chain-based calcium sodium aluminosilicate hydrate (C-(N-)A-S-H) gel. AAFA represents a typical member of low-calcium AAM, where the main reaction product is the network-based N-A-S-H gel. The research on AAFA can be traced back to the early 1990s, when AAFA concrete with high engineering properties was proposed, but under the terminology of 'mineral polymer' [1,42]. Other terms like 'geopolymer' [3,43], 'inorganic polymer' [44,45] have also been used to describe low-calcium AAM. Praised for its excellent properties such as chemical- and thermal-resistance, AAFA has been designed for a variety of applications including stabilization of toxic and radioactive wastes [46], fire-resistant coating [47], furnace lining [48], and railway sleeper [49].

Fly ash, as the main component of AAFA, can vary significantly from source to source, or over time from the same source [50]. To help standardize the use of fly ash in construction materials, ASTM C618-12a [51] classifies coal fly ash into two categories: Class F and Class C. Class F fly ash has more than 70 wt.% SiO_2+Al_2O_3+Fe_2O_3, while Class C fly ash contains 50-70 wt.% SiO_2+Al_2O_3+Fe_2O_3. Class C fly ash typically has higher CaO content than Class F fly ash, although the criterion of 10 % CaO used to distinguish these two classes has been eliminated in ASTM C618-12a since 2012 [51]. While AAFA can be made from both Class F fly ash and Class C fly ash, research has primarily focused on Class F fly ash, since Class C fly ash-based AAM is very likely to encounter issues related to setting rates and rheology [52,53]. Without specific claim, AAFA usually refers to that using Class F fly ash, which is also adopted in this research.

In the realm of AAFA's constituents, alkaline activators encompass sodium/potassium hydroxide, silicate, sulfate, and carbonate. Among them, sodium hydroxide and silicate stand out as favorable choices for activators, excelling in both performance and economic aspects in the activation of fly ash [1,18].

2.3 Experimental studies of AAFA

2.3.1 Reaction mechanism of AAFA

2.3.1.1 Dissolution of fly ash

Fly ash mainly consists of glassy aluminosilicates and crystalline phases [54]. When encountering an alkaline solution, glassy aluminosilicates can dissolve while most crystalline phases like quartz, mullite and magnetite remain unreacted, as shown in Figure 2.1 [55]. The aluminosilicate glass is a network formed by Si and Al tetrahedra with alkali or alkali-earth metals (e.g. Na or Ca) as network modifiers [54]. The dissolution of glassy aluminosilicates starts with the release of the network modifiers via ion exchanges. After that the network is broken down gradually through hydrolysis of Al-O and Si-O bonds, thereby releasing Al and Si species to the solution [56]. Hydrolysis is preferred at the Al–O site in the beginning since a higher energy is needed to break a Si-O bond compared to an Al-O bond [57,58]. With the liberation of Al, the fully tetrahedrally coordinated Si in the network turns partially detached and becomes reactive [57]. As a result, the dissolution rate of Si starts to increase and gradually becomes congruent with that of Al, corresponding to a stoichiometric stage [57,59]. However, Newlands et al. dissolved synthetic fly ash in a NaOH solution and reported a lower dissolution rate of Al compared to Si during the whole dissolution test [60].

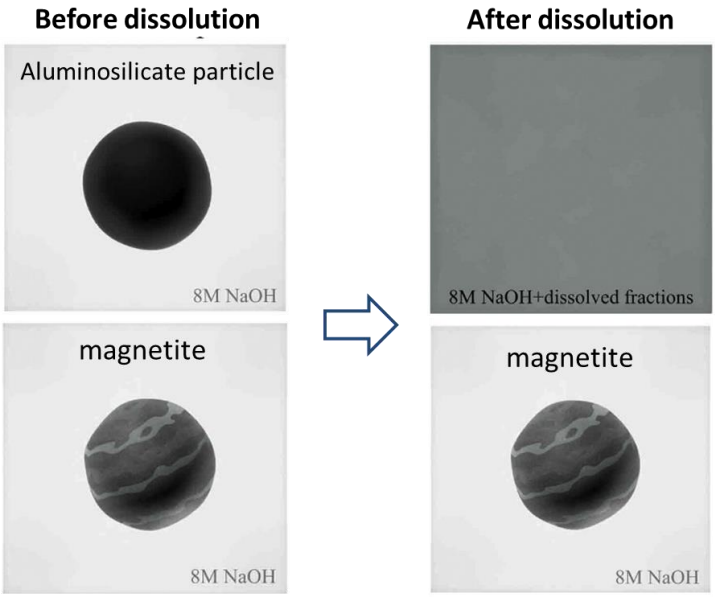

Figure 2.1 Schematic images of the dissolution behavior of different fly ash particles. Redrawn from [55].

The dissolution rate of fly ash is affected by several factors, e.g. reactivity of fly ash [59,61], surface area of fly ash [62], pH of the solution [55,63] and temperature [55,63]. There are mainly two models to describe the dissolution reaction of glass (not only limited to fly ash). The first one is based on diffusion through a reaction layer [64]. For instance, Chen et al. [63] reported that the dissolution of fly ash in a KOH solution can be divided into three stages and described by the following modified Jander equation with different reaction grades (N):

$$\ln\left[1-(1-\alpha)^{1/3}\right]=\frac{1}{N}lnK_N+\frac{1}{N}lnt \tag{2.1}$$

where α is the reaction degree, K_N is a constant and t is the reaction time.

The first stage corresponds to α < 0.1 and N = 1, where the process is dominated by the dissolution of fly ash. The second stage refers to 0.1 < α < 0.45 and N = 2, where the process is controlled by the diffusion through a thin layer of reaction products. In the last stage (α > 0.45 and N > 2), more reaction products are formed and diffusion continues to control the reaction. However, such a model is empirical and not able to describe the effect of the factors mentioned above [65].

The second model utilizes a chemical-affinity law based on the transition state theory [64–66]. Equation 2.2 is commonly used to describe the dissolution rate of silicate glass at different stages [67]:

$$r=r_+(1-\exp\left(-\frac{A^*}{\sigma RT}\right)) \tag{2.2}$$

where r and r_+ refer to overall and forward dissolution rate, respectively, A^* stands to the chemical affinity, σ is the ratio of the rate of dissolution of the activated complex relative to the overall reaction rate, R represents the ideal gas constant and T designates the absolute temperature.

The forward dissolution rate r_+ in the Equation 2.2, also known as maximum dissolution rate, refers to the dissolution rate of glass at the far-from-equilibrium condition [67,68]. It is commonly modeled by the Equation 2.3 [19,65,69]:

$$r_+=k_0 10^{\pm\eta\cdot pH}\exp\left(\frac{-E_a}{RT}\right) \tag{2.3}$$

where k_0 is the intrinsic rate constant, η is the pH power law coefficient, E_a is the apparent activation energy.

The effects of temperature and pH of the solution on the dissolution rate are considered in Equation 2.3. Since r_+ is normalized by the surface area, the effect of surface area of glass is also taken into account. As for the effect of glass itself, Vienna et al. collected the forward dissolution rate from 19 glasses, and found that the parameter k_0 in Equation 2.3 was affected by the glass composition, indicating a correlation between k_0 and glass composition [19].

2.3.1.2 Gelation and polymerization

After the dissolution of fly ash, the concentration of various ionic species in the pore solution increases rapidly until the solution is saturated or even oversaturated. The solid reaction products start to precipitate and grow in the concentrated solution. Extensive research has investigated the reaction process of AAFA and divided it into several stages: dissolution-gelation-polymerization-growth (see Figure 2.2), although different terms were used [23,70–72]. In the gelation stage, most studies reported that an Al-rich phase (Gel 1) was formed first and transformed into a Si-rich phase (Gel 2) afterward [72–74]. In a high-silicate alkaline solution, however, Rees et al. [75] claimed that Si-rich gel could be directly formed without the formation of Al-rich gel. The connectivity of the gel network keeps increasing during polymerization, leading to a three-dimensional gel structure on the atomic to a nanometric scale. As a small water-to-binder ratio is usually utilized in AAFA paste, the hardened matrix can form rapidly, leading to a limited time and space available for crystal growth. As a result, most solid reaction products remain amorphous [23,71].

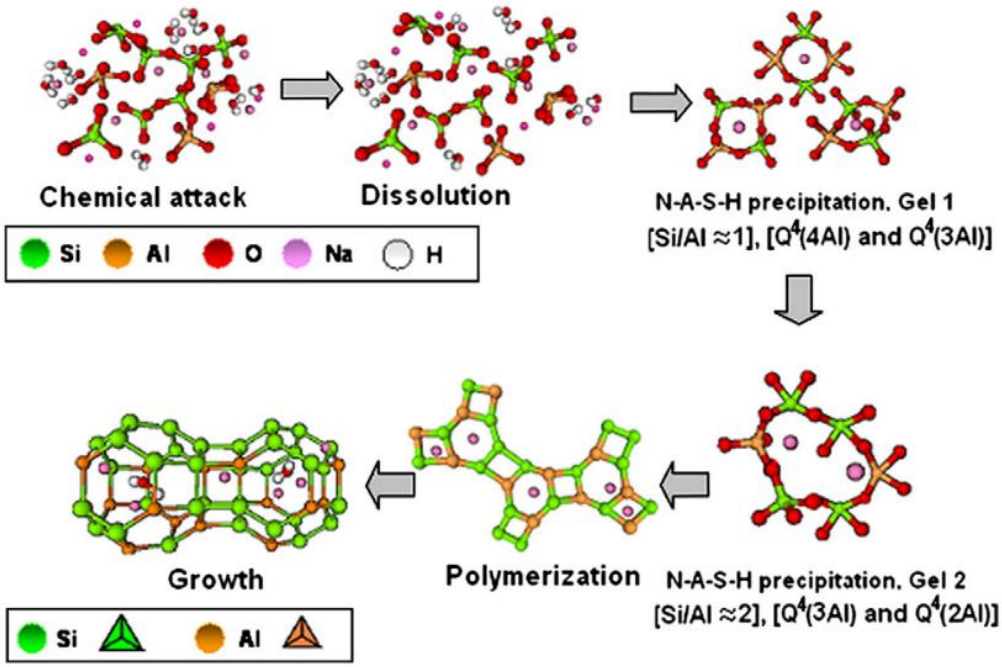

Figure 2.2 Descriptive model for alkaline activation reaction [71].

2.3.1.3 Reaction kinetics

The reaction kinetics of AAFA binders has been usually evaluated by using isothermal calorimetry, which can produce a heat flow of the reaction over time. As can be seen in Figure 2.3, an exothermic peak (peak I) can be found immediately after the contact of fly ash and activator, regardless of the mixing method [76–78]. This peak is assigned to the wetting and dissolution of fly ash. Another exothermic peak (Peak II) emerged after the initial peak in the NaOH-activated system curing at elevated temperature [76,78,79]. The secondary peak, also called acceleration peak, is related to polymerization and formation of reaction products. The induction period between the first peak and second peak can be shortened with the increase in temperature [76,78,79]. In contrast, such multiple-peak calorimetric response was not found at room temperature, indicating the importance of elevated temperature curing. For silicate-activated systems, only a single peak was observed even at elevated temperatures [33,77]. This peak is labeled as a combination of the dissolution peak and acceleration peak as dissolution and polymerization happened almost concurrently [77,80].

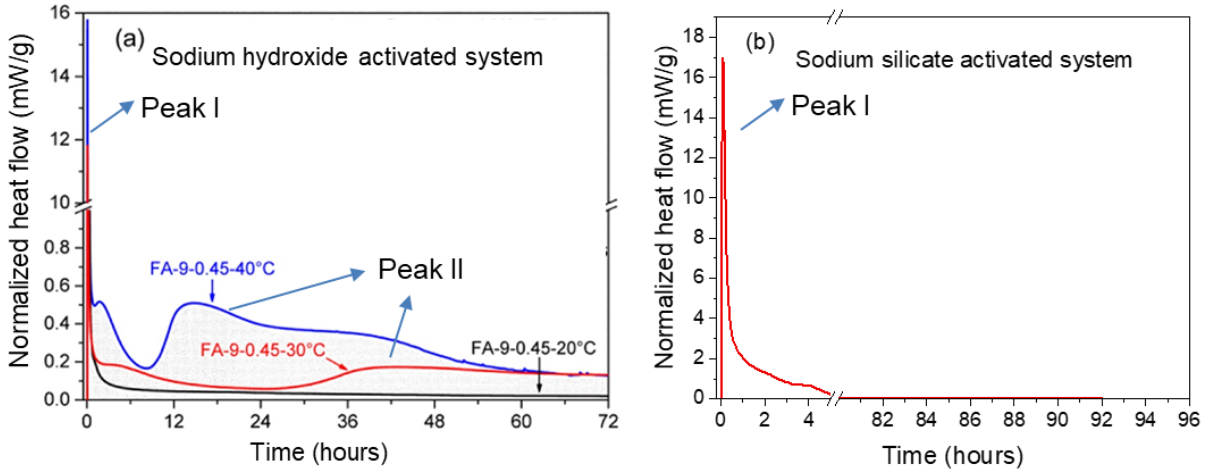

Figure 2.3 Heat flow of (a) sodium hydroxide-activated fly ash paste cured at different temperatures [76] and (b) sodium silicate-activated fly ash paste cured at 50 °C, redrawn from [77].

2.3.2 Reaction products of AAFA

2.3.2.1 N-A-S-H gel

The main reaction product of AAFA is sodium/potassium aluminosilicate hydrate gel, which is mostly abbreviated as N-A-S-H since Na is the most used alkali. N-A-S-H gel primarily consists of Si tetrahedra and Al tetrahedra linked by bridging oxygen, with ionically bound Na^+ to balance the negative Al tetrahedron, as shown in Figure 2.4. The structure of N-A-S-H gel is generally described as a highly cross-linked, X-ray amorphous and pseudo-zeolitic three-dimensional network [81]. Due to the complex structure, solid-state magic angle spinning nuclear magnetic resonance (MAS NMR) turned out to be one of the most effective techniques for analyzing N-A-S-H gel. According to NMR findings, it is usually believed that, in N-A-S-H gel, Si is predominately present in Q^4(mAl) environment, where m can range from 1 to 4 depending on the Si/Al ratio of the gel [82], while Al mainly exists as Q^4(4Si) site, since Al-O-Al bonding is not preferred thermodynamically [14,70,83]. However, new findings have been reported recently by using improved testing methods or advanced devices. Combining MAS NMR technique with selective dissolution method, Gao et al. found that the newly formed Q^4 (removing those from unreacted fly ash) only accounted for 15.7 % - 35.4 % of the reaction products [84]. Apart from Q^4 sites, Q^3 to Q^0 were all detected in AAFA paste. Although room temperature curing can explain the presence of poorly polymerized Q^2 to Q^0 sites, it can still indicate that Si tetrahedra in N-A-S-H gel do not primarily exist as Q^4(mAl) as stated in some literature [82,85]. In addition, Al is not always present in a tetrahedron. Six coordinated Al was used to believe only from raw material [70], but it has been found recently in N-A-S-H gel through high-resolution NMR spectra [86]. This type of Al plays the role of charge-balancing for Al tetrahedron. Based on it, a new model for N-A-S-H gel was proposed as shown in Figure 2.5.

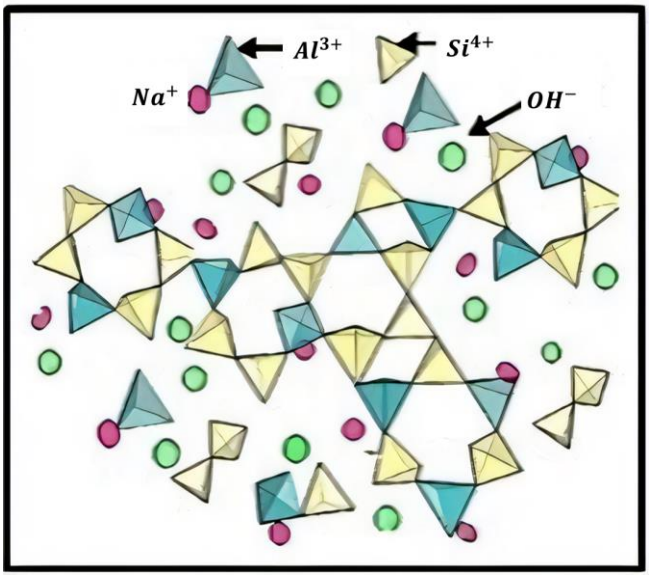

Figure 2.4 Schematic of N-A-S-H gel structure, redrawn from [87].

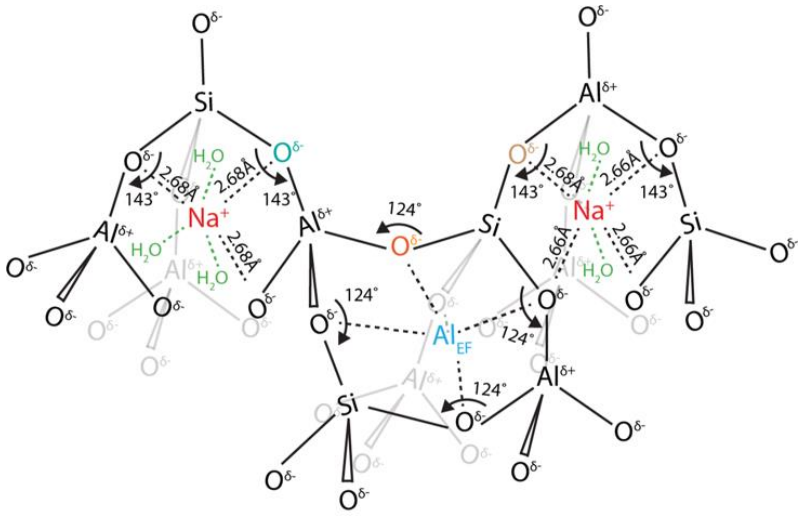

Figure 2.5 Structural model for a segment of N-A-S-H gel [86].

The chemical composition of N-A-S-H gel can be expressed by the general formula of $Na^+[(SiO_2)_nAlO_2]^-\cdot wH_2O$ [82]. It is generally believed that Na/Al ratio should be equal to 1 for charge balancing [88]. In contrast, Si/Al ratio in N-A-S-H gel can vary widely, depending on raw materials, mix and curing regime [21,84,85,89]. The study of the Si/Al ratio in N-A-S-H gel is usually on the basis of AAFA paste through NMR technique or energy dispersive spectroscopy (EDS). A mean Si/Al ratio of 2.7 was found in N-A-S-H gel of sodium silicate-activated fly ash system, while reducing to 1.7 in the sodium hydroxide-activated counterpart in [21]. Bakharev [90] also found a similar trend of Si/Al in these two systems: Si/Al mainly in the range of 1.6-3 in the silicate-activated system while in the range of 1-2 in the hydroxide-activated system. By contrast, Si/Al ratio of N-A-S-H gel was found at around 1.4 for a sodium silicate-activated fly ash curing at room temperature in [84], while it was up to 2.5-4.6 for a sodium silicate-activated fly ash curing at high temperature in [91]. In the work of Bhagath Singh [89], Si/Al ratio of N-A-S-H gel was found to fall within the range of 2 to 3.3 for sodium silicate-activated fly ash system curing from 1 day to 90 days at different curing temperatures. Although there are some variations in Si/Al ratio of N-A-S-H gel in AAFA paste in the above research, it can be found that, on average, Si/Al of N-A-S-H gel in a silicate-activated system is higher than that in hydroxide-activated counterpart as silicate activator provides extra Si species to form N-A-S-H gel. However, not all Si species of silicate activator would form a solid product and some may interfere with the experimental measurement of Si/Al. As a result, the Si/Al ratio of N-A-S-H gel in AAFA paste could be overestimated. The 'H' in N-A-S-H gel refers to the chemically bound water. Only a few works investigated the quantity of chemically bound water in N-A-S-H gel, it is commonly believed that its amount is not as high as that in C-A-S-H gel [92,93].

2.3.2.2 N-C-A-S-H gel

N-A-S-H gel can interact with Ca to form calcium-substituted sodium aluminosilicate (N, C)-A-S-H gel [94], although another two abbreviations, N-(C)-A-S-H and N-C-A-S-H, are more often used. In literature, N-C-A-S-H gel is often found in AAFA systems blended with a small amount of slag or cement [16,26,94,95]. The chemical compositions of N-A-S-H gel and N-C-

A-S-H gel in AAFA system and alkali-activated slag and fly ash blended system, respectively, are plotted in the CaO-SiO_2-Al_2O_3 ternary phase diagrams in Figure 2.6. It is clear to see that, in addition to the data identified as N-C-A-S-H gel, the N-A-S-H gel in AAFA system also contains a small amount of Ca, although less than that in N-C-A-S-H gel in alkali-activated slag and fly ash blended system. This is because Class F fly ash also contains a small amount of Ca, which is highly likely to be incorporated into N-A-S-H gel. As only a small number of Ca ions replaces Na, N-C-A-S-H gel still maintains a 3D structure like N-A-S-H gel. Hence, N-(C-)A-S-H gel hereafter is used to refer to N-A-S-H gel and/or N-C-A-S-H gel.

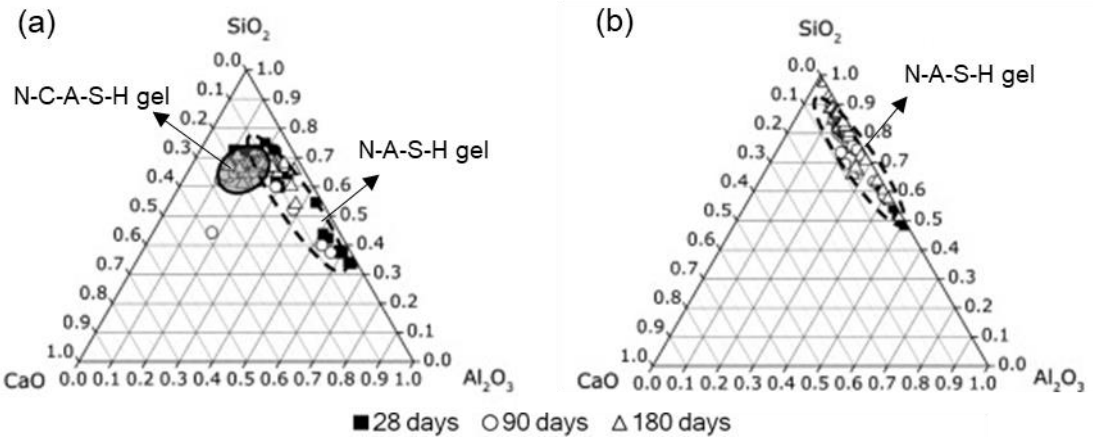

Figure 2.6 Ternary phase diagram of EDX data for (a) alkali-activated slag and fly ash binder with 25 wt.% slag and 75 wt.% fly ash (b) alkali-activated fly ash binder. Data included in the dashed circles correspond to an N-A-S-H gel, and the dashed solid circle to an N-C-A-S-H gel. Redrawn from [16].

Table 2.1 Secondary reaction products in AAFA paste.

Sodium hydroxide-activated system	Sodium silicate-activated system
sodalite [90,96–99], Na-chabazite [90,97], cancrinite [97,99], Na-P1 [90]	sodalite [90,97,100,101], Na-chabazite [90,97,100], cancrinite [97], Linde Type A [90], Na-P1 [90], zeolite P [97,100], zeolite Y [97], natrolite [100], phillipsite [97], faujasite [96]

2.3.2.3 Other reaction products

Apart from N-(C-)A-S-H gel, there could be some crystalline zeolites as the secondary reaction products in AAFA, as summarized in Table 2.1. The presence of zeolite in AAFA mainly depends on the alkaline activator and curing temperature. High temperature is a favorable condition for the formation of zeolite [99,102]. Most studies listed in Table 2.1 employed a curing temperature higher than 80 °C. The type of zeolite in AAFA also varies with different types of alkaline activators. Sodalite (mainly hydroxysodalite) with a Si/Al of 1 is often found in sodium hydroxide-activated systems or low-modulus sodium silicate-activated systems [96,97]. High silicate concentration would hinder the formation of sodalite [75,98]. It is also reported that the soluble silica in the reaction medium can hinder the formation of zeolite at early curing ages [97]. However, it can be seen from Table 2.1 that more types of zeolites are found in sodium silicate-activated systems than in sodium hydroxide-activated systems, as the former offers a wider range of SiO_2/Na_2O, thereby providing more opportunities for the formation of various types of zeolites.

2.3.3 Pore solution of AAFA

Pore solution is also a significant component in AAFA matrix. It can play an important role in the chemical reaction and formation of reaction products, since both the dissolution of fly ash and the formation of reaction products happen in the pore solution. Despite its significance, there are only a few studies devoted to pore solution chemistry of AAFA. Paudel et al. [103] found a decreasing trend of pH in the pore solution of AAFA concrete over time, which was opposite in PC concrete. Williamson et al. [104] reported that, after 7 days, around 75 % of Na in the activator was consumed for the AAFA mortar. Increasing Na concentration in the activator only resulted in a slight increasing Na concentration in the pore solution, indicating that most of the Na ions were consumed. The concentration of various ions in the pore solution of AAFA was studied systematically in Zuo's research [105], where a model was proposed to describe the evolution of the ions concentration in the pore solution of AAFA paste as shown in Figure 2.7. The concentrations of most types of elements, such as Ca, Al and Fe, increase initially due to the dissolution of fly ash, and then decrease with time due to the formation of solid reaction products. The evolution of Si concentration can have three different patterns, depending on the initial Si concentration. In addition, the concentrations of Na and OH^- exhibit a decreasing trend with time, whereas an opposite trend is found for the concentration of S.

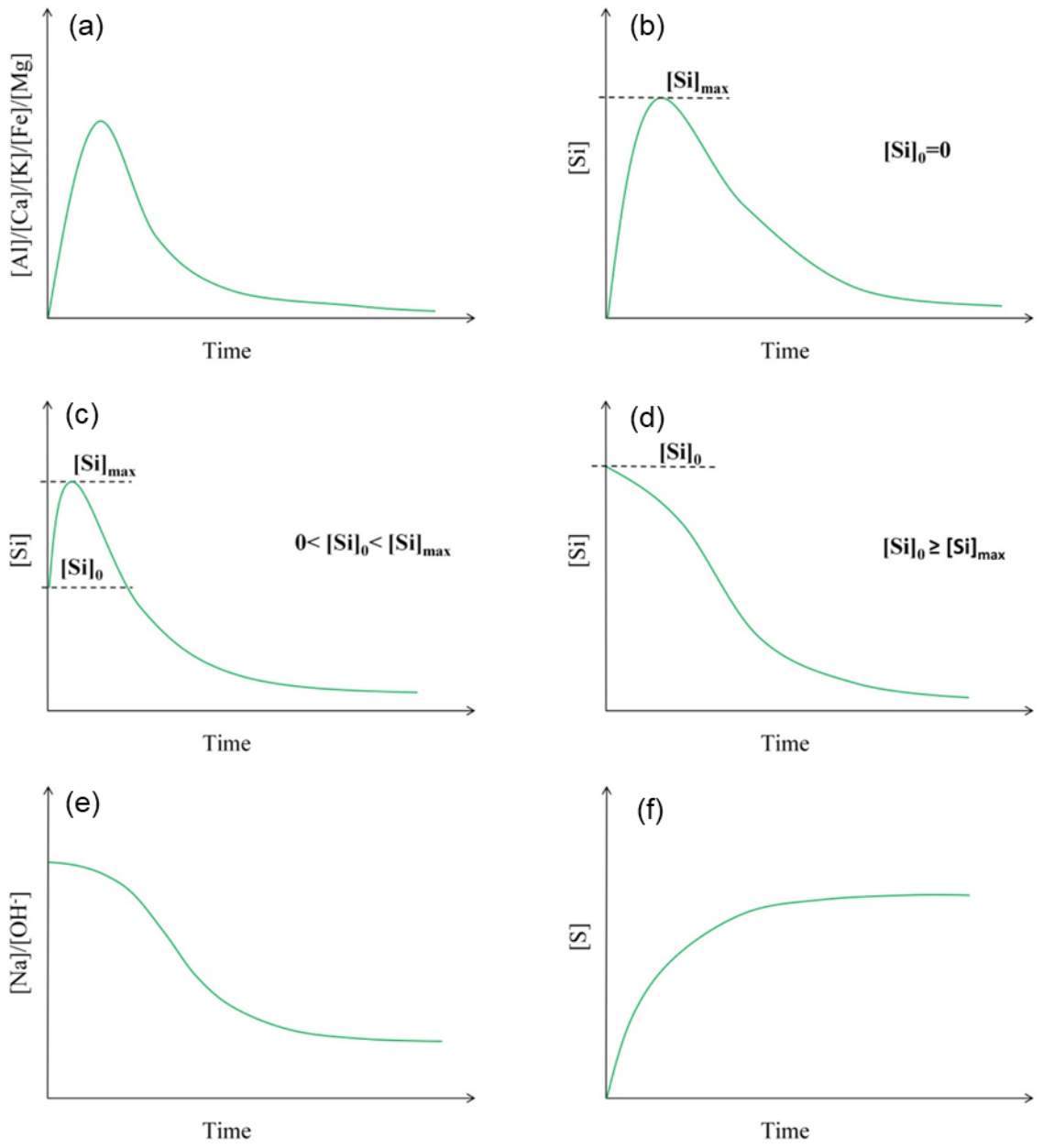

Figure 2.7 Conceptual models of ion concentration development in the pore solution of AAFA paste. (a) Al, Ca, K, Fe and Mg ions, (b) Si ($[Si]_0 = 0$), (c) Si ($0 < [Si]_0 < [Si]_{max}$), (d) Si ($[Si]_0 \geq [Si]_{max}$), (e) Na and OH^-, (f) S. $[Si]_0$ is the concentration of Si in the alkaline activator. $[Si]_{max}$ is the maximum concentration of Si [105].

2.3.4 Microstructure of AAFA

A hardened AAFA matrix contains several phases, i.e. solid reaction products, unreacted fly ash particles and pores, as shown in Figure 2.8 [44]. Note that pore solution cannot be viewed from SEM/BSE image. The effect of the content of SiO_2 in the activator on the microstructure of AAFA has been studied in [96], as shown in Figure 2.9. The results show that the content of SiO_2 in the activator has a considerable influence on the microstructure.

A porous and loose microstructure (Figure 2.9(a) and 2.9(b)) is observed for samples activated by sodium hydroxide or low-modulus sodium silicate, while a dense microstructure (Figure 2.9(c) and 2.9(d)) was formed by using high-modulus sodium silicate activator [96]. Furthermore, a dark grey rim around unreacted fly ash particles was observed in the sodium hydroxide-activated system as shown in Figure 2.9(a), which is attributed to the growth of reaction products on the surface of fly ash grains. On the other hand, due to the presence of soluble Si species in the sodium silicate-activated system, reaction products can participate and grow homogeneously in the matrix.

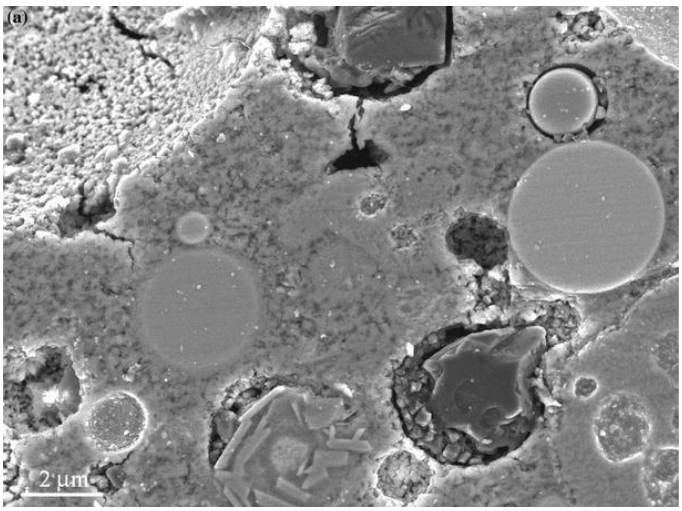

Figure 2.8 BSE image of AAFA showing reaction products, fly ash particles and pores [44].

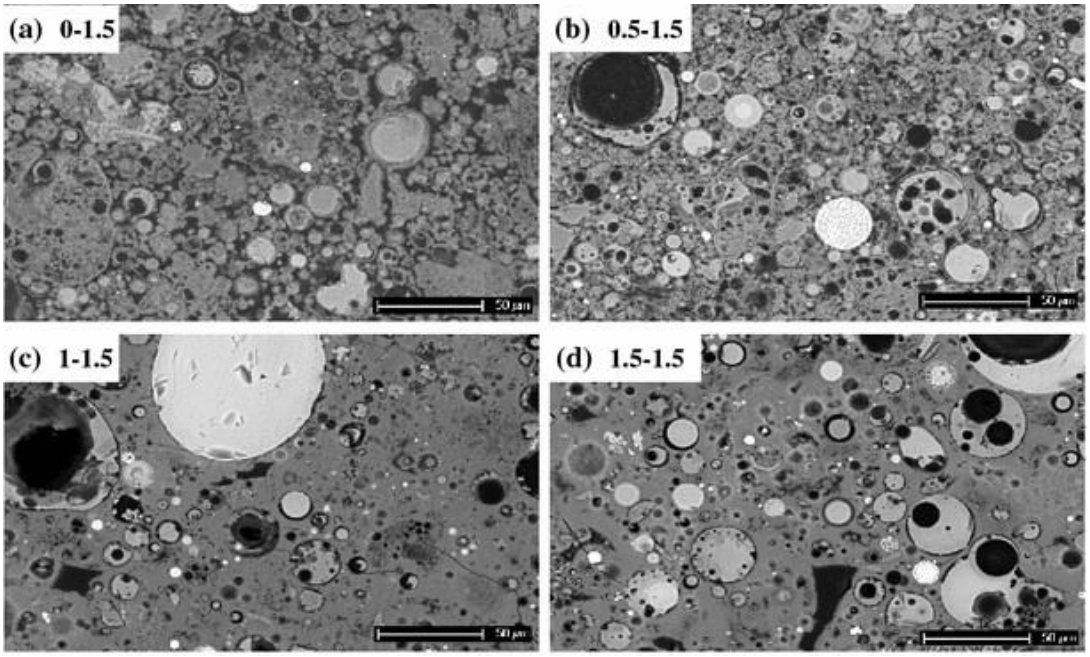

Figure 2.9 BSE images of AAFA activated with sodium hydroxide/sodium silicate after 28 days of curing at 40 °C. The numbers on the label refer to the mol content of SiO_2 and Na_2O with respect to fly ash, respectively [96].

2.4 Simulation studies of AAFA

In addition to experimental techniques, the development of computing power has led to an increasing number of modeling techniques for simulating the reaction and structure of cementitious materials. In terms of characteristic length, the modeling techniques applied to cementitious materials span from macro-, meso-, micro- and nano-scales. This section particularly focuses on the nanoscale and microscale levels, as the research objects of this thesis are below the paste level. At the nanoscale, MD simulation is one of the most widely used methods for investigating the behaviors of atoms and molecules. At the microscale, thermodynamic modeling is a typical tool to study chemical reactions and phase assemblage. In addition, several numerical models, such as GeoMicro3D [40], HYMOSTRUC3D-E [37] and µic [39], have been developed to describe the three-dimensional microstructure of cementitious materials. The application of these simulation techniques has gained remarkable achievement in cement-based materials and exhibited promising potential for AAFA.

2.4.1 Molecular dynamics simulation of AAFA

MD simulation is a powerful method for predicting the evolution of a nanoscale system by tracking the trajectories of atoms and molecules over time using Newton's equations of motion [106]. The interactions between atoms, which govern their movement, are calculated through potential functions. These functions and their associated parameters are collectively known as the force field or interatomic potential. The accuracy and reliability of the simulation depend heavily on the quality of the force field, as it defines the nature and strength of atomic interactions, ultimately determining the precision of the simulation results [107,108]. The properties of a system in equilibrium, e.g. structural, mechanical and transport properties, can be determined by MD simulation, making it a promising tool for studying the nano feature of AAFA [109].

Recently, the atomic structure and mechanical properties of N-A-S-H gel have been studied through MD simulation by using different initial structures and force fields. As N-A-S-H gel shows remarkable similarities with sodium aluminosilicate (NAS) glasses, Sadat et al. [110] built an NAS model from an initial configuration of silica glass to investigate the properties of N-A-S-H gel. They found that the structure of the NAS model, including the amount of edge-sharing tetrahedra, non-bridging oxygen, and pentacoordinate Al atoms, has a huge impact on the mechanical performance. Zhang et al. [111] also constructed an NAS model and then applied the grand-canonical Monte Carlo method to obtain an N-A-S-H model to study the effect of water on the properties of N-A-S-H gel. Using the reactive force field ReaxFF, a new molecular model of N-A-S-H gel was built from a sodalite initial framework, exhibiting full Q^4 polymerization and an X-ray broad peak at 20˚-30˚ 2θ [112]. Wang et al. [113] constructed the N-A-S-H model with a Si/Al of 1 and 2 from $Na_2Si_2O_5$ glass using the COMPASS force field. Instead of using a similar structure as the initial model, Zhang et al. [114] conducted the simulation that started from aluminate and silicate monomers by using a reactive Feuston−Garofalini force field, resulting in the formation of N-A-S-H gel. A similar model construction method was utilized in Guan's research [115], where different types of oligomers with various Si/Al from 1 to 3 were used in the initial structure and the force field

ReaxFF was employed. The type of oligomers has been found to impact the structure of the simulated N-A-S-H gel.

The effect of using different initial configurations and force fields on the structure and properties of modeled N-A-S-H gel has been summarized in [108]. A noticeable difference in the distribution of Si-O-Si and Si-O-Al bond angles using different force fields was observed. It is also reported that reactive force field like ReaxFF is able to form high-coordinated Al atoms, making them more suitable for simulating N-A-S-H gel compared to non-reactive force fields [108]. In addition, the effect of Si/Al ratio on the mechanical properties of N-A-S-H gel is still a matter of debate. In Wang's results [113], N-A-S-H gel with a Si/Al ratio of 1 has a larger elastic modulus than that of 2, whereas elastic modulus showed a mildly increasing trend with an increasing Si/Al ratio in [112,115]. Sadat et al. [110] found that Young's modulus of N-A-S-H gel decreased with Si/Al ratio, while ultimate tensile strength increased with Si/Al ratio from 1 to 3 but decreased with Si/Al ratio from 3 to 4. These discrepancies are probably due to the different modeling methods.

2.4.2 Thermodynamic study of AAFA

Thermodynamic modeling is a theoretically rigorous and computationally efficient tool to predict chemical reactions under thermodynamic equilibrium. For a closed system at constant temperature and pressure, thermodynamic equilibrium means the minimal Gibbs free energy of the system and thus no spontaneous tendency for change [31]. For a given input composition of the system, thermodynamic modeling coupled with relevant thermodynamic databases can compute the equilibrium phase assemblages based on Gibbs free energy minimization. The reliability of thermodynamic modeling results deeply relies on the accuracy of the thermodynamic database [116]. Thermodynamic modeling has been widely used to study the reactions of cement and AAS by using the Cemdata18 thermodynamic database [29,31,32]. However, thermodynamic modeling of AAFA has been rarely reported yet due to the incomplete thermodynamic database of N-(C-)A-S-H gel. Generally, a thermodynamic database contains several parameters, including solubility product, heat capacity, enthalpy, entropy and Gibbs free energy of substances. Among them, solubility product is the key parameter that controls the chemical reaction.

To measure the solubility of N-(C-)A-S-H gel, synthesis of pure N-(C-)A-S-H gel is crucial, after that a solubility test can be performed with the synthesized N-(C-)A-S-H gel. There are mainly three routes to synthesizing N-(C-)A-S-H gel in the literature. The first one is through alkali-activation of synthetic aluminosilicate precursor [24,86]. However, the N-(C-)A-S-H gel formed in this way would most likely contain the unreacted solid precursor. Moreover, crystalline phases like faujasite can form by using this method [34]. Another one involves a 'dissolution-precipitation' process, which utilizes at least one type of solid reactant such as SiO_2 powder [117,118]. However, this approach can suffer from similar limitations as the previous method. For these reasons, pure N-(C-)A-S-H gel has been synthesized more commonly by using the sol-gel method, where only solutions (often sodium silicate and aluminum nitrate solutions) are employed as reactants [35,87,119,120]. N-A-S-H gels with target Si/Al ratio of 1 and 2 have been most commonly synthesized. N-A-S-H gel with a Si/Al

ratio greater than 2 has been rarely reported, although the Si/Al ratio of N-A-S-H gel in AAFA paste can exceed 2 as mentioned above, especially for silicate-activated system. The reason behind it lies in that it could be a challenge to synthesize high Si/Al N-A-S-H gel. Furthermore, the reported Si/Al ratios in synthesized N-A-S-H gels are somewhat inconsistent in the literature. García-Lodeiro et al. [87] and Gomez-Zamorano et al. [35] reported achieving a final Si/Al ratio of 2 with an initial ratio of 2, whereas Williamson et al. [120] only obtained N-A-S-H gel with Si/Al ratio of 1 irrespective of the initial Si/Al ranging from 1 to 2. This also indicates the difficulty of synthesizing high Si/Al N-A-S-H gel.

So far, experimental measurements of the solubility product for N-A-S-H gels have been limited to Si/Al ratios of 1 and 2. No experimental data exists for N-A-S-H gels with Si/Al ratios higher than 2, or for N-C-A-S-H gels. Although Zuo [33] determined the solubility product of N-(C-)A-S-H gel with a Si/Al ratio ranging from 1 to 4 and a fixed Ca/Al ratio of 0.45, this determination was made by optimizing the fit of the thermodynamic model to the chemistry data in the literature. Table 2.2 summarizes the solubility product (expressed in log format) of N-(C-)A-S-H gels based on the given dissolution reactions in different works. It should be noted that it should keep both the chemical formula of N-(C-)A-S-H gel and the dissolution reaction constant when comparing the solubility product. Thus, some log K_{sp} values were recalculated for fair comparison as also shown in Table 2.2. The log K_{sp} values from these studies show significant variability. For instance, the log K_{sp} value of N-A-S-H gel with a Si/Al of 1 ranges from -5.86 [34] to -11.37 [33]. A difference of 1 in log value corresponds to a tenfold difference in the solubility product, leading to substantial discrepancies in thermodynamic modeling calculations. Overall, the existing solubility products of N-(C-)A-S-H gels are not only incomplete but also incompatible.

Table 2.2 Chemical reactions and log K_{sp} values for N-(C-)A-S-H gels. Data from [33–36].

Samples[(a)]	Temperature	Log K_{sp}	Dissolution reactions
NASH1 [33]	25 ˚C	-6.51	$(Na_2O)_{0.5} \cdot (Al_2O_3)_{0.5} \cdot (SiO_2)_1 \cdot (H_2O)_1 + 2OH^- \leftrightarrow SiO_3^{2-} + AlO_2^- + Na^+ + 2H_2O$
		-11.37[(c)]	$(Na_2O)_{0.5} \cdot (Al_2O_3)_{0.5} \cdot (SiO_2)_1 \cdot (H_2O)_1 \leftrightarrow (SiO_2)_{aq} + AlO_2^- + Na^+ + H_2O$
NASH2 [33]	25 ˚C	-8.01	$(Na_2O)_{0.5} \cdot (Al_2O_3)_{0.5} \cdot (SiO_2)_2 \cdot (H_2O)_1 + 4OH^- \leftrightarrow 2SiO_3^{2-} + AlO_2^- + Na^+ + 3H_2O$
		-17.72[(c)]	$(Na_2O)_{0.5} \cdot (Al_2O_3)_{0.5} \cdot (SiO_2)_2 \cdot (H_2O)_1 \leftrightarrow 2(SiO_2)_{aq} + AlO_2^- + Na^+ + H_2O$
NASH3 [33]	25 ˚C	-9.51	$(Na_2O)_{0.5} \cdot (Al_2O_3)_{0.5} \cdot (SiO_2)_3 \cdot (H_2O)_1 + 6OH^- \leftrightarrow 3SiO_3^{2-} + AlO_2^- + Na^+ + 4H_2O$
		-24.09[(c)]	$(Na_2O)_{0.5} \cdot (Al_2O_3)_{0.5} \cdot (SiO_2)_3 \cdot (H_2O)_1 \leftrightarrow 3(SiO_2)_{aq} + AlO_2^- + Na^+ + H_2O$
NASH4 [33]	25 ˚C	-11.01	$(Na_2O)_{0.5} \cdot (Al_2O_3)_{0.5} \cdot (SiO_2)_4 \cdot (H_2O)_1 + 8OH^- \leftrightarrow 4SiO_3^{2-} + AlO_2^- + Na^+ + 5H_2O$
		-30.44[(c)]	$(Na_2O)_{0.5} \cdot (Al_2O_3)_{0.5} \cdot (SiO_2)_4 \cdot (H_2O)_1 \leftrightarrow 4(SiO_2)_{aq} + AlO_2^- + Na^+ + H_2O$

Table 2.2 (continued) Chemical reactions and log K_{sp} values for N-(C-)A-S-H gels. Data from [33–36].

NASH1 [34]	25 ˚C	-5.86[(b)]	$(Na_2O)_{0.3} \cdot (Al_2O_3)_{0.49} \cdot (SiO_2)_1 \cdot (H_2O)_n - 0.38OH^- \leftrightarrow (SiO_2)_{aq} + 0.98AlO_2^- + 0.6Na^+ + (n\text{-}0.19)H_2O$
NASH2 [34]	25 ˚C	-9.89[(b)]	$(Na_2O)_{0.38} \cdot (Al_2O_3)_{0.47} \cdot (SiO_2)_2 \cdot (H_2O)_n - 0.18OH^- \leftrightarrow 2(SiO_2)_{aq} + 0.94AlO_2^- + 0.76Na^+ + (n\text{-}0.09)H_2O$
NASH1 [35]	25 ˚C	-9.05	$(Na_2O)_{0.45} \cdot (Al_2O_3)_{0.45} \cdot (SiO_2)_1 \cdot (H_2O)_{2.48} \leftrightarrow (SiO_2)_{aq} + 0.9AlO_2^- + 0.9Na^+ + 2.48H_2O$
	50 ˚C	-8.65	
NASH2 [35]	25 ˚C	-13.16	$(Na_2O)_{0.52} \cdot (Al_2O_3)_{0.48} \cdot (SiO_2)_2 \cdot (H_2O)_{3.76} \leftrightarrow 1.92(SiO_2)_{aq} + 0.08HSiO_3^- + 0.96AlO_2^- + 1.04Na^+ + 3.68H_2O$
	50 ˚C	-12.20	
	25 ˚C	-13.50[(c)]	$(Na_2O)_{0.52} \cdot (Al_2O_3)_{0.48} \cdot (SiO_2)_2 \cdot (H_2O)_{3.76} \leftrightarrow 2(SiO_2)_{aq} + 0.96AlO_2^- + 1.04Na^+ + 0.08OH^- + 3.68H_2O$
	50 ˚C	-12.51[(c)]	
NASH1 [36]	50 ˚C	-3.16	$(Na_2O)_{0.51} \cdot (Al_2O_3)_{0.51} \cdot (SiO_2)_1 \cdot (H_2O)_n + 2OH^- \leftrightarrow H_2SiO_4^{2-} + 1.02Al(OH)_4^- + 1.02Na^+ + (n-2)H_2O$
		-7.59[(c)]	$(Na_2O)_{0.51} \cdot (Al_2O_3)_{0.51} \cdot (SiO_2)_1 \cdot (H_2O)_n \leftrightarrow (SiO_2)_{aq} + 1.02Al(OH)_4^- + 1.02Na^+ + (n-2)H_2O$
Faujasite[(d)] [36]	50 ˚C	-5.82	$(Na_2O)_{0.51} \cdot (Al_2O_3)_{0.51} \cdot (SiO_2)_1 \cdot (H_2O)_n + 2OH^- \leftrightarrow H_2SiO_4^{2-} + 1.02Al(OH)_4^- + 1.02Na^+ + (n-2)H_2O$
		-10.24[(c)]	$(Na_2O)_{0.51} \cdot (Al_2O_3)_{0.51} \cdot (SiO_2)_1 \cdot (H_2O)_n \leftrightarrow (SiO_2)_{aq} + 1.02Al(OH)_4^- + 1.02Na^+ + (n-2)H_2O$
NCASH1 [33]	25 ˚C	-8.51	$(Na_2O)_{0.05} \cdot (CaO)_{0.45} \cdot (Al_2O_3)_{0.5} \cdot (SiO_2)_1 \cdot (H_2O)_1 + 2OH^- \leftrightarrow SiO_3^{2-} + AlO_2^- + 0.45Ca^{2+} + 0.1Na^+ + 2H_2O$
NCASH2 [33]	25 ˚C	-10.01	$(Na_2O)_{0.05} \cdot (CaO)_{0.45} \cdot (Al_2O_3)_{0.5} \cdot (SiO_2)_2 \cdot (H_2O)_1 + 4OH^- \leftrightarrow 2SiO_3^{2-} + AlO_2^- + 0.45Ca^{2+} + 0.1Na^+ + 3H_2O$
NCASH3 [33]	25 ˚C	-11.51	$(Na_2O)_{0.05} \cdot (CaO)_{0.45} \cdot (Al_2O_3)_{0.5} \cdot (SiO_2)_3 \cdot (H_2O)_1 + 6OH^- \leftrightarrow 3SiO_3^{2-} + AlO_2^- + 0.45Ca^{2+} + 0.1Na^+ + 4H_2O$
NCASH4 [33]	25 ˚C	-13.01	$(Na_2O)_{0.05} \cdot (CaO)_{0.45} \cdot (Al_2O_3)_{0.5} \cdot (SiO_2)_4 \cdot (H_2O)_1 + 8OH^- \leftrightarrow 4SiO_3^{2-} + AlO_2^- + 0.45Ca^{2+} + 0.1Na^+ + 5H_2O$

[(a)]: The number after 'NASH' or 'NCASH' refers to the Si/Al ratio. For instance, NASH1 stands for N-A-S-H gel with a Si/Al ratio of 1, NCASH1 stands for N-A-S-H gel with a Si/Al ratio of 1.
[(b)]: The log K_{sp} is taken from the results at 28 days, which is almost identical to those at 90 days.
[(c)]: Re-calculation based on $(SiO_2)_{aq}$ species for comparison.
[(d)]: Crystalline N-A-S-H.

With the determined solubility product, the standard Gibbs free energy of reaction $\Delta_r G^0$ and thus the standard Gibbs free energy of formation $\Delta_f G^0$ of N-(C-)A-S-H gel can be calculated from Equation 2.4 with the known solubility product in [33–35]:

$$\Delta_r G^0 = -RT \ln K_{sp} = \sum_i v_i \, \Delta_f G_i^0 \tag{2.4}$$

where v_i is the stoichiometric reaction coefficient.

The standard heat capacity and entropy of N-(C-)A-S-H gel, seldom reported, can be determined using the additivity method [121–123]. The standard enthalpy of formation of the N-(C-)A-S-H gel can be calculated from the standard entropy and Gibbs free energy.

Apart from thermodynamic data of N-(C-)A-S-H gel, a thermodynamic database for zeolite, the secondary reaction product of AAFA, is also needed to perform thermodynamic modeling of AAFA. Ma et al. [124,125] measured the solubility products of various zeolites, thereby proposing a thermodynamic database for zeolites. Together with the fitting-derived database of N-(C-)A-S-H gel, Zuo [33] carried out thermodynamic modeling of AAFA reaction using GEMS. The evolution of the phase assemblages in AAFA paste over time is shown in Figure 2.10. It can be seen that N-(C-)A-S-H gel was the main reaction product in sodium hydroxide-activated system and sodium silicate-activated system, while natrolite, a type of zeolite, was found as the secondary reaction product. However, the thermodynamic results have not been validated by experiment. Especially, the existence of goethite, portlandite and brucite in AAFA has not been reported in the existing literature.

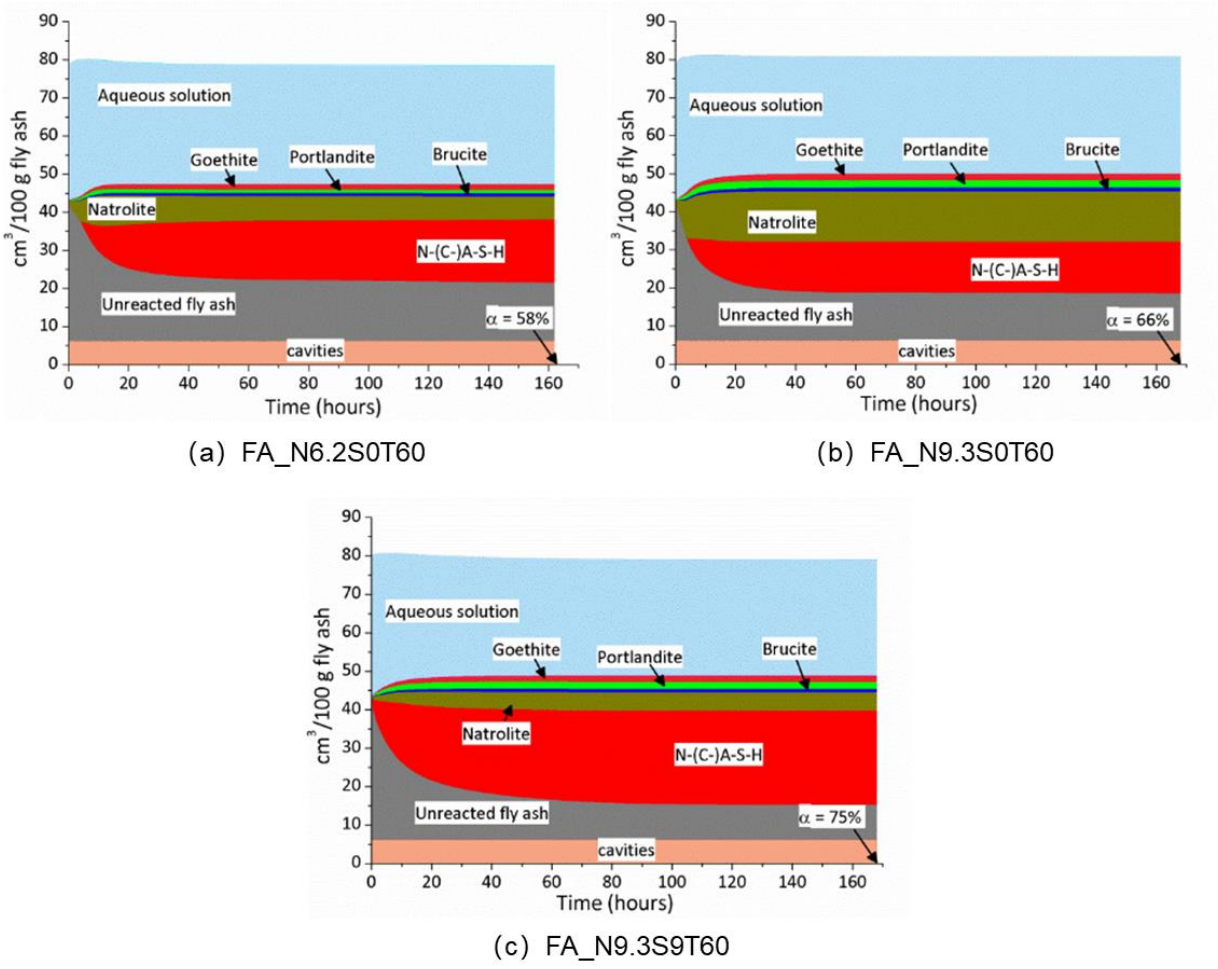

Figure 2.10 Thermodynamic modeling of AAFA reaction at 60 ˚C. In the notations, N and S stand for the weight percentages of Na_2O and SiO_2 with respect to fly ash [33].

2.4.3 Reaction and microstructural simulation - GeoMicro3D

Most numerical models for microstructural development, such as HYMOSTRUC3D-E [37] and µic [39], have been developed for PC-based cementitious materials, which are not the focus of this thesis and will not be discussed here. To date, no studies have been reported on simulating the 3D microstructure of AAFA. However, the GeoMicro3D model [40] has been designed to simulate the chemical reaction and 3D microstructure development of AAS. In this model, the reaction degree, phase assemblages and 3D microstructure of AAS can be simulated with the physicochemical information of raw materials and mixture as input.

Given that both AAFA and AAS are classified as AAMs, it is worthwhile to explore the potential for extending the GeoMicro3D model to AAFA systems. The following section presents the underlying mechanism by which the GeoMicro3D program functions. First of all, the spatial distribution of real-shape slag particles in the liquid alkaline activator was simulated by Anm materials model [126]. Under the attack of alkali, the dissolution of slag was described through the dissolution of single oxide, e.g. SiO_2, Al_2O_3, CaO, according to

transition state theory (See section 2.3.1.1). After dissolution, the diffusion of dissolved ions was modelled by lattice Boltzmann method (LMB) [127,128]. Once the system reaches the state of saturation or oversaturation as the proceeding of dissolution, the probability of nucleation was described by the Poisson distribution [129], while the formation of reaction products were modelled quantitatively through thermodynamic modeling. This algorithm (see Figure 2.11) can be adapted for AAFA if these critical issues can be addressed: (a) the dissolution rate of fly ash and (b) thermodynamic modeling of AAFA.

Figure 2.12 shows a case study of GeoMicro3D applied to AAS paste [40]. The development of 3D microstructure of AAS with visualized phases including slag, reaction products and pores was simulated. Furthermore, the simulation results of AAS at 28 days showed a comparable degree of reaction, capillary porosity and ion concentration in the pore solution with experimental data, indicating the robustness of GeoMicro3D model. The appealing results suggest that GeoMicro3D can be developed to a promising tool to simulate the 3D microstructure development of AAFA. A more detailed introduction of GeoMicro3D model will be given in Chapter 7.

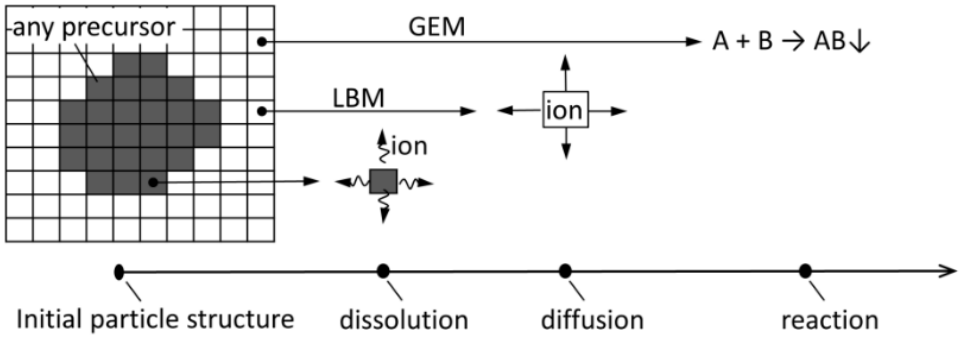

Figure 2.11 Schematic algorithm of GeoMicro3D. A and B denote ions. AB denotes a solid reaction product [33].

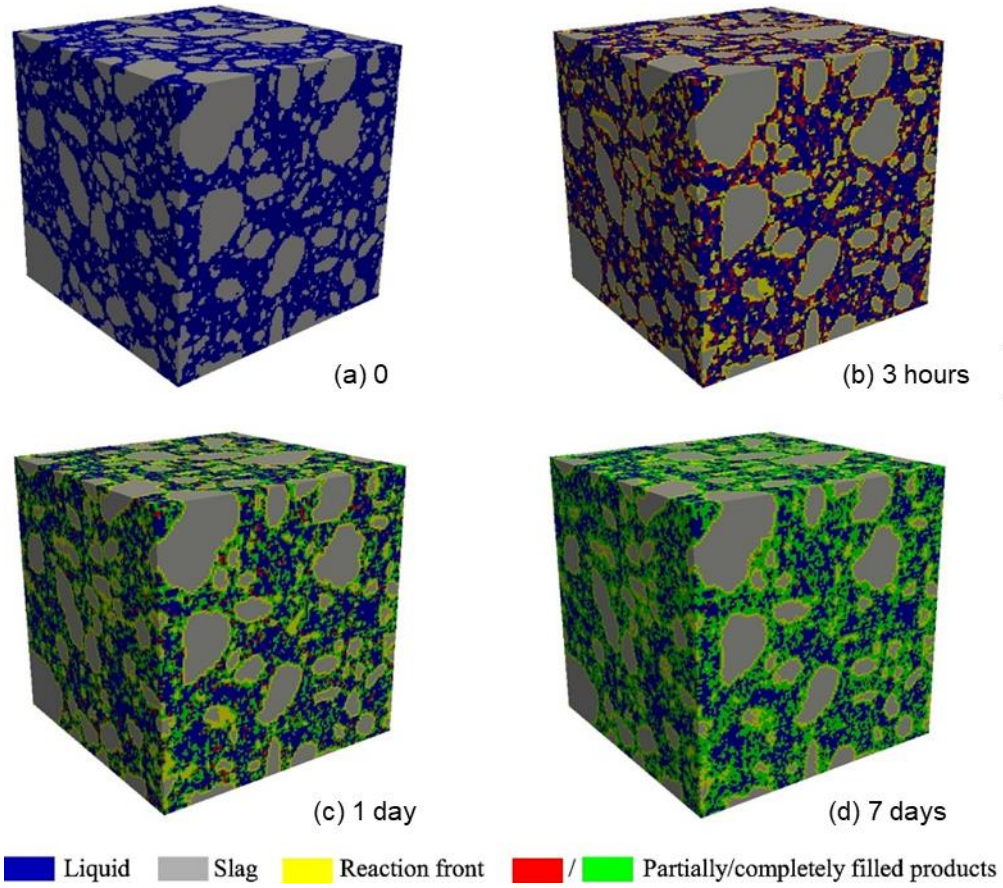

Figure 2.12 3D microstructure of AAS at different ages with a simulation size of 125 µm × 125 µm × 125 µm [40].

2.5 Summary of the literature study and research gap

Based on the state of the art in the experimental and numerical studies on the reaction and microstructure of AAFA, the summary and research gap can be drawn:

1. Dissolution of fly ash is the first step of AAFA reactions. The dissolution rate of fly ash is influenced by many parameters such as chemical composition of fly ash, pH of the solution, and temperature. So far, only a few models have been proposed to describe the dissolution of fly ash or silicate glass. However, a model that considers the effect of all important variables on the dissolution rate of fly ash is still lacking.
2. Reaction products of AAFA contain N-(C-)A-S-H gel with various Si/Al ratios and different types of zeolites. The chemical composition and type of reaction products are strongly dependent on the chemistry of raw materials, mixture design and curing conditions. However, the possible range of Si/Al of N-(C-)A-S-H gel in AAFA paste remains uncertain. Accurate determination through experimental techniques is challenging primarily due to potential interference from other phases.
3. MD simulation offers a promising opportunity to study the atomic nature of N-(C-)A-S-H gel. Different initial configurations and force fields have been used to construct

N-A-S-(H) gel model by MD simulation. However, MD simulation of N-(C-)A-S-H gel to investigate its chemical composition, specifically the Si/Al and Ca/Al ratios, has not yet been reported.

4. Thermodynamic modeling coupled with thermodynamic databases is a powerful tool to study chemical reactions and predict the equilibrium phase assemblages. While thermodynamic databases for various zeolites have been developed, the database for N-(C-)A-S-H gels remains incomplete. The solubility product values of N-A-S-H gels with Si/Al ratios from 1 to 2, as determined through solubility experiments, are inconsistent in the literature. Furthermore, there is a notable absence of reported solubility product values for N-A-S-H gels with Si/Al ratios exceeding 2 and for N-C-A-S-H gel. Consequently, the scope of thermodynamic modeling for AAFA has been constrained due to these limitations.
5. Synthesis of N-(C-)A-S-H gel facilitates the exploration of the solubility product of pure N-(C-)A-S-H gel. However, synthesis of N-A-S-H gel with a Si/Al higher than 2 has not been reported in the literature. In addition, the condition for the synthesis of N-A-S-H gel with a Si/Al of 2 is still a matter of debate. In summary, there is a need to delve into the methodology for synthesizing N-(C-)A-S-H gel to address these gaps in knowledge.
6. No numerical model currently exists for predicting the evolution of 3D microstructure of AAFA, which limits the ability to further predict its microstructure-related properties. GeoMicro3D is a dedicated numerical model for 3D microstructure of AAS, which covers particle parking, dissolution of slag, diffusion of ions, nucleation and thermodynamic modeling. However, to extend GeoMicro3D for the prediction of 3D microstructural development of AAFA, the development of fly ash dissolution model and the implementation of thermodynamic modeling of AAFA are two main challenges to be addressed.

Chapter 3

Molecular dynamics simulation of N-(C-)A-S-H gel

3.1 Introduction

Sodium aluminosilicate hydrate (N-A-S-H) gel is the primary reaction product of alkali-activated fly ash (AAFA) paste. The hyphen in N-A-S-H indicates an uncertain stoichiometry with a main variable Si/Al ratio. Multiple factors, such as the chemical composition of fly ash, type and dosage of alkaline activator, curing time and temperature, can affect the Si/Al ratio of N-A-S-H gel [84,85,89]. As a result, the reported range of Si/Al ratio in N-A-S-H gel varies a lot in the literature [21,89–91], as reviewed in Chapter 2. Furthermore, the accuracy of Si/Al ratio characterization by NMR or SEM-EDS is questionable, especially in silicate-activated systems, where silicate species from the activator can interfere, potentially leading to overestimation. Given that N-A-S-H gel is difficult to separate from the hardened AAFA paste, any attempts to measure the Si/Al ratio using experimental techniques would always face the problem mentioned above. Apart from that, fly ash usually contains a few amounts of calcium, which can readily combine with N-A-S-H gel to form N-(C-)A-S-H gel [16,94]. However, there has been limited research on determining the amount of Ca that can be incorporated into N-A-S-H gel in AAFA paste. The uncertainties of chemical compositions and atomic structure of N-(C-)A-S-H gel pose a significant challenge to understanding the reaction and microstructure of AAFA paste.

Molecular dynamics (MD) simulation has offered a potential approach to explore the chemical composition as well as the nano-structure of N-(C-)A-S-H gel. Several N-A-S-H gel models have been built using MD simulation as reviewed in Chapter 2. However, most of these models were constructed empirically based on a specific structure like a zeolite or aluminosilicate glass, which is not suitable for investigating the range of the chemical compositions of N-A-S-H gels. In addition, MD simulation of N-C-A-S-H gel has not been reported yet.

In this chapter, the formation of N-(C-)A-S-H gels with different Si/Al ratios and Ca/Al ratios is investigated by MD simulation. Instead of using a zeolite or aluminosilicate glass phase as the initial configuration, the N-(C-)A-S-H gel model is obtained from the reaction of Si monomers and Al monomers. The route to construct N-(C-)A-S-H gel model is derived from the polymerization of silica sols introduced by Feuston [130]. Similar approaches have been applied successfully to model the formation of C-S-H structure [131] and geopolymer gel [114]. This method enables to mimic the polymerization process and provides a possible range of chemical composition of N-(C-)A-S-H gel. Meanwhile, a detailed analysis is performed on the final simulated structure, including chemical formula, bonding information, X-ray diffraction, and Q^n distribution. The results and conclusions obtained in this chapter can provide insight into the chemical and structural information of N-(C-)A-S-H gel, which will guide the synthesis of N-(C-)A-S-H gel in Chapter 4.

3.2 Methodology

3.2.1 Model construction

The initial configuration of the model was built using the PACKMOL package [132]. $Si(OH)_4$, $Al(OH)_3$, NaOH and $Ca(OH)_2$ (optional) molecules were placed randomly in a cubic box. The minimum size of the simulation box should be larger than the size that can reveal the general features of the simulated structure, whereas the maximum size of the simulation box should be determined also based on the computational efficiency. Considering these two concerns, the size of the simulation box was set at 25 × 25 × 25 $Å^3$. A similar size of simulation box was used in [111,114]. The molecules in the box were distant from each other by at least 2 Å. According to the chemical compositions of worldwide coal fly ash in [133], the maximum Si/Al in fly ash mostly located in 1.5-3.0, while the majority of minimum Si/Al in fly ash is around 1.0-1.3. Given that silicate activators introduce extra SiO_2, the Si/Al ratio in silicate-activated fly ash paste is slightly higher than that in fly ash. Hence, in order to encompass the prevailing Si/Al ratio variations in AAFA, the initial Si/Al ratio was set from 1.0 to 4.0 to represent the typical Si/Al ratios encountered in AAFA compositions. The Na/Al ratio was fixed at 1 to maintain the charge balance. To study the effect of Ca on N-A-S-H gel, extra $Ca(OH)_2$ was added to the system with a Ca/Al ratio of 0.25 and 0.5, which can cover the Ca/Al ratio in fly ash according to [133]. For the N-A-S-H system, the density of the system was set at around 2 g/cm^3, which was aligned with [134,135], while slightly elevated (around 2.3 g/cm^3) for the N-C-A-S-H system. The amounts of different types of molecules can be determined based on the density, Si/Al and Ca/Al ratio, as exemplified in Table 3.1.

With the initial configuration, MD simulation was executed by employing the large-scale atomic/molecular massively parallel simulator (LAMMPS) [136]. As explained in Chapter 2, the interaction between atoms in MD simulation is described in a force field. In this work, a reactive force field (ReaxFF), developed by van Duin [137], was adopted to describe the interactions among the atoms and molecules, as ReaxFF is capable of simulating chemical reactions. The detailed potential functions and parameters can be found in [138–140].

Table 3.1 The composition and density of initial configurations (in a cubic box with a size of 25 × 25 × 25 $Å^3$).

Si/Al	Ca/Al	Number of $Si(OH)_4$	Number of $Al(OH)_3$	Number of NaOH	Number of $Ca(OH)_2$	Density(g/cm^3)
1.0	-	92	92	92	-	2.10
1.5	-	108	72	72	-	2.01
2	-	117	65	65	-	2.02
2.5	-	130	52	52	-	1.99
3.0	-	138	46	46	-	1.99
4.0	-	144	36	36	-	1.93
3.0	0.25	156	52	52	13	2.35
3.0	0.5	150	50	50	25	2.36

The simulation spanned a total duration of 2150 picoseconds (ps) with a time step of 0.25 femtoseconds (fs). It comprised several distinct stages: First, the system was relaxed in the Canonical ensemble (NVT) at 300 K for 100 ps to mitigate the impact of the initial arbitrary arrangement. Then, the temperature was raised linearly up to 2000 K for the next 100 ps and subsequently kept at 2000 K for 1000 ps. The velocity of atoms is controlled by temperature in MD simulation. Hence, high temperature was adopted to accelerate the chemical reaction. Next, the system was cooled down to 300 K at a rate of 2.2 K/ps. Finally, equilibrium was achieved at 300 K for 200 ps, resulting in a system comprising N-(C-)A-S-H cluster, water molecules and other small species.

3.2.2 Chemical and structural characterization

Visual Molecular Dynamics (VMD) software [141] was used to visualize the snapshots of the model. N-(C-)A-S-H cluster was obtained from the generated system configuration using Open Visualization Tool (OVITO) [142] with the following pair-wise cutoff radii as a criterion: 1.9 Å for Si-O, 2.0 Å for Al-O, 1.06 Å for H-O, 3.5 Å for Na-Al and 2.7 Å for Ca-O. These cutoff radii serve as distance thresholds to establish bonding interactions, thereby determining which atoms are considered as a part of the N-(C-)A-S-H cluster. Several structural features of the simulated N-(C-)A-S-H cluster were analyzed: (a) Bond length and bond angle were calculated based on the coordinate information. (b) The X-ray diffraction (XRD) patterns were obtained by the virtual diffraction method [143] implemented in LAMMPS. (c) Q^n distribution was calculated by counting the number of different types of Q^n to reveal the topology of the N-(C-)A-S-H gel. Note that the results in this research are the average of the simulations based on the three different initial configurations of the system.

3.3 The effect of Si/Al ratio on the formation of N-A-S-H gel

3.3.1 Polymerization process

During simulation, $Si(OH)_4$ and $Al(OH)_3$ monomers went through a polymerization process and eventually formed a three-dimensional crosslinked structure. The polymerization process can be revealed by the evolution of Q^n, which represents the environment of Si or Al, including Si sites (Si^n) and Al sites (Al^n). The superscript n (n=0-4 in a tetrahedron) stands for the number of bridging oxygen that Si or Al is bonded. A schematic diagram for different Q^n sites is shown in Figure 3.1 Generally, Q^1 belongs to the end sites; Q^2 represents the middle groups in chains or cycles; Q^3 refers to branched structure; and Q^4 denotes a fully crosslinked structure, like rings or cages [144,145].

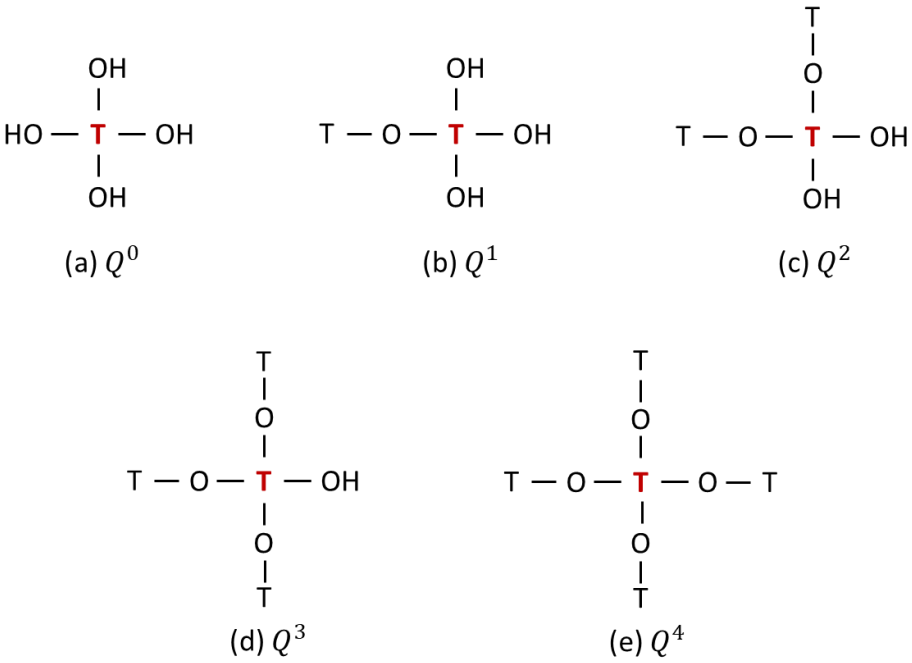

Figure 3.1 Schematic diagram for different Q^n sites. T refers to the Si or Al atom.

Figure 3.2 shows the evolution of Q^n in the system with Si/Al ratio of 1.0. The other Si/Al ratios exhibit a similar trend, which can be found in Appendix A. It can be seen from Figure 3.2 that Q^0 occupied 100 % at the beginning, which represented $Si(OH)_4$ and $Al(OH)_3$ monomers. All $Si(OH)_4$ and $Al(OH)_3$ monomers stayed randomly without any contact in the initial configuration.

For Si sites, as simulation time went by, Si^0 decreased since it reacted and transferred to higher polymerized sites Q^n (n=1-4). Meanwhile, Si^1 emerged first, followed by Si^2, Si^3 and Si^4 in sequence. It indicates that monomers reacted to form oligomers, and then large clusters were formed by the polymerization of oligomers. The amount of Si^n mainly fluctuated at the beginning and reached an equilibrium state after 1250 ps. After simulation for 2150 ps, most Si^0 sites were consumed, whereas a small amount of Si^0 remained unreacted. This is because a 100 % reaction degree is not possible to achieve on a realistic computational timescale.

For Al sites, the development mirrored that of Si sites, following a similar polymerization process but with some differences. First, all Al^0 sites were consumed completely at the end. Additionally, some pentacoordinated Al (Al^5) and trace quantities of six-coordinated Al (Al^6) were found besides tetracoordinated Al (Al^1, Al^2, Al^3 and Al^4). Note that the superscripts in Al^5 and Al^6 are different from those in Al^n (n=1-4) sites, where n stands for the number of bridging oxygen, while the superscripts in Al^5 and Al^6 denote the coordination number of Al. The schematic of Al^n (n=1-4), Al^5 and Al^6 is presented in Figure 3.3 to show their structural differences. The presence of Al^5 and Al^6 will be further discussed below. In addition, The number of Al^n sites changed during 1250-1875 ps as the temperature decreased from 2000 K to 300 K, primarily affecting the evolution of Al^4 and Al^5 sites, as Al^5 site became more stable at lower temperatures. Overall, the simulation process is in accordance with the geopolymerization process in practice [13,146].

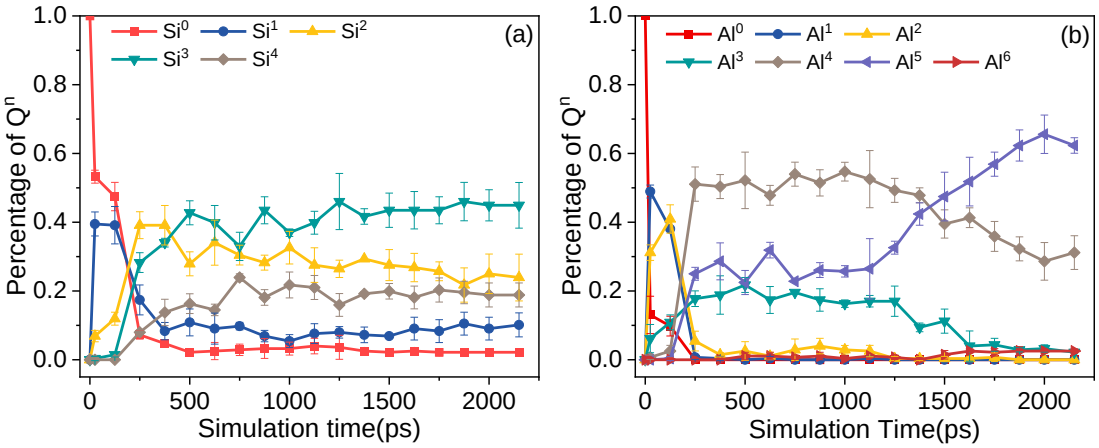

Figure 3.2 Evolution of Q^n sites for (a) Si sites and (b) Al sites in the case of Si/Al=1.0.

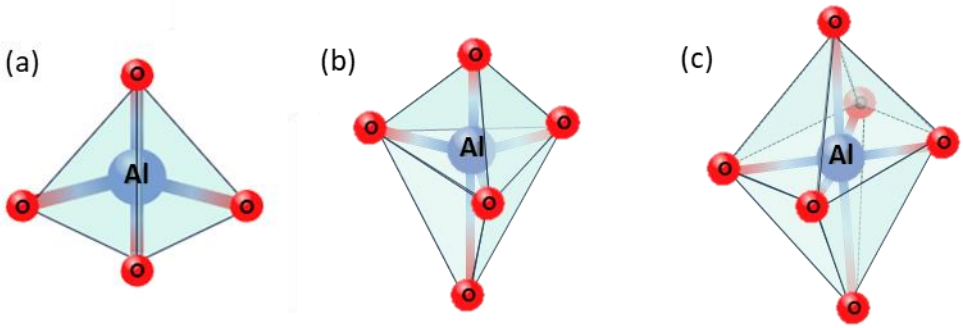

Figure 3.3 Schematic diagram for (a) Al^n (n=1-4) tetrahedron, (b) Al^5 trigonal bipyramidal and (c) Al^6 octahedron.

Si/Al ratio is found to impact the reaction rate, which can be revealed by the amounts of reactants, i.e. Si^0 and Al^0 sites, over time, as shown in Figure 3.4. It's clear that Si^0 declines the most rapidly and dramatically at the lowest Si/Al ratio. The decreasing rate of Si^0 becomes progressively slower with a higher Si/Al ratio, resulting in a larger fraction of the remaining Si^0. In contrast, the effect of the Si/Al ratio has a less pronounced effect on the reaction rate of Al sites. It can be seen that the percentage of Al^0 sites plummet to 0 at the early stage regardless of the Si/Al ratios. Besides, Al is consumed earlier and faster than Si according to their decreasing trend, which is in accord with the experimental finding that Al-rich gel forms early and transforms into Si-rich gel later during polymerization [75,85]. As the Al^0 sites are all consumed, the reaction degree can be basically expressed by the proportion of consumed Si^0, i.e. 1 minus the proportion of remaining Si^0. The reaction degree, as shown in Figure 3.5, is above 85 % regardless of the Si/Al ratio. Moreover, the system with a lower Si/Al ratio can have a higher reaction degree.

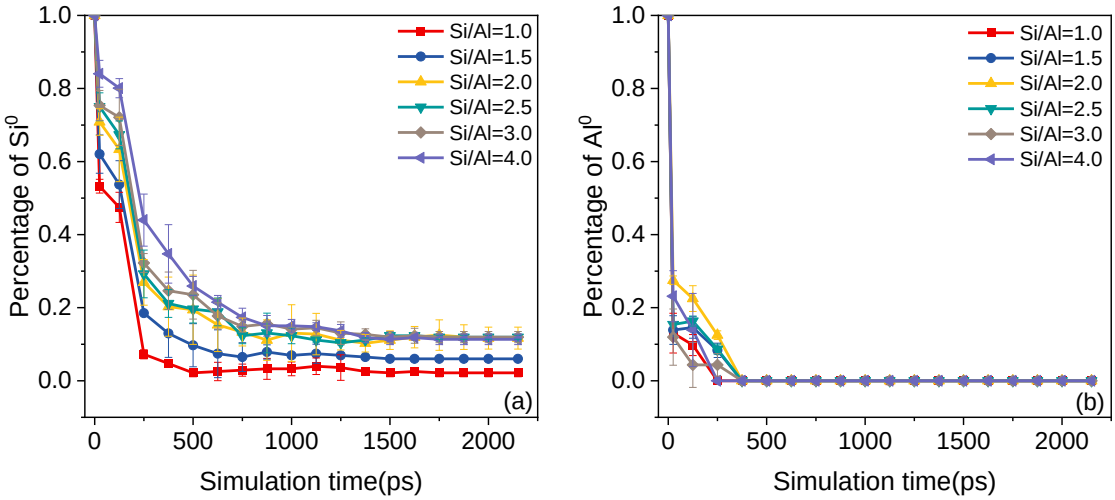

Figure 3.4 Evolution of (a) Si^0 and (b) Al^0 sites as time at different Si/Al ratios.

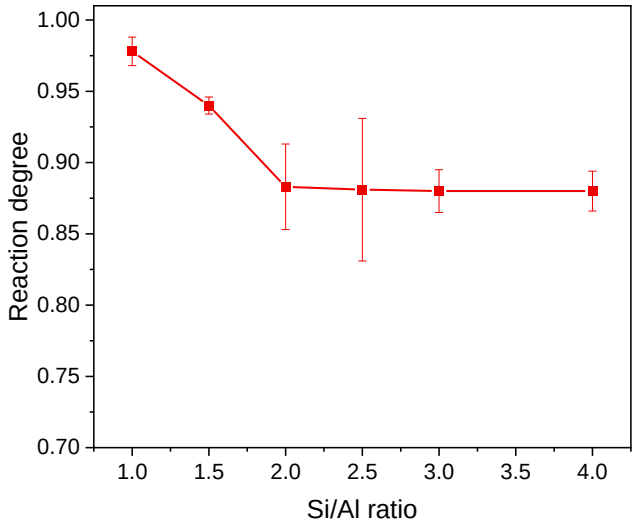

Figure 3.5 Effect of Si/Al ratio on the reaction degree.

After polymerization, the final configurations with different Si/Al ratios all contain a 3D crosslinked network (the biggest cluster, proved to be N-A-S-H gel hereinafter), some small species, water molecules and individual atoms. Among them, N-A-S-H gel, the oligomers and water molecules are the reaction products, while the rest species and individual atoms are the unreacted components. Figure 3.6(a) provides a snapshot of one of the final configurations, illustrating this assemblage. The biggest cluster was extracted from the whole system, as shown in Figure 3.6(b), to further study the chemical composition and structure of N-A-S-H gel formed. All of the Si atoms (green particles) are arranged in a tetrahedral unit within the structure of N-A-S-H gel, while Al atoms (blue particles) exhibit a polyhedral configuration, including the tetrahedral structure for Al^4 site and the trigonal bipyramidal structure for Al^5 site. Sodium atoms (yellow particles) stay in the space within the oligomers.

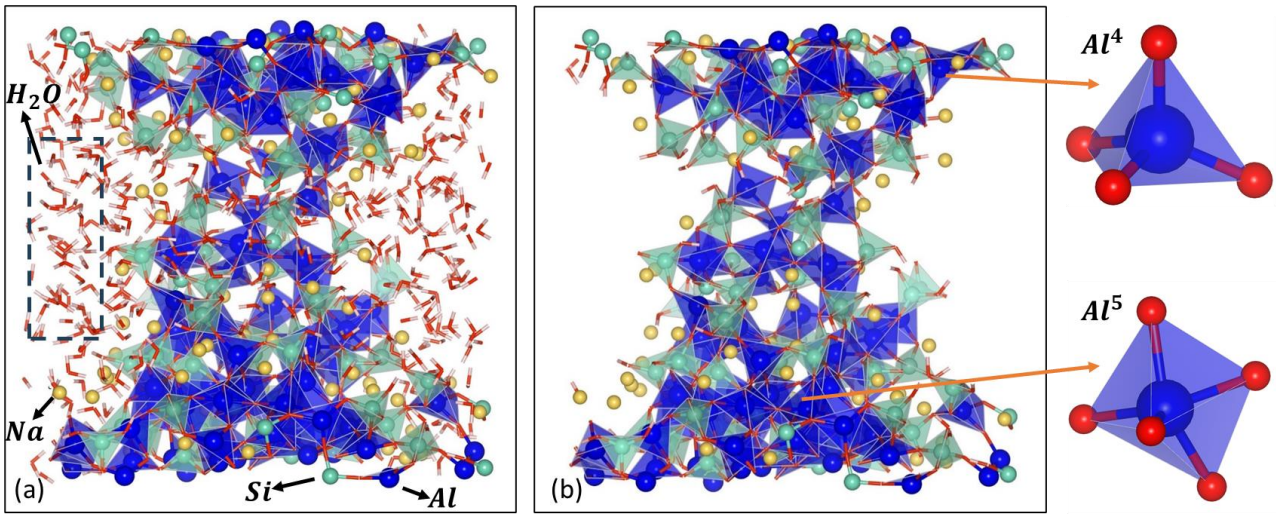

Figure 3.6 Snapshot of (a) the whole system and (b) N-A-S-H gel model for Si/Al=1; Green refers to Si, blue refers to Al, red refers to O, pink refers to H, and yellow refers to Na.

3.3.2 Chemical and structural properties of simulated N-A-S-H gel

3.3.2.1 Chemical composition

The Si/Al ratio and the chemical composition of the obtained N-A-S-H gel (e.g. Figure 3.6(b)) are shown in Table 3.2. The Si/Al ratio of the obtained N-A-S-H gel is slightly lower than the initial Si/Al ratio. This difference is increasingly obvious with a higher Si/Al ratio. This is because more Si remained as Si^0 site in a system with a higher Si/Al ratio as can be seen in Figure 3.4. Moreover, the Si/Al ratio of the obtained N-A-S-H gel in all systems is below 3, indicating that the formation of N-A-S-H gel with a high Si/Al ratio (higher than 3) is not preferable. The reason behind this relates to the bond energy of Si-O-Al and Si-O-Si, which will be discussed hereinafter. It should be noted that the Si/Al ratio in the following parts still refers to the initial Si/Al ratio in the system in order to keep consistent with earlier discussions.

Table 3.2 Chemical composition of the N-A-S-H gel model with various initial Si/Al ratios.

Initial Si/Al ratio	Si/Al ratio in simulated N-A-S-H gel	Formula of simulated N-A-S-H gel*
1.0	0.98±0.01	$Na_{77}Al_{92}Si_{91}O_{404}H_{91}$
1.5	1.40±0.03	$Na_{58}Al_{72}Si_{102}O_{402}H_{122}$
2.0	1.63±0.13	$Na_{52}Al_{60}Si_{106}O_{397}H_{138}$
2.5	2.01±0.04	$Na_{37}Al_{52}Si_{103}O_{378}H_{151}$
3.0	2.23±0.08	$Na_{31}Al_{46}Si_{105}O_{381}H_{173}$
4.0	2.93±0.10	$Na_{21}Al_{36}Si_{99}O_{346}H_{167}$

*Note that the chemical formula here shows one of the simulation results, not the average.

3.3.2.2 Bond length and bond angle

Bond length and bond angle are two basic parameters to describe the atomic structural feature of N-A-S-H gel. There are mainly two types of bond angles, i.e. O-T-O and T-O-T (T refers to Si or Al), building the skeleton of N-A-S-H gel. The former depicts the internal bond angle within a tetrahedron, while the latter describes the connection between the tetrahedra/polyhedra, as shown in Figure 3.7. Both bond length and bond angle can be calculated through the corresponding atomic coordinates.

The average bond lengths for Si-O and Al-O are shown in Table 3.3. The average Si-O bond length at around 1.61-1.62 Å is shorter than the Al-O bond length at around 1.85-1.86 Å. It's well known that longer bond length is associated with smaller bond energy [147]. Consequently, the bond formation energy of Al-O is lower than that of Si-O. This can explain why Al sites react more quickly and earlier than Si sites as mentioned above. The average Si-O and Al-O bond lengths from this work are compared with other simulation works from Wang et al. [113], Sadat et al. [148] and experimental results from White et al. [149], as also shown in Table 3.3. The average Si-O bond length is in good agreement with both simulated results and experimental results. However, the average Al-O bond length in this work is a bit longer than those reported in other studies. More interestingly, the average Al-O bond length of N-A-S-H gel built in this work is a bit longer than the experimental result [149], while both Al-O bond lengths from the other simulation work [113,148] are shorter than the experimental result [149]. The underlying reason lies in the different fractions of pentacoordinated Al in N-A-S-H gel structure. The Al-O bond length for pentacoordinated Al is found longer than that for tetrahedral coordinated Al. The N-A-S-H gel structure in [113] does not have pentacoordinated Al and the N-A-S-H gel structure in [148] only has a very small amount of pentacoordinated Al. As a result, the Al-O bond length from these two studies is shorter than the experimental value. Based on the distribution of Al sites in Section 3.3.2.4, there are more than 50 % pentacoordinated Al in the N-A-S-H gel structures built in this work. This makes the average Al-O bond length a little bit longer than those reported in other works.

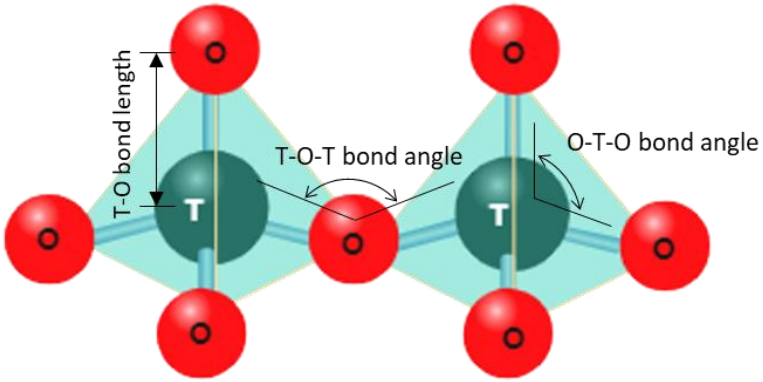

Figure 3.7 Schematic diagram for a dimer with TO_4 units (T refers to Si or Al).

Table 3.3 Average bond length of N-A-S-H model compared to other works.

Bonds	This work	Sadat et al.[148]	Wang et al.[113]	White et al.[149]
Si-O	1.61-1.62 Å	1.61 Å	1.65-1.67Å	1.63 Å
Al-O	1.85-1.86 Å	1.77 Å	1.75-1.77Å	1.80 Å

The distributions of Si-O and Al-O bond lengths for all N-A-S-H gels with different Si/Al ratios are shown in Figure 3.8. A small shift to the right can be observed both from the Si-O and Al-O bond length distribution curves as the Si/Al ratios increased from 1.0 to 4.0. That means a higher Si/Al ratio leads to longer bond length. This finding is supported by Wang's research [113].

Figure 3.9 illustrates the distribution of O-Si-O bond angle and O-Al-O bond angle for all N-A-S-H models. The distribution of O-Si-O bond angle has a main peak at around 110° regardless of the Si/Al ratios. Compared with O-Si-O, two main differences can be noticed from the distribution of O-Al-O bond angle: (i), O-Al-O bond angle has a much broader range than that of O-Si-O; (ii), the distribution of O-Al-O bond angle exhibits two humps at around 95° and 150°, respectively. These two features indicate that Al environments are more diverse than those of Si. That indicates the existence of Al provides N-A-S-H gel with a more flexible skeleton. According to the Q^n information and snapshot above, all Si exists as SiO_4 tetrahedra in the obtained N-A-S-H models, while the Al environments include AlO_4 tetrahedra and AlO_5 trigonal bipyramidal. In a regular tetrahedron, the O-T-O bond angles are 109°. That is why the O-Si-O bond angles in SiO_4 tetrahedra mainly correspond to the range from 95°-125°. However, the O-Al-O bond angles in an AlO_5 trigonal bipyramidal structure can range from an acute angle to a very large obtuse angle. Therefore, there are an amount of O-Al-O bond angles located at around 80° and 150°, respectively.

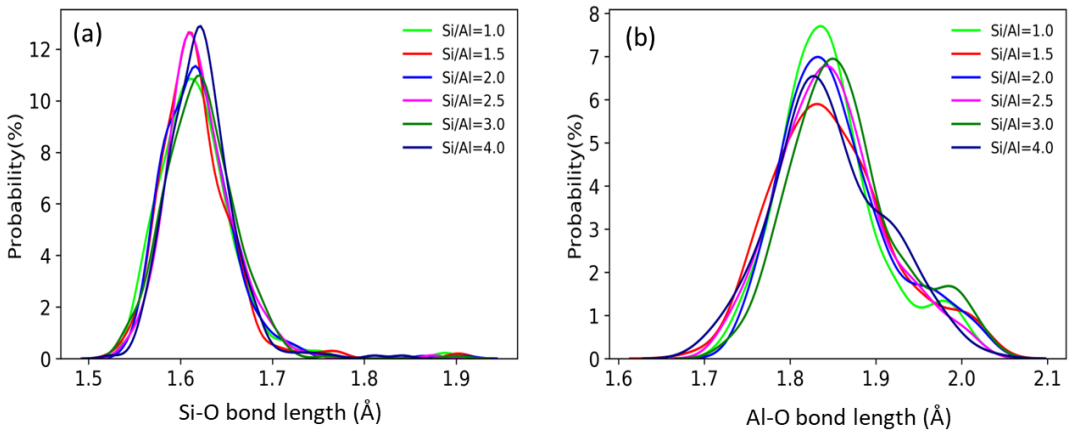

Figure 3.8 Bond length distribution of (a) Si-O and (b) Al-O for all N-A-S-H gel models.

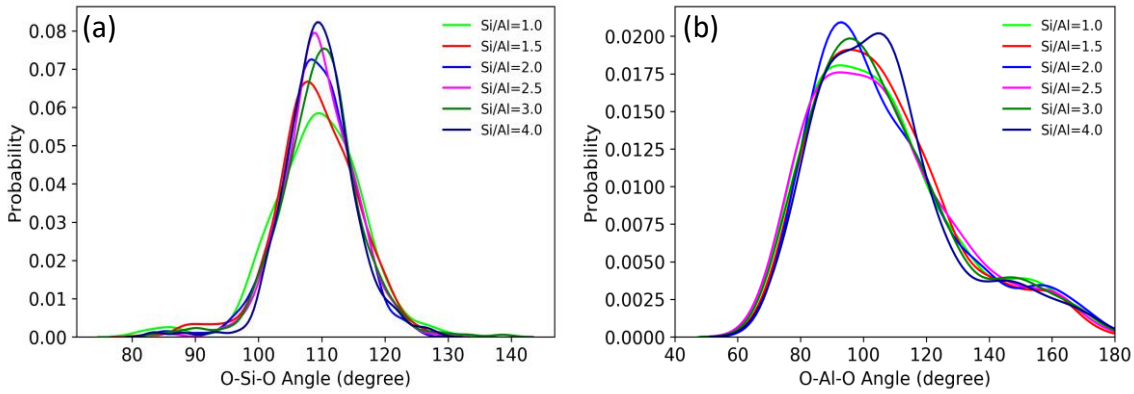

Figure 3.9 Bond angle distribution for (a) O-Si-O and (b) O-Al-O for all N-A-S-H gel models.

There are three types of T-O-T bonds in the obtained N-A-S-H gel structures, i.e. Al-O-Al, Si-O-Al and Si-O-Si. The linkage of the basic units (i.e. Si tetrahedra and Al polyhedra) of N-A-S-H gel can be characterized by the fraction of the T-O-T bonds, as shown in Figure 3.10. It can be seen that Si-O-Al accounts for the majority (around 70 %) of T-O-T bonds. Si-O-Si only represents a small proportion even at high Si/Al ratios. This indicates that a [SiO_4] tetrahedron tends to link with a [AlO_4] tetrahedron instead of a [SiO_4] tetrahedron. It is interesting to note that a small percentage of Al-O-Al bonds was found in all the obtained N-A-S-H gel models. Although Loewenstein's rule of nearest-neighbor Al avoidance is widely obeyed in many research, Al-O-Al is not strictly forbidden and has been found in some cases [82,114,150–152]. The presence of Al-O-Al is supported by both the experimental results [82] and simulation results [114,152]. To further evaluate the ordering of Si and Al cations in N-A-S-H gel structures, the probabilities forming these types of T-O-T bonds were calculated through the following equations by assuming a random distribution of Si and Al around bridging oxygens [153,154]:

$$P_{Si-O-Si} = \frac{N_{Si}(N_{Si}-1)}{(N_{Si}+N_{Al})(N_{Si}+N_{Al}-1)} \tag{3.1}$$

$$P_{Al-O-Al} = \frac{N_{Al}(N_{Al}-1)}{(N_{Si}+N_{Al})(N_{Si}+N_{Al}-1)} \tag{3.2}$$

$$P_{Si-O-Al} = \frac{2N_{Si}N_{Al}}{(N_{Si}+N_{Al})(N_{Si}+N_{Al}-1)} \tag{3.3}$$

where N_{Si} and N_{Al} are the numbers of Si and Al atoms, respectively.

It can be seen from Figure 3.10 that the proportion of Al-O-Al from MD simulation is similar to that calculated from random distribution. However, the amount of Si-O-Al from MD simulation is higher than that from random distribution, while a converse situation is found in the case of Si-O-Si. These differences confirm that a Si site has a higher tendency to form bonds with an Al site rather than with another Si site. Similar results were found in [155].

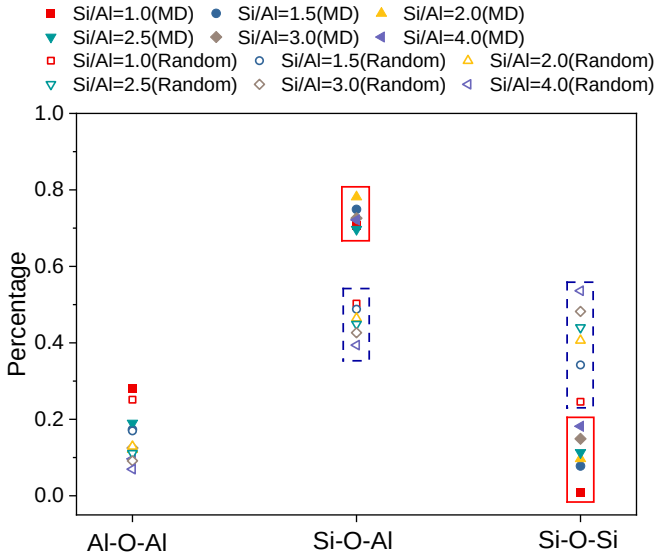

Figure 3.10 Fraction of different types of T-O-T bonds from MD simulations (solid dots) and calculations from random bond distribution (hollow dots).

Figure 3.11 shows the distribution of T-O-T bond angles in N-A-S-H gel with a Si/Al of 1, while the results of other Si/Al ratios are given in Appendix A. Al-O-Al bond angle has a main peak at around 155° while Si-O-Si bond angle mainly located at 140°, both of which are in a good agreement with [152]. A very broad peak can be seen in the range of 80°-180° for Si-O-Al bond angle, which indicates the existence of different types of Si-O-Al sites. This is consistent with the experimental results in [86], which also identified two types of Si-O-Al sites, characterized by bond angles of 124.4° and 143.4°, respectively.

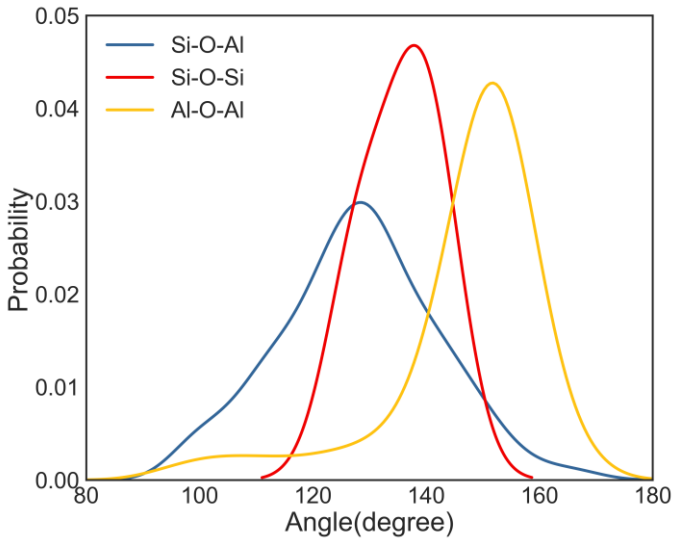

Figure 3.11 Bond angle distribution of Al-O-Al, Si-O-Al and Si-O-Si for N-A-S-H gel with a Si/Al of 1.

3.3.2.3 X-ray diffraction

XRD pattern can verify the amorphous nature of the obtained N-A-S-H gel. A broad peak from 20°-40° 2θ, which is a characteristic feature of N-A-S-H gel [35,97], can be observed for all XRD patterns with different Si/Al ratios in Figure 3.12. In addition, a visible shift towards the small angle is observed as the Si/Al ratio increases. Identical trending was obtained in Lee's work [156], where the typical hump is located at 28.54°, 26.85°, and 26.27° 2θ for the geopolymer paste with Si/Al ratios of 1.5, 3.5 and 4.0, respectively (see Figure 3.12(b)). Lee et al. believed that this difference was a result of different degrees of polymerization. However, this explanation does not consider the structures of N-A-S-H gels with different Si/Al ratios and cannot explain why a lower Si/Al ratio leads to a shift to a larger angle in the XRD pattern.

In this work, the probable reason for the lower Si/Al ratio located at a higher 2θ angle is that N-A-S-H gel structure with a lower Si/Al ratio is more compact than that with a higher Si/Al ratio. According to Bragg's law, a higher angle corresponds to a smaller interplanar spacing. From the aforementioned analysis of bond length, N-A-S-H gel structure with a lower Si/Al ratio has shorter Si-O and Al-O bond lengths, indicating a more compact structure with smaller interplanar spacing. That is why the XRD hump for N-A-S-H gel structure with a lower Si/Al ratio is centered on a higher 2θ angle compared to that with a higher Si/Al ratio.

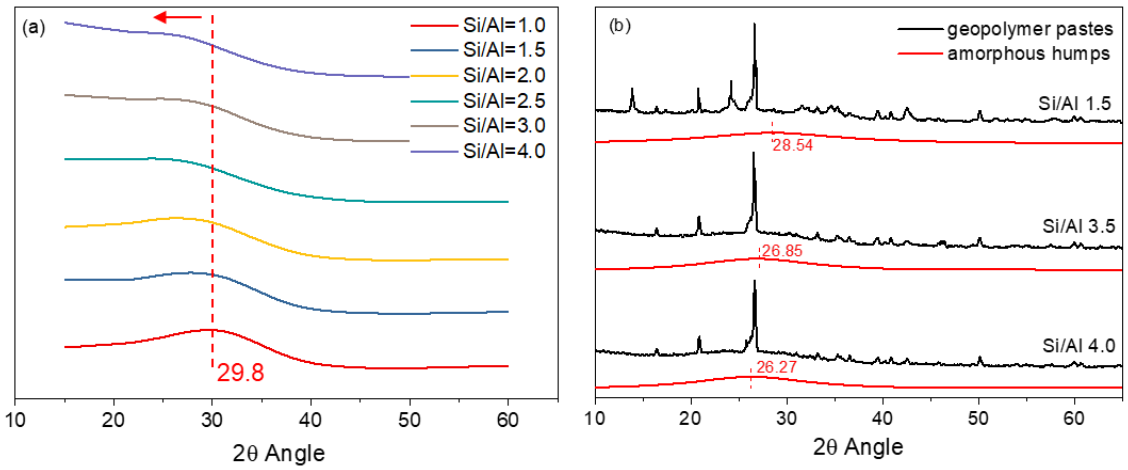

Figure 3.12 XRD patterns of (a) all simulated N-A-S-H gel with different Si/Al ratios and (b) geopolymer paste at the age of 28 days adapted from Lee's experimental study [156].

3.3.2.4 Q^n distribution

Q^n distribution is the most important structural index to explain how Si and Al are linked in the framework. The Q^n sites distribution for all N-A-S-H gel structures with different Si/Al ratios is illustrated in Figure 3.13. Four types of Si^n units, Si^1, Si^2, Si^3, and Si^4, are found in all N-A-S-H gel structures, indicating a complex network. The total proportions of Si^3 and Si^4 range from 38 % to 65 %. This is slightly lower than the corresponding experimental data (43-77 %) of the reaction products AAFA paste in [84]. The lower percentage of Si^3 and Si^4 in the simulated structure is probably due to the size of the simulated system. A system containing around one thousand atoms is not a large system. As a result, the final structure obtained is a relatively small cluster with a large surface, containing more end sites Si^1 and chain sites Si^2.

The distribution of Al is shown in Figure 3.13(b). Al^4 and Al^5 are the two main Al sites for all the simulated structures with different Si/Al ratios. It is generally believed that Al always stays tetrahedrally coordinated and Al^4 is the main existing form based on NMR results [70,85]. As mentioned above, it was once believed that pentacoordinated Al (Al^5) and six-coordinated Al (Al^6) in AAFA pastes originated solely from unreacted raw materials [14,70]. This view changed when Walkley et al. proposed, for the first time, an N-A-S-H gel model containing six-coordinated Al [86]. These six-coordinated Al atoms are considered as a charge-balance role like Na^+ ions to compensate for Al tetrahedra. Actually, pentacoordinated Al and six-coordinated Al have been found as the charge-balance roles in aluminosilicate glass systems in many early reports [157–159]. In this study, a trace of Al^6 sites was found during simulation. The non-tetrahedra Al mainly exists as Al^5. The presence of Al^5 is also detected in some N-A-S-H gel structures built by MD simulation [111,134,160]. Around 50-60 % of pentacoordinate Al was formed in the final obtained structures in this study, which is consistent with the result in Zhang's work (45.2 %) [111].

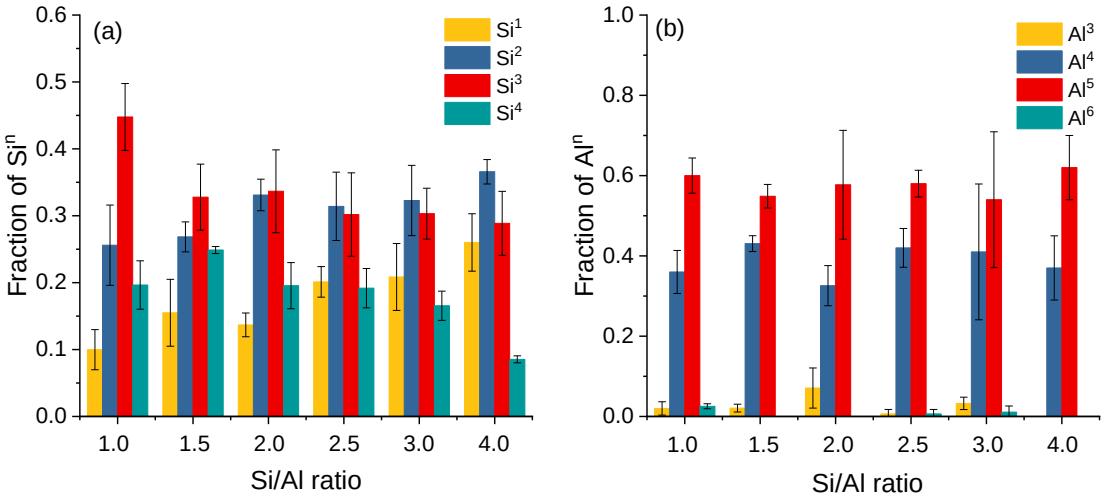

Figure 3.13 Distribution of (a) Si^n sites and (b) Al^n sites within all N-A-S-H gel models with different Si/Al ratios.

The connectivity of the obtained structure relies on the ratio of highly polymerized Si sites to lowly polymerized Si sites. Thus, the ratio (Si^3 and Si^4)/(Si^1 and Si^2) is a meaningful index to reveal the effect of Si/Al ratio on the connectivity of the structure. As can be seen from Figure 3.14, there is an overall downward trend in the ratio (Si^3 and Si^4)/(Si^1 and Si^2) as Si/Al ratios increase from 1.0 to 4.0. That means the structures at lower Si/Al ratios (e.g. 1.0 or 1.5) are more crosslinked compared with those at higher Si/Al ratios (e.g. 3.0 and 4.0). This result has confirmed the fact that lower Si/Al ratios tend to form a 3D network (more Si^3 and Si^4), while higher Si/Al ratios prefer a 2D structure (more Si^1 and Si^2) [3,161].

The environment for Si^4 is complex, containing five possible Si species Si^4(mAl), where m (m=0,1,2,3,4) refers to the number of Al connected to the Si^4 tetrahedron (see Figure 3.1(e)). Analysis of the distribution of Si^4(mAl) can further understand the connectivity between Si and Al. The fraction of five Si^4(mAl) sites is shown in Figure 3.15. Si^4(4Al) is the major Si^4 site for the structure with lower Si/Al ratios. When the Si/Al ratio increases to 4.0, Si^4(3Al) makes up the largest proportion of Si^4(mAl) sites instead of Si^4(4Al). Generally, Si^4(3Al) and Si^4(4Al) are the two main Si^4 sites for all the structures. The distribution of Si^4(mAl) in this work is similar to the results from Lyu et al. [162] and Duxson et al. [82], as also shown in Figure 3.15. These results indicate that a Si^4 tetrahedron tends to connect with more than 2 Al tetrahedra. ^{29}Si MAS NMR experimental results also show that polyhedral connection is mainly Al-O-Si-O-Al in zeolites with Si/Al of 1-3 [163,164]. The mechanism behind this lies in that Si-O-Al is preferred over Si-O-Si to be formed from thermodynamic and kinetic points of view [83,165].

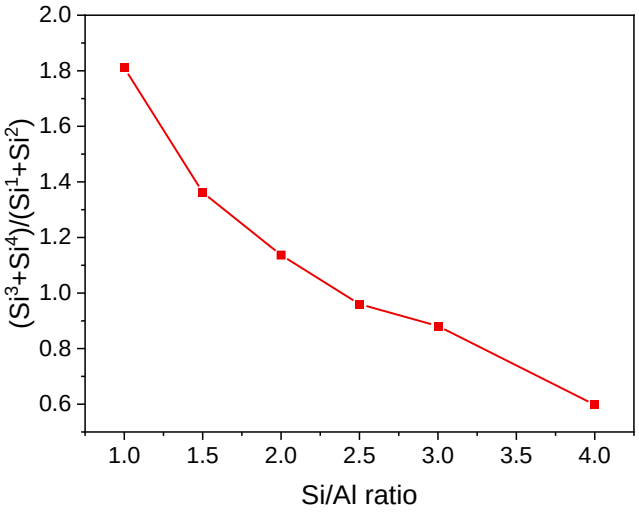

Figure 3.14 (Si^3 and Si^4)/(Si^1 and Si^2) as a function of Si/Al ratio.

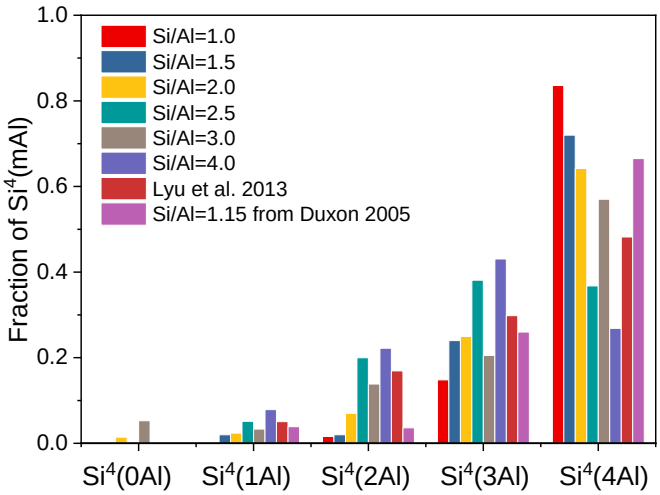

Figure 3.15 Distribution of $Si^4(mAl)$ within all N-A-S-H gel models with different Si/Al ratios. Part of data were from [82,162].

The reason for different tendencies of cross-link with different Si/Al ratios is now clear. The results of bond angle and $Si^4(mAl)$ reveal that the Si site would link with the Al site in preference. That means one Si site can link with 3-4 Al sites in an Al-rich system, but unlikely link with 3-4 Si sites in a Si-rich system. As a result, more Q^3 and Q^4 are more likely to form in an Al-rich system, while more Q^1 and Q^2 tend to form in a Si-rich system. As the distribution of Q^n determines the degree of polymerization of a structure, the N-A-S-H gel structure became more depolymerized as Si/Al is increased, aligning with the findings in [155].

3.4 The effect of Ca/Al ratio on the formation of N-C-A-S-H gel

3.4.1 Polymerization process

Figure 3.16 illustrates that the simulation process in the NaOH-$Si(OH)_4$-$Al(OH)_3$-$Ca(OH)_2$ system also followed a similar polymerization process in the non-Ca system as shown in Section 3.3.1, albeit with some differences. Firstly, the dominant Si sites in the stable stage of the simulation were Si^1 and Si^2 in the NaOH-$Si(OH)_4$-$Al(OH)_3$-$Ca(OH)_2$ system, while Si^2 and Si^3 became the predominant sites in the system without Ca. More discussion including the reason behind it will be further elaborated in the part of Q^n distribution. Another main difference is the proportion of Al^6. More six-coordinated Al was formed in the NaOH-$Si(OH)_4$-$Al(OH)_3$-$Ca(OH)_2$ system compared to that in the non-Ca system, which indicates the existence of Ca can promote the formation of Al^6. Note that all Al polyhedra in the framework, namely AlO_4, AlO_5 and AlO_6, carry negative charges and require cations for charge-balance. The type of cation can affect the type of Al polyhedron. Ca has a larger size compared to Na. The space within the oligomers would increase with the increase of AlO_6, enabling it to carry Ca with a large size. In addition, Ca is a less weakly polarized cation than Na, thereby exerting a weaker electrostatic attraction on the surrounding oxygen. As a result,

Ca tends to promote the formation of larger AlO_6 polyhedra rather than tightly bound AlO_4 tetrahedra.

At the end of simulation, the biggest cluster N-C-A-S-H gel was obtained from the system, as shown in Figure 3.17. N-C-A-S-H gel also exhibited a 3D crosslinked network linked by Si tetrahedra and Al polyhedra. Six-coordinated Al was present in the octahedron. The location of Ca was similar to that of Na, as it stayed within the space among the oligomers to compensate for the negative charge of Al polyhedra.

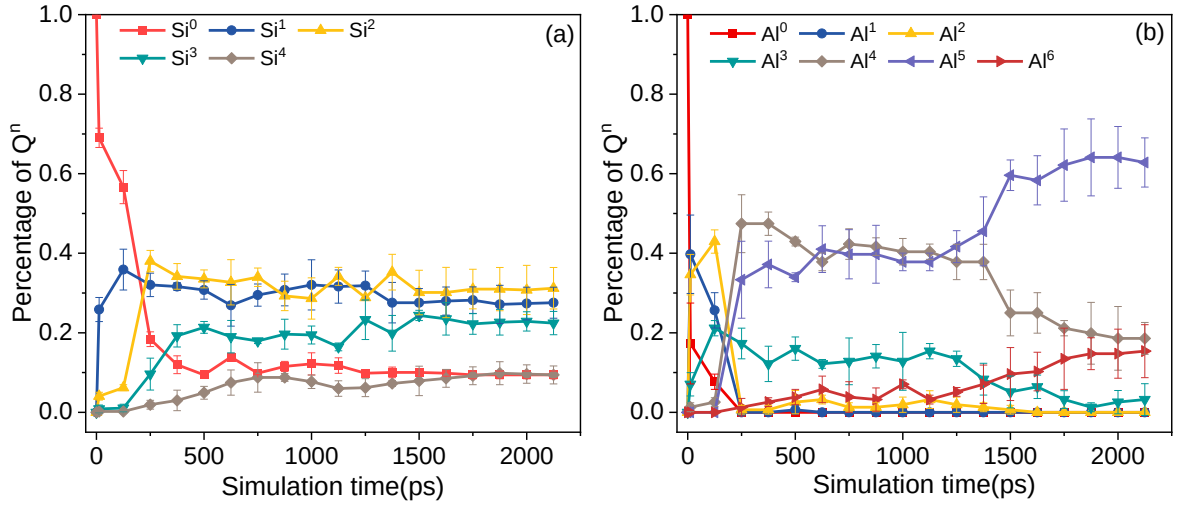

Figure 3.16 Evolution of Q^n sites for (a) Si sites and (b) Al sites in the case of Ca/Al=0.25.

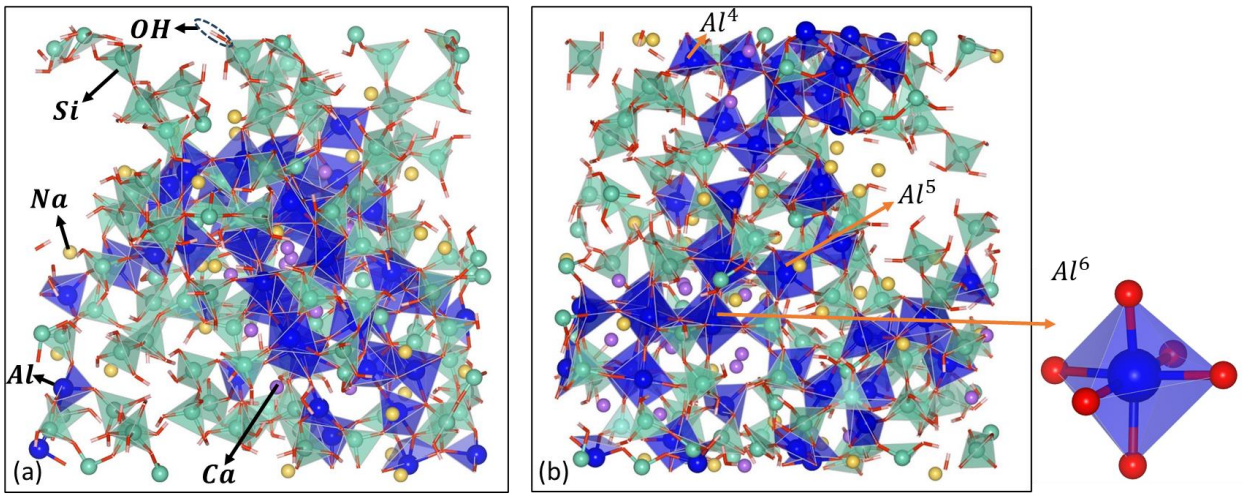

Figure 3.17 Snapshots of N-C-A-S-H gel models: (a) Ca/Al=0.25 and (b) Ca/Al=0.5; Green refers to Si, blue refers to Al, red refers to O, pink refers to H, yellow refers to Na, and purple refers to Ca.

3.4.2 Chemical and structural properties of simulated N-C-A-S-H gel

3.4.2.1 Chemical composition

The chemical composition of the obtained N-(C-)A-S-H gel is summarized in Table 3.4. The Ca/Al ratio of the obtained N-(C)-A-S-H gel is exactly identical to the initial Ca/Al ratio, indicating complete incorporation of Ca. In contrast, the Na/Al ratio of the obtained N-(C-)A-S-H gel is lower than the initial Na/Al ratio of 1. Additionally, a slight decreasing trend of the Na/Al ratio of the obtained N-(C-)A-S-H gel can be observed as the Ca/Al ratio increases. As both Ca and Na act as charge-balancing cations in the structure of N-(C-)A-S-H gel, these two findings suggest that Ca is prioritized over Na in the N-(C-)A-S-H gel. This is consistent with Garcia-Lodeiro's study [119], which demonstrated that Ca replaces Na in the N-(C-)A-S-H gel until all available Ca is consumed. Besides, although the Si/Al ratios of the obtained N-(C-)A-S-H gels with different Ca contents are all lower than the initial Si/Al ratio of 3, the incorporation of Ca slightly increases the obtaining Si/Al ratio from 2.23 to 2.36.

3.4.2.2 Bond length and bond angle

The average Si-O bond length in the obtained N-C-A-S-H gels with a Ca/Al ratio of 0.25 and 0.5 is around 1.62 Å, which is identical to the Si-O bond length in the N-A-S-H gel. This indicates that the incorporation of Ca does not affect the Si-O bond length. Regarding the Al-O bond, the average length increases from 1.86 Å in the N-A-S-H gel to 1.89 Å in the N-C-A-S-H gels. Geometrically, the Al-O bond in Al^5 and Al^6 sites is longer than that in the Al^4 site, as can be seen from Figure 3.3. Therefore, the longer bond length in N-C-A-S-H gel with a higher Ca/Al ratio can be attributed to the increase in Al^5 and Al^6 sites (see Section 3.4.2.4).

The bond angle distributions for O-Si-O and O-Al-O in the N-(C-)A-S-H gel models are illustrated in Figure 3.18. The incorporation of Ca into N-(C-)A-S-H gel does not influence the O-Si-O bond angle distribution, as all Si atoms are presented in a tetrahedral structure. However, obvious changes can be found in the O-Al-O bond angle distribution with the incorporation of Ca. As the Ca/Al ratio increases, the peak at around 100° (Ca/Al=0) slightly shifts to a smaller angle, accompanied by a more pronounced peak at around 160°. These changes are also attributed to the higher fraction of Al^5 and Al^6 and lower fraction of Al^4 in N-C-A-S-H gel compared to that in N-A-S-H gel structure. As discussed above, Al^4 tetrahedron is characterized by an angle of around 109°, while Al^5 sites are organized in the trigonal bipyramidal structure (Figure 3.3(b)), which owes the acute angle of around 70° and the obtuse angle of around 160°. The Al^6 site is arranged in the octahedron structure (Figure 3.3(c)), with an angle of around 90°. As a result, with an increasing Ca/Al ratio, the peak at around 100° moves to a smaller angle, and the peak at around 160° becomes more obvious.

Table 3.4 Chemical composition of the N-(C)-A-S-H gel model with various initial Ca/Al ratios.

Initial Ca/Al ratio	Ca/Al ratio of N-(C-) A-S-H	Na/Al ratio of N-(C-)-A-S-H	Si/Al ratio of N-(C-)-A-S-H	Formula of N-(C-)-A-S-H*
0	0	0.73±0.07	2.23±0.08	$Na_{31}Al_{46}Si_{105}O_{381}H_{173}$
0.25	0.25±0.00	0.72±0.08	2.35±0.12	$Na_{36}Ca_{13}Al_{52}Si_{116}O_{445}H_{208}$
0.50	0.50±0.00	0.63±0.07	2.36±0.13	$Na_{32}Ca_{25}Al_{50}Si_{112}O_{340}H_{224}$

*Note that the chemical formula here is not the average result.

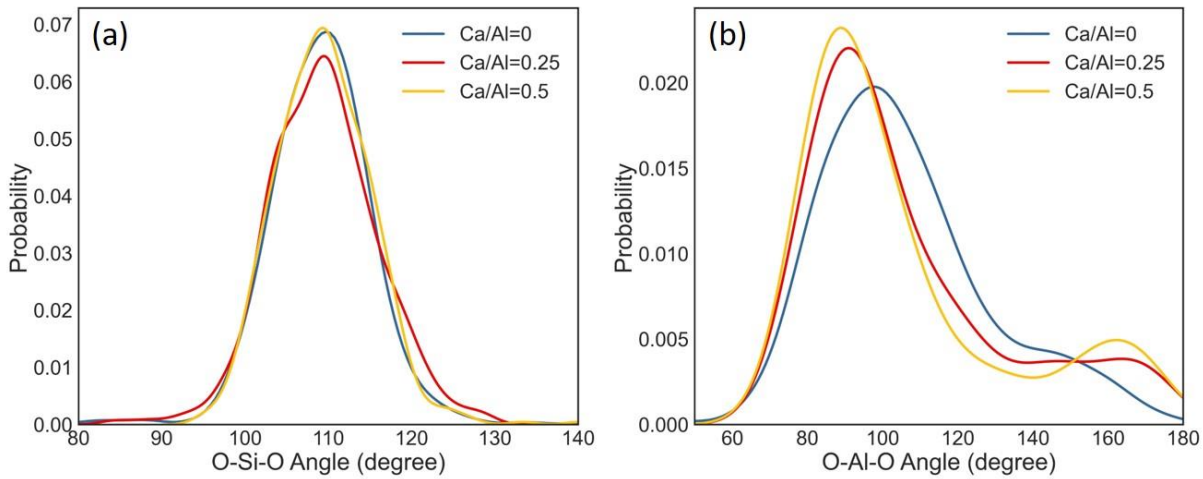

Figure 3.18 Bond angle distributions for (a) O-Si-O and (b) O-Al-O for the N-(C-)A-S-H gel models.

The fraction of different types of T-O-T bonds in the N-(C-)A-S-H gel models is shown in Figure 3.19. The increase in Ca/Al ratio leads to a decrease in the proportion of the Si-O-Al bond, together with an increasing proportion in another two bonds, i.e. Si-O-Si and Al-O-Al. However, the Si-O-Al bond is still the main type of T-O-T bond, accounting for over 60 % of the total. This result again confirms that the formation of the Si-O-Al bond takes priority over the Si-O-Si bond. This conclusion can further be reinforced by the comparison between the fraction of T-O-T bonds from MD simulation and random distribution, as also shown in Figure 3.19. The proportion of the Si-O-Al bond from the MD simulation is markedly higher than that from the random distribution, while correspondingly the proportion of the Si-O-Si bond from the MD simulation is lower compared to the random distribution. This result confirms that the Si-O-Al bond is more likely to form than the Si-O-Si bond.

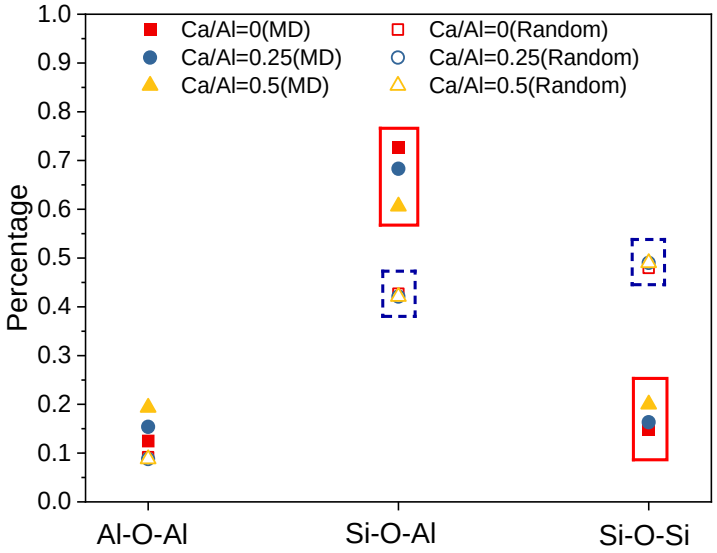

Figure 3.19 Fraction of different types of T-O-T bonds for the N-(C-)A-S-H gel models.

Figure 3.20 shows the distribution of T-O-T bond angles in N-(C-)A-S-H gel. The incorporation of Ca slightly changes the T-O-T bond angles in N-C-A-S-H gel compared to those in N-A-S-H gel, while the amount of Ca incorporated does not affect the T-O-T bond angles by comparing Ca/Al=0.25 and Ca/Al=0.5. As Ca is mainly presented near the Al site, it would affect the linkage between a [SiO_4] tetrahedron and a [AlO_n] polyhedron, thereby influencing the Si-O-Al bond angle changing from 134˚ to 129˚. In addition, there is a change in the proportion of [AlO_n] with the incorporation of Ca, which is shown in Section 3.4.2.4, leading to a shift in the Al-O-Al bond angle from 150˚ to 156˚.

3.4.2.3 X-ray diffraction

The XRD patterns of the simulated N-(C-)A-S-H gels with different Ca/Al ratios are shown in Figure 3.21(a). XRD curves of both N-C-A-S-H gels exhibited a hump at around 28° 2θ, implying that N-C-A-S-H gels retained the amorphous nature as N-A-S-H gels. Compared to N-A-S-H gel (Ca/Al=0), however, the incorporation of Ca leads to a modest shift toward higher 2θ angles. A similar trend was found in alkali-activated slag and fly ash (AASFA) paste [95], as shown in Figure 3.21(b). As the fraction of slag in AASFA increased, the hump at 20°-40° 2θ, corresponding to a mix of fly ash and the reaction product, also shifted toward higher 2θ angles. Since slag contains more Ca than fly ash, it is believed that the reaction product N-C-A-S-H gel in AASFA with more slag contains a higher level of Ca. Thus, the trend found in AASFA paste in [95] is in good agreement with this work. Although one can doubt the shift of the hump in AASFA paste can be due to the content of fly ash itself, as fly ash also displays a hump at a relatively low 2θ (around 20°-30°), further evidence to support the XRD hump's shift with Ca content will be presented in the part of the experimental synthesis of N-(C-)A-S-H gel (Chapter 4).

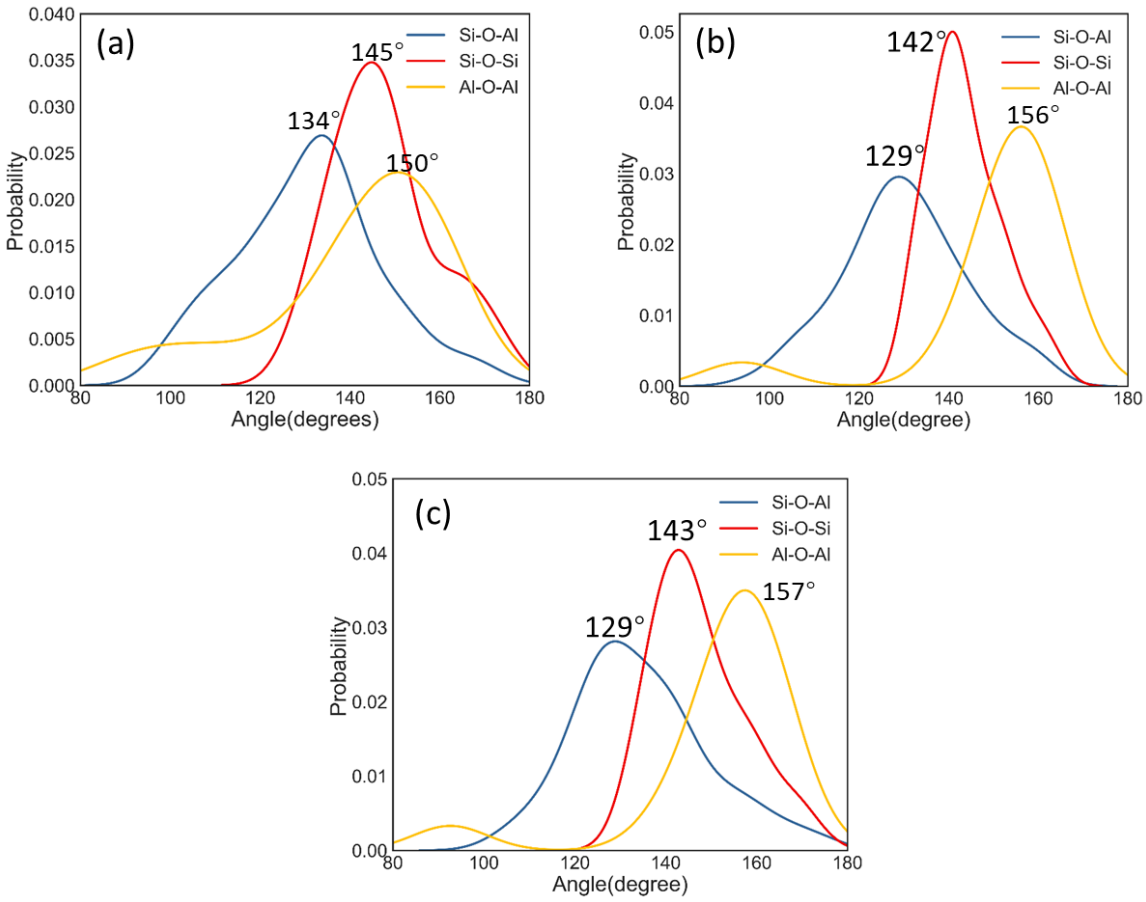

Figure 3.20 Bond angle distribution of Al-O-Al, Si-O-Al and Si-O-Si for N-(C-)A-S-H gel with (a) a Ca/Al ratio of 0, (b) a Ca/Al ratio of 0.25, (c) a Ca/Al ratio of 0.5.

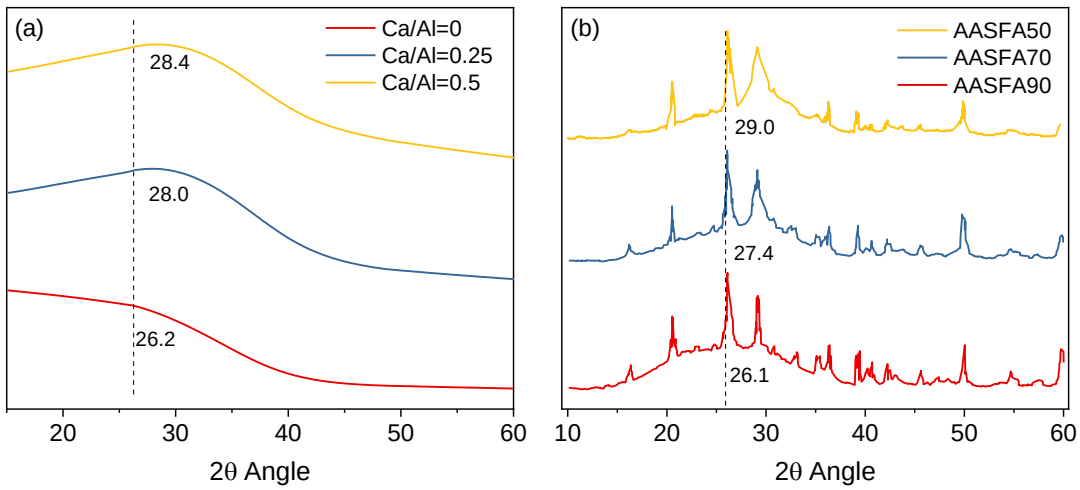

Figure 3.21 XRD patterns of (a) the simulated N-(C-)A-S-H gels with different Ca/Al ratios, and (b) alkali-activated slag and fly ash paste, data from [95]. Note that the number after 'AASFA' refers to the mass percentage of fly ash to the total binder. According to the chemical compositions of fly ash and slag used in [95], the initial Ca/Al ratio in AASFA50, AASFA70 and AASFA90 was 1.5, 0.9 and 0.5, respectively.

3.4.2.4 Q^n distribution

The Q^n distribution for all N-(C-)A-S-H gels with different Ca/Al ratios is illustrated in Figure 3.22. Si^2 and Si^3 are two dominant sites according to the distribution of Si^n, which is a little bit different from the results in Figure 3.16, where Si^2 is found to be dominant, followed by Si^1. This is because the Q^n fraction refers to the whole system in Figure 3.16, while standing for the biggest cluster in Figure 3.22. Some isolated small species like Q^0 and Q^1 were removed from the whole system to obtain the biggest cluster. Besides, as Ca/Al ratio increased, there is a modest increase in the proportion of Si^1 and Si^2, accompanied by a slight decrease in the proportion of Si^3 and Si^4. This correlation is further revealed by analyzing the ratio (Si^3 and Si^4)/(Si^1 and Si^2) as a function of Ca/Al ratio in Figure 3.23. An obvious decreasing trend in the ratio of (Si^3 and Si^4)/(Si^1 and Si^2) can be found with the increasing Ca/Al ratio. This finding is consistent with the NMR result of AAFA and AASFA pastes in [84], where more Q^1 and Q^2 were detected in AASFA paste compared to those in AAFA paste. This implies that the incorporation of Ca reduces the 3D network linkage, i.e. polymerization degree, of the N-(C-)A-S-H gel structure.

N-(C-)A-S-H gel with and without Ca showed a clear difference in Al^n distribution (Figure 3.22(b)). As mentioned above, the incorporation of Ca into N-(C-)A-S-H gel can promote the formation of six-coordinated Al. The fraction of Al^6 increases from 1 % to 26 % as Ca/Al ratio increases from 0 to 0.5. In contrast, the percentage of Al^4 decreases apparently with an increase in Ca/Al ratio (corresponding to a decreasing Na/Al ratio). This demonstrates that the coordination of Al is influenced by the type of cation involved.

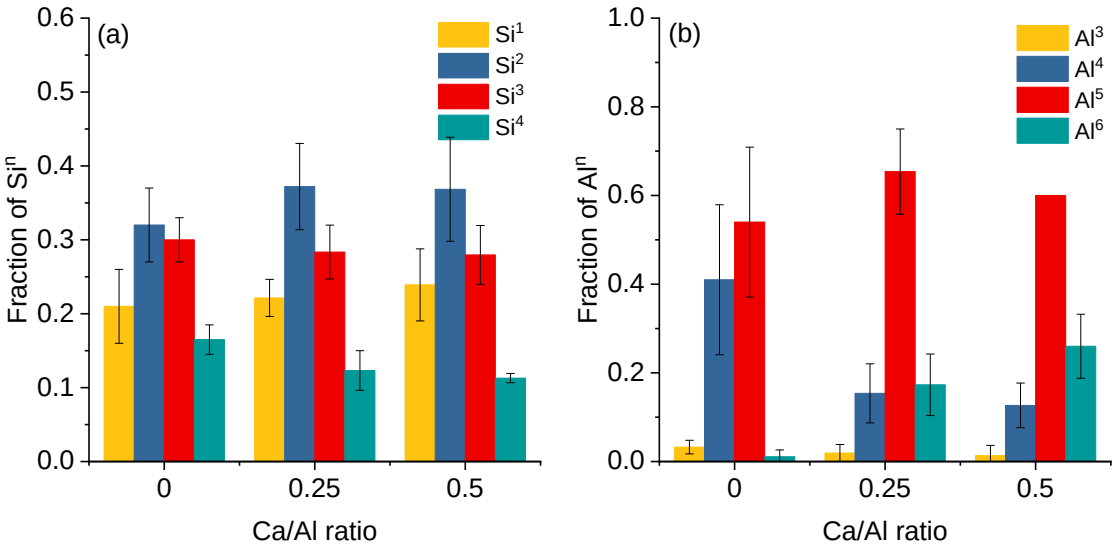

Figure 3.22 Distribution of (a) Si^n sites and (b) Al^n sites within the N-C-A-S-H gel models with different Ca/Al ratios.

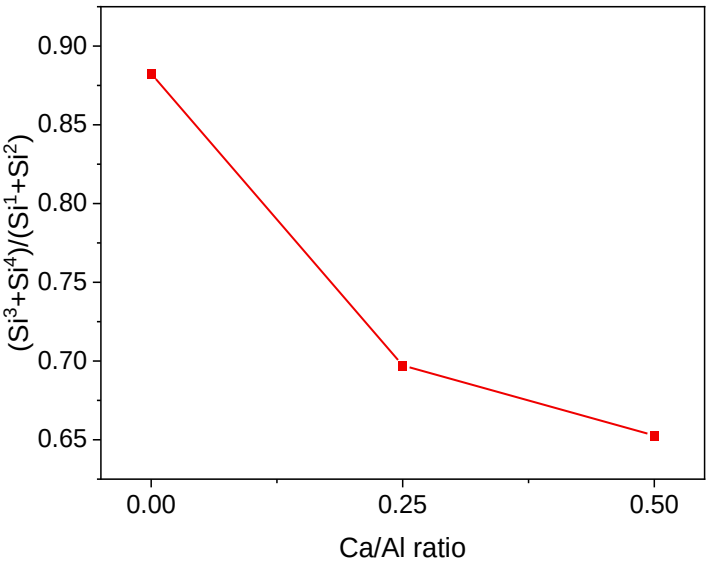

Figure 3.23 (Si^3 and Si^4)/(Si^1 and Si^2) as a function of Ca/Al ratio.

Figure 3.24 shows the fraction of Si^4(mAl) of N-(C-)A-S-H gel with different Ca/Al ratios. The corporation of Ca alters the distribution of Si^4(mAl). An increase in Ca/Al ratio results in a decrease in Si^4(4Al) and a concomitant increase in Si^4(2Al) and Si^4(3Al). However, a Si^4 tetrahedron still exhibits the same tendency to connect with more than 2 Al tetrahedrons as previously noted, given the fact that Si^4(3Al) and Si^4(4Al) account for more than 50 % regardless of Ca/Al ratio.

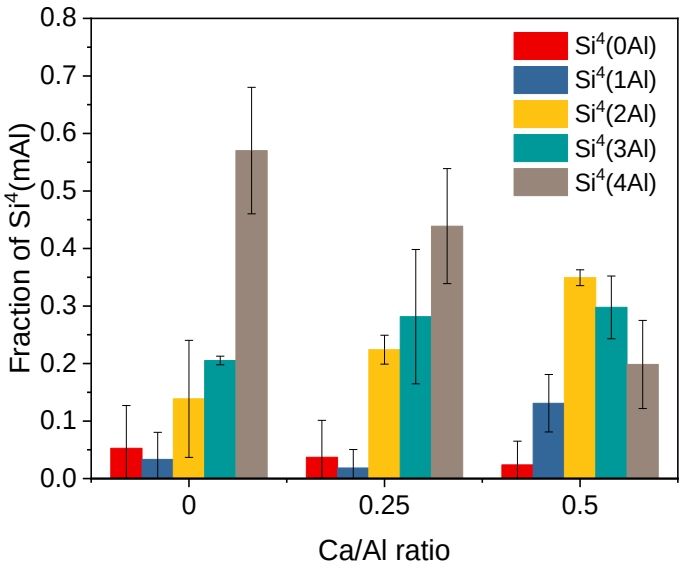

Figure 3.24 Distribution of Si^4(mAl) within all N-(C-)A-S-H gel models with different Ca/Al ratios.

3.5 Conclusions

In this chapter, the N-(C-)A-S-H gel models with various Si/Al and Ca/Al ratios are built by reactive MD simulation via mimicking the polymerization process. The possible range of chemical composition of N-(C-)A-S-H gel, in terms of Si/Al and Ca/Al ratios, is explored. The atomic structure of N-(C-)A-S-H gel is also studied in terms of bond length, bond angle, XRD analysis, Q^n distribution. Based on the results and discussion, the following remarks can be made:

1. During simulation, the initial system containing Si monomers, Al monomers and NaOH, regardless of $Ca(OH)_2$, went through a polymerization process, in accordance with what happened in real geopolymerization. The equilibrium configuration at the end of the simulation contained a 3D cross-link structure (N-(C-)A-S-H gel), some oligomers, water molecules and other species.
2. With the Si/Al ratio covering from 1 to 4 in the initial configuration, the Si/Al ratios of the obtained N-(C-)A-S-H gel ranged from 1 to 3. The Si/Al ratio of the obtained N-(C-)A-S-H gel consistently fell below the initial Si/Al ratio, with a more significant decrease observed in higher Si/Al gels. This phenomenon can be attributed to the lower formation energy of Si-O-Al compared to Si-O-Si bonds. In contrast, the Ca/Al ratio of the obtained N-(C-)A-S-H gel was always identical to the initial one, while the Na/Al ratio was not only lower than the initial one, but also lowered with the increasing Ca/Al ratio. These indicate that N-(C-)A-S-H gel is more likely to incorporate with Ca than Na and exhibits a tendency to accept all available Ca in a low-Ca system. Based on these findings, it is proposed that a Si/Al ratio from 1 to 3 and a Ca/Al ratio from 0 to 0.5 can represent the chemical composition range of N-(C-)A-S-H gel in a mature AAFA paste.
3. In N-(C-)A-S-H gel, the Si-O-Al bond is the major type of T-O-T bond, i.e. Si-O-Si, Si-O-Al and Al-O-Al, regardless of the incorporation of Ca. This suggests a preference for Si sites to bond with Al sites over other Si sites, reinforced by a comparison of T-O-T bond angle proportions between random distribution and MD simulation. Besides, both O-Al-O and Si-O-Al bond angles exhibit a highly broad range, implying a complicated Al environment, which is further confirmed in the result of Q^n distribution.
4. All N-(C-)A-S-H gel show X-ray amorphous, regardless of their Si/Al and Ca/Al ratios, while the position of the X-ray hump is dependent on the Si/Al and Ca/Al ratios. A shift toward smaller 2θ angles is observed with an increase in Si/Al ratio, whereas an opposite trend is observed with Ca/Al ratio. The results are in good agreement with experimental results, providing strong evidence for the reliability of the N-(C-)A-S-H gel model.
5. According to Q^n distribution, all Si atoms present in a tetrahedron environment with a four-coordinate configuration, while multi-coordinated Al atoms (Al^4, Al^5 and Al^6) are found in the polyhedron arrangement. The existence of Al^5 and Al^6 in N-(C-)A-S-H gel model provides strong support to the current knowledge that Al^5 and Al^6 do not only come from raw material. An increase in Si/Al or Ca/Al ratio leads to a less cross-linked N-(C-)A-S-H gel structure, indicated by the decreasing index (Si^3 and Si^4)/(Si^1 and Si^2).

According to the chemical compositions of N-(C-)A-S-H gels obtained in this chapter, synthesis of the corresponding N-(C-)A-S-H gels will be carried out in Chapter 4. Besides, the characterization of the modeled N-(C-)A-S-H gels in this chapter will be adopted to compare with the synthesized N-(C-)A-S-H gels.

Chapter 4

Synthesis and characterization of N-(C-)A-S-H gel

4.1 Introduction

To establish a reliable thermodynamic database of N-(C-)A-S-H gel, synthesis of pure N-(C-)A-S-H gel is a crucial step. According to the results in Chapter 3, N-(C-)A-S-H gel with a Si/Al ratio from 1 to 3 and a Ca/Al ratio from 0 to 0.5 can generally represent the chemical composition of the main reaction product in AAFA paste. So far, the Si/Al ratio of synthesized N-A-S-H gel in the reported literature is mainly within the range of 1 to 2 [35,87]. Instances of successful synthesis of N-A-S-H gel with a Si/Al ratio surpassing 2 are notably scarce. Moreover, Williamson et al. [120] claimed that they were not able to obtain N-A-S-H gel with a Si/Al ratio of 2 with a similar mixture (identical initial Si/Al ratio) used in [35,87]. Instead, they found that the Si/Al ratio was much less than 2. These observations indicate that achieving high Si/Al ratios in N-A-S-H gel synthesis can be challenging.

In addition, less attention has been paid to the synthesis of N-C-A-S-H gel as compared to N-A-S-H gel. An attempt was made to synthesize N-C-A-S-H gel with various Ca/Si and Si/Al ratios using a dissolution-precipitation approach [118]. However, achieving pure N-C-A-S-H gel through this method proved challenging, as unreacted raw materials and secondary reaction products were detected. Overall, there is a need to explore the mixtures and conditions for synthesizing N-(C-)A-S-H gel with the target Si/Al and Ca/Al ratios.

In this chapter, N-(C-)A-S-H gels with Si/Al ratios ranging from 1 to 3 and Ca/Al ratios ranging from 0 to 0.5 are synthesized by using the sol-gel method, chosen for its efficiency and ability to produce pure products as reviewed in Chapter 2. In order to address the problem of achieving high Si/Al ratios of N-(C-)A-S-H gel, firstly, the synthesis mixtures and conditions reported in the literature are assessed for their effectiveness in producing the target N-(C-)A-S-H gel. In the second step, mixtures are tailored to produce N-A-S-H gels with high Si/Al ratios, and the underlying mechanism is analyzed. Lastly, N-(C-)A-S-H gels are synthesized based on the developed mixtures, and their chemical compositions and structures are thoroughly characterized. The N-(C-)A-S-H gels synthesized in this chapter will undergo the dissolution test in Chapter 5.

4.2 Materials and methods

4.2.1 Materials

The following solutions were prepared using deionized water and reagent-grade chemicals:

- As a source of Si and Na, sodium silicate solutions with various concentrations of 0.1 M, 0.2 M, 0.3 M, and 1 M were prepared using $Na_2SiO_3 \cdot 5H_2O$ and deionized water.
- As an Al-providing source, aluminum nitrate solutions with concentrations of 0.1 M and 1 M were prepared using $Al(NO_3)_3 \cdot 9H_2O$ and deionized water.
- As a Ca-providing source, a 0.5 M calcium nitrate solution was prepared using $Ca(NO_3)_2 \cdot 4H_2O$ and deionized water.
- pH regulator: NaOH solutions with concentrations of 1 M or 10 M were prepared using pellets of NaOH (>98 %) and deionized water. A HNO_3 solution (>65 %, Honeywell) was also used if necessary.

4.2.2 Synthesis of N-(C-)A-S-H gel

To synthesize N-A-S-H gel with various Si/Al ratios, sodium silicate solution was first mixed with the pH regulator and stirred for 30 minutes to reach a stable state. Aluminum nitrate solution was then added drop by drop to the stirring solution. A total of 15 synthesis systems were studied, covering five influencing factors, i.e. reaction time, reaction temperature, initial Si/Al, concentration of reactants and pH of matrix. Detail synthesis conditions for all N-A-S-H gel are given in Table 4.1. Except for the samples N3_7days and N3_ice, other samples, without specific declaration in their labels, were synthesized for 1 day at 20 ˚C. In order to examine the synthesis mixtures and conditions in the literature [35,36,87], samples N1, N2, N3, N3_7days, N3_ice and N10 were prepared with 0.1 M aluminum nitrate solution and various concentrations of sodium silicate solutions. Among them, N1, N2, N3 and N10 were designed to study the effect of initial Si/Al ratio. N3_7days was reacted for 7 days at 20 ˚C to study the effect of reaction time, and N3_ice was placed in an ice-bath (2-5 ˚C) for 1 day, mirroring the condition adopted in [87], to study the effect of reaction temperature. Samples N3_lc, N3_mc and N3_hc were prepared by using different concentrations of reactants to study the effect of concentration, while N3_hc_mpH and N3_hc_lpH were synthesized by adding different amounts of HNO_3 solution to investigate the effect of pH. Note that the entire procedure was carried out in a N_2-filled glove box to avoid carbonation.

For the synthesis of N-C-A-S-H gel with various Si/Al and Ca/Al ratios, a 1 M sodium silicate solution was first mixed with a 0.5 M calcium nitrate solution and the pH regulator, followed by stirring for 30 minutes. Next, a 1 M aluminum nitrate solution was added slowly to the stirring solution. The quantity of the solutions was adjusted to obtain target Si/Al and Ca/Al ratios, as shown in Table 4.2. The procedure for the synthesis of N-C-A-S-H gel was carried out for a duration of 1 day at 20 ˚C.

After stirring for 1 day (or 7 days), the suspension was centrifuged at 5000 rpm for 5 min to separate the solid reaction product, i.e. gel, and liquid. The liquid was filtered using a 0.45 µm syringe filter for further analysis. The gel was triple-washed by fully dispersing in deionized water to remove nitrates and unbound sodium, followed by 100 ml of >96 vol.%

ethanol solution for the last wash. The amount of washing water was found to affect the measured Na/Al ratio of the gels significantly. The Na/Al ratio in the N-A-S-H gel is supposed to be 1 in theory. In this work, at least 1500 ml of washing water was used to obtain a reasonable Na/Al. Note that the amount of washing water should be adjusted according to the amount of synthesized solid gels. In the end, the gel was dried in a vacuum desiccator, using a saturated $CaCl_2$ solution as a desiccant, until the relative humidity reached equilibrium, i.e. RH=33 %. The dried gels were then prepared for further characterization. The procedure to synthesize N-(C-)A-S-H gel is depicted in Figure 4.1.

Table 4.1 Synthesis mixtures and conditions for N-A-S-H gel.

Samples[(a)]	Na_2SiO_3	$Al(NO_3)_3$	pH regulator	Target Si/Al	pH[(b)]
N1	200ml, 0.1M	200ml, 0.1M	20ml 10M NaOH	1	13.53
N2	200ml, 0.2M	200ml, 0.1M	20ml 10M NaOH	2	13.60
N3	200ml, 0.3M	200ml, 0.1M	20ml 10M NaOH	3	13.68
N3_7days	200ml, 0.3M	200ml, 0.1M	20ml 10M NaOH	3	13.72
N3_ice	200ml, 0.3M	200ml, 0.1M	20ml 10M NaOH	3	13.70
N10	100ml, 1M	100ml, 0.1M	10ml 10M NaOH	3	13.87
N3_lc_n	200ml, 0.3M	200ml, 0.1M	-	3	12.93
N3_mc_n	200ml, 0.3M	20ml, 1M	-	3	13.18
N3_hc_n	300ml, 1M	100ml, 1M	-	3	13.50
N3_hc_mpH_a	300ml, 1M	100ml, 1M	5ml HNO_3	3	13.19
N3_hc_lpH_a	300ml, 1M	100ml, 1M	10ml HNO_3	3	12.62
N1_hc_hpH[(c)]	50ml, 1M	50ml, 1M	20ml 10M NaOH	1	13.64
N2_hc_lpH_n	200ml, 1M	100ml, 1M	-	2	11.97
N2.8_hc_hpH_n	280ml, 1M	100ml, 1M	-	2	13.46
N5_hc_hpH_a	200ml, 1M	40ml, 1M	10ml HNO_3	3	13.40

(a) 'N' stands for N-A-S-H gel; the number after 'N' refers to the initial Si/Al ratio; 'l' indicates low; 'm' indicates medium and 'h' indicates high while 'c' signifies concentration; ice represents 'ice bath'; 'n' indicates no NaOH solution while 'a' indicates adding acid (HNO_3). For example, 'N3_hc_lpH_a' represents a gel with an initial Si/Al of 3, using a high concentration (i.e. 1M) of reactants, synthesized at relatively low pH (below 13), with the addition of HNO_3.
(b) The pH of filtrate was measured at room temperature. The measurement is given in Section 4.2.3.
(c) Extra 200ml of deionized water was added to this mixture to avoid the formation of impurities.

Table 4.2 Synthesis mixtures for N-C-A-S-H gel.

Samples	Na_2SiO_3	$Al(NO_3)_3$	$Ca(NO_3)_2$	pH regulator	Target Si/Al	Target Ca/Al	pH
NC1_0.25	100 ml	100 ml	50 ml	40 ml NaOH (10 M)	1	0.25	13.50
NC1_0.5	100 ml	100 ml	100 ml	40 ml NaOH (10 M)	1	0.5	13.41
NC2_0.25	140 ml	40 ml	24 ml	10 ml NaOH (1 M)	2	0.25	13.55
NC2_0.5	140 ml	40 ml	44 ml	20 ml NaOH (1 M)	2	0.5	13.42
NC3_0.25	240 ml	40 ml	26 ml	10.5ml HNO_3	3	0.25	13.37
NC3_0.5	240 ml	40 ml	42 ml	8ml HNO_3	3	0.5	13.54

Note: 'NC' stands for N-C-A-S-H gel; the number after 'NC' refers to the target Si/Al and Ca/Al, respectively. An extra 200ml of deionized water was added to samples NC1_0.25 and NC1_0.5 to keep consistent with sample N1_hc_hpH.

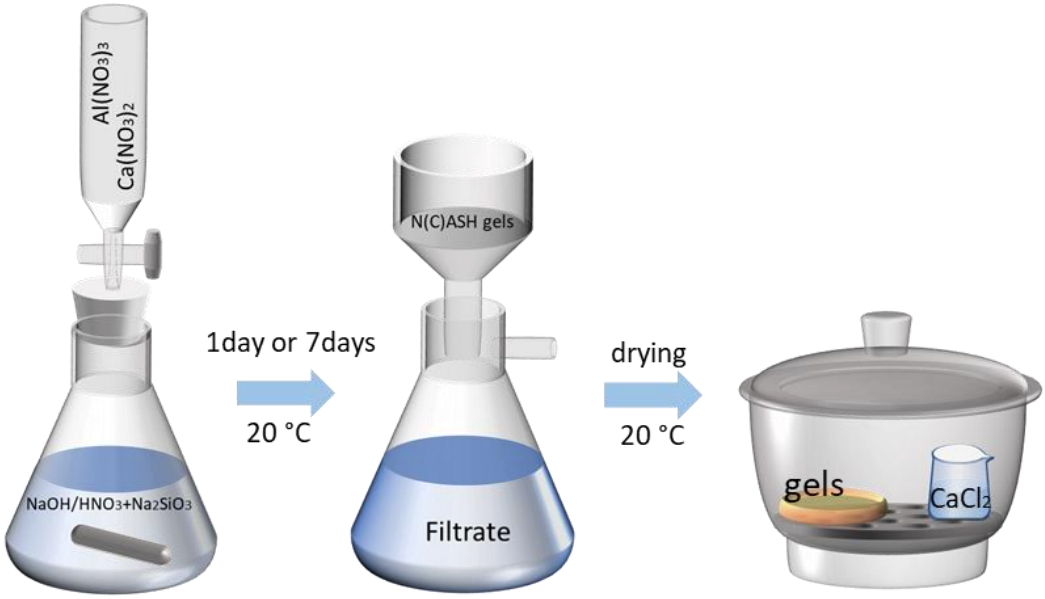

Figure 4.1 Schematic procedure of the synthesis of N-(C-)A-S-H gel.

4.2.3 Characterization of the synthesized solid product and filtrated solution

After synthesis, two parts were obtained: solid reaction product (gels) and filtrate. The chemical compositions of gels were measured using X-ray fluorescence (XRF) with a Panalytical Axios Max WD-XRF spectrometer on loose powder.

According to the definition in [166,167], non-evaporable water refers to the water cannot be removed by D-drying or equivalent procedures, e.g. drying at 105 ˚C. In this work, the quantity of non-evaporable water in N-(C-)A-S-H gel was determined by using thermogravimetric analysis (TGA). TGA data were recorded on a thermoanalyzer TG-449-F3-Jupiter instrument on approximately 10 mg samples at a heating rate of 10 ˚C/min from 40-1000 ˚C, except in the middle stage staying at 105 ˚C for 6h to remove evaporable water in the samples.

The stoichiometric coefficients a, b, c, d in the formula of N-(C-)A-S-H gel $(Na_2O)_a(CaO)_b(Al_2O_3)_c(SiO_2)_d(H_2O)_e$ can be calculated based on the XRF results, while e can be calculated based on the TGA results using the following Equations:

$$\frac{18e'}{62a + 56b + 102c + 60d + 18e'} = f_{water\_total} \tag{4.1}$$

$$e = e' f_{water\_nc} / f_{water\_total} \tag{4.2}$$

where e' is the stoichiometric coefficient in $(Na_2O)_a(CaO)_b(Al_2O_3)_c(SiO_2)_d(H_2O)_{e'}$ (here, H_2O refers to all water retained by the gel instead of non-evaporable water), f_{water_total} refers to the mass loss from 40-1000 ˚C in the TGA result, while f_{water_nc} refers to the mass loss for non-evaporable water in the TGA result (see Figure 4.6).

X-ray diffraction (XRD) analysis was carried out to study the phase composition of the solid reaction product on a Bruker D8 Advance diffractometer at 45 KV and 40 mA using CuKα radiation. The powder samples were scanned from 5° to 90° 2θ at a rate of 2 seconds per step and a step size of 0.02° 2θ.

The molecular structure of the solid reaction product was investigated using Fourier transform infrared (FTIR) spectroscopy. FTIR measurement was conducted using Nicolet™ iS50 FTIR Spectrometer over the wavelength range of 400 to 4000 cm^{-1} with a resolution of 4 cm^{-1}. A total of 32 scans were collected per measurement.

To determine the pH of the filtrate, the concentration of OH^- was measured through titration against 0.1 M hydrochloride acid. The concentration of Si and Al in the filtrate was measured by a Perkin Elmer Optima 5300 DV ICP-OES (inductively coupled plasma optical emission spectroscopy) spectrometer after dilution with nitric acid (0.2 vol.%). According to the theory of mass balance, the quantity of Si and Al in the obtained N-(C-)A-S-H gel can also be determined by calculating the difference between initial amounts of Si and Al and the respective amounts in the filtrate. The Si/Al ratios derived via this approach can be compared with those obtained by XRF, thereby enhancing the reliability of the data.

4.3 Results and discussion

This section is divided into three main parts. The first part addresses the inconsistencies found in the literature by initially synthesizing N-A-S-H gels using the mixtures and conditions adopted from previous studies. The second part focuses on exploring the key factors influencing the synthesis of N-A-S-H gel with a high Si/Al ratio, accompanied by a detailed analysis of the underlying mechanism. Through a systematic examination of different influencing factors, an optimized synthesis route for achieving a high Si/Al N-A-S-H gel is proposed. The third part involves the synthesis and characterization of N-(C-)A-S-H gels with varied Si/Al and Ca/Al ratios.

4.3.1 Verification of the existing sol-gel method

The obtained Si/Al ratios in synthesized N-A-S-H gels, derived from different initial Si/Al ratio in this work and from literature, are summarized in Table 4.3. In this work, when the initial Si/Al ratio increased from 1 to 3, the Si/Al ratio of the synthesized N-A-S-H gels obtained by XRF and mass balance calculation remained at 1 – 1.4. The Si/Al ratios obtained by XRF are consistent with those calculated by mass balance, indicating the reliability of the results. The maximum Si/Al ratio achieved was 1.9 in mixture N10, which was still low for an initial Si/Al ratio of 10. Similar results were observed in [36], as also shown in Table 4.3. They found that the obtained Si/Al ratio could only increase if the Si/Na ratio was also increased. For instance, they found that an increase in the Si/Na ratio from 0.1 to 0.2 led to an increase in the Si/Al ratio from 1.01 to 1.30, using an initial Si/Al of 2. This indicates that the concentration of Na, and thus the pH, has a significant influence on the obtained Si/Al ratio. The results from this work and from [36] both show that the obtained Si/Al value is much lower than its corresponding initial Si/Al, except for the case of an initial Si/Al ratio of 1.

Table 4.3 Obtained Si/Al of synthesized N-A-S-H gels from this work and literature.

	N1	N2	N3	N10
Initial Si/Al	1	2	3	10
Obtained Si/Al by XRF	1.05	1.13	1.33	1.89
Obtained Si/Al by mass balance	1.06	1.36	1.39	1.97
Literature Si/Al by mass balance	0.98 [36]	1.01 [36],1.30 [36]	-	2.39 [36]
Literature Si/Al by EDX	1.45 [87], 1.11 [35]	2.19 [87], 2.08 [35]	-	-
Literature Si/Al by NMR	1.36 [87]	1.62 [87]	-	-

In contrast, the obtained Si/Al ratios in N-A-S-H gels approached the target of 1 and 2 in [35,87]. This might be partially related to the measurement technique (see Table 4.3) or to variations in synthesis conditions. An ice bath was employed in [87] to lower the reaction temperature, while the reaction time was extended to 7 days in [35]. To further explore the effect of reaction temperature and reaction time on the resulting Si/Al ratio, mixtures N3, N3_ice and N3_7days were studied. As shown in Table 4.4, lowering the reaction temperature (N3_ice) slightly increased the obtained Si/Al ratio from 1.33 to 1.46, while extending the reaction time from 1 day (N3) to 7 days (N3_7days) hardly affected the Si/Al ratio of the N-A-S-H gel.

The structure of the synthesized N-A-S-H gel was characterized by XRD as shown in Figure 4.2. The broad XRD humps at around 30° 2θ indicate that only amorphous N-A-S-H gels was formed. N3_ice and N10 were slightly carbonated due to unavoidable contact with air during the post-treatment of the samples. No significant shift of this broad XRD peak was observed among the different Si/Al ratios of the N-A-S-H gels. According to experimental results in [156] and simulation results in Chapter 3 (see Figure 3.12), the hump at around 30° 2θ is expected to be shifted to a smaller angle as the Si/Al ratio increases. The absence of such a shift in the synthesized N-A-S-H gels suggests that their Si/Al ratios were almost identical. This is consistent with the XRD results of two synthesized N-A-S-H gels reported in [35], which also showed a high degree of similarity, indicating close Si/Al ratios despite the authors' claim of Si/Al ratios of around 1 and 2, respectively.

Table 4.4 Effect of reaction temperature and reaction time.

	N3	N3_ice	N3_7days
Initial Si/Al	3	3	3
Obtained Si/Al by XRF	1.33	1.46	1.34
Obtained Si/Al by mass balance	1.39	1.59	1.51

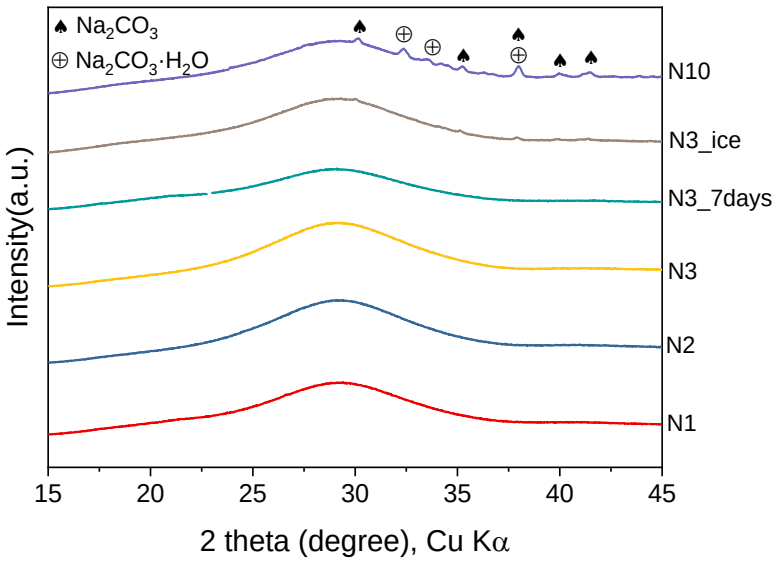

Figure 4.2 XRD patterns for synthesized N-A-S-H gels.

The FTIR technique is much more sensitive in detecting structural changes of amorphous aluminosilicates, as it is sensitive to short-range structural order [168]. FTIR spectra of these five synthesized N-A-S-H gels are compared and shown in Figure 4.3. The main band centered at around 950-980 cm^{-1} is assigned to asymmetric stretching vibrations of Si–O–T (T refers to Si or Al) bonds. A minor shift towards a higher wavenumber is observed as Si/Al increases, which can be attributed to the vibration of the Si-O-Si band at a higher wavenumber than the Si-O-Al band, due to the stronger electronegativity of Si^{4+} [124] and then higher binding energy of Si-O-Si [169]. Furthermore, the shift of this band to a higher wavenumber is highly consistent with the corresponding increment of the obtained Si/Al ratio in gels.

Overall, the results in this section have suggested that, except for the Si/Al ratio of 1, other targeted Si/Al ratios (≥2) cannot be achieved by using the existing mixtures and conditions. Reaction temperature and reaction time have little effect on the resulting Si/Al ratio in N-A-S-H gel. However, the finding in [36] reveals that a lower pH may facilitate obtaining N-A-S-H gel with a higher Si/Al. Furthermore, the usage of reactants with higher concentrations, as adopted in [170], is another option to achieve a high Si/Al ratio in the synthesized N-A-S-H gel. Therefore, the effects of concentration of reactants and pH on the obtained Si/Al ratio of the N-A-S-H gel are further investigated in the subsequent section.

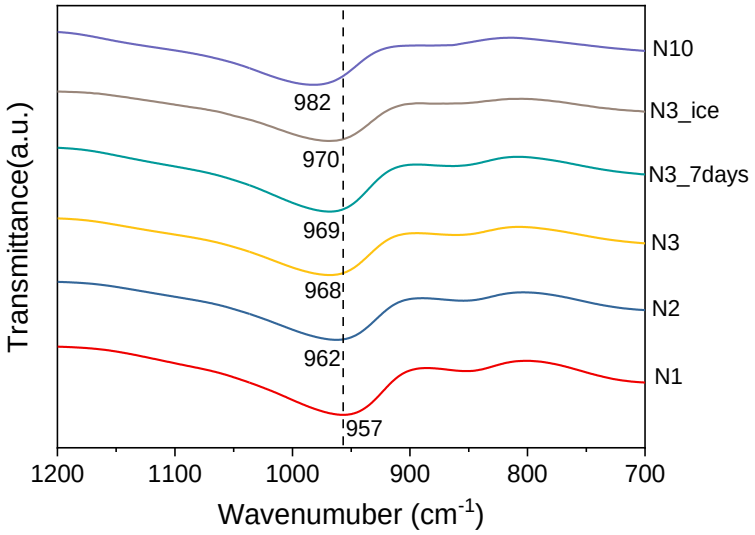

Figure 4.3 FTIR spectra for synthesized N-A-S-H gels.

4.3.2 Modification of mixtures for synthesizing N-A-S-H gels with high Si/Al

4.3.2.1 The effect of concentration of reactants and pH

The pH of the mixing solution was firstly lowered by omitting additional NaOH solution. Note that it is not feasible to determine the initial pH of the mixture, the pH herein refers to the pH of the filtrate subsequent to synthesis. This adjustment resulted in a decrease in the pH value of the filtrate from 13.7 (N3) to 12.9 (N3_lc_n), while simultaneously increasing the resulting Si/Al ratio from 1.3 (N3) to 1.8 (N3_lc_n), as shown in Table 4.4 and 4.5, respectively. This result underlines the strong effect of pH, which will be discussed in more detail further below. Next, the effect of the concentration of the reactants on the resulting Si/Al ratio was investigated, as summarized in Table 4.5. An increase in the concentration of Si and Al in the mixture resulted in a higher Si/Al ratio of the N-A-S-H gel. The Si/Al ratios calculated based on mass balance are slightly higher than those obtained by XRF. However, even using the highest concentration of reactants (N3_hc_n), the resulting Si/Al ratio was only 2.23, still lower than the target Si/Al ratio of 3. Note that the pH value also increased as the concentration of reactants increased, as shown in Table 4.1, which hindered the formation of high Si/Al N-A-S-H gel. Thus, in addition to adopting a high concentration of reactants, further adjustments to the pH level are necessary to achieve the target Si/Al ratio.

Lowering the amount of NaOH, and consequently lowering the pH, is crucial for increasing the Si/Al ratio, as indicated by the comparison between N3 and N3_lc_n, whose only difference is the absence of additional NaOH in the latter (see Table 4.1). This was further investigated on variants of sample N3_hc_n, where different amounts of HNO_3 were added (see Table 4.1). Table 4.6 shows a clear increase in Si/Al of N-A-S-H gels with a decrease in pH values. At pH 12.6, the obtained Si/Al ratio (2.74) was already close to the target Si/Al ratio of 3. In summary, a high Si/Al ratio of up to 3 could be reached with a combination of using a high concentration of reactants (on the order of 1 M) and low pH (less than 13).

Table 4.5 Effect of concentration of reactants on the obtained Si/Al ratio.

	N3_lc_n	N3_mc_n	N3_hc_n
Initial Si/Al	3	3	3
Si/Al in N-A-S-H gel determined by XRF	1.83±0.02	1.92±0.02	2.23±0.02
Si/Al in N-A-S-H gel determined by mass balance	2.00	2.06	2.27

Note: "N3_lc_n," "N3_mc_n," and "N3_hc_n" indicate gels with an initial Si/Al ratio of 3, prepared using low, medium, and high concentrations of reactants, respectively, without adding NaOH.

Table 4.6 Effect of pH on the obtained Si/Al.

	N3_hc_n	N3_hc_mpH_a	N3_hc_lpH_a
pH	13.5	13.2	12.6
Initial Si/Al	3	3	3
Obtained Si/Al by XRF	2.23	2.35	2.74
Obtained Si/Al by mass balance	2.27	2.48	2.92

Note: 'N3_hc_n' denotes a gel with an initial Si/Al ratio of 3, prepared using a high concentration of reactants, without NaOH. 'N3_hc_mpH_a' denotes a gel with an initial Si/Al ratio of 3, prepared using a high concentration of reactants, medium pH, with the addition of acid (HNO_3). 'N3_hc_lpH_a' denotes a gel with an initial Si/Al ratio of 3, prepared using a high concentration of reactants, low pH, with the addition of acid (HNO_3).

4.3.2.2 Mechanism for achieving high Si/Al ratio in synthesized N-A-S-H gel

It is now clear that the concentration of reactants and pH are two significant factors affecting the obtained Si/Al in synthesized N-A-S-H gel. To further reveal the underlying mechanism, the composition of the filtrated solution was analyzed by ICP-OES. Figure 4.4 illustrates the effect of the initial concentration of reactants on the concentration of Si and Al remaining in the filtrated solution. It can be found from Figure 4.4(a) that a higher percentage of Si was consumed when the initial concentration was higher, indicating that more Si was bound in the solid reaction product. This result is consistent with the XRF data of the synthesized N-A-S-H gels, where a higher Si/Al was observed using a higher concentration of reactants (see Table 4.5). In contrast, more than 95 % of Al was consumed for all cases, as shown in Figure 4.4(b), and only a trace amount of Al remained in the filtrated solution even at the elevated initial concentration of Al. The results above indicate a high affinity of Al to form solid N-A-S-H gel, which aligns with the findings in Chapter 3. From all cases shown in Figure 4.4, it can be found that the proportion of Si incorporated into the gel is lower than that of Al. As a result, the Si/Al ratio in the N-A-S-H gel is lower than the corresponding initial Si/Al ratio as shown in Table 4.5. Taking N3_lc_n as an example, 66 % of Si and nearly 100 % of Al were consumed to form N-A-S-H gel, resulting in the Si/Al ratio of 1.8 in the synthesized N-A-S-H gel, which is lower than the initial (target) Si/Al ratio of 3. By increasing the concentration of reactants, a greater proportion of Si can be consumed to form N-A-S-H gel, thereby increasing the obtained Si/Al ratio.

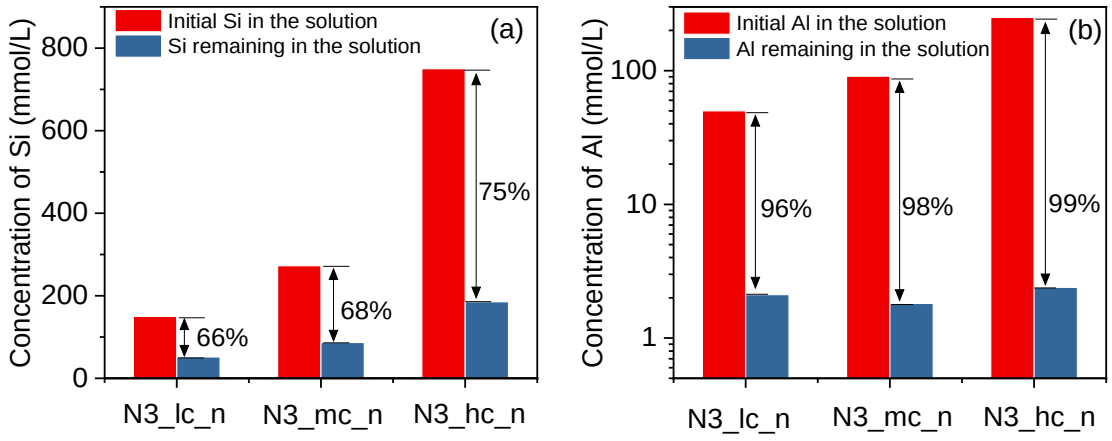

Figure 4.4 Effect of concentration of reactants on the ion concentrations in the filtrated solution.

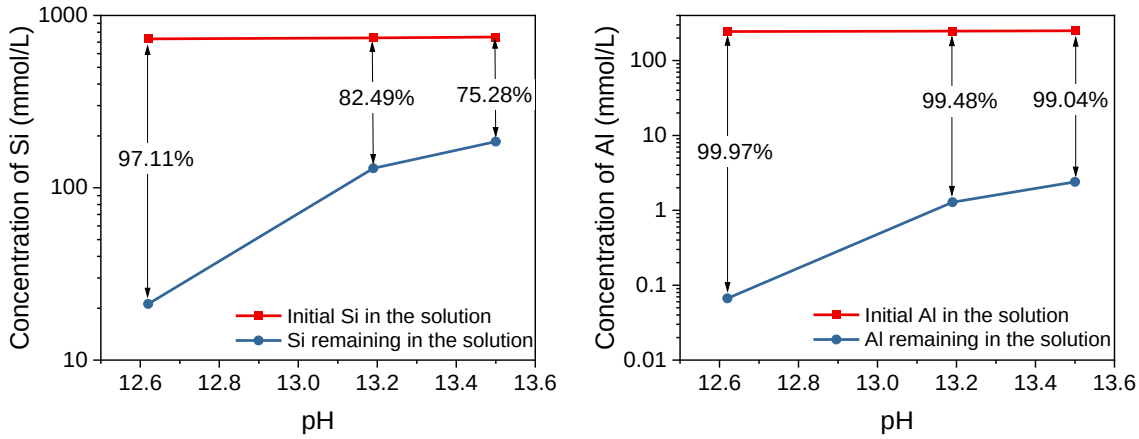

Figure 4.5 Effect of pH on the ion concentrations in the filtrated solution.

Figure 4.5 represents the effect of pH on the concentration of Si and Al remaining in the solution. Again, a negligible amount of Al was detected in the solution for all samples, suggesting substantial Al consumption. In addition, it's noteworthy that Si concentration significantly increased with elevated pH values. This is attributed to the strong tendency of Si to form negatively charged aqueous complexes under basic pH conditions, including species such as $SiO_4H_3^-$, $SiO_4H_2^{2-}$ and $Si_4O_8(OH)_4^{4-}$ [171]. This leads to an increased tendency of particularly Si, but also of Al, to remain in solution, rather than in the solid phase. The same tendency has also been observed for Si and Al in the so-called C-A-S-H phases [172]. Due to the lower solubility of Si at lower pH, more Si is able to form solid N-A-S-H gel. As a result, higher Si/Al can be obtained with decreasing pH, as shown in Table 4.6. When pH was lowered to 12.6 as in the case of N3_hc_lpH_a, around 97 % of Si and almost 100 % of Al had been incorporated into the reaction products. As a result, a Si/Al ratio of 2.7 was achieved in the obtained N-A-S-H gel, which is close to the initial Si/Al ratio of 3.

In summary, the key to obtaining high Si/Al N-A-S-H gel is to ensure that a high fraction of the initial Si precipitates as gel, which depends primarily on a relatively low pH, with a secondary influence from high initial concentrations.

4.3.2.3 Optimal route for synthesis of high Si/Al N-A-S-H gels

Inspired by the success of achieving N-A-S-H gel with a Si/Al ratio near 3 in the case of N3_hc_lpH_a, sample N2_hc_lpH_n was synthesized at a relatively low pH, aiming the obtainment of N-A-S-H gel with a Si/Al ratio of 2 (see Table 4.1). It can be seen from Table 4.7 that, by using an initial Si/Al of 2 and pH of filtrate of 12.0, the obtained Si/Al ratio, i.e. 1.9, was close to the target Si/Al ratio of 2. This demonstrates that the target Si/Al ratio can be achieved using the same initial Si/Al ratio, as long as the pH is carefully adjusted to ensure the major part of Si forms N-A-S-H gel.

It should be noted that the N-A-S-H gel synthesized at relatively low pH values may differ from the real reaction product in AAFA paste formed at much higher pH values. The pH in the pore solution in AAFA pastes at 28 days ranges from 13.4 to 13.8, based on an initial water-to-binder ratio of 0.35 [105], while in the present work, the final pH values ranged from 12.0 to 12.6. The differences in conditions required are mainly related to the amount of water (solution) present. In AAFA pastes, a very low water-to-solid ratio is generally used, resulting in extremely high ion concentrations. As a result, even at high pH values, substantial amounts of Si and Al will end up in solid phases due to solubility consideration. In contrast, the sol-gel method employs a high water-to-solid ratio, resulting in a relatively low concentration of solution. In this case, pH plays a more dominant role than the concentration of reactants. This is why it is difficult to achieve a Si/Al ratio above 1 at very high pH values using the sol-gel procedure as shown in Section 4.3.1. To mimic the real environment in the pore solution of AAFA paste, it would be better to synthesize N-A-S-H gel at high pH environment. Achieving a high Si/Al ratio under such elevated pH conditions necessitates the use of an initial Si/Al ratio considerably higher than the target Si/Al ratio. Following this guiding principle, the second series of samples was synthesized as shown in Table 4.7. An initial Si/Al ratio of 2.8 was adopted in mixture N2.8_hc_hpH_n to obtain N-A-S-H gel with a final Si/Al ratio of 2 at a pH of 13.46, while an initial Si/Al ratio of 5 was needed to obtain a target Si/Al ratio of 3 at a pH of 13.40.

Table 4.7 Two options to synthesize N-A-S-H gels with Si/Al ratios of 2 and 3.

Series	Samples	pH of filtrate	Initial Si/Al	Target Si/Al	Obtained Si/Al by XRF
Series 1	N2_hc_lpH_n	11.98	2	2	1.88
	N3_hc_lpH_a	12.62	3	3	2.74
Series 2	N2.8_hc_hpH_n	13.46	2.8	2	1.95
	N5_hc_hpH_a	13.40	5	3	2.81

Note: ‘N’ stands for N-A-S-H gel; the number after ‘N’ refers to the initial Si/Al ratio; ‘hc’ indicates using a high concentration of reactants; ‘lpH’ and ‘hpH’ signify low and high pH, respectively; ‘n’ indicates no NaOH solution while ‘a’ indicates adding acid (HNO_3).

4.3.3 Characterization of the synthesized N-(C-)A-S-H gels

4.3.3.1 N-A-S-H gels with Si/Al from 1 to 3

Chemical composition of N-A-S-H gels

N-A-S-H gels with Si/Al ratios of 1, 2 and 3 were synthesized successfully at high pH using three mixtures: N1_hc_hpH, N2.8_hc_hpH_n and N5_hc_hpH_a, respectively (see Table 4.1). In order to maintain a pH level as high as that in AAFA paste, extra NaOH solution was added in the mixture N1_hc_hpH, nothing to N2.8_hc_hpH_n while HNO_3 was added for N5_hc_hpH_a, as detailed in Table 4.1.

The chemical compositions of three synthesized N-A-S-H gels were determined by XRF and mass balance, as summarized in Table 4.8. The target Si/Al ratios, namely 1, 2 and 3, were obtained successfully. Basically, Si/Al ratios determined by XRF and mass balance are consistent with each other. Na/Al ratio determined by mass balance calculation was not shown because the content of Na was washed away and not quantified.

The amount of non-evaporable water was also determined. As can be seen from Figure 4.6, the mass of all samples decreased during drying at 105 °C until a constant mass loss (< 0.1 %/h) was reached at 6 h, corresponding to the loss of evaporable water. Subsequently, the temperature was increased at a rate of 10 °C /min up to 1000 °C, resulting in a mass loss of around 5 %, which was assigned to the loss of non-evaporable water in the N-A-S-H gels. It is generally believed that N-A-S-H gels contain relatively little non-evaporable water [93]. According to the TGA results, the stoichiometric coefficient m in synthesized N-A-S-H gels, $(Na_2O)_1(SiO_2)_{1-3}(Al_2O_3)_1(H_2O)_m$, ranges from 1-1.5. However, Rahier et al. [92] reported an even lower m of 0.4 in a geopolymer gel $(Na_2O)_1(SiO_2)_{3.4}(Al_2O_3)_1(H_2O)_m$. This difference might be due to the variations in the liquid-to-solid ratio employed in the respective studies. In this work, synthesis of N-A-S-H gel via sol-gel method requires a high liquid-to-solid ratio (around 8-16), while a low liquid/solid ratio of around 2.5 was used to prepare geopolymer gel in [92]. In contrast, the amount of non-evaporable water determined in this work is much closer to the reality compared to the reported N-A-S-H gel synthesized also via sol-gel method. Gomez-Zamorano et al. [35] reported an even higher stoichiometry factor m of 5 to 8 for $(Na_2O)_1(SiO_2)_{1-2}(Al_2O_3)_1(H_2O)_m$ and Williamson et al. [36] reported an m value of 4-5 for $(Na_2O)_1(SiO_2)_1(Al_2O_3)_1(H_2O)_m$, i.e. values at least ten times larger than those in geopolymer [92]. The difference in the values obtained in this work and the literature [35,36] can be attributed, at least partially, to variations in the temperature range used to determine the non-evaporable water. Previous studies [35,36] involved assessing the total mass loss within the temperature range of 40 or 50 °C to 975 °C. This method tends to overestimate the amount of non-evaporable water by approximately three to four times higher than the approach employed in this work.

Based on the results of XRF and TGA, the chemical compositions of three types of N-A-S-H gels are listed in Table 4.9.

Table 4.8 Average Si/Al and Na/Al in synthesized N-A-S-H gels

	N1_hc_hpH	N2.8_hc_hpH_n	N5_hc_hpH_a
$(Si/Al)_{XRF}$	1.10	1.95	2.81
$(Si/Al)_{Mass\ balance}$	1.17	2.24	3.35
$(Na/Al)_{XRF}$	1.08	1.18	1.21

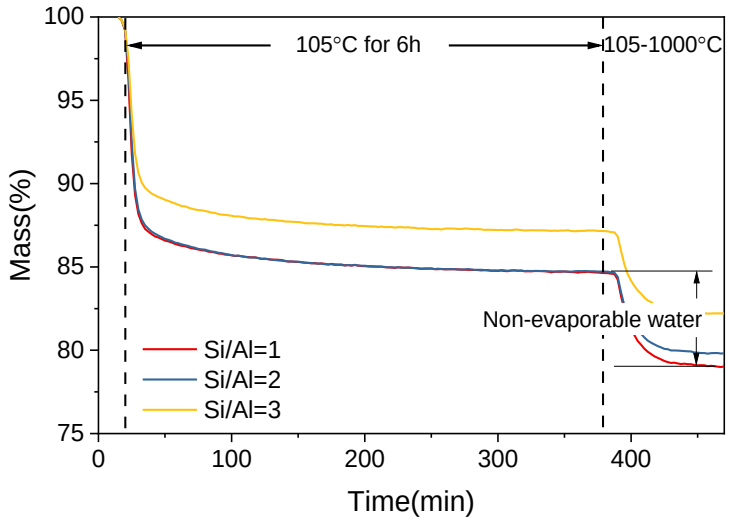

Figure 4.6 Thermogravimetric analysis of synthesized N-A-S-H gels with Si/Al from 1 to 3.

Table 4.9 Chemical composition of synthesized N-A-S-H gels.

Samples	Non-evaporable water	Chemical composition
N1_hc_hpH	5.59 %	$(Na_2O)_{1.1}(SiO_2)_{2.2}(Al_2O_3)_1(H_2O)_{0.99}$
N2.8_hc_hpH_n	4.84 %	$(Na_2O)_{1.2}(SiO_2)_4(Al_2O_3)_1(H_2O)_{1.18}$
N5_hc_hpH_a	4.90 %	$(Na_2O)_{1.2}(SiO_2)_{5.6}(Al_2O_3)_1(H_2O)_{1.47}$

XRD patterns of N-A-S-H gels

N-A-S-H gels with various Si/Al ratios all exhibited a single amorphous hump in XRD curves, as shown in Figure 4.7. The hump shifted towards small angles as Si/Al increased, which is entirely in line with observations in AAFA pastes [156], where XRD humps at 28.5°, 26.9°, and 26.3° were observed for Si/Al of 1.5, 2.5, 4.5, respectively. It is the first time that an observable shift towards lower 2θ with increasing Si/Al in XRD has been reported for synthesized N-A-S-H gels, indicating a clear difference in the chemical composition. Such a shift was also observed in Chapter 3 (see Figure 3.12), where the underlying reason was explored.

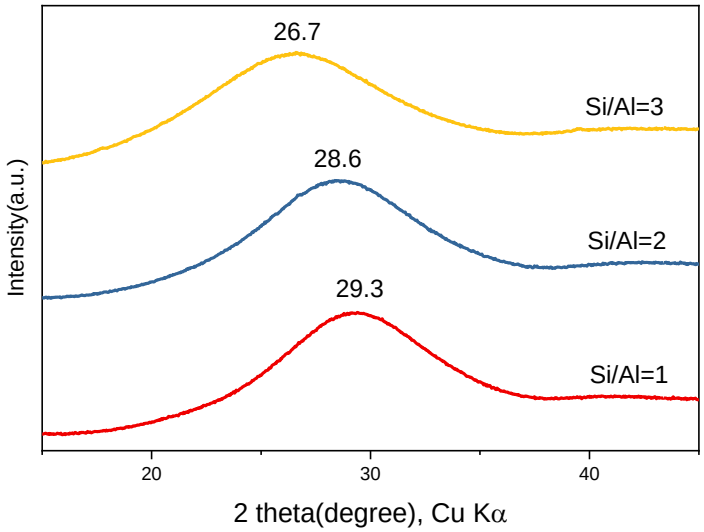

Figure 4.7 XRD patterns for synthesized N-A-S-H gels with Si/Al from 1 to 3.

FTIR spectra of N-A-S-H gels

The FTIR spectra of these synthesized N-A-S-H gels with various Si/Al ratios are shown in Figure 4.8. The assignment of the bands in FTIR spectra is summarized in Table 4.10. The main band in the region between 1250-920 cm^{-1} is attributed to the asymmetric stretching vibrations of Si–O–T (T refers to Si or Al) [173,174]. This band is a typical signal indicating the formation of N-A-S-H gel [73,119]. The position of the main band contains vital information about the Si/Al ratio and connectivity of the N-A-S-H gel framework [75,175]. A noticeable shift towards a higher wavenumber is observed as Si/Al ratio increases from 1 to 3. The band appearing at 920-800 cm^{-1} is likely associated with asymmetric stretching of AlO_4^- group [176]. The band becomes less pronounced with a higher Si/Al ratio, indicating a lower Si-O-Al link fraction. A similar trend was observed as the Si/Na ratio increased in [177]. The band centered at around 690 cm^{-1} is assigned to symmetrical stretch vibrations of Si–O–T [24,178]. A weak band at around 570 cm^{-1} is contributed by the ring vibration of the TO_4 tetrahedron [24]. The weak nature of the band is due to the absence of crystalline phases [75]. Finally, the band located at around 1640 cm^{-1} is corresponding to the bending vibration of H-O-H [98,124]. Overall, the wavenumbers and the number of IR bands for each N-A-S-H gel are in good agreement with those in [24,119]. Based on the above chemical composition and structural information, it can be concluded that the target N-A-S-H gels with various Si/Al ratios from 1 to 3 were successfully synthesized.

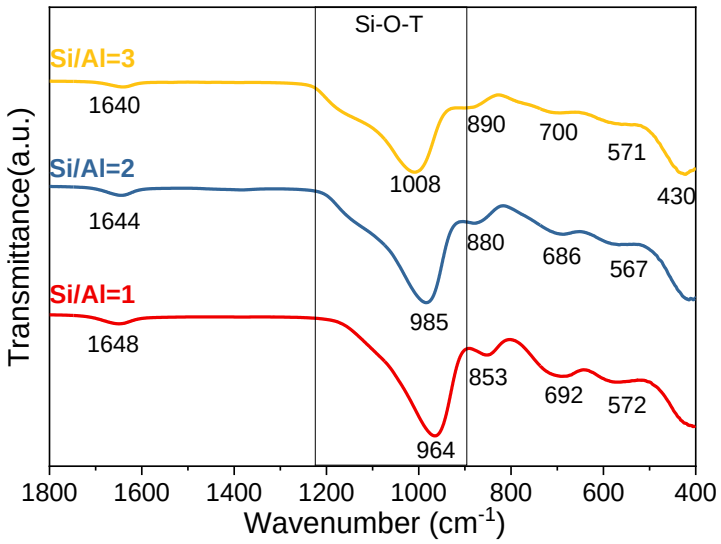

Figure 4.8 FTIR spectra for synthesized N-A-S-H gels with Si/Al from 1 to 3.

Table 4.10 Assignment of bands in FTIR spectra of N-(C-)A-S-H gels.

Position	Assignment	Ref
1640-1648	bending vibration of H-O-H	[98,124]
900-1250	asymmetric stretching of Si–O–T	[173,174]
853-890	asymmetric stretching of AlO_4^-	[176]
686-700	symmetrical stretching of Si–O–T	[24,178]
567-581	ring vibration of the TO_4	[24]
420-430	bending vibration of T-O	[124]

4.3.3.2 N-C-A-S-H gels with Ca/Al from 0.25 to 0.5

N-C-A-S-H gels were synthesized following a similar synthesis route of N-A-S-H gels, with the addition of $Ca(NO_3)_2{\cdot}4H_2O$ as a Ca-providing reactant. The target Si/Al ratio of N-C-A-S-H gel also ranged from 1 to 3, while the target Ca/Al ratios were 0.25 and 0.5. The chemical composition of the synthesized N-C-A-S-H gels, measured by XRF, is shown in Table 4.11. By adjusting the initial Si/Al ratio and the pH of the system, N-C-A-S-H gels with three target Si/Al ratios, i.e. 1, 2 and 3, were obtained. The resulting Ca/Al ratios of all synthesized N-C-A-S-H gels are also very close to the target Ca/Al ratios, 0.25 and 0.5. In addition, the resulting Ca/Al ratio is slightly smaller than the initial Ca/Al ratio, except for the samples NC1_0.25 and NC1_0.5. This is related to the different phases formed in different mixtures, which will be discussed below, combined with the results of XRD. Furthermore, it is worth noting that an increase in Ca/Al ratio leads to a decrease in Na/Al ratio for all cases, which is in good agreement with the simulation results in Chapter 3 (see Table 3.4). This further confirms the conclusion that Ca is preferred over Na for incorporation into N-C-A-S-H gel. It can been also observed that Na/Al ratio of the synthesized N-C-A-S-H gels increases with an increase in Si/Al ratio. This can be attributed to the significantly higher initial Na/Al ratio in the mixtures targeting a higher Si/Al ratio.

Table 4.11 Chemical compositions of synthesized N-C-A-S-H gels.

Samples	Initial Si/Al	Si/Al in N-C-A-S-H gel	Initial Ca/Al	Ca/Al in N-C-A-S-H gel	Initial Na/Al	Na/Al in N-C-A-S-H gel
NC1_0.25	1	1.09	0.25	0.29	2.4	0.69
NC1_0.5	1	1.04	0.5	0.59	2.4	0.49
NC2_0.25	3.5	2.04	0.3	0.22	7.0	1.08
NC2_0.5	3.5	2.20	0.55	0.44	7.0	0.99
NC3_0.25	6	3.10	0.33	0.25	12	1.39
NC3_0.5	6	2.83	0.53	0.43	12	1.28

The XRD patterns of the synthesized N-C-A-S-H gels are shown in Figure 4.9. All samples show a hump at around 30° 2θ, which can be assigned to the amorphous N-C-A-S-H gel. However, two additional phases, calcite and calcium aluminate hydrate ($Ca_2Al(OH)_7{\cdot}3H_2O$, or referred to as $C_2AH_{6.5}$), are also detected both in samples NC1_0.25 and NC1_0.5 (Figure 4.9(a). The presence of these extra Ca-containing phases leads to a higher resulting Ca/Al ratio compared to those in other samples. The formation of calcite is due to carbonation since these two samples were synthesized in air. However, the presence of $Ca_2Al(OH)_7{\cdot}3H_2O$ indicates the challenge in obtaining pure N-C-A-S-H gel with a Si/Al ratio of 1 in such a mixture.

In contrast, the XRD pattern shows a single hump for samples NC2_0.25, NC2_0.5, NC3_0.25 and NC3_0.5 as shown in Figure 4.9(b). Couple with XRF results, it indicates that pure N-C-A-S-H gels with target Si/Al and Ca/Al ratios have been achieved. Thus, only the N-C-A-S-H gel with a Si/Al ratio of 2 and 3 will be further discussed in the following sections. It can also be seen from Figure 4.9(b) that the hump shifts to a higher 2θ angle with an increase in Ca/Al ratio, which is consistent with the simulation results in Chapter 3 (see Figure 3.21).

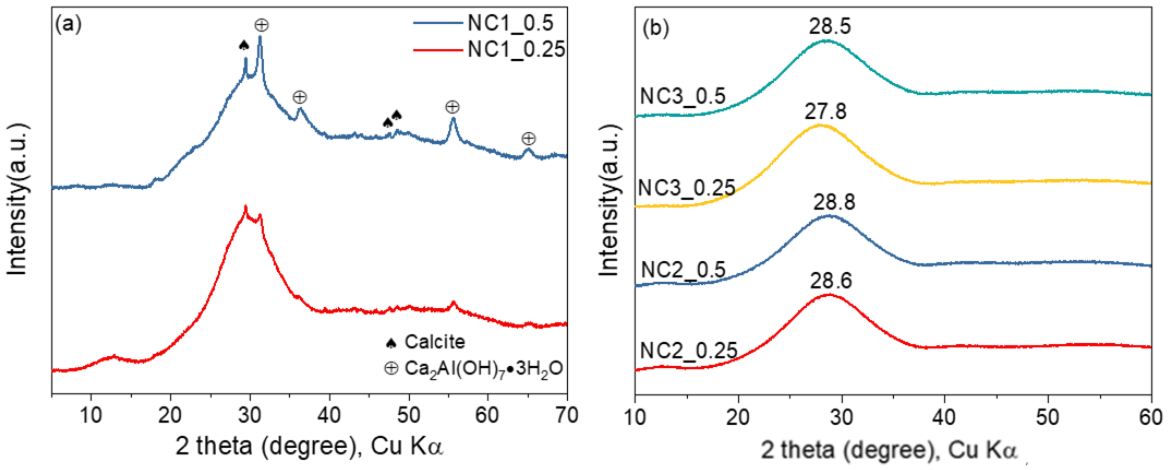

Figure 4.9 XRD patterns of synthesized N-C-A-S-H gels with various Ca/Al ratios (0.25 and 0.5) and Si/Al ratio of 1 in (a), Si/Al ratio of 2 and 3 in (b).

An identical TGA measurement was performed to determine the amount of non-evaporable water in the synthesized N-C-A-S-H gels, and the results are shown in Figure 4.10. The mass loss occurring at the temperature ramping stage (105-1000 °C) was assigned to the removal of non-evaporable water in the N-C-A-S-H gels. The amount of non-evaporable water in the N-C-A-S-H gels is summarized in Table 4.11. Couple with the XRF results, the chemical composition of all synthesized N-C-A-S-H gels can be determined, as also presented in Table 4.12.

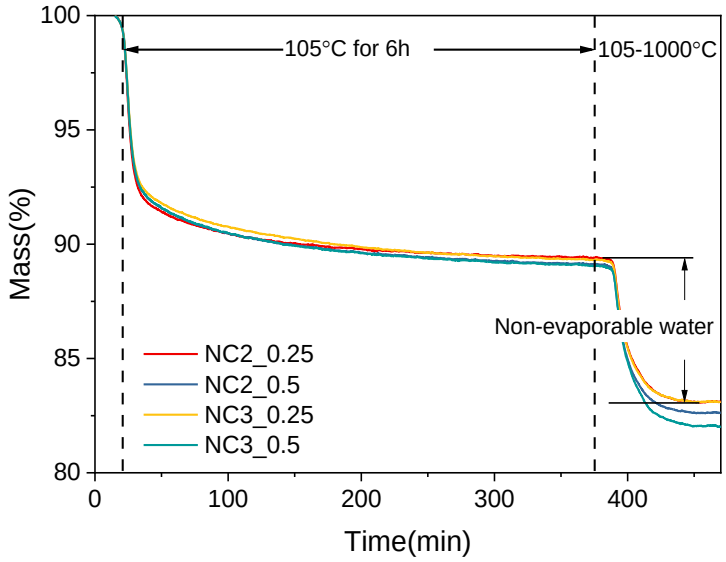

Figure 4.10 TGA of synthesized N-C-A-S-H gels with various Ca/Al ratio.

Table 4.12 Chemical composition of synthesized N-C-A-S-H gels.

Samples	Non-evaporable water	Chemical composition
NC2_0.25	6.4%	$(Na_2O)_{0.5}(CaO)_{0.22}(SiO_2)_{2.04}(Al_2O_3)_{0.5}(H_2O)_{0.93}$
NC2_0.5	6.5%	$(Na_2O)_{0.5}(CaO)_{0.44}(SiO_2)_{2.2}(Al_2O_3)_{0.5}(H_2O)_{1.04}$
NC3_0.25	6.4%	$(Na_2O)_{0.7}(CaO)_{0.25}(SiO_2)_{3.1}(Al_2O_3)_{0.5}(H_2O)_{1.26}$
NC3_0.5	7.1%	$(Na_2O)_{0.68}(CaO)_{0.43}(SiO_2)_{2.8}(Al_2O_3)_{0.5}(H_2O)_{1.35}$

Figure 4.11 illustrates the FTIR spectra of the synthesized N-(C-)A-S-H gels with a Ca/Al ratio ranging from 0 to 0.5, and a Si/Al ratio of 2 and 3. Similar to N-A-S-H gel, the FTIR spectra of N-C-A-S-H gel also show a main band located from 1250-920 cm^{-1}, which is related to the asymmetric stretching vibrations of Si–O–T [173]. Basically, the main band not only becomes narrow but also moves to a lower wavenumber with the increase in Ca/Al. This finding implies that N-(C-)A-S-H gel becomes less polymerized with a higher incorporation of Ca, which is in accordance with the Q^n distribution of simulated N-(C-)A-S-H gel in Chapter 3 (see Figure 3.22 and 3.23). However, it's worth noting that NC2_0.25 and NC2_0.25 deviate slightly from this pattern due to variations in their Si/Al ratios. Specifically, the Si/Al ratio of NC2_0.5 is slightly higher than that of NC2_0.25, resulting in a small band between 1200-1150 cm^{-1} observed in NC2_0.5. As a result, the main band in NC2_0.5 appears broader than that in NC2_0.25. Additionally, the small band at around 880 cm^{-1} becomes less obvious as more Ca is incorporated, especially in the case of Si/Al=2 (Figure 4.11(a)). As summarized in Table 4.10, this band is probably attributed by asymmetric stretching of AlO_4^-. According to the simulation results in Chapter 3 (see Figure 3.22), the quantity of [AlO_4] tetrahedra decreased as more Ca is incorporated. This can account for the fact that a higher Ca/Al in N-(C-)A-S-H gel leads to a less prominent band at 880 cm^{-1}. The bands at around 581 cm^{-1} and 420 cm^{-1} are attributed by the ring vibration of the TO_4 and bending vibration of T-O, respectively [24,124].

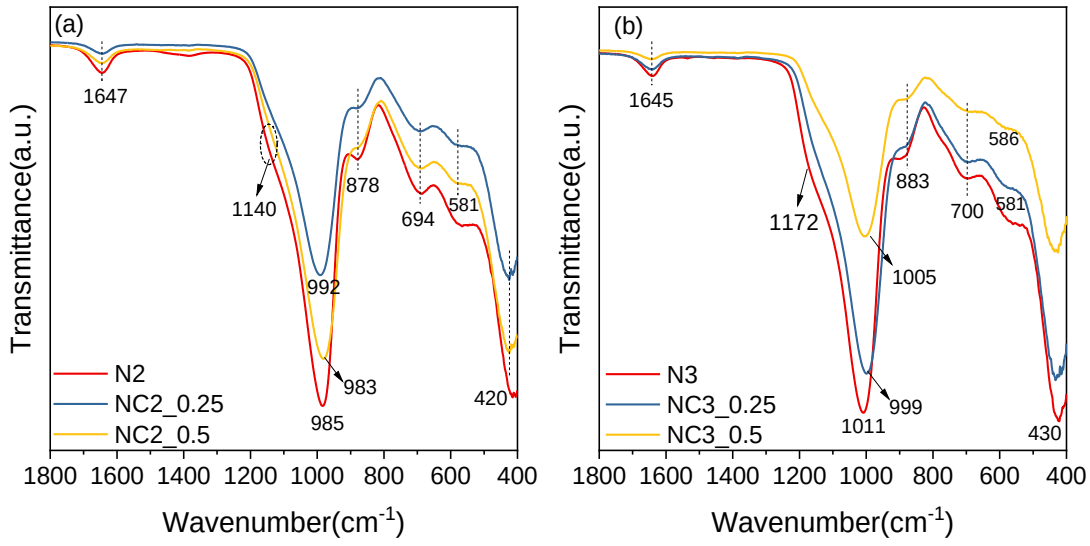

Figure 4.11 FTIR spectra of synthesized N-(C-)A-S-H gels with (a) a Si/Al ratio of 2 and (b) a Si/Al ratio of 3.

4.4 Conclusions

The mixtures and conditions based on the sol-gel method have been developed in this chapter to synthesize N-(C-)A-S-H gels with Si/Al ratios ranging from 1 to 3 and Ca/Al ratios from 0 to 0.5. A systematic study was conducted to investigate the influence of reaction temperature, reaction time, initial Si/Al ratio, reactant concentrations, and pH values of the filtrate on the final Si/Al ratio in the synthesized N-A-S-H gels. The Si and Al concentrations in the filtrate were analyzed by ICP-OES to elucidate the underlying mechanism for obtaining high Si/Al N-(C-)A-S-H gel. Using the proposed optical route, pure amorphous N-(C-)A-S-H gels with the target Si/Al and Ca/Al ratios were successfully synthesized and characterized. Based on the results and discussion, the following remarks are made:

1. The existing mixtures and reaction conditions for sol-gel methods reported in the literature only produced N-A-S-H gel with Si/Al ratio near 1, even at high initial Si/Al in the mixing solutions. The reaction temperature and reaction time had little effect on increasing the Si/Al ratio in the N-A-S-H gel.
2. The key factors to obtain N-A-S-H gel with high Si/Al ratio were to lower the pH values and use concentrated solutions. Under basic conditions, lowering the pH value reduces the tendency of Si to remain in solution, thereby allowing a higher Si/Al ratio in the N-A-S-H gel. This poses a challenge for the synthesis of high Si/Al N-A-S-H gels at very high pH, i.e. in the range of the alkalinity of pore solutions in AAFA paste. To achieve it, an initially higher Si/Al ratio than the target ratio must be employed.
3. N-A-S-H gels with different Si/Al ratios differ in structure according to XRD and FTIR patterns. An increase of Si/Al ratio of N-A-S-H gel leads to a shift toward lower 2θ angle in the XRD patterns, in good agreement with the simulation results in Chapter 3. Furthermore, the position of the Si-O-T asymmetric stretching band correlates closely with the Si/Al ratio of N-A-S-H gel.
4. N-C-A-S-H gel shows a higher affinity for Ca than Na as evidenced by the chemical composition of N-C-A-S-H gel, which is in accordance with the simulation results in Chapter 3. XRD and FTIR results show that the Ca/Al ratio in N-(C-)A-S-H gel can also impact its structure, consistent with the findings in Chapter 3.

The N-(C-)A-S-H gels with various Si/Al and Ca/Al ratios synthesized in this Chapter will undergo dissolution experiments to determine their solubility in Chapter 5.

Chapter 5

Solubility and thermodynamic properties of N-(C-)A-S-H gels

5.1 Introduction

A thermodynamic database of N-(C-)A-S-H gels, encompassing their solubility products and other thermodynamic properties, i.e. the Gibbs free energy, heat capacity, entropy, enthalpy, and molar volume, is indispensable for studying the chemical reactions involved in alkali-activation of fly ash. However, current research lacks experimentally derived solubility products of N-C-A-S-H gels and N-A-S-H gels with Si/Al ratios exceeding 2. While some studies have measured solubility products for N-A-S-H gels with Si/Al ratios below 2, inconsistencies have been noted, as highlighted in Chapter 2. Due to the absence of solubility product data, the thermodynamic properties of N-(C-)A-S-H gels are inadequate and incomplete, which hinders the investigation of reactions and phase assemblages of alkali-activated fly ash (AAFA) through thermodynamic modeling. Therefore, it becomes imperative to verify and expand the existing thermodynamic data of N-(C-)A-S-H gels.

The primary objective of this chapter is to establish a comprehensive thermodynamic database for the synthesized N-(C-)A-S-H gels as detailed in Section 4.3.3 in Chapter 4. Initially, dissolution experiments of N-(C-)A-S-H gels are conducted at different temperatures until reaching an equilibrium state. Subsequently, the solid residue phase is characterized through XRD measurement, while the solution composition is determined using ICP-OES and a pH meter. This data is then utilized to calculate the solubility products of N-(C-)A-S-H gels. Furthermore, the effects of the Si/Al ratio, crystallization and temperature on the solubility products are analyzed. Finally, thermodynamic properties of N-(C-)A-S-H gels are derived from the experimentally determined solubility products at 25 °C, and validated through the solubility products measured at higher temperatures (40 and 60 °C). The results of this chapter will lay a solid foundation for the thermodynamic modeling of AAFA in Chapter 6.

5.2 Materials and methods

5.2.1 Raw materials

This chapter utilized seven types of N-(C-)A-S-H gels with various Si/Al and Ca/Al ratios synthesized in Chapter 4. Specifically, they include three N-A-S-H gels (see Table 4.9) and four types of N-C-A-S-H gels (see Table 4.11). The three N-A-S-H gels with Si/Al ratios from 1 to 3 are denoted as N1, N2 and N3 for clarity in this chapter, while four N-C-A-S-H gels share the same notations used in Chapter 4, i.e. NC2 _0.25, NC2_0.5, NC3_0.25 and NC3_0.5,

where the initial number represents the Si/Al ratio and the second denotes the Ca/Al ratio. In addition, deionized water was also used.

5.2.2 Dissolution experiments

N-(C-)A-S-H gel was dispersed into deionized water with a solid-to-water ratio of 20 g/L in a tube. The tube contained a nearly full solution, indicating little air inside. In addition, the tube was tightly sealed to avoid air penetration, and thus carbonation. According to the results in [34,124], the dissolution of N-A-S-H gel and zeolite at room temperature was near equilibrium after around 1 month, which means that their solubility product remained relatively stable after 1 month. Thus, the dissolution test in this work was conducted in a shaker moving at a speed of 220 rpm and maintained at 25 °C for 2 months, at 40 and 60 °C for 1 month, respectively. After equilibrium time, the suspension was filtered using Whatman 42 filter paper (2.5 μm) to obtain the solid and aqueous phases. The solid residue was then freeze-dried until a constant weight was obtained. For each sample, triplicate measurements were performed and the average results are presented.

5.2.3 Solid and aqueous phases characterization

The solid residue after dissolution at 60 °C underwent XRD analysis to ascertain any phase transition during the dissolution process. The procedures and details of performing XRD are described in Section 4.2.3. The pH of the filtrated aqueous phase was measured with a pH meter at room temperature (25 °C) and corrected to 40 °C and 60 °C. The pH differences caused by temperatures were calculated with the Gibbs free energy minimization program GEM-Selektor V3 (GEMS) [41]: -0.58 for 40 °C and -0.98 for 60 °C. The concentrations of Si, Al, Na and Ca in the filtrated aqueous phase were measured using an ICP-OES spectrometer with the same procedures described in Section 4.2.3.

5.2.4 Thermodynamic modeling

GEMS was employed to determine the solubility product and thermodynamic properties of N-(C-)A-S-H gels. The general thermodynamic data for solid, aqueous, and gaseous phases involved in the system were taken from the PSI/Nagra [171] and Cemdata18 [32].

The following dissolution reaction was used to calculate the solubility products for the synthesized N-(C-)A-S-H gels:

$$(Na_2O)_a(CaO)_b(Al_2O_3)_c(SiO_2)_d(H_2O)_e \rightarrow 2a\ Na^+ + b\ Ca^{2+} + 2c\ AlO_2^- + d\ SiO_2^0 + 2(a+b-c)\ OH^- + (e-a-b+c)H_2O \quad (5.1)$$

The subscripts a, b, c, d and e, referring to the stoichiometry of the elements in the gels, can be found in Table 4.9 and Table 4.12.

Correspondingly, the solubility products can be determined using the following equations:

$$K_{sp} = \{Na^+\}^{2a} \cdot \{Ca^{2+}\}^b \cdot \{AlO_2^-\}^{2c} \cdot \{SiO_2^0\}^d \cdot \{OH^-\}^{2(a+b-c)} \cdot \{H_2O\}^{(e-a-b+c)} \quad (5.2)$$

where {i} refers to the activity of the dissolved species i, i.e. Na^+, Ca^{2+}, AlO_2^-, SiO_2^0, OH^- and H_2O. The activity can be calculated with GEMS from the measured concentration (m_i) using $\{i\} = \gamma_i \cdot m_i$, where γ_i is the activity coefficient and can be computed using the built-in extended Debye-Hückel equation in GEMS [31]:

$$\log \gamma_i = \frac{-A_y z_i^2 \sqrt{I}}{I + B_y a_i \sqrt{I}} + b_y I \quad (5.3)$$

where z_i is the charge of species i, I is the effective molal ionic strength [116], A_y and B_y are temperature-dependent coefficients (A_y =0.51, B_y =0.33 at 25 °C), a_i is the ion size parameter, which is set at 3.31 Å for NaOH-based solutions [179], and b_y is a semi-empirical parameter (~0.098 for NaOH solutions at 25 °C) [179].

Once the solubility product is determined, the Gibbs free energy of reaction $\Delta_r G^0$, and thus the Gibbs free energy of formation $\Delta_f G^0$can be calculated according to Equation 5.4:

$$\Delta_r G^0 = \sum_i v_i \Delta_f G_i^0 = -RTlnK_{sp} \quad (5.4)$$

where R is the universal gas constant 8.3145 J/mol/K, T represents absolute temperature in K, v_i is the stoichiometric reaction coefficient, $\Delta_f G_i^0$ stands for the Gibbs free energy of the formation of the species used in the reaction.

The apparent Gibbs free energy of formation at any desired temperature $\Delta_a G_T^0$ can be calculated according to Equation 5.5 [180]:

$$\Delta_a G_T^0 = \Delta_f G_{T_0}^0 - S_{T_0}^0 (T - T_0) + \int_{T_0}^{T} C_P^0 dT - \int_{T_0}^{T} \frac{C_P^0}{T} dT \quad (5.5)$$

where T_0 = 298.15 K, $\Delta_f G_{T_0}^0$ refers to the Gibbs free energy of formation at 298.15 K, $S_{T_0}^0$ denotes the standard entropy at 298.15 K, while C_P^0 corresponds to the standard heat capacity. Since C_P^0 can be assumed to remain constant within a narrow temperature range of 20-80 °C [124,181], Equation 5.5 can expressed as:

$$\Delta_a G_T^0 = \Delta_f G_{T_0}^0 - S_{T_0}^0 (T - T_0) + C_{T_0}^0 \left(Tln\frac{T}{T_0} - T + T_0 \right) \quad (5.6)$$

Standard values of heat capacity C_p^0 and entropy S^0 were estimated using the additivity method ($\Delta_r C_p^0 = 0 \; or \; \Delta_r S^0 = 0$), which is expected to yield reliable results if suitable components are chosen [123,180]. In this work, faujasite Y ($Na_2Al_2Si_4O_{12}{\cdot}8H_2O$), calcium oxide, sodium hydroxide, quartz and zeolitic H_2O were used for additivity calculation using the following Equation 5.7. Furthermore, the entropy term was further corrected for volume changes according to Eq. 62 in [121], which found that accounting for volume changes enhanced the accuracy of the entropy correction.

$$\Phi^0_{(Na_2O)_a(CaO)_b(Al_2O_3)_c(SiO_2)_d(H_2O)_e} = c\Phi^0_{Na_2Al_2Si_4O_{12}\cdot 8H_2O} + (2a - 2c)\Phi^0_{NaOH} + \quad (5.7)$$

$b\Phi^0_{CaO} + (\mathrm{d} - 4\mathrm{c})\Phi^0_{SiO_2} + (\mathrm{e} - \mathrm{a} - 7\mathrm{c})\Phi^0_{H_2O}$

where Φ^0 represents C_p^0 or S^0. The thermodynamic data of components are provided in Appendix B (Table B.1).

To assess the accuracy of C_p^0 or S^0, the solubility product $\log K_T$ at different temperatures were calculated using the 3-term extrapolation function (see Equation 5.8) in GEMS, to compare to the experimentally determined $\log K_T$ [122].

$$\log K_T = a + \frac{b}{T} + c\ lnT \tag{5.8}$$

where

$\mathrm{a} = \left[\Delta S^0_{T_0} - \Delta C^0_{p,T_0}(1 + lnT_0)\right]/2.303\mathrm{R}$

$\mathrm{b} = (-\Delta H^0_{T_0} + \Delta C^0_{p,T_0} T_0)/2.303\mathrm{R}$

$\mathrm{c} = \Delta C^0_{p,T_0}/2.303R$

T_0 represents the temperature at 298.15 K, ΔS and ΔC_P denote the changes in entropy and heat capacity of the reaction at T_0.

The standard molar volume V^0 was also estimated from density calculations using the method in [182], with the following equations:

$$\rho^{sc}_{N(C)ASH} = N_A \rho'_{N(C)ASH} \left[\frac{\left(\frac{Na_2O}{SiO_2}\right) b^{sc}_{Na_2O} + b^{sc}_{SiO_2} + \left(\frac{CaO}{SiO_2}\right) b^{sc}_{CaO} + \left(\frac{Al_2O_3}{SiO_2}\right) b^{sc}_{Al_2O_3} + \left(\frac{H_2O}{SiO_2}\right) b^{sc}_{H_2O}}{M_{N(C)ASH}} \right] \tag{5.9}$$

$$V^0 = M_{N(C)ASH}/\rho'_{N(C)ASH} \tag{5.10}$$

where $\rho^{sc}_{N(C)ASH}$ is the scattering length density, taken as $3.4\times10^{-14}\mathrm{m}^{-2}$ from [183], $\rho'_{N(C)ASH}$ is the predicted density of a N-(C-)A-S-H end-member, N_A is Avogadro's number (6.02×10^{23}), b^{sc} parameters are the neutron scattering lengths for Na_2O, SiO_2, CaO, Al_2O_3 and H_2O, which were taken as 13.06 fm, 15.8 fm, 10.5 fm, 24.3 fm and -1.68 fm, respectively. Ratios $\frac{Na_2O}{SiO_2}$, $\frac{CaO}{SiO_2}$, $\frac{Al_2O_3}{SiO_2}$ and $\frac{H_2O}{SiO_2}$ are molar composition ratios of a N-(C-)A-S-H end-member, and $M_{N(C)ASH}$ is the molar mass of a N-(C-)A-S-H end-member.

5.3 Results and discussion

5.3.1 Characterization of solid and aqueous phases

During the dissolution of N-A-S-H gels, three types of elements, i.e. Si, Al and Na, were released into the solution, and their concentrations were measured and depicted in Figure

5.1. Notably, Na is consistently the dominant element in the filtrate, independent of the temperature. It is expected that Na is the easiest element to dissolve, as it only serves as the network modifier in the structure of N-A-S-H gel, unlike Si or Al, which act as the network former. The dissolutions of Si and Al are closely related to the Si/Al ratio in the N-A-S-H gel. For N-A-S-H gel with a Si/Al ratio of 1 (N1), the concentration of Al was higher than that of Si, regardless of the temperature, while opposite results are found in high Si/Al ratio (i.e. N2 and N3). Moreover, the Si/Al ratio in the filtrated solution in N2 and N3 samples is much higher than the Si/Al ratio in original N-A-S-H gels. This phenomenon is particularly pronounced in the gels with higher Si/Al ratio. This indicates that a high Si/Al N-A-S-H gel can only form in an extremely Si-rich environment.

Similarly, the compositions of the filtrated solutions after N-C-A-S-H gels dissolved are shown in Figure 5.2. Again, the dominant element in the filtrated solution is still Na, while Ca, also as the network modifier, is the least soluble. Although this is partly attributed to the difference in their contents in the N-C-A-S-H gel, this finding confirms that N-C-A-S-H gel has a higher affinity to Ca than Na, as found in Chapters 3 and 4. The concentrations of Si and Na both increase slightly as temperature increases. Conversely, the concentrations of Al and Ca first increase and then decrease with the increase in temperature. Similar trends have been found in the dissolution of C-(A)-S-H gels in the literature [184,185], which reported the concentrations of Ca and Al do not increase monotonically with temperature, but showed a decreasing trend at relatively high temperatures. The relationship between the solubility and temperature, as well as the corresponding possible reasons, will be discussed in Section 5.3.2.

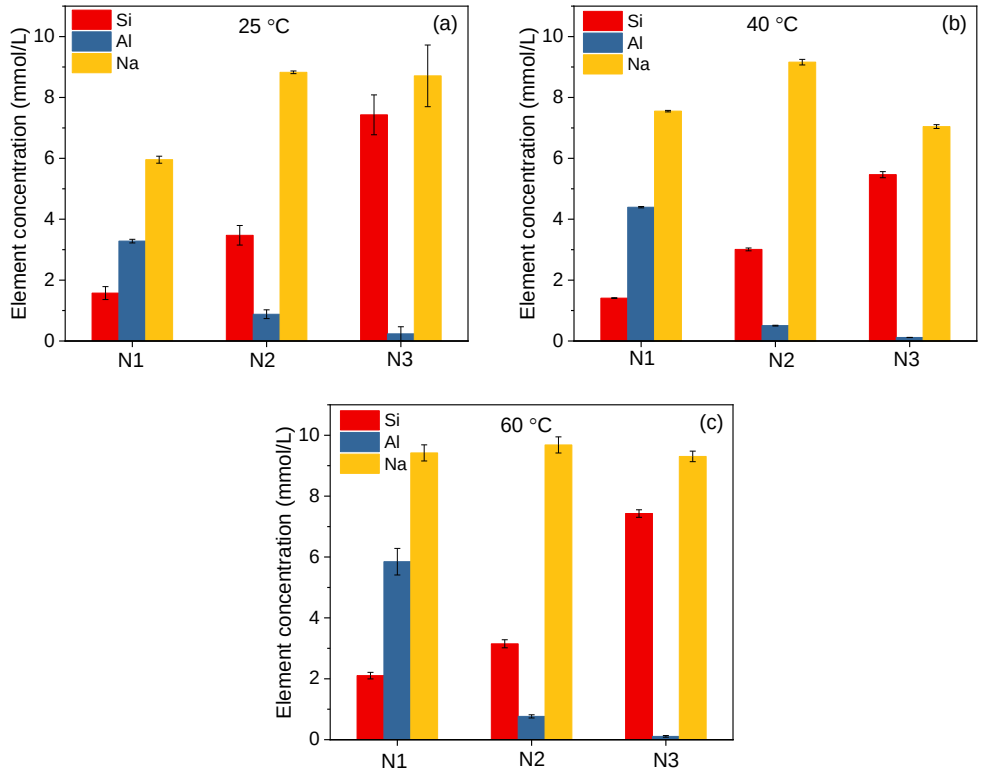

Figure 5.1 Concentration of Si, Al and Na in the filtrated solution after immersion of the N-A-S-H gel in water at (a) 25 °C, (b) 40 °C, and (c) 60 °C.

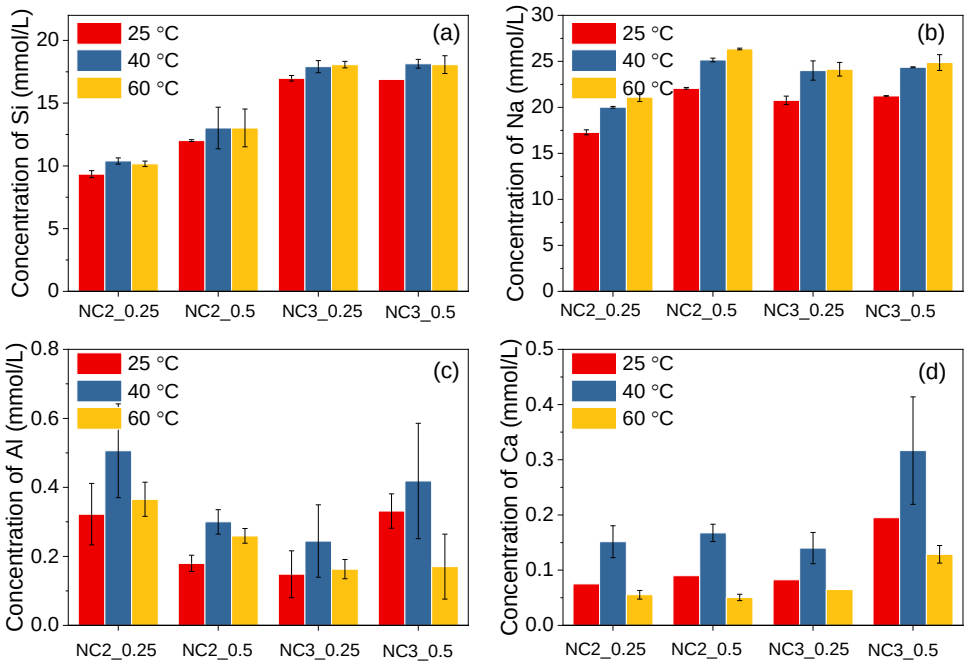

Figure 5.2 Concentrations of (a) Si, (b) Na, (c) Al and (d) Ca in the filtrated solution after immersion of the N-C-A-S-H gel in water at different temperatures.

Apart from the elemental compositions, the pH values of the filtrated solutions were also measured, as shown in Appendix B (see Table B.2). The element compositions and the pH values of the filtrated solutions will be used to determine the solubilities of the N-(C-)A-S-H gels.

As N-(C-)A-S-H gels tend to undergo phase transformation at high temperatures, the phases of N-(C-)A-S-H gels after dissolution at 60 °C were characterized using the XRD technique. The XRD patterns in Figure 5.3 confirmed that the post-dissolution gels maintained their amorphous structure and did not transform to a new crystalline phase at high temperatures. Notably, the XRD humps of the gels did not move after dissolution, except N3, where the variation is probably due to the change in Si/Al ratio. As can be seen in Figure 5.1, the $Si_{dissolved}/Al_{dissolved}$ ratio markedly surpasses the original Si/Al ratio of N3, suggesting that the Si/Al ratio in the residue (N3) is less than 3. It has been already found in Chapter 3 and Chapter 4 that the XRD hump of the N-(C-)A-S-H gel with a smaller Si/Al ratio is located at a higher 2θ angle. This can explain why a hump shift toward higher 2θ angles was observed upon the dissolution of N3. Nevertheless, the XRD results affirm the absence of phase transformation during the dissolution test at high temperatures. This observation indicates that the solubility was measured based on pure N-(C-)A-S-H gel.

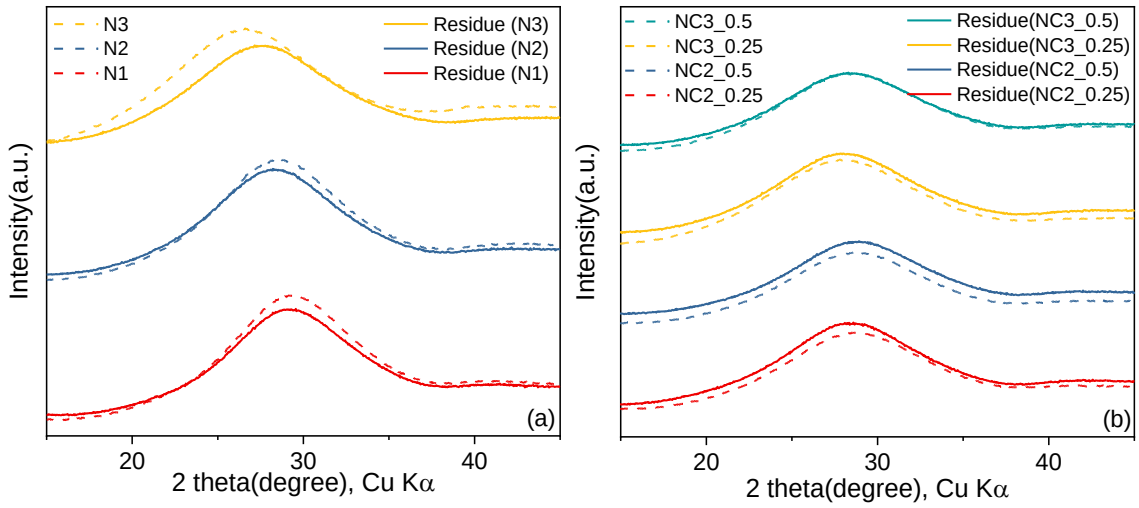

Figure 5.3 XRD patterns of remaining solid phase after dissolution at 60 ˚C for 1 month. XRD patterns of N-(C-)A-S-H gels before dissolution were plotted in dash lines for comparison. (a) N-A-S-H gels, (b) N-C-A-S-H gels.

5.3.2 Solubility products of N-(C-)A-S-H gel

The solubility products of N-A-S-H gels at different temperatures were calculated based on the dissolution reactions listed in Table 5.1. Note that the chemical compositions of the N-A-S-H gel are slightly modified to achieve a Na/Al ratio of 1, assuming that the slight surplus of Na observed by XRF was due to the presence of some water with a high concentration of Na. Figure 5.4 shows the log K_{sp} values of the synthesized N-A-S-H gels with three different Si/Al ratios, and compared to K_{sp} values derived from the dissolution reactions using the same species, i.e. Na^+, AlO_2^-, SiO_2^0 and OH^- (if necessary for charge balance) from literatures. For cases where different species were used, a transformation was performed to recalculate the solubility products (see Table 2.2). It can be seen that the log K_{sp} values of N-A-S-H gels increase with temperature, indicating a greater solubility at a higher temperature. The log K_{sp} values of N-A-S-H gels synthesized in this work, with Si/Al ratios of 1.1 and 2.0, closely match those of amorphous N-A-S-H gels reported in the studies by Williamson et al. [36] and Gomez-Zamorano et al. [35]. However, the N-A-S-H gel synthesized by Walkley et al. [34] exhibit less negative log K_{sp} values. This may be partly because of the lower Na content in the N-A-S-H gel by Walkley et al. [34]. Additionally, the N-A-S-H gel in [34] was derived through alkali activation of synthetic glass instead of the sol-gel method, implying a potentially distinct structure, which could be another reason for the discrepancy. In contrast, N-A-S-H gels with different Si/Al ratios from [33] all showed notably more negative log K_{sp} values than those obtained in this work. Furthermore, the difference between the solubility products of N-A-S-H gels from this work and [33] becomes more pronounced as Si/Al increases. A further comparison and discussion will be made in the following.

Table 5.1 Dissolution reactions used to calculate solubility products of N-A-S-H gels per 1 mol of Si.

N-A-S-H gels	Dissolution reactions
N1	$(Na_2O)_{0.46}(Al_2O_3)_{0.46}(SiO_2)_1(H_2O)_{0.54} \rightarrow 0.92\ Na^+ + 0.92\ AlO_2^- + SiO_2^0 + 0.54\ H_2O$
N2	$(Na_2O)_{0.25}(Al_2O_3)_{0.25}(SiO_2)_1(H_2O)_{0.35} \rightarrow 0.5\ Na^+ + 0.5\ AlO_2^- + SiO_2^0 + 0.35\ H_2O$
N3	$(Na_2O)_{0.18}(Al_2O_3)_{0.18}(SiO_2)_1(H_2O)_{0.31} \rightarrow 0.36\ Na^+ + 0.36\ AlO_2^- + SiO_2^0 + 0.31\ H_2O$

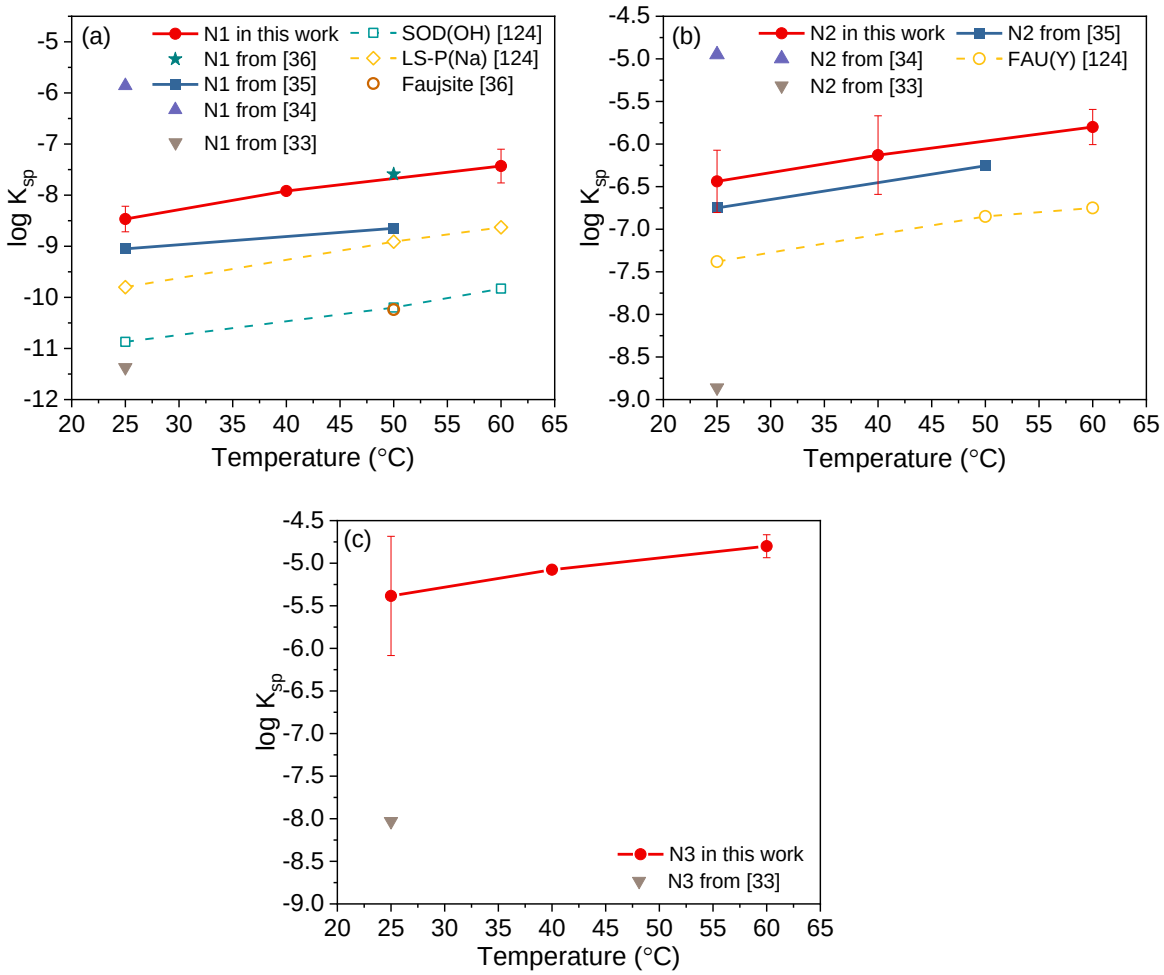

Figure 5.4 Log solubility products of synthesized N-A-S-H gels and zeolites after normalizing per mole of Si, (a) Si/Al ratio = 1, (b) Si/Al ratio = 2, (c) Si/Al ratio = 3. Error bars correspond to the two sided 95 % confidence interval. Literature data for N-A-S-H derived from [33–36] and for zeolites (Faujasite(FAU(Y)), hydroxysodalite (SOD(OH)) and gismondine (LS-P(Na)) from [36,124]*).*

The comparison in Figure 5.4 reveals some discrepancies between the solubility products of N-A-S-H gel obtained in this work and the literature. Since N-A-S-H gel can be considered as a disordered form of zeolite, especially the ABC-6 family of zeolites [99], the accuracy of the data obtained in this work and in the literature was further validated by comparing solubility products between N-A-S-H gel and zeolites. Hydroxysodalite ($Na_8Al_6Si_6O_{24}(OH)_2{\cdot}2H_2O$), a member of the ABC-6 family, and Gismondine: LS-P ($Na_2Al_2Si_2O_8{\cdot}3.8H_2O$) [124] as well as faujasite [36] are selected to compare with N-A-S-H gel with a Si/Al ratio of 1, while faujasite Y ($Na_2Al_2Si_4O_{12}{\cdot}8H_2O$) [124], also belonging to ABC-6 family, were chosen for comparison with N-A-S-H gel with a Si/Al ratio of 2. The log K_{sp} values of these zeolites from [36,124], normalized to 1 mole of Si, are also plotted in Figure 5.4. Except the N-A-S-H gels in [33], all types of zeolites have lower log K_{sp} values compared to the amorphous N-A-S-H gels, indicating that the gels have a higher solubility. This is reasonable as zeolites have a crystalline structure that is considered more stable and less likely to dissolve than

amorphous gels. Similar results were also found in [36], where a clear decrease in solubility was observed from N-A-S-H gel to faujasite. This finding suggests the reliability of the solubility products of N-A-S-H gel obtained in this work and in [35,36]. The log K_{sp} value of hydroxysodalite (SOD(OH) in Fig. 5.4(a)) is the smallest, with several log K_{sp} units smaller than N-A-S-H gel with a Si/Al ratio of 1. This is because it contains extra Na^+ and OH^- compared with the chemical composition of N-A-S-H gel with a Si/Al ratio of 1 in this work, which lowers the log K_{sp} value mathematically if normalized to 1 Si. In contrast, the log K_{sp} value of faujasite Y (FAU(Y) in Fig. 5.4(b)) is only around 1 log K_{sp} unit more negative than that of N2 in this work, implying that N-A-S-H gel might have an atomic structure similar to that of faujasite. Overall, the consistency observed between the solubility products of N-A-S-H gels synthesized in this study and those reported in [35,36], as well as the slightly higher solubility of N-A-S-H gels than zeolites, support the reliability of the solubility products of N-A-S-H gels obtained in this work. These trustworthy solubility products can serve as a solid basis for further determining the other thermodynamic data.

To study the effect of the Si/Al ratio on the solubility product of N-A-S-H gel, the log K_{sp} values should be normalized to the same number of framework TO_4, i.e., SiO_4+AlO_4. Both the log K_{sp} values of N-A-S-H gel from this work and from [35] exhibit an increasing trend with an increase in Si/Al ratio, as can be seen in Figure 5.5. This is partly because of lower Na content in higher Si/Al N-A-S-H gel, which means a smaller coefficient a is used in Equation 5.2 to calculate the solubility products, resulting in less negative log K_{sp} value due to purely mathematical reasons. However, it is important to observe that the rise in the log K_{sp} value is more pronounced when transitioning from Si/Al=2 to Si/Al=3 compared to the shift from Si/Al=1 to Si/Al=2. This indicates that the formation of N-A-S-H gel with a high Si/Al ratio is thermodynamically less favored. This is strongly supported by the MD simulation results in Chapter 3 and the experimental results in Chapter 4. Furthermore, it could help to explain why the synthesis of N-A-S-H gel with a Si/Al ratio up to 3 is challenging and has previously not been reported in literature.

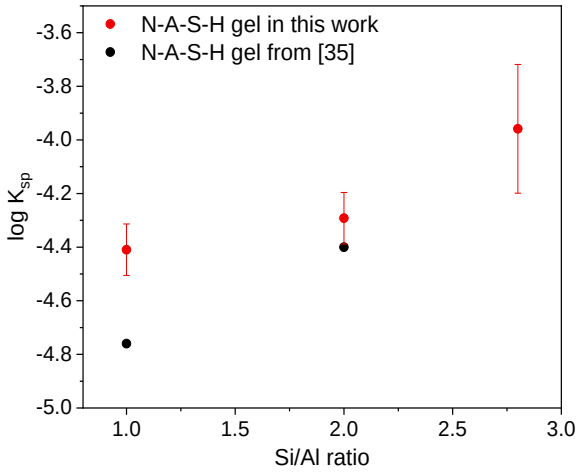

Figure 5.5 Effect of Si/Al ratio on log solubility products of synthesized N-A-S-H gels normalized to 1 mole of (SiO_4+AlO_4) at 25 °C. Error bars correspond to the two sided 95 % confidence interval.

The solubility products of N-C-A-S-H gels at different temperatures were calculated using Equation 5.2 based on the dissolution reactions listed in Table 5.2. The incorporation of Ca into N-A-S-H gels is found to affect the relationship between the solubility and temperature. In contrast to N-A-S-H gels, the solubility products of all N-C-A-S-H gels do not follow a monotonically increasing trend as a function of temperature as shown in Figure 5.6. The solubility products of N-C-A-S-H gels reach their maximum at 40 °C and then slightly decrease at 60 °C. This phenomenon has been observed in some Ca-containing materials, e.g. C-S-H gel [184], C-(N)-S-H gel [35], C-(N-)A-S-H gels [35,184,185], tobermorite [186], $Ca(OH)_2$ [184], and $CaSO_4$ [187]. The retrograde solubility of $Ca(OH)_2$ and $CaSO_4$ is believed due to the exothermic nature of their dissolution reactions. However, it is still a matter of debate why the solubility of Ca-containing gel decreased with temperature. Gomez-Zamorano et al. [35] believed that the dissolution of C-(N)-S-H gel is also an exothermic process, as indicated by the negative enthalpy of dissolution. However, this is unconvincing as they obtained the enthalpy of the dissolution according to the solubility product. Lothenbach et al. [186] attributed this phenomenon to the transformation of C-S-H gel to crystalline tobermorite at high temperatures. However, in this work, no crystalline phase was observed after dissolution. The incorporation of Ca is believed to be responsible for the decreased solubility of N-C-A-S-H gel with increasing temperature, which is consistent with the trend observed in Ca-containing phases in the above literature. As shown in Section 5.3.1, less Ca and Al dissolved as temperature increased from 40 °C to 60 °C. As a result, the solubility of N-C-A-S-H gels shows a decreasing trend with increasing temperature, although more Si and Al dissolved with the increase in temperature. However, the mechanisms outlined in [35,186] for the reduction in K_{sp} at elevated temperature need to be further verified.

Table 5.2 Dissolution reactions used to calculate solubility products of N-C-A-S-H gels per 1 mol of Si.

N-C-A-S-H gels	Dissolution reactions
NC2_0.25	$(Na_2O)_{0.25}(CaO)_{0.11}(Al_2O_3)_{0.25}(SiO_2)_1(H_2O)_{0.46} \rightarrow 0.11Ca^{2+} + 0.5Na^{+} + 0.5AlO_2^{-} + SiO_2^{0} + 0.22OH^{-} + 0.35H_2O$
NC2_0.5	$(Na_2O)_{0.23}(CaO)_{0.2}(Al_2O_3)_{0.23}(SiO_2)_1(H_2O)_{0.47} \rightarrow 0.2Ca^{2+} + 0.46Na^{+} + 0.46AlO_2^{-} + SiO_2^{0} + 0.4OH^{-} + 0.27H_2O$
NC3_0.25	$(Na_2O)_{0.23}(CaO)_{0.08}(Al_2O_3)_{0.16}(SiO_2)_1(H_2O)_{0.41} \rightarrow 0.08Ca^{2+} + 0.46Na^{+} + 0.32AlO_2^{-} + SiO_2^{0} + 0.3OH^{-} + 0.26H_2O$
NC3_0.5	$(Na_2O)_{0.24}(CaO)_{0.15}(Al_2O_3)_{0.18}(SiO_2)_1(H_2O)_{0.48} \rightarrow 0.15Ca^{2+} + 0.48Na^{+} + 0.36AlO_2^{-} + SiO_2^{0} + 0.42OH^{-} + 0.27H_2O$

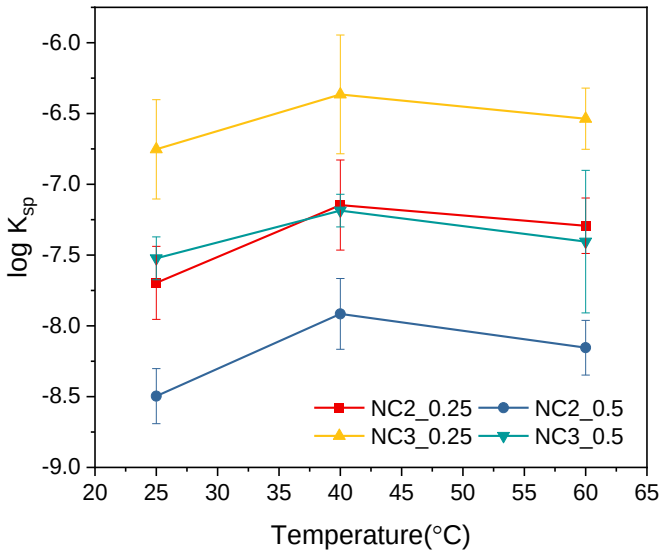

Figure 5.6 Log solubility products of synthesized N-C-A-S-H gels after normalizing per mole of Si at different temperatures.

Figure 5.7 illustrates the effect of Ca/Al ratio on the log K_{sp} of N-(C-)A-S-H gels. Regardless of Si/Al ratio, the presence of Ca in the gel stabilized the gel as visible by the strong decrease of the solubility products (log K_{sp}) with the Ca-content. This finding can explain why Ca tends to be incorporated into N-A-S-H gel to form N-C-A-S-H gel.

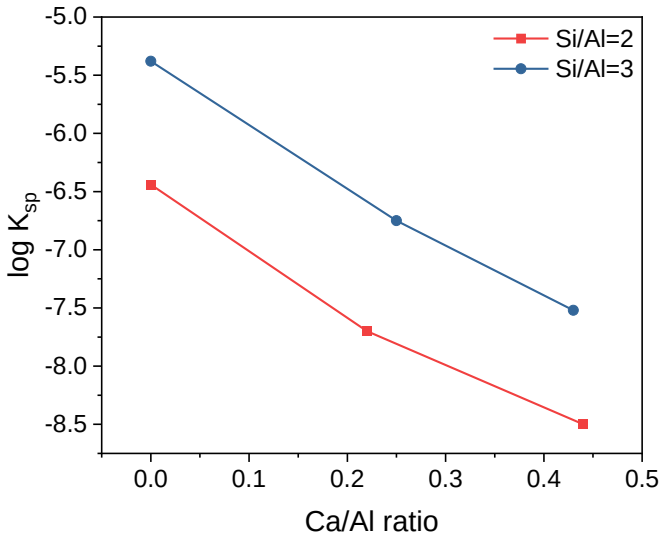

Figure 5.7 Effect of Ca/Al ratio on log K_{sp} of synthesized N-(C-)A-S-H gels at 25 ˚C.

5.3.3 Thermodynamic data of N-(C-)A-S-H gel

Based on the measured log K_{sp} values at 25 ˚C, the Gibbs free energy of formation $\Delta_f G^0$ of N-(C-)A-S-H gels at 25 ˚C was calculated as detailed in Equation 5.4. The heat capacity C_p^0 and entropy S^0 of the N-(C-)A-S-H gels were estimated using the additivity method according to Equation 5.7. And finally the enthalpies $\Delta_f H^0$ of N-(C-)A-S-H gels were calculated automatically in GEMS using the Gibbs free energy and the entropy [32]. The thermodynamic properties of N-(C-)A-S-H gels with various Si/Al ratios and Ca/Al ratios at 25 ˚C are shown in Table 5.3.

In GEMS, the changes in the solubility products with temperature depend on the differences in the heat capacity C_p^0 and entropy S^0 between the species in solution and the N-(C-)A-S-H gels as detailed Equation 5.8. To evaluate the accuracy of C_p^0 and S^0 calculated in this work, the solubility products of N-(C-)A-S-H gels, derived through Equation 5.8 in GEMS, were compared with experimental results (Figure 5.4 and 5.6), as illustrated in Figure 5.8. For N-A-S-H gels as shown in Figure 5.8(a), the GEMS-derived solubility increases with temperature, which is in agreement with the experimental observations. Furthermore, the GEMS-derived results match very well with the experimental data, verifying the accuracy of the estimated heat capacity C_p^0 and entropy S^0 data of the N-A-S-H gels. For N-C-A-S-H gels as shown in Figure 5.8(b), the GEMS-derived solubility also shows an increasing trend with temperature, regardless of the approach used to calculate the heat capacity and entropy. Although the trend of the GEMS-derived solubility as the function of temperature do not follow the experimental findings, the GEMS-derived solubility still fits the experimentally measured data well, indicating that the estimated heat capacity C_p^0 and entropy S^0 data of the N-C-A-S-H gels are in a reasonable range.

Table 5.3 Standard thermodynamic properties of N-(C-)A-S-H gels at 25 ˚C.

N-(C-)A-S-H gels	$\Delta_f G^0$ (kJ/mol)	$\Delta_f H^0$ (kJ/mol)	S^0 (J/mol/K)	C_p^0 (J/mol/K)	V^0 (cm^3/mol)
$Na_{0.92}Al_{0.92}Si_1O_{3.84}{\cdot}0.54H_2O$	-2012.05	-2157.26	125	153	56.63
$Na_{0.5}Al_{0.5}Si_1O_3{\cdot}0.35H_2O$	-1497.86	-1601.24	101	106	43.46
$Na_{0.36}Al_{0.36}Si_1O_{2.72}{\cdot}0.31H_2O$	-1299.11	-1425.58	73	92	38.85
$Na_{0.5}Ca_{0.11}Al_{0.5}Si_1O_{3.11}{\cdot}0.46H_2O$	-1601.60	-1719.89	93	116	45.06
$Na_{0.46}Ca_{0.2}Al_{0.46}Si_1O_{3.12}{\cdot}0.47H_2O$	-1621.68	-1740.18	96	117	45.38
$Na_{0.46}Ca_{0.08}Al_{0.32}Si_1O_{2.79}{\cdot}0.41H_2O$	-1411.41	-1513.32	95	105	40.33
$Na_{0.48}Ca_{0.15}Al_{0.36}Si_1O_{2.93}{\cdot}0.48H_2O$	-1514.08	-1625.24	100	113	42.51

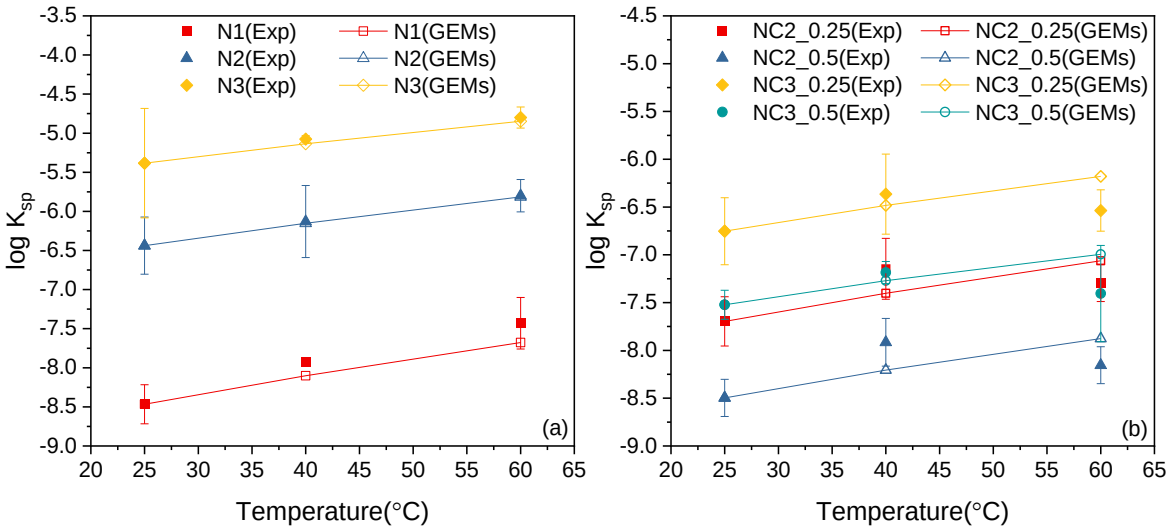

Figure 5.8 Comparison between the measured solubility products, log K_{sp}, and the temperature extrapolations from thermodynamic modeling. Error bars correspond to the two sided 95 % confidence interval.

5.4 Conclusions

In this chapter, the solubility products of the synthesized N-(C-)A-S-H gels with a Si/Al ratio from 1 to 3 and a Ca/Al ratio from 0 to 0.5 were determined via dissolution tests at different temperatures. Other thermodynamic data were determined based on the experimentally derived solubility products. A thermodynamic database of N-(C-)A-S-H gels with various Si/Al ratios and Ca/Al ratios has been established. Based on the results and discussion, the following remarks are made:

1. The solubility products of N-A-S-H gels with Si/Al ratios of 1 and 2 are in good agreement with those reported in the literature, and higher than those of zeolites with the same Si/Al ratios. The solubility product of N-A-S-H gels with a Si/Al ratio of 3 has been determined through experiment for the first time and is much larger than those with lower Si/Al ratios, indicating that the formation of N-A-S-H gel with high Si/Al ratio is thermodynamically little favored, as already observed in Chapter 3 and Chapter 4.
2. The temperature dependent solubility products of N-A-S-H gels derived from estimated heat capacity and entropy data agree closely with the experimentally observed trends. This result supports the validity of the thermodynamic properties of N-A-S-H gels determined in this work.
3. With the incorporation of Ca, the solubility of N-C-A-S-H gel determined from experiments first increases and then slightly decreases with temperature. This is because the amount of dissolved Ca and Al decreases at high temperatures. Although the solubility products derived from heat capacity and entropy do not strictly follow this trend, they are still in agreement with the experimental data. This indicates that the estimated heat capacity and entropy values are still reasonable.

Chapter 6

Reaction kinetics and thermodynamic modeling of alkali-activated fly ash paste

---

6.1 Introduction

Thermodynamic modeling serves as a robust approach for anticipating chemical reactions at thermodynamic equilibrium. This method can provide valuable insights into the components and quantities of each phase in binder materials [29,188]. Despite its effectiveness, little work has been carried out on the thermodynamic modeling of alkali-activated fly ash (AAFA), primarily due to the scarcity of a thermodynamic database of the main reaction product, N-(C-)A-S-H gels. The establishment of a thermodynamic database for N-(C-)A-S-H gels in Chapter 5 paves the way for the investigation of AAFA through thermodynamic modeling in this chapter. However, thermodynamic modeling does not consider the reaction kinetics. In order to predict the evolution of the phase assemblage of AAFA over time, it is imperative to first determine the kinetics process and then integrate it with the thermodynamic modeling.

This chapter starts with an experimental characterization of AAFA paste to gather fundamental information on reaction kinetics and microstructure of the matrix. Isothermal heat release and energy dispersive spectroscopy mapping are combined to elucidate the kinetics process. Microstructure and pore solution are characterized using experimental techniques to validate the thermodynamic modeling results. Coupled with the kinetics process obtained from experiments, the evolution of simulated phase assemblages of AAFA paste is predicted as a function of time by thermodynamic modeling. Furthermore, the simulated compositions in solid and aqueous phases are analyzed and compared to the experimental data. The thermodynamic modeling of AAFA developed in this chapter will be incorporated into the thermodynamic modeling module of the GeoMicro3D model in Chapter 7.

6.2 Materials and methods

6.2.1 Raw materials and mixtures

In this chapter, fly ash was used as the precursor to prepare AAFA paste. The chemical composition of fly ash, determined by X-ray fluorescence spectroscopy (XRF), is listed in Table 6.1. According to the definition in [189], the fly ash used in this work can be classified into Class F. The density of fly ash is 2.13 g/cm^3. The particle size distribution (PSD) of fly ash was measured using laser diffraction, as shown in Figure 6.1. The d_{50} of fly ash is 43.3 µm. The amorphous content of fly ash was measured as 79.3 % by using the quantitative XRD analysis (QXRD), which is described in the following. It is assumed that only the amorphous

phase in fly ash is reactive, while the crystals are considered non-reactive. Based on the content of crystalline SiO_2 and Al_2O_3 from QXRD results, the reactive SiO_2 and Al_2O_3 were determined as 44.4 % and 17.9 %, respectively.

Two conventional systems, i.e. sodium hydroxide (NH) and sodium silicate (NS) activated systems, were chosen for the investigation of AAFA paste. The alkali activators were prepared by sodium hydroxide (>98 wt. %) pellets, sodium silicate solution (27.5 wt.% SiO_2, 8.25 wt.% Na_2O and 64.25 wt.% H_2O) and deionized water. Although varying mixtures can result in diverse microstructures and properties of AAFA, the primary focus of this study is not to delve into these parameters. Hence, representative mixture designs from [33] were adopted in this work. As shown in Table 6.2, for the NH-activated system, the Na_2O content in the activator was 9.3 wt.% with respect to fly ash. The modulus Ms (molar ratio SiO_2/Na_2O) of the activator was 0. The water-to-fly ash ratio was 0.35. For the NS-activated system, the same Na_2O dosage and water-to-fly ash ratio were used, but with a modulus of 1. Due to the relatively low reactivity of fly ash, thermal curing is commonly applied to AAFA [90,190]. In this work, all samples were cured in sealed condition at 40 °C and 60 °C until the age of testing.

Table 6.1 Chemical compositions and components of fly ash (by wt.%).

Oxides	SiO_2	Al_2O_3	Fe_2O_3	CaO	MgO	K_2O	Na_2O	P_2O_5	TiO_2	SO_3	LOI
	56.75	24.58	5.76	3.93	2.10	1.40	1.27	1.17	1.03	0.68	1.33
Components	Amorphous phase		Quartz		Mullite		Maghemite		Calcite		
	79.3		10.1		9.6		0.7		0.3		

LOI: loss on ignition.

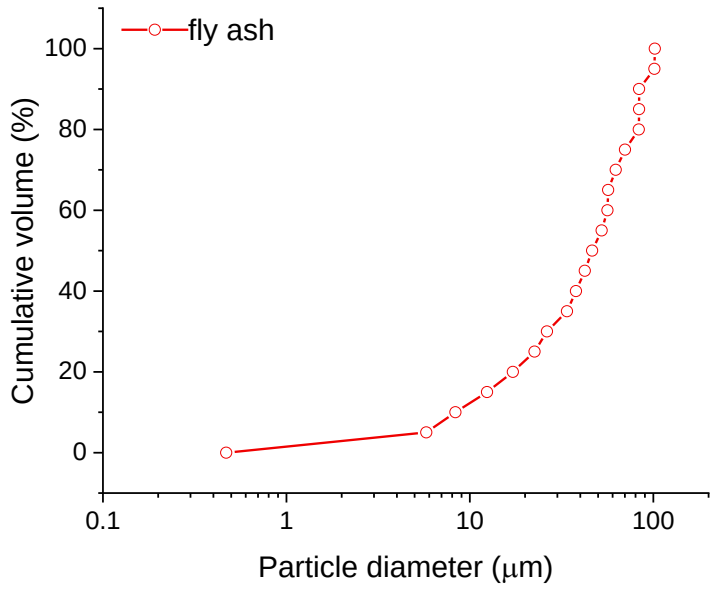

Figure 6.1 Particle size distribution of fly ash.

Table 6.2 Mixture compositions and curing temperatures.

Samples	Na_2O(wt.%)	Modulus	Water to ash ratio	Curing temperature
NH	9.3	0	0.35	40/60 °C
NS	9.3	1	0.35	40/60 °C

6.2.2 Experimental characterization on AAFA paste

6.2.2.1 Isothermal calorimetry test

In-situ isothermal calorimetry tests were performed by using a TAM-Air-314 isothermal calorimeter to study the reaction kinetics of AAFA pastes at 40 °C and 60 °C. Calibration was carried out before each measurement. Around 4 grams of fly ash was loaded in the glass ampoule, while the activator solution was stored in an attached syringe. The admix ampoule was placed in the calorimeter for around 3 hours to reach a stable heat flow baseline. After that, the activator solution was injected into the glass ampoule and mixed with fly ash using a built-in stirring shaft. Heat flow was recorded until 7 days. The calorimetry results were normalized by the mass of fly ash.

6.2.2.2 Characterization of reaction product and pore solution

The components of AAFA were analyzed by using XRD, FTIR and TGA techniques. In-depth insights into the atomic compositions of the AAFA matrix were acquired via scanning electron microscopy/energy dispersive spectroscopy (SEM-EDS). The unreacted fly ash and reaction products in the AAFA matrix were distinguished via image analysis. To measure the ion concentrations and pH in the pore solution of AAFA paste, ICP-OES technique and titration method were employed, respectively. These experimental results serve as crucial inputs for evaluating the accuracy and reliability of thermodynamic modeling results. Detailed descriptions of each method are provided below.

XRD, FTIR and TGA analysis

After 7 days and 28 days of curing, the samples were ground to powder for XRD, FTIR and TGA analysis. During grinding, isopropanol was added to halt any ongoing reactions. Detailed procedures can be seen in [191]. For XRD and FTIR measurements, the same procedures were performed as described in Section 4.2.3. For TGA measurement, it was carried out on around 20 mg of powders at a heating rate of 10 °C/min from 40 °C to 1000 °C. For QXRD test, 10 wt. % of silicon powder was used as the internal standard material. The Rietveld quantitative analysis was performed using the BGMN-based program Profex [192] to determine the content of each phase.

SEM-EDS analysis

For SEM-EDS analysis, the samples cured for 7 days and 28 days were sectioned into about 1 cm thick slices and immersed in isopropanol for 2 weeks to stop reactions. Isopropanol was renewed 3 times in the first week. Subsequently, samples were dried at 25 °C in a vacuum oven for around 1 week. After that, the samples were impregnated with epoxy and polished with successively finer grades of silicon carbide papers and polishing discs [193]. Before performing SEM-EDS, the polished samples were sputter coated with carbon. Following that,

the samples were examined by a FEI QUANTA FEG 650 ESEM equipped with a solid-state EDS detector in backscattered electron (BSE) mode. The working distance was set as 10 mm. The accelerating voltage used was 15 kV, which was recommended and commonly used for the SEM-EDS quantitative analysis in many studies [194–196], as it is the optimal choice with consideration of the spatial resolution, interaction volume and adequate excitation of the FeKα peak [197]. The images and EDS maps were collected with a magnification of 1000×, a resolution of 1024×682 and a pixel size of 0.4 µm. The spectral images were obtained using a dwell time of 143 µs per pixel over 20 frames. The total acquisition time of a map is 2000s. Phase segmentation was carried out on 15-20 maps by image analysis to further analyze microstructure and determine degree of reaction of fly ash.

Segmentation of BSE image

According to previous studies [195,198], the grey levels of reaction products and most unreacted fly ash were similar, posing challenges in phase segmentation. An optimized method is proposed in this work to distinguish fly ash and reaction products, moving beyond the reliance solely on grey level histograms. Each image was segmented into three phases, i.e. fly ash, reaction products and pores, by using Otsu's method [199], which finds the thresholds on atomic counts and grey levels. The detailed conditions for segmentation are illustrated in Figure 6.2. Since the epoxy contains a little Cl, only the regions devoid of Cl were considered further. Notably, due to a noticeable disparity in Na content between fly ash and other phases, regions lacking Na and exhibiting a low grey level were designated as fly ash. Additionally, dark regions lacking Na but containing Fe were also classified as fly ash, considering some Fe-containing fly ash particles displayed high grey level values. In contrast, regions containing Na while simultaneously displaying a low grey level were categorized as reaction products. Any region that did not meet the criteria for fly ash or reaction products was identified as pores. The final phase segmentation of AAFA is shown in Section 6.3.2.4.

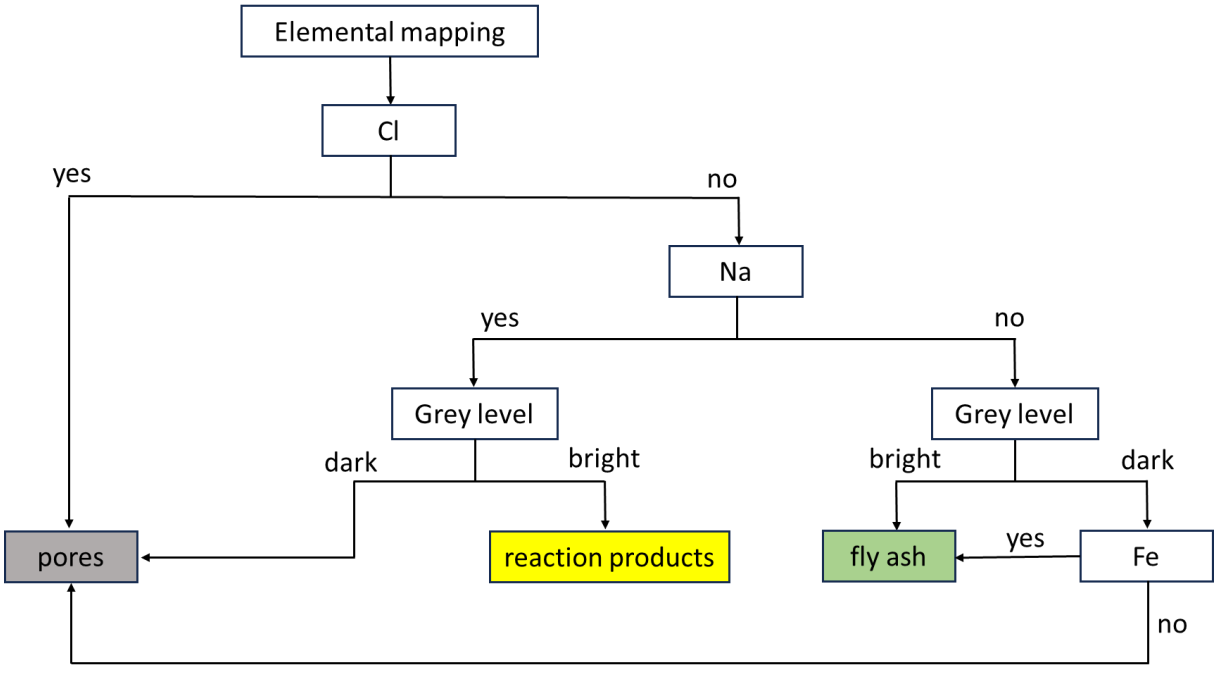

Figure 6.2 The overall flowchart of the segmentation of BSE image.

Pore solution chemistry

To analyze the aqueous chemical information, pore solutions of the pastes at curing ages of 3, 7 and 28 days were extracted following the method depicted in [200]. The cylinder paste with a diameter of about 34 mm and a height of about 70 mm was inserted into the hollow steel cylinder with a fitting size of the paste. A maximum force of 300-600 kN, depending on the type and reaction degree of the pastes, was applied to extract the pore solutions [201]. For each sample, around 0.5-2 ml of pore solution was collected. Shortly after extraction, the pore solution underwent filtration using a 0.45 µm syringe filter. The OH^- concentration of the pore solution was immediately measured by titration against 0.1 M HCl standard solution. The concentrations of Si, Al, Na, Ca, Fe, Mg and K were determined by using ICP-OES, as described in Section 4.2.3.

6.2.2.3 Degree of reaction

The degree of reaction of fly ash at certain curing ages was determined by the phase segmentation through image analysis described in Section 6.2.2.2. Previous study [202] has already shown that the area fraction in two dimensions can be reasonably equated to the volume fraction in three dimensions. Thus, with the area fraction of fly ash derived from image analysis, the degree of reaction at a certain curing age can be calculated by using the following equation:

$$\alpha(t) = (1 - F_t/F_0) \times 100\ \% \tag{6.1}$$

where $\alpha(t)$ is the degree of reaction of fly ash at age t, F_t is the volume fraction of fly ash at age t, and F_0 is the initial volume fraction of fly ash. This method has been used to calculate the degree of reaction in many studies [33,194,203].

To obtain the reaction degree as a function of time, it is usually assumed a linear proportionality between reaction degree and heat release, which can be described by Equation 6.2 [33,204]. Based on the degree of reaction at 7 days determined by image analysis and cumulative heat release of the AAFA paste at 7 days, the maximum heat release ($Q_{max\ \_\exp}$) can be calculated using Equation 6.2. Since the cumulative heat release obtained from the experiment was only available up to 7 days, $Q(t)$ was fitted using Equation 6.3 [205], with the parameters listed in Table 6.3, to describe the cumulative heat release over an extended time. Consequently, the reaction degree of fly ash as a function of time can be calculated with Equation 6.4. It should be noted that the parameter $Q_{max\_\exp}$ in Equation 6.4 cannot be simply interchanged with the fitting maximum heat release $Q_{max\_fit.}$ As outlined in [204,206], the maximum heat release obtained from Equation 6.3 tends to be underestimated significantly, resulting in an overestimation of reaction degree.

$$\alpha(t) = Q(t)/Q_{max\_\exp} \tag{6.2}$$

$$Q\ (t) = Q_{\max\_fit}\exp(-(\frac{\lambda}{t})^{\beta}) \tag{6.3}$$

$$\alpha(t) = Q_{\max\_fit}\exp(-(\frac{\lambda}{t})^{\beta})/Q_{max\_\exp} \tag{6.4}$$

Table 6.3 The calculated maximum heat release (Q_{max_fit}) and the fitting parameters.

Sample	$Q_{\max\_fit}$ (J/g)	λ	β
NH_40 °C	195	38.6	0.74
NS_40 °C	146	26.7	0.46
NH_60 °C	195	5.2	0.82
NS_60 °C	146	4.2	0.62

6.2.3 Thermodynamic modeling

The thermodynamic modeling of AAFA paste was performed in GEMS at 40 °C and 60 °C, using the PSI/Nagra [171] and Cemdata18 [32] thermodynamic databases to describe the thermodynamic data for general solid, aqueous, and gaseous phases. In addition, thermodynamic models for N-(C-)A-S-H gel, developed in Chapter 5, and the thermodynamic data for zeolites [124] were also added to describe the reaction products of AAFA.

The built-in extended Debye-Huckel equation was used to compute the activity coefficients of the aqueous species, as detailed in Equation 5.3 in Chapter 5. It should be noted that this equation is more applicable up to 1-2 molal ionic strength [179,207], while AAFA pore solutions usually have a higher ionic strength (referring to 1-3 molal in AAS system [105]). However, research has shown comparable modeling results between the extended Debye-Huckel equation and the Pitzer model, especially at later ages [204]. Thus, the extended Debye-Huckel equation was chosen in this research considering its direct implementation in GEMS and the comparable results with the Pitzer model.

The components in fly ash considered in the thermodynamic modeling include SiO_2, Al_2O_3, Fe_2O_3, CaO, MgO, Na_2O and K_2O, while the others are omitted due to their minimal quantities. These amorphous oxides are assumed to dissolve congruently in thermodynamic modeling, whereas the crystalline phases are considered not involved in dissolution. The chemical composition of fly ash used for thermodynamic modeling are shown in Table 6.4.

The formation of zeolites was partly suppressed during the thermodynamic modeling to prevent the thermodynamically more stable zeolites from forming instead of the observed N-(C-)A-S-H gel. The reason behind it lies in that the solubility of zeolite is lower than that of N-(C-)A-S-H gel as discussed in Chapter 5. However, in reality, the formation of zeolites is often kinetically hindered while N-(C-)A-S-H gel precipitates instead [208]. The suppression of zeolites is based on the XRD and QXRD results of AAFA paste. In the NH-activated system, the hydroxysodalite (SOD(OH)) content remains around 3 % regardless of curing age and temperature. Consequently, the upper limit for the quantity of SOD(OH) is set at 0.005 M (4.84 g) for 100 g of fly ash, while other zeolites are suppressed. In the NS-activated system, all zeolites are inhibited due to the absence of any zeolite phases. The formation of hematite, magnetite and goethite was also prevented due to the kinetic reason.

Table 6.4 Chemical compositions of amorphous fly ash used for thermodynamic modeling (by wt.%).

SiO_2	Al_2O_3	Fe_2O_3	CaO	MgO	K_2O	Na_2O
44.4	17.9	5.1	3.6	2.1	1.4	1.3

6.3 Results and discussion

6.3.1 Isothermal heat release

The rate of heat evolution and cumulative heat release of AAFA pastes determined by isothermal calorimetry are shown in Figure 6.3. It can be seen that different alkali-activated systems show various calorimetric responses. Regardless of temperature (40 °C or 60 °C), the NH-activated system always exhibited multi-peaks calorimetric response, while only a single wide exothermic peak was observed in the NS-activated system. For both systems, the dissolution peak, corresponding to the initial peak, was captured completely using the in-situ approach. The NH-activated system with a higher pH showed a quicker and stronger calorimetric response than the NS-activated system. After the stage of dissolution, the NH-activated system underwent an induction period, followed by two distinct small peaks, which were attributed to the polycondensation process [77]. The presence of these individual peaks suggested a multi-step reaction, in alignment with the gel evolution theory [93,209]. Similar calorimetric responses were also found in [76]. In contrast, the NS-activated system experienced polycondensation immediately due to the presence of soluble silica in the activator, which allows the formation of aluminosilicate oligomers after the dissolution of fly ash. As a result, the exothermic responses resulting from dissolution and polycondensation were superimposed, leading to the observation of a single wide peak in the NS-activated system [80].

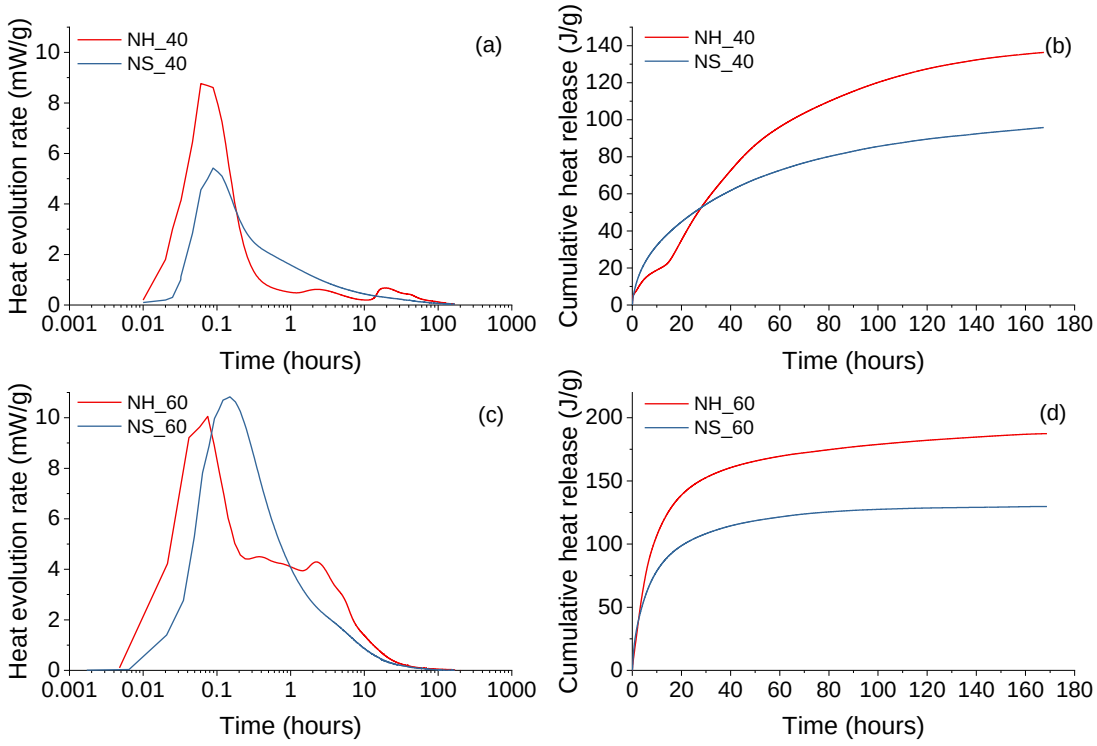

Figure 6.3 Heat evolution rate and cumulative heat release for AAFA pastes cured at 40 °C and 60 °C.

6.3.2 Microstructure characterization

6.3.2.1 XRD analysis

The XRD patterns of fly ash and AAFA pastes cured for 7 days and 28 days are shown in Figure 6.4. In addition to the amorphous phase, fly ash also contains crystalline phases including quartz, mullite and magnetite. These crystalline phases remain evident in the XRD patterns of AAFA pastes, as they are non-reactive and hardly dissolved. The main reaction product of AAFA is an amorphous gel (i.e. N-(C-)A-S-H gel), as evidenced by the newly appeared broad hump at 20-40° 2θ [21,97]. Hydroxysodalite is found in the NH-activated system, while no zeolite phase is formed in the NS-activated system. This finding is consistent with [97,210], which also confirms that hydroxysodalite is preferred to form in low SiO_2 environments. In addition, a small peak located at around 29° 2θ (marked in the dash line box) was found in the NH-activated system but absent in the NS-activated system. Although calcite (due to carbonation) is mainly responsible for this peak, it should be noted that the peak of C-(N-)A-S-H gel is also located at this position [76,211]. The potential existence of C-(N-)A-S-H gel will be further discussed based on the FTIR results given below and in the thermodynamic modeling section. Besides, increasing curing temperature from 40 °C to 60 °C does not affect the type of reaction products.

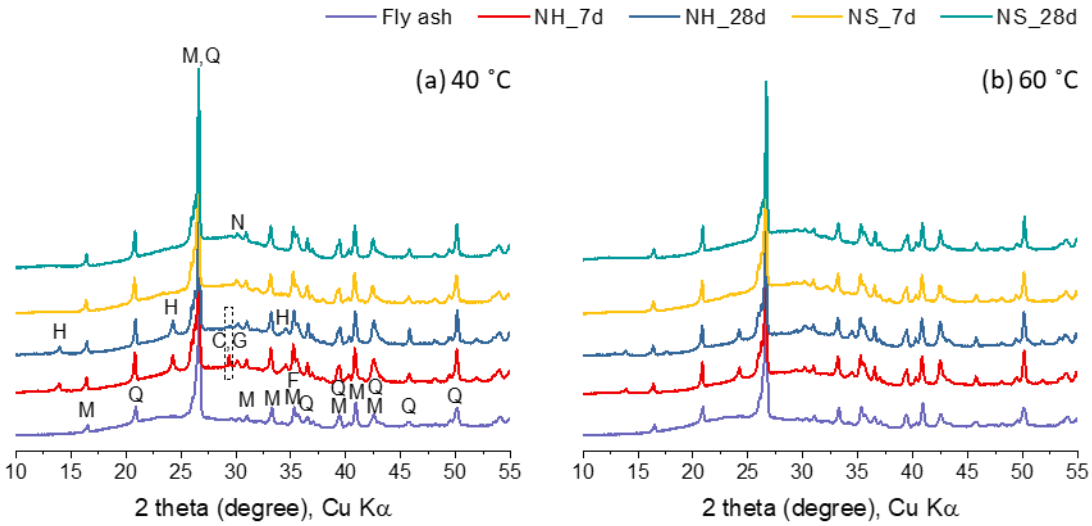

Figure 6.4 XRD patterns of fly ash and AAFA pastes cured for 7 and 28 days at (a) 40 °C and (b) 60 °C. H: hydroxysodalite; M: mullite; Q: quartz; N: natrite; G: C-(N-)A-S-H gel; C: calcite; F: magnetite.

6.3.2.2 FTIR analysis

To further characterize nanostructure of AAFA paste, FTIR analysis was conducted on both fly ash and AAFA pastes cured at different temperatures and ages, as shown in Figure 6.5. The quartz in fly ash is responsible for a series of bands at around 1150, 1084, 796–778 (double band), 697, 668, 522 and 460 cm^{-1} [212]. The mullite can contribute to the bands at around 1180–1130 cm^{-1} and 560–550 cm^{-1}, while the amorphous phase in the fly ash typically shows a band around 996 cm^{-1} [173]. These overlapping bands result in an IR spectrum for fly ash marked by a primary broad band between 1250 and 850 cm^{-1}, a dual band at 795–777 cm^{-1}, a minor band at 559 cm^{-1}, and a robust band at 448 cm^{-1}.

Compared to fly ash, the main band of AAFA pastes exhibited varying degrees of wavenumber shift towards lower values. This new signal, centered at around 969-998 cm^{-1}, is attributed to the main reaction product, i.e. N-(C-)A-S-H gel. The location of this band, corresponding to the asymmetric stretching vibrations of Si-T-O bonds, can indicate the polymerization level of the N-(C-)A-S-H gel. A higher wavenumber of this band can be observed with the increase in reaction time or curing temperature, signifying the formation of a more polymerized N-(C-)A-S-H gel. In addition, the band in the NS-activated system also vibrated at a higher wavenumber in comparison to that in the NH-activated system. This discrepancy mainly stems from the higher Si/Al ratio of N-(C-)A-S-H gel formed in the NS-activated system as opposed to the NH-activated system. According to the results in Chapter 4 (see Figure 4.8 and Figure 4.11), the wavenumber of the Si-O-T asymmetric stretching band in N-(C-)A-S-H gel increases with a higher Si/Al ratio. Also, low Ca/Si C-(A-)S-H phases have their main band at around 960 cm^{-1} [213–215], which could also contribute to the observed signal. The sharp band at 969 cm^{-1} for sample NH-7d would also be another support for the formation of C-(N-)A-S-H gel in the NH-activated system. Another new but small band, as highlighted within the black dashed rectangle, can be found in the NH-activated system, but negligible in the NS-activated systems. This band arises from the formation of hydroxysodalite [75,124], an observation that aligns with the XRD result. Furthermore, the new band at near 1652 cm^{-1} is assigned to the bending vibration of H-O-H bond [75,90]. The small peak at around 1436-1446 cm^{-1}, characteristic of asymmetric stretching vibrations of C-O bond, indicates that some samples were carbonated [170,216].

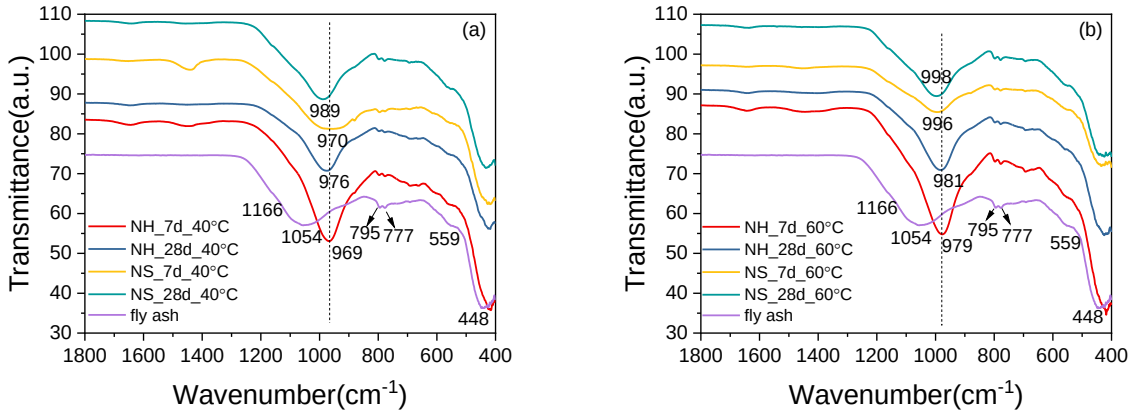

Figure 6.5 FTIR curves of fly ash and AAFA cured for 7 and 28 days at (a) 40 °C and (b) 60 °C.

6.3.2.3 TGA

The thermogravimetric (TG) and differential thermogravimetric (DTG) analysis were carried out to facilitate the identification of reaction products, as shown in Figure 6.6. All samples presented a pronounce mass loss peak within the range of 80-250 °C, which is attributed to the dehydroxylation of N-(C-)A-S-H gel [91]. NS-activated systems showed a more substantial mass loss compared with NH-activated systems, implying the formation of a higher quantity of N-(C-)A-S-H gel. Moreover, an increase in temperature of this peak can be observed in the following three scenarios: (a) a prolongation of curing age; (b) an elevation in curing temperature; (c) in the sodium silicate activated systems compared to their counterparts. The heightened decomposition temperature indicates a stronger binding of water within the gel structure [16,217,218]. From 250 to 1000 °C, a gradual mass loss can be observed across all samples, which could be associated with the burning of carbon in the fly ash [219], dehydroxylation of the silanol groups [24] or the decomposition of carbonates [220]. Furthermore, the decrease in mass loss from 800 to 1000 °C in the NH-activated systems is more notable than in the NS-activated systems. This further confirms the formation of hydroxysodalite in NH-activated systems, as the dehydroxylation of hydroxysodalite can contribute to the mass loss at around 800-900 °C [221].

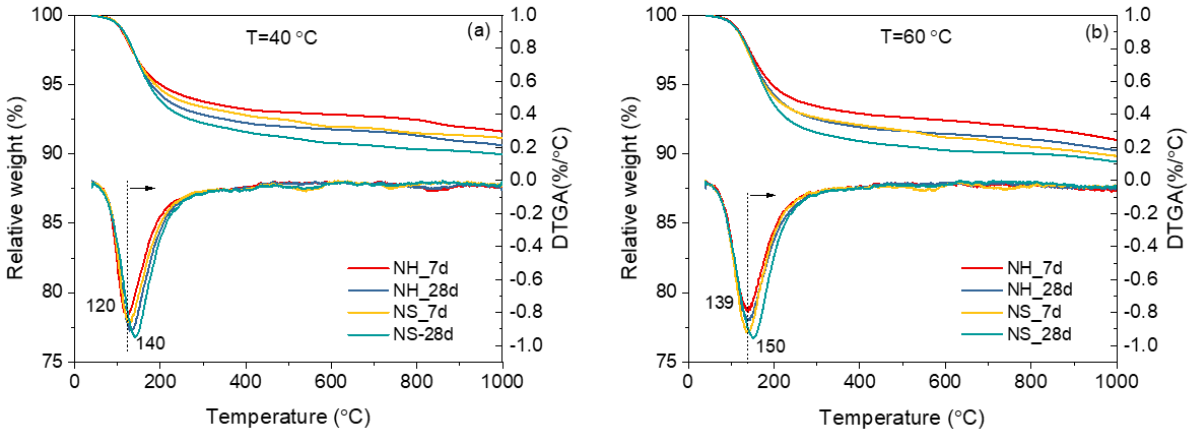

Figure 6.6 TG-DTG curves of fly ash and AAFA pastes cured for 7 and 28 days at (a) 40 °C and (b) 60 °C.

6.3.2.4 SEM-EDS analysis

The microstructures of the hardened AAFA pastes at different curing ages and temperatures can be observed in Figures 6.7 and 6.8, corresponding to the NH-activated system and NS-activated system, respectively. In accordance with the observations of [21,96], the NH-activated system displayed a loose and porous microstructure (Figure 6.7), irrespective of curing ages and temperatures. Conversely, a significantly dense and homogeneous microstructure was observed in the NS-activated system (Figure 6.8). The reason lies in that the extra soluble SiO_2 in sodium silicate activator facilitates the formation of more reaction products uniformly within the matrix, leading to a compact microstructure. However, more cracks were found in the NS-activated system, which could be caused by drying shrinkage. The denser microstructure (with smaller pores) of the NS-activated system can lead to higher capillary tension during drying, increasing susceptibility to shrinkage-induced cracking.

As also shown in Figure 6.7 and 6.8, three phases in the AAFA pastes, i.e. unreacted fly ash, reaction products and pores, were segmented according to the method described in Section 6.2.2.3. Through this segmentation, it becomes possible to identify not only the fly ash particles, but also those dissolving into small entities lacking distinct edges. Additionally, a typical difference between NH-activated system and NS-activated system was observed: the former exhibited a ring of reaction products around the edges of fly ash particles, whereas the latter showed a more evenly distributed distribution of reaction products.

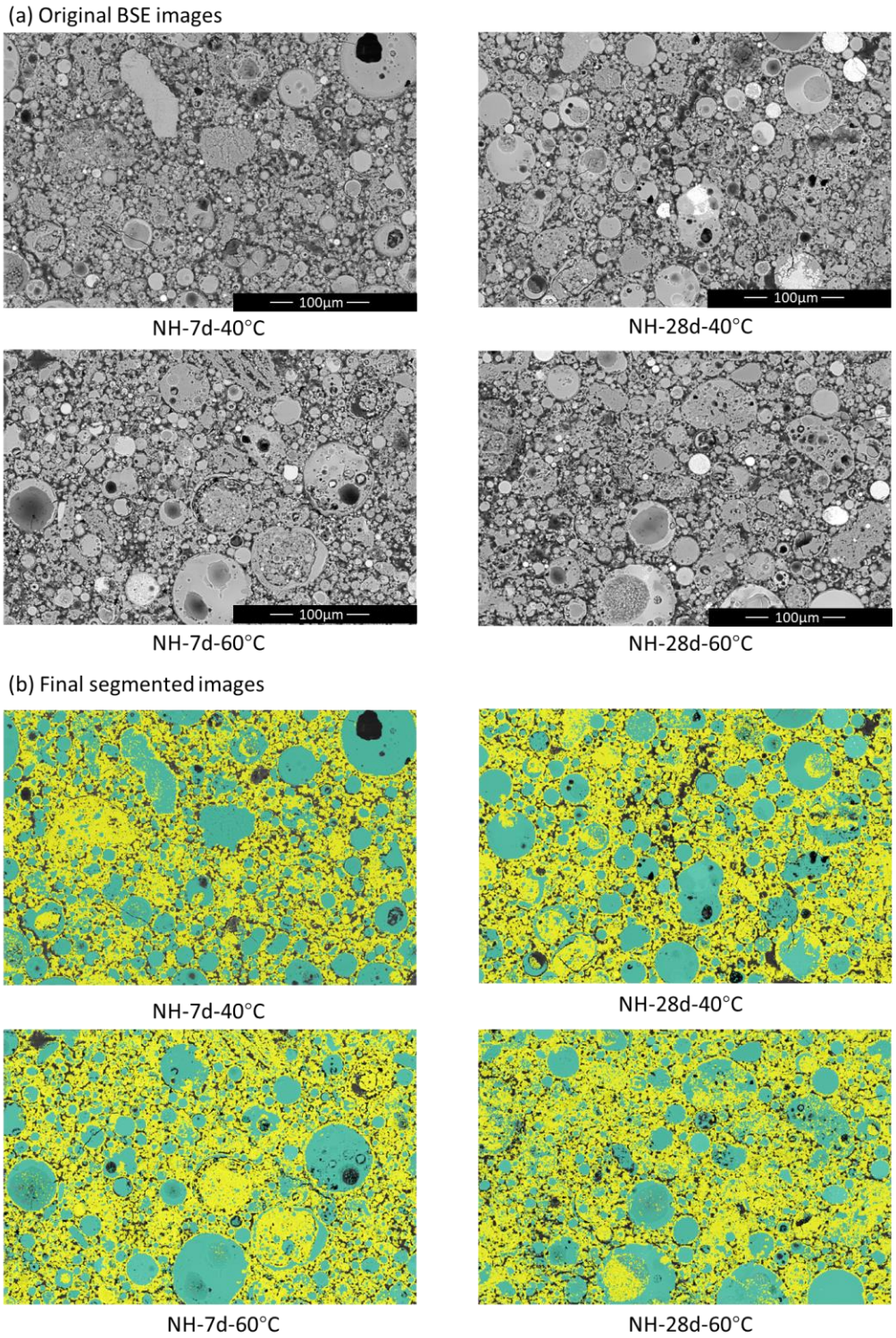

Figure 6.7 (a) Original SEM-BSE micrographs of NH-activated fly ash pastes cured at 7 days and 28 days under varied temperatures. (b) Segmented micrographs of NH-activated fly ash pastes. Green zone: unreacted fly ash; Yellow zone: reaction products; Dark zone: pores.

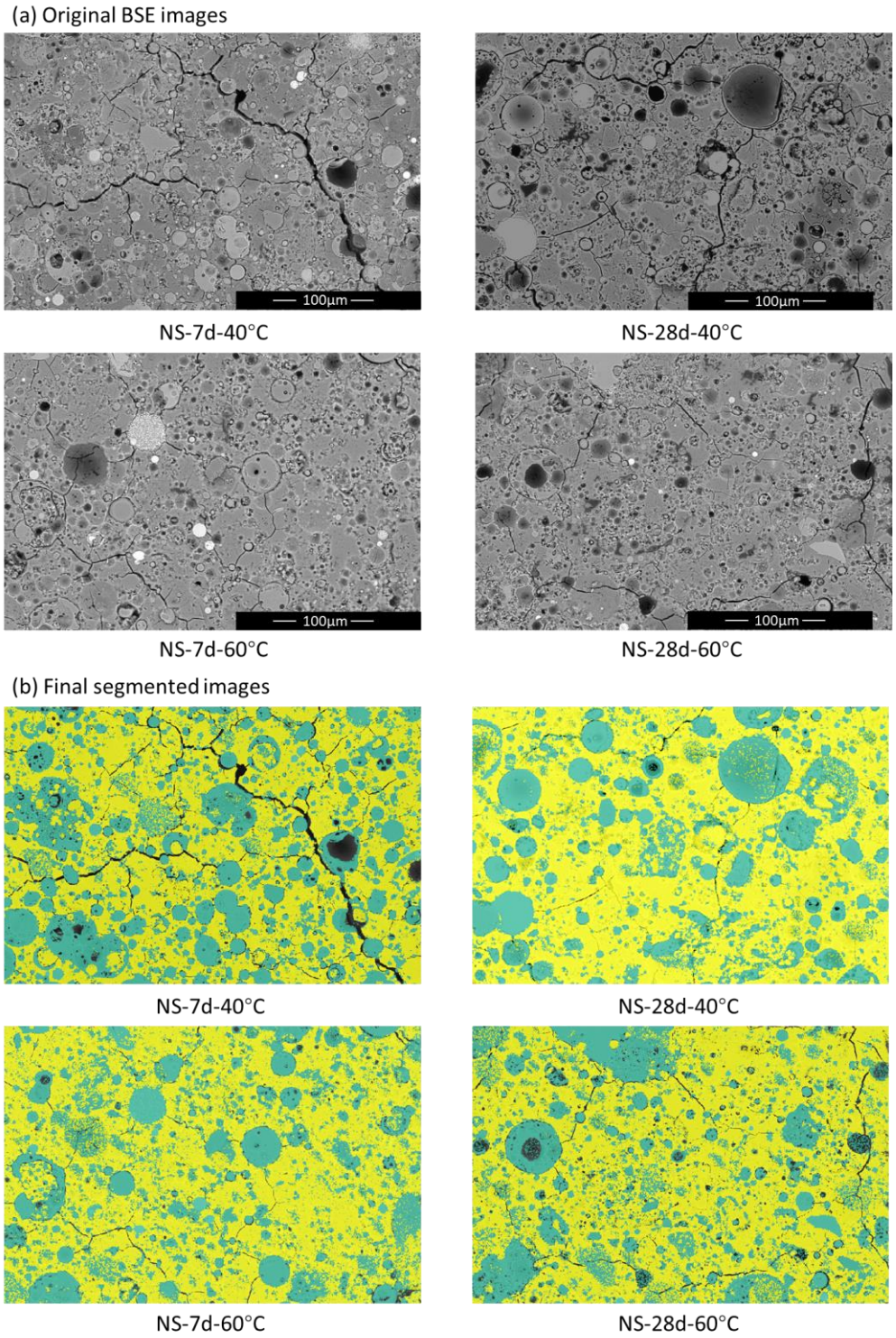

Figure 6.8 (a) Original SEM-BSE micrographs of NS-activated fly ash pastes cured at 7 days and 28 days under varied temperatures. (b) Segmented micrographs of NS-activated fly ash pastes. Green zone: unreacted fly ash; Yellow zone: reaction products; Dark zone: pores.

The chemical compositions, in terms of Si/Al and Ca/Al ratios, of the reaction products are further investigated from the elemental mapping results. Figures 6.9 and 6.10 illustrate the maps of Si/Al and Ca/Al ratios in the reaction products within the NH-activated system and NS-activated system, respectively. For the NH-activated system, the Si/Al ratio predominantly remained below 3 in most areas of the reaction product, while the NS-activated system exhibited a Si/Al ratio exceeding 3 across the majority of the reaction product. This arises not only from the formation of the N-(C-)A-S-H gel with a higher Si/Al ratio, but also from the Si species brought by sodium silicate activator. For both systems, a Ca/Al ratio of around 0.2 was homogeneously distributed within the reaction product zone. This confirms that Ca tends to be incorporated into N-A-S-H gel to form N-(C-)A-S-H gel even in low-Ca alkali-activated binder. Concurrently, the average Si/Al and Ca/Al ratios of the reaction products formed in these two systems are provided in Table 6.5. In the NH-activated system, the Si/Al ratio predominantly spans between 1-3, while in the NS-activated system, this ratio tends to exceed 3 slightly. Apart from that, the former demonstrates an upward trend in Si/Al ratio as time progresses, while the latter shows a decline in Si/Al ratio over the same period. This observed phenomenon suggests that the stability of N-(C-)A-S-H gel with a Si/Al ratio surpassing 3 may be thermodynamically unfavorable, aligning with MD simulation results in Chapter 3 and the solubility data in Chapter 5 (Figure 5.5). The Ca/Al ratio was measured at around 0-0.4 across the reaction products in both systems. Moreover, the Ca/Al ratio in the NS-activated system is slightly higher than that in the counterpart.

Table 6.5 Average Si/Al and Ca/Al ratio in the reaction products in AAFA pastes.

Samples	Si/Al	Ca/Al
NH-7d-40˚C	2.3±0.9	0.21±0.17
NH-28d-40˚C	2.5±0.9	0.21±0.16
NH-7d-60˚C	2.4±0.9	0.20±0.16
NH-28d-60˚C	2.5±1.0	0.21±0.17
NS-7d-40˚C	3.2±1.0	0.27±0.18
NS-28d-40˚C	3.1±1.0	0.22±0.16
NS-7d-60˚C	3.3±1.0	0.27±0.18
NS-28d-60˚C	3.2±1.0	0.25±0.18

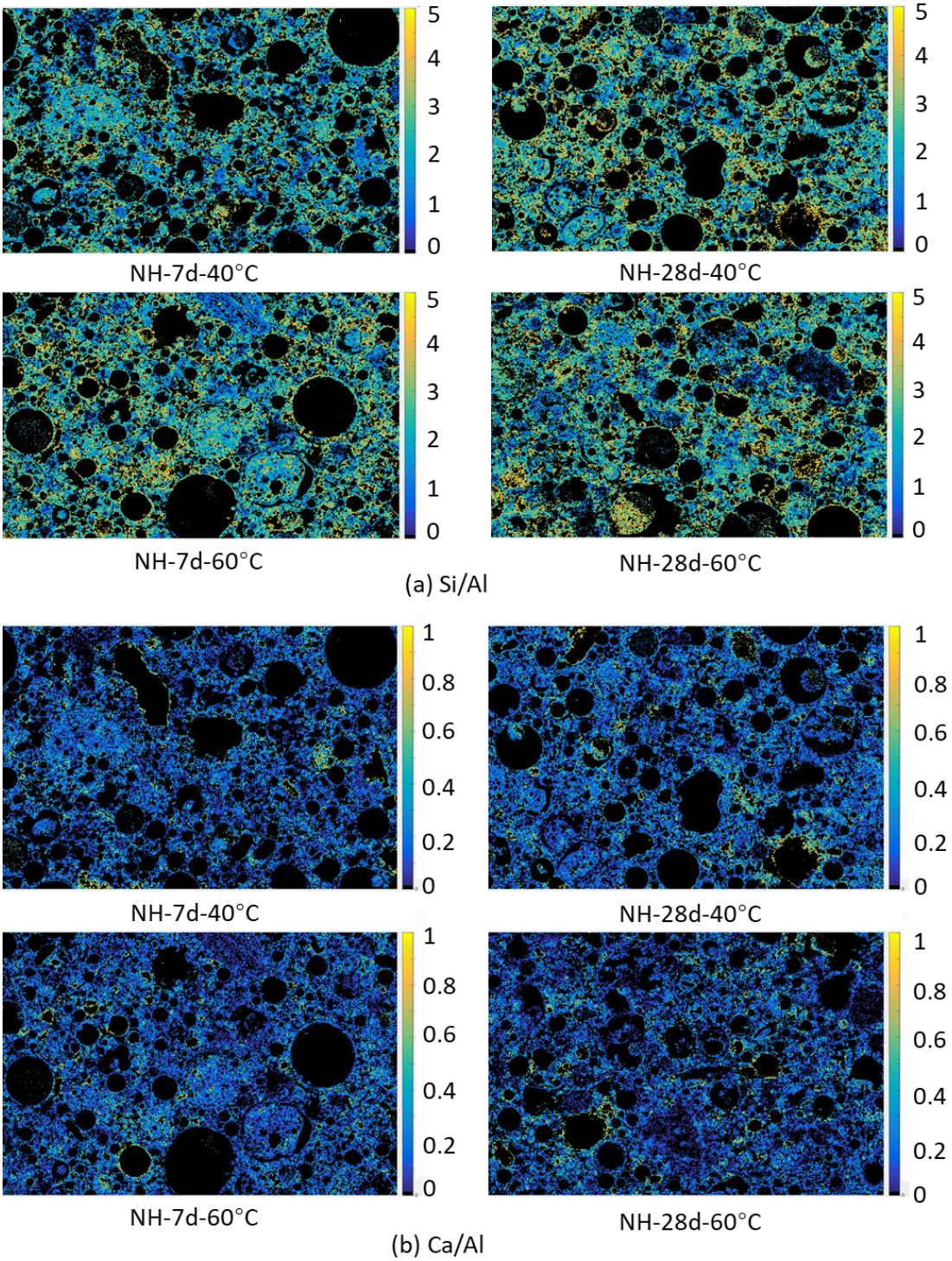

Figure 6.9 (a) Si/Al and (b) Ca/Al maps for the reaction products in NH-activated fly ash pastes.

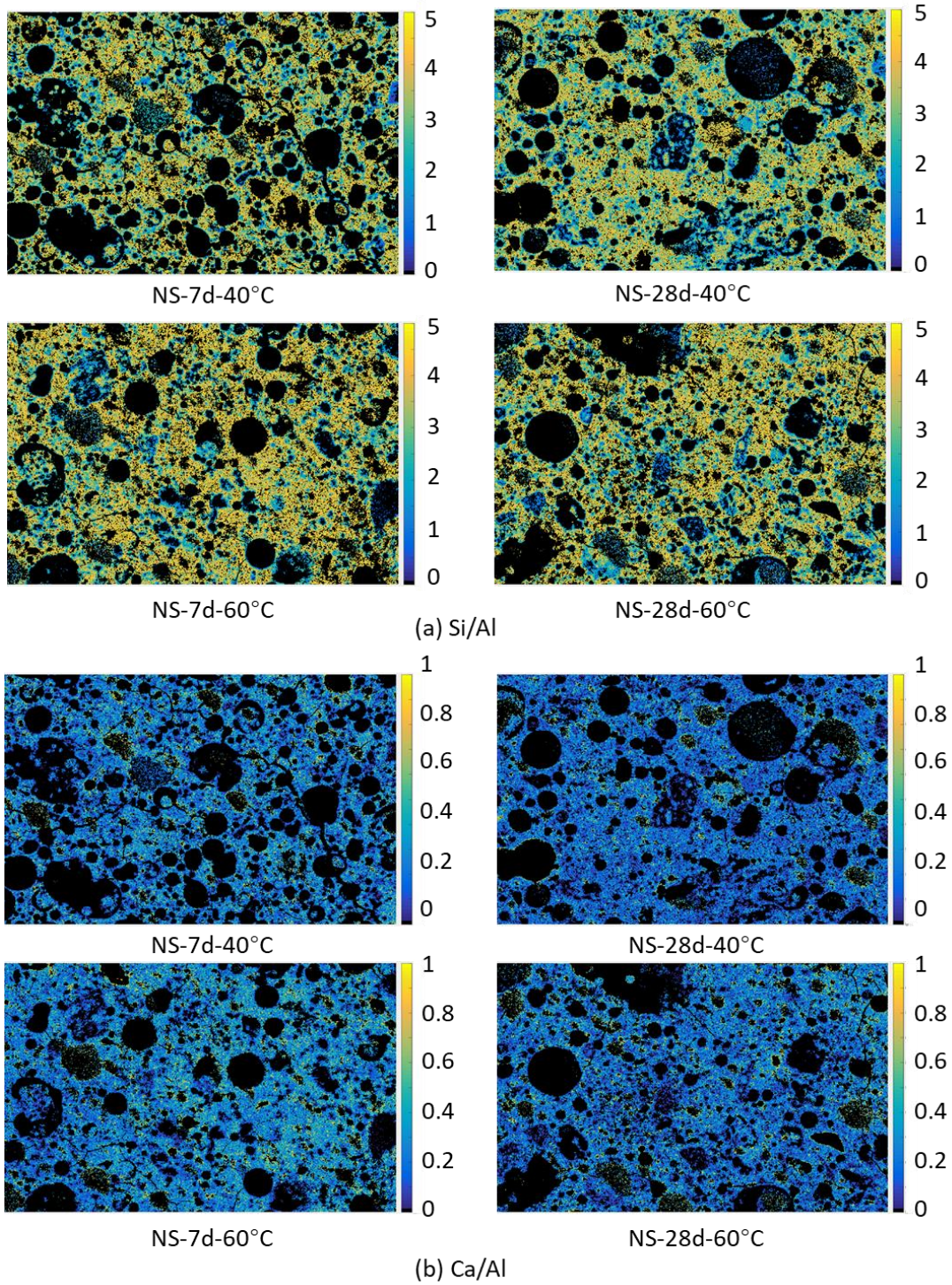

Figure 6.10 (a) Si/Al and (b) Ca/Al maps for the reaction products in NS-activated fly ash pastes.

6.3.3 Pore solution composition

The concentrations of Si, Al, K, Na, Ca, Mg, and Fe, as well as the pH in the pore solutions in the AAFA pastes are presented as a function of time in Figure 6.11, except for the pastes cured at 40 °C for 3 days, whose pore solutions failed to be extracted. A decreasing trend as time can be found for the concentrations of all elements, since the formation rate of solid reaction products exceeds the dissolution rate of the fly ash during this period. The effects of temperature and activator type on the elemental concentrations also rely on their influences on the formation rate and dissolution rate. All elemental concentrations decreased with the increase in temperature, indicating that higher temperature contributed more to the formation rate of reaction products. Concerning the activator type, using sodium hydroxide speeds up the dissolution of fly ash compared with using sodium silicate. Additionally, the soluble SiO_2 in sodium silicate accelerates the formation of reaction products. These combined effects lead to a higher elemental concentration in the pore solution of the NH-activated system than the counterpart. In addition, the decreasing amplitude of elemental concentration from 3 days to 7 days is larger than that from 7 days to 28 days, indicating a slowing down of the formation rate.

However, it is somewhat unexpected to observe a higher Si concentration in the pore solution of the NH-activated system than that in the NS-activated system. To further explain it, the relationship between the Si concentration and the pH in the pore solution for all AAFA samples is examined as shown in Figure 6.12. A decreasing trend in Si concentration is evident with the decrease in pH in the pore solution, attributed to the lower solubility of Si in lower pH conditions [171]. This suggests that the concentration of Si in the pore solution is highly dependent on the pH. The relatively low pH in the NS-activated system diminishes the likelihood of Si existing in an aqueous state, thereby promoting the participation of Si. As a result, less Si remains in the pore solution in the NS-activated system compared to its counterpart.

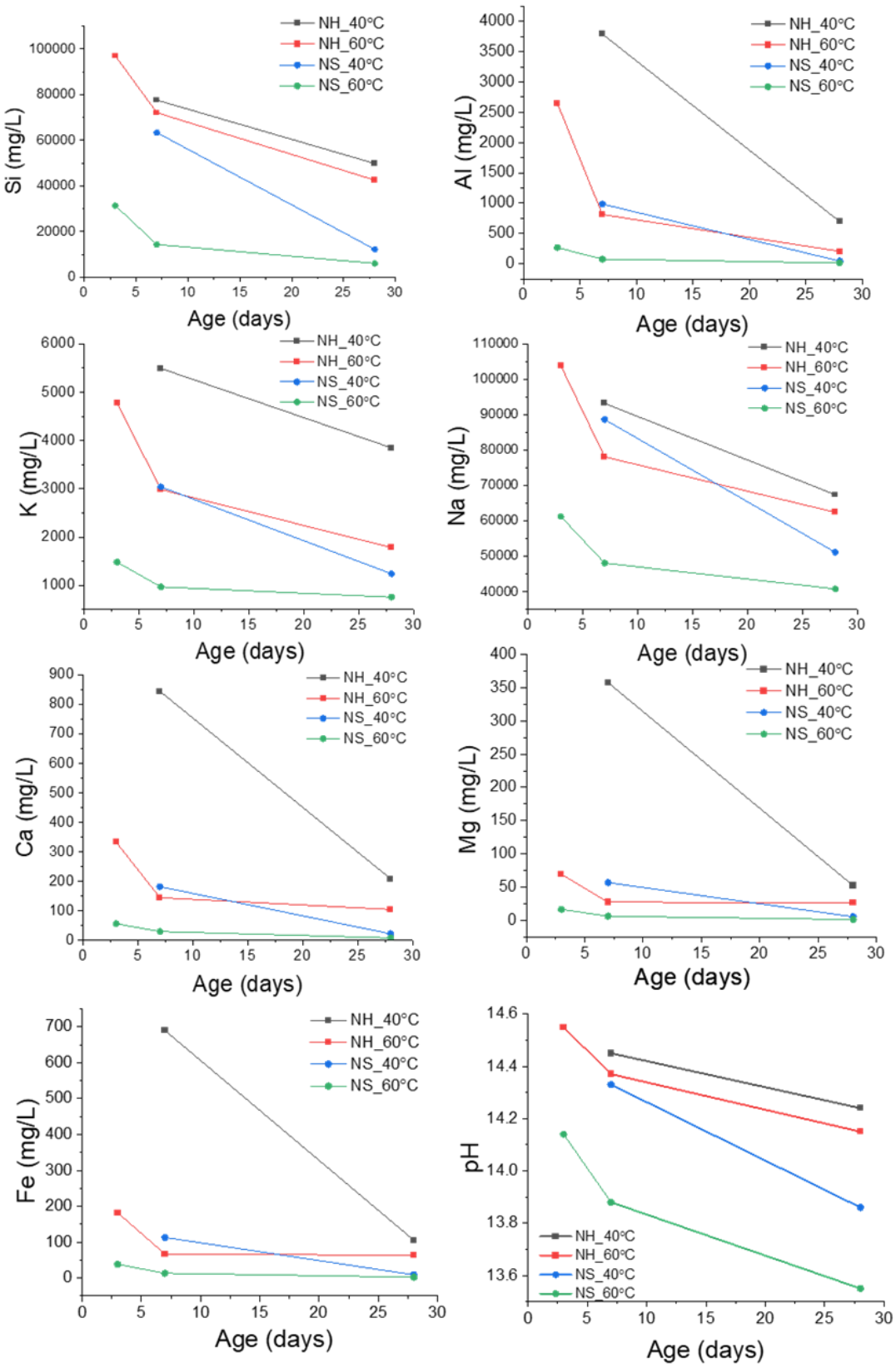

Figure 6.11 Elementary concentrations of the pore solutions in AAFA pastes.

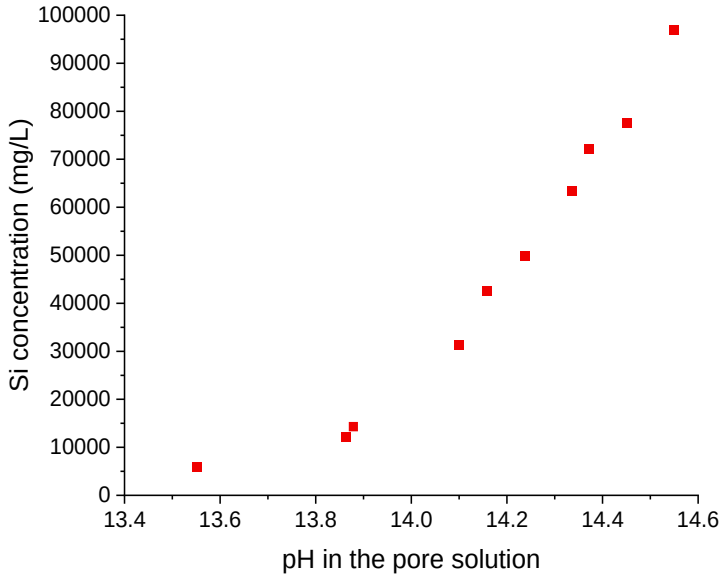

Figure 6.12 Relationship between Si concentration and pH in the pore solution of AAFA paste.

6.3.4 Reaction degree

The reaction degree of fly ash obtained from image analysis (Equation 6.1) and calculated based on the fitting calorimetric data (Equation 6.4) is shown in Figure 6.13. The reaction degree of fly ash exhibits a notable rise during its early age (before 7 days) and became relatively stable afterward, indicating a decrease in reaction rate. A similar trend was observed in [70]. The reduced reaction rate at a later stage can be attributed to the reduced pH value, as well as the increasing formation of reaction products over time, which limits the interaction between fly ash and alkali activator solution. The reaction degree of fly ash in the NH-activated system and NS-activated system is close. Sodium hydroxide, owing to its elevated pH, tends to enhance the dissolution of fly ash. On the other hand, sodium silicate aids in the formation of reaction products, leading to an increase in undersaturation degree of pore solution and, consequently, promoting the dissolution of fly ash. As a result, the fraction of fly ash that reacted is comparable in these two systems. However, despite a similar reaction degree, the microstructure in the NS-activated system is more compact due to a higher fraction of reaction products, as observed in TGA and segmented SEM images. Additionally, it can be seen that increasing curing temperature also enhances the reaction degree, especially at an early age. This phenomenon is primarily attributed to the heightened dissolution rate of fly ash facilitated by elevated temperatures, which will be further investigated in Chapter 7. Thus, elevating curing temperature can promote the reaction degree of fly ash, which also leads to the formation of a greater quantity of reaction product, as corroborated by TGA and SEM-EDS findings. Overall, the reaction degree of fly ash after 7 and 28 days of curing falls within the range of approximately 30-45 %, in agreement with the results in [70,198], of which the content of amorphous phase in fly ash and mixture design are similar to this study.

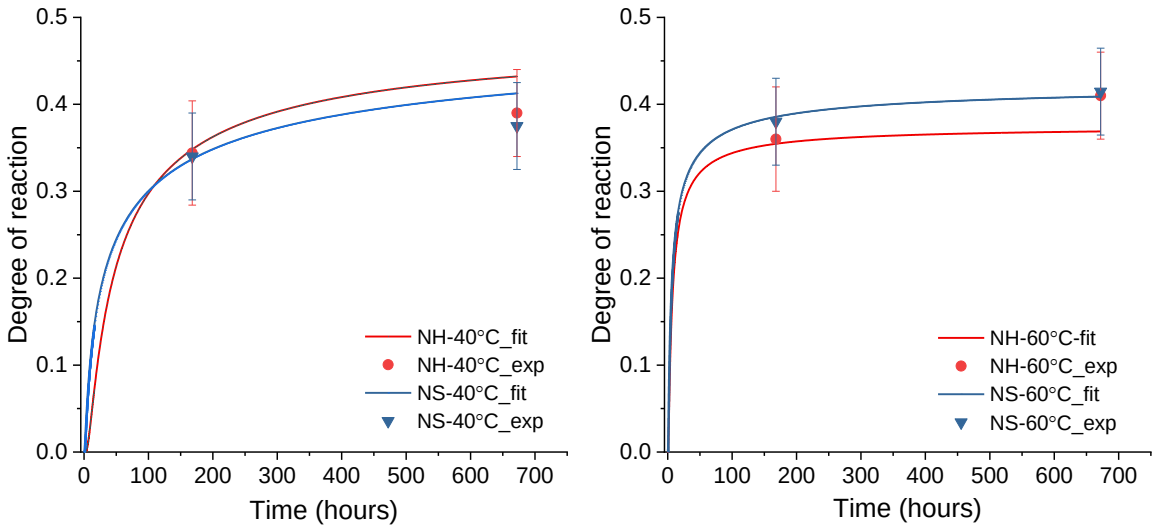

Figure 6.13 Degree of reaction of fly ash in AAFA pastes cured at 40 °C and 60 °C.

6.3.5 Thermodynamic modeling of chemical reactions in AAFA paste

Thermodynamic modeling of AAFA paste, in combination with the kinetic process developed in Figure 6.13, is carried out to offer valuable insights into the characteristics of both solid and aqueous phases as a function of time. In the interest of conciseness, only the results obtained from curing at 40 °C are presented below, while results from curing at 60 °C are given in Appendix C.

6.3.5.1 Evolution of simulated phase assemblages of AAFA paste

The evolution of phase assemblages of AAFA pastes cured at 40 °C is shown in Figure 6.14. Over time, there is an observable decrease in the fraction of fly ash, coinciding with the formation of a series of reaction products. Although the main reaction product is N-(C-)A-S-H gel in both NH-activated system and NS-activated system, it's noteworthy that the latter system yields a greater quantity of N-(C-)A-S-H gel compared to the former system. This result is in line with the findings of TGA and SEM-EDS mapping. In addition, a series of secondary reaction products are found in both systems, including C-(N-)A-S-H gel, brucite ($Mg(OH)_2$), magnesium silicate hydrate (M-S-H) and ferrihydrite-mc (FeOOH, mc refers to microcrystalline). These secondary phases are challenging to detect by experimental techniques due to their limited presence in the samples. However, the existence of C-(N-)A-S-H gel is consistently observed in the NH-activated system, whereas only a negligible amount of C-(N-)A-S-H gel is initially formed (0-2 days) and subsequently disappears in the NS- activated system. This agrees with the XRD results as shown in Figure 6.4 and the FTIR results in Figure 6.5, where minor signals for C-(N-)A-S-H gel were also found in the NH-activated system but absent in the NS-activated system. In addition, the presence of hydroxysodalite (SOD(OH)) in NH-activated system and its absence in NS-activated system are also in accordance with the XRD and FTIR results.

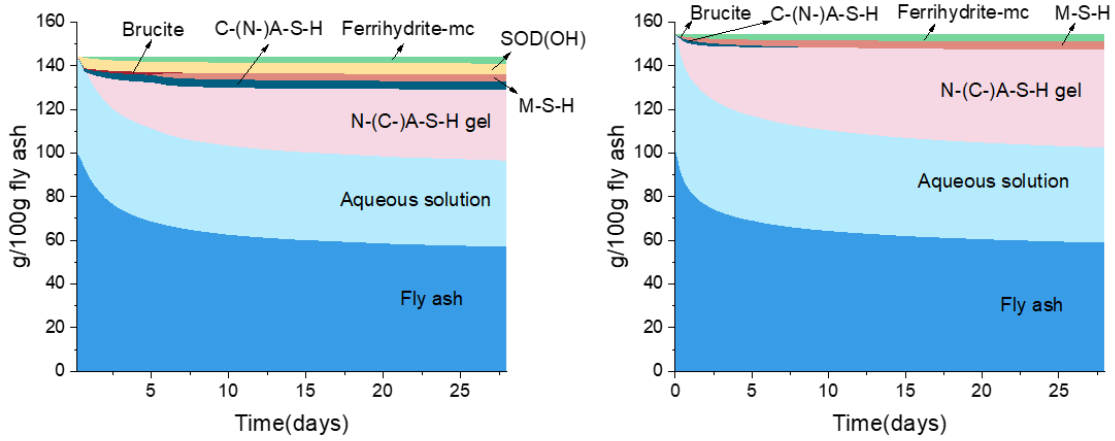

Figure 6.14 Simulated phase assemblages of AAFA pastes cured at 40 °C as a function of time. (a) NH-activated system, (b) NS-activated system.

Although the main reaction product in both NH-activated system and NS-activated system is N-(C-)A-S-H gel, it is expected that there will be distinctions in the characteristics of this gel formed in these two systems. Since N-(C-)A-S-H gel is treated as a solid solution containing seven end members, including three types of N-A-S-H gels and four types of N-C-A-S-H gels (see Table 5.3), the differences in N-(C-)A-S-H gel in different systems can be distinguished from the fractions of components in N-(C-)A-S-H gel, as illustrated in Figure 6.15. For NH-activated system, the principal components in N-(C-)A-S-H gel is N-A-S-H gel with a Si/Al ratio of 1 (N1), followed by N-C-A-S-H gel with a Si/Al ratio of 3 and a Ca/Al ratio of 0.5 (N3_0.5). In contrast, the NS-activated system primarily yields N3_0.5 as the dominant component, and it also forms a greater abundance of high Si/Al gels (e.g., N2, N3_0.25) while producing fewer low Si/Al gels (specifically N1) compared to the NH-activated system. This indicates that the N-(C-)A-S-H gel formed in the NS-activated system has a higher Si/Al ratio than that in the NH-activated system, which aligns with the SEM-EDS mapping results (see Table 6.3). It is interesting to observe the absence of N-A-S-H gel with a Si/Al ratio of 3 (N3) in both systems, even though high Si/Al N-(C-)A-S-H gel is expected to form in the NS-activated system. The reason behind it would be the high solubility of N3, as shown in Figure 5.5. A further discussion regarding it will be presented in the following.

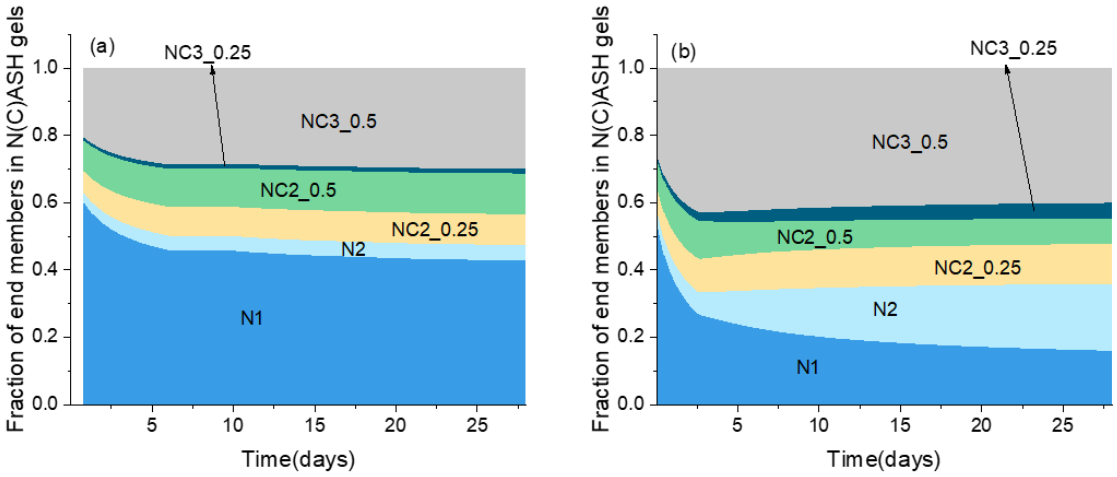

Figure 6.15 Mole proportions of end members in simulated N-(C-)A-S-H gels formed in AAFA pastes cured at 40 °C. (a) NH-activated system, (b) NS-activated system.

Figure 6.16 provides an overview of the Si/Al and Ca/Al ratios in the solid reaction products, both from experimental data and thermodynamic modeling. The simulated Si/Al ratio in the NH-activated fly ash cured from 7 to 28 days ranges from 1.64 to 1.72, which is slightly smaller than that in SEM-EDS mapping results (from 2.3 to 2.5). As expected, a higher simulated Si/Al ratio in the NS-activated system is observed compared to its counterpart. However, the discrepancy between experimental data and thermodynamic modeling data is more pronounced in the NS-activated system. In this system, the simulated Si/Al ratio ranges from 2.1 to 2.2 in curing age of 7 to 28 days, lower than the SEM-EDS mapping results (from 3.2 to 3.0). This discrepancy is linked to the overestimation of Si concentration and underestimation of Al concentration in the simulated aqueous phase. The reasons for the underestimation of simulated Si/Al ratio in solid reaction products include two parts. Firstly, in the thermodynamic modeling, lower Si/Al N-(C-)A-S-H gel tends to form due to its lower solubility as shown in Figure 5.5. However, in reality, the formation of reaction products is influenced by various factors beyond solubility, allowing for the potential formation of high Si/Al N-(C-)A-S-H gel, even if it is less thermodynamically favored. Secondly, the limitation of the N-(C-)A-S-H gel database prevents the formation of N-(C-)A-S-H gel with exceptionally high Si/Al ratios. Since the maximum Si/Al ratio of N-(C-)A-S-H gel developed in this research is only up to 3, it is not possible to obtain the reaction products with an average Si/Al ratio as high as in the SEM-EDS mapping results (above 3). Additionally, the thermodynamic data of N-(C-)A-S-H gel was determined based on the gel synthesized for 1 day, while in reality N-(C-)A-S-H gel could transform into more stable gels over time. Future work should investigate the effect of synthesis time on the solubility of N-(C-)A-S-H gel and consider expanding the database to include gels with higher Si/Al ratios. However, it is worth noting that the formation of N-A-S-H gel with a Si/Al up to 3 is improbable, as evident in Figure 6.15, let alone higher Si/Al ratio. This suggests the direction to expand the database of N-(C-)A-S-H gel should focus on achieving a higher Si/Al ratio in N-C-A-S-H gel, rather than N-A-S-H gel. For Ca/Al ratio, it can be seen from Figure 6.16(b), the simulated results in both systems match well with or are slightly smaller than the experimentally measured data.

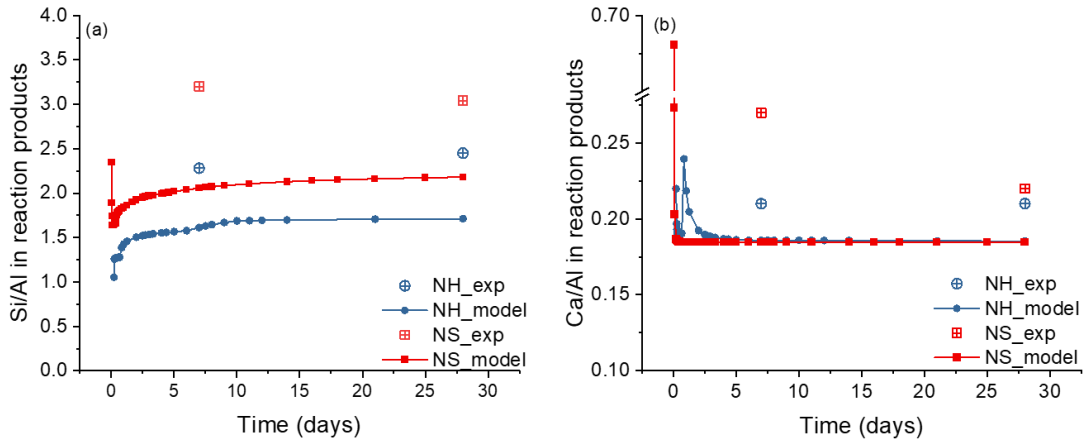

Figure 6.16 Experimental and modeling (a) Si/Al ratio and (b) Ca/Al ratio in reaction products in AAFA pastes cured at 40 °C.

A comparison was made between the volume fraction of reaction products obtained from experiment and thermodynamic modeling, as shown in Table 6.6. Both experimental and modeling results show an increase in the volume fraction of reaction products over time for NH-activated and NS-activated systems. Furthermore, a higher fraction of reaction products was observed in NS-activated system compared to its counterpart. The thermodynamic modeling results also followed the same trend. However, the volume fraction of the reaction products determined by thermodynamic modeling was lower than experimental results for all cases. This underestimation can be mainly attributed to the difference in C-(N-)A-S-H gel and N-(C-)A-S-H gel between modeling and experiment. In reality (experiment), these gels contain a small amount of physically absorbed water [40], which are not considered in thermodynamic modeling. As a result, the volume of these gels in the thermodynamic database is lower than that formed in reality.

To address this discrepancy, the quantities of physically absorbed water in C-(N-)A-S-H gel were calculated using the method outlined in [40]. However, the existing literature does not provide data regarding the amount of physically absorbed water in N-(C-)A-S-H gel. Therefore, it is assumed in this work that the mass loss between 40-105 °C in TGA results (refer to Figure 4.6 and 4.10) was attributed to the physically absorbed water in N-(C-)A-S-H gel. After incorporating the presence of physically absorbed water in N-(C-)A-S-H gel and C-(N-)A-S-H gel, the updated volume fraction of reaction products was increased, as shown in Table 6.6. However, despite the adjustment, they are still lower than those determined by SEM-EDS. The reason behind it is related to the underestimated porosity using SEM-EDS. As mentioned in Section 6.2.2.2, the pixel size in SEM-EDS images is 0.4 µm, meaning that pores smaller than 0.4 µm are not identifiable. As a result, the volume fraction of porosity is underestimated, while the volume fraction of reaction products is overestimated. Thus, even after considering the water retained in N-(C-)A-S-H gel and C-(N-)A-S-H gel, the volume fractions of reaction products determined in GEMS are still lower than those obtained through image analysis.

Table 6.6 Comparison of the volume fraction of reaction products obtained from experiment (SEM-EDS) *and thermodynamic modeling (GEMS).*

Volume fraction of reaction products	Image analysis (SEM-EDS)	GEMS	GEMS with consideration of water in gels
NH-7d	54 %	37.6 %	42.8 %
NS-7d	62 %	38.9 %	43.6 %
NH-28d	61 %	42.5 %	48.8 %
NS-28d	67 %	45.7 %	49.6 %

Note: the volume fraction of reaction products is calculated by dividing the volume of reaction products by the sum of the volumes of both reaction products and unreacted fly ash.

6.3.5.2 Evolution of compositions in aqueous phases

Figure 6.17 presents a comparison between the simulated and experimental elemental concentrations in the pore solution of NH-activated fly ash cured at 40 °C. From Figure 6.17(a) and (b), it can be seen that both the modeling concentrations of the Si and Al exhibited an increasing trend with time, followed by a subsequent decrease, eventually reaching a stable state. This trend describes well the dissolution of fly ash and the formation of solid reaction products during reactions. Moreover, the simulated results are in good agreement with the experimental data. For Figure 6.17(c) and (d), a declining trend can be observed both for the concentrations of the Na and OH^- as a function of time, which is attributed to the consumption of the activator. The simulated concentrations of Na and OH^- match well with the experimental results both at 7 days and 28 days. As shown in Figure 6.17(e), the simulated concentration of K is higher than experimental data. This is related to the absence of a solid K-containing phase in the modeling due to a lack of relevant database, while in reality the dissolved K might be incorporated into N-A-S-H gel to form (N,K)-A-S-H gel. As a result, in thermodynamic modeling, all dissolved K remains in the aqueous phase, leading to an overestimation of its concentration. Conversely, an underestimation of the simulated concentration of Fe, Ca and Mg at 7 days can be found in Figure 6.17(f), (g) and (h), respectively. This could be attributed to the overestimation of the amount of different solid phases formed during reaction, since thermodynamic modeling predicts an equilibrium condition, while in reality solutions might be oversaturated due to a slow formation of solid phases. In addition, in many cases, initially poorly crystalline phases may form, which exhibit higher solubility, leading to higher concentrations in the experiment.

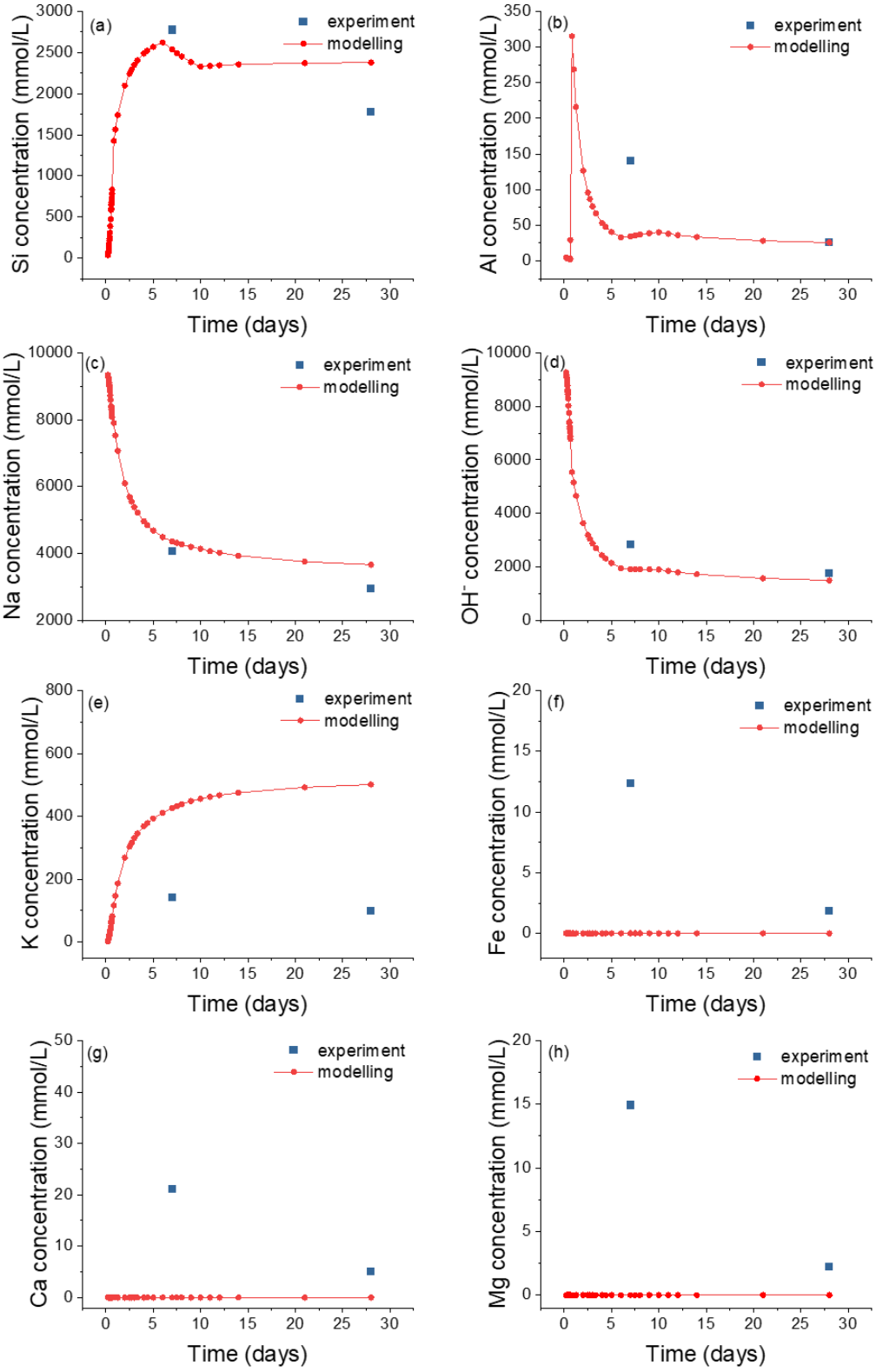

Figure 6.17 Experimental and modeling element concentrations in the pore solutions of NH-activated fly ash cured at 40 °C.

The experimental and modeling element concentrations in the pore solutions of NS-activated fly ash cured at 40 °C are shown in Figure 6.18. The trends observed in the concentrations of various elements are consistent with those observed in the NH-activated system (Figure 6.17). However, the agreement between the simulated results and experimental data is not as strong as it was in the NH-activated system. The simulated Si concentration is overestimated, whereas the simulated Al concentration is underestimated at 7 days. These discrepancies can be partly attributed to the underestimation of the Si/Al ratio within the reaction products (as shown in Figure 6.16(a)). Additionally, the high ionic strength in the NS-activated system, reaching around 5-10 molarity, challenges the accuracy of the extended Debye-Huckel equation used for computing activity coefficients, designed for an optimal range of 1-2 molarity. As a result, the modeling struggles to accurately depict the chemical environment in the aqueous phase. Although the simulated Na concentration aligns with the experimental data, the OH^- concentration is underestimated probably affected by the overestimated Si and underestimated Al. For the other elements, i.e. K, Fe, Ca and Mg, their results closely resemble those in the NH-activated system.

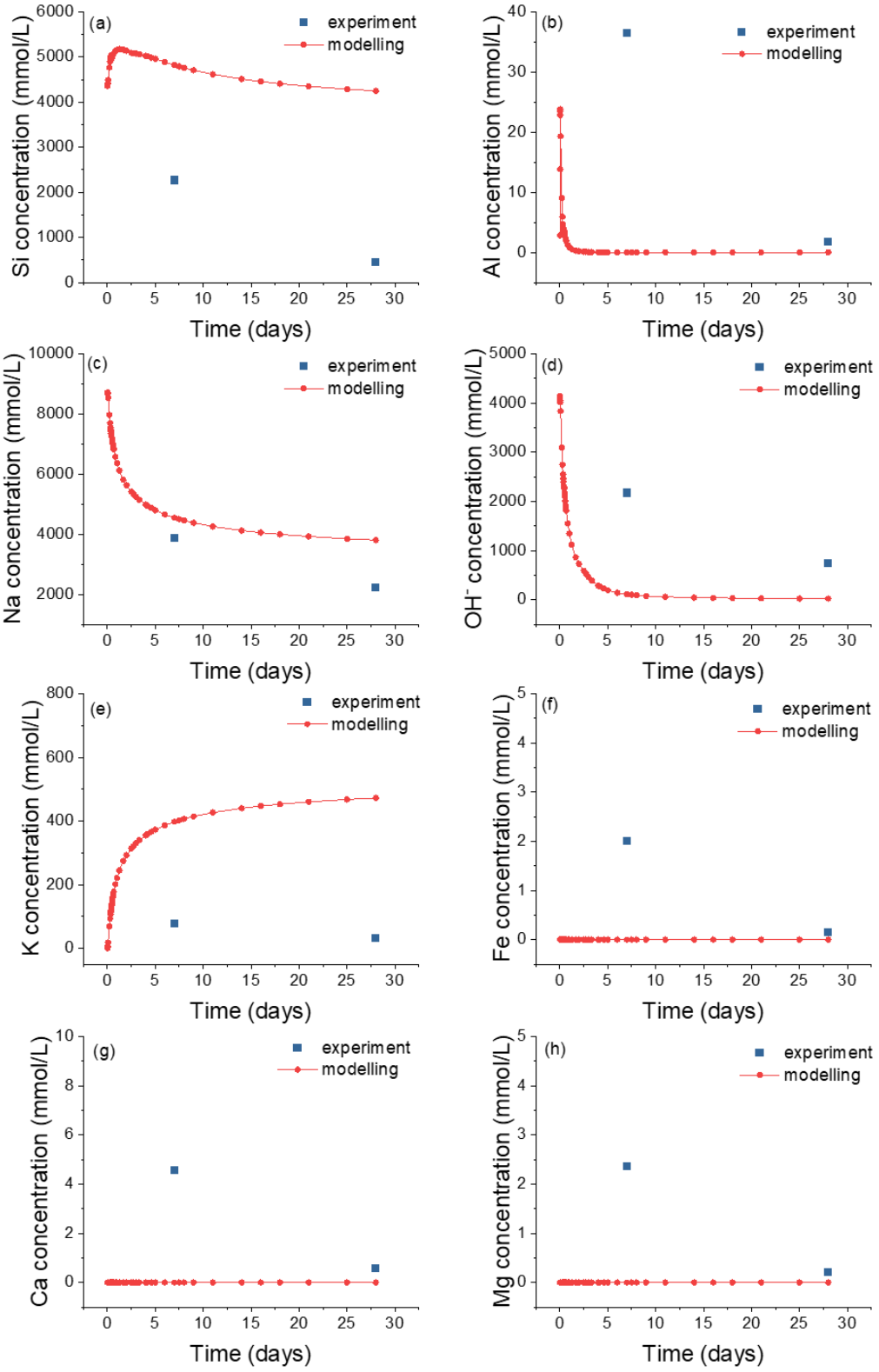

Figure 6.18 Experimental and modeling element concentrations in the pore solutions of NS-activated fly ash cured at 40 °C.

6.4 Conclusions

In this chapter, the reaction kinetics and the microstructure of AAFA paste were investigated experimentally. Thermodynamic modeling was conducted to study the reactions and phase assemblages of AAFA. The results derived from experiment and modeling were compared. Based on the results and discussion, the following remarks are made:

1. Despite a similar degree of reaction, the experimental results revealed that the NS-activated system yielded more reaction products and thus a more compact microstructure than those in NH-activated system. Moreover, the main reaction product, i.e. N-(C-)A-S-H gel, in the NS-activated system showed a higher Si/Al and Ca/Al ratio compared to that in its counterpart.
2. The thermodynamic modeling can predict the phase assemblage in AAFA paste over time, capturing even minor phases that fall beyond the detection limit of experimental techniques. The primary simulated reaction product aligns with the experimental results, indicating the formation of N-(C-)A-S-H gel. In addition, the modeling results showed a higher amount of N-(C-)A-S-H gel with a higher Si/Al ratio in the NS-activated system, which is in accordance with the experimental findings. However, the simulated Si/Al ratio in the reaction products is lower than the experimentally measured data, with this underestimation being more pronounced in the NS-activated system than in the NH-activated system.
3. The simulated element concentration, specifically Si, Al, Na and OH^-, in the pore solution matched well with the experimental data in the NH-activated system. However, an overestimation of Si concentration and underestimation of Al concentration in the pore solution were observed in the thermodynamic modeling of NS-activated fly ash. This discrepancy may be attributed to the high ionic strength in the NS-activated system, the limited thermodynamic data for N-(C-)A-S-H gel, or a slow transformation into more stable gels with lower solubility.
4. The accuracy of thermodynamic modeling of NS-activated fly ash requires improvement. One approach to achieve that is to upgrade the thermodynamic database of N-(C-)A-S-H gel by incorporating higher Si/Al ratios in the N-C-A-S-H gel.

Chapter 7

Dissolution of fly ash and simulation of 3D microstructure of AAFA

7.1 Introduction

The prediction of the 3D microstructure of alkali-activated fly ash (AAFA) is crucial for connecting mixture design with engineering properties. GeoMicro3D model, as briefly introduced in Chapter 2, was originally developed to simulate the reaction process and microstructure formation of alkali-activated slag (AAS). The development of the thermodynamic modelling of AAFA, as carried out in Chapter 6, is the crucial step to update GeoMicro3D model in order to make it available to simulate the reaction kinetics and microstructure formation of AAFA. However, the dissolution module in the original GeoMicro3D is not capable of modelling the dissolution rate of fly ash. Furthermore, there is lacking a universal function predicting the dissolution rate of fly ash in alkaline solution, which limits the current model to simulate the reaction process and microstructural evolution when fly ash is used as the precursor.

This chapter commences with an introduction to the framework and principles of GeoMicro3D, shedding light on its potential and inherent limitations. Subsequently, the experimental dissolution of fly ash in NaOH solution is performed to reveal the dissolution kinetics of fly ash. Based on these results, a prediction function is established to describe the dissolution rate of fly ash. This function is then incorporated into GeoMicro3D, enabling simulations of fly ash dissolution in NaOH solution. The simulation results are compared with experimental data to validate the accuracy of the predicted dissolution rate. Finally, the thermodynamic modeling of AAFA, developed in Chapter 6, is integrated into GeoMicro3D to simulate the reaction process and 3D microstructural evolution of AAFA. The simulated results using the extended GeoMicro3D are analyzed with respect to 3D microstructure, phase assemblage evolution, degree of reaction of fly ash, pore solution chemistry, and porosity. Relevant experimental results are also presented to validate the extended GeoMicro3D model.

7.2 GeoMicro3D model

7.2.1 An introduction to GeoMicro3D model

GeoMicro3D model was first developed to simulate the reaction process and 3D microstructure formation of alkali activated slag (AAS). The model mainly contains five modules: (i) simulation of the initial structure; (ii) dissolution of slag; (iii)diffusion of ions; (iv)

nucleation of reaction products; and (v) thermodynamic modelling. The basic procedure and method in each part will be introduced below.

(i) Simulation of the initial structure

In this module, the extended Anm material model [222] was adopted to simulate the initial spatial distribution of precursor (e.g. slag or fly ash) in an alkaline activator, thereby building an initial structure as an input. It should be noted that the simulation of the initial structure was the only module designed to be compatible with both slag and fly ash, while the subsequent modules within GeoMicro3D were exclusively developed for slag. To simulate the real shape of particles, their surface was described by Equations 7.1 and 7.2 in a 3D spherical polar coordinate system.

$$r(\theta,\varphi) = \sum_{n=0}^{\infty}\sum_{m=-n}^{n} a_{nm}Y_{nm}(\theta,\varphi) \tag{7.1}$$

$$Y_{nm}(\theta,\varphi) = \sqrt{\frac{(2n+1)(n-m)!}{4\pi(n+m)!}}P_{nm}(cos\theta)^{e^{im\varphi}} \tag{7.2}$$

where $r(\theta,\varphi)$ refers to the distance from the particle center of mass to the surface point. a_{nm} is the spherical harmonic expansion coefficient. $Y_{nm}(\theta,\varphi)$ is the spherical harmonic function. θ stands for the polar angle. φ represents the azimuthal angle. n and m are the indices $(-n \le m \le n)$. $P_{nm}(cos\theta)$ denotes the associated Legendre polynomial. i is the square root of -1.

Figure 7.1(a) shows a precursor particle with a real shape described by Equation 7.1. With the database of spherical harmonic coefficients of slag or fly ash particles, the Anm model is able to park particles one by one into a container, thereby constructing a 3D structure containing precursor and liquid to represent the initial structure of AAS or AAFA. The structure was converted into digital voxels. Each voxel has the same element composition as the precursor or activator. Figure 7.1(b) provides an example of a simulated initial structure of AAFA by using Anm model.

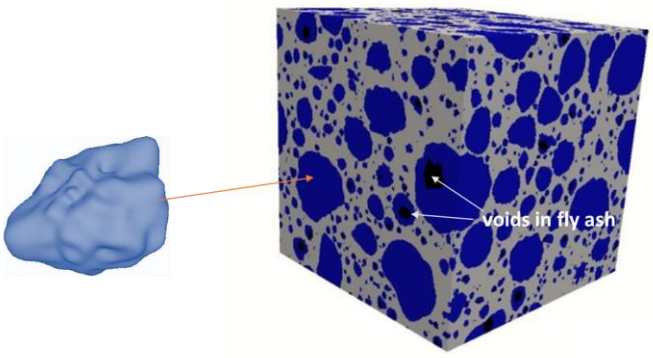

(a) A real-shape particle of precursor (b) the simulated initial structure for AAFA paste

Figure 7.1 (a) An irregular shape particle described by spherical harmonics. (b) Digital image of the simulated initial particle parking structure using real-shape particles for AAFA paste. The blue particle represents fly ash. The black zone denotes the hollow void within a fly ash particle. Redraw from [33].

(ii) Simulation of the dissolution of slag

The dissolution of slag was described as the dissolution of individual constituent oxide. The dissolution of silica, aluminum oxide and calcium oxide in an alkaline solution can be described as follows:

$$SiO_2 + 2OH^- \rightarrow H_2O + SiO_3^{2-} \quad (7.3)$$

$$Al_2O_3 + 2OH^- \rightarrow H_2O + 2AlO_2^- \quad (7.4)$$

$$CaO + H_2O \rightarrow 2OH^- + Ca^{2+} \quad (7.5)$$

According to the transition state theory [66], as also mentioned in Section 2.3.1.1, the overall dissolution rate of these oxides can be described by Equation 7.6. The following equation, derived from Equation 2.2, can describe the dissolution behavior of various glass from far-from-equilibrium state to near-to-equilibrium state.

$$r = r_+\left(1 - \frac{IAP}{K_{sp}}\right) \quad (7.6)$$

where r_+ is the forward dissolution rate, which refers to the dissolution rate of glass at the far-from-equilibrium condition [67,68]. IAP is the ion activity product. K_{sp} is the solubility product of the oxides. More details on the derivation of Equation 7.6 can be found in [40].

The far-from-equilibrium state for glass dissolution usually contains two stages, as shown in Figure 7.2. Initially, there is a short period of non-steady state where the dissolution rate varies with time, followed by a steady state with a constant dissolution rate.

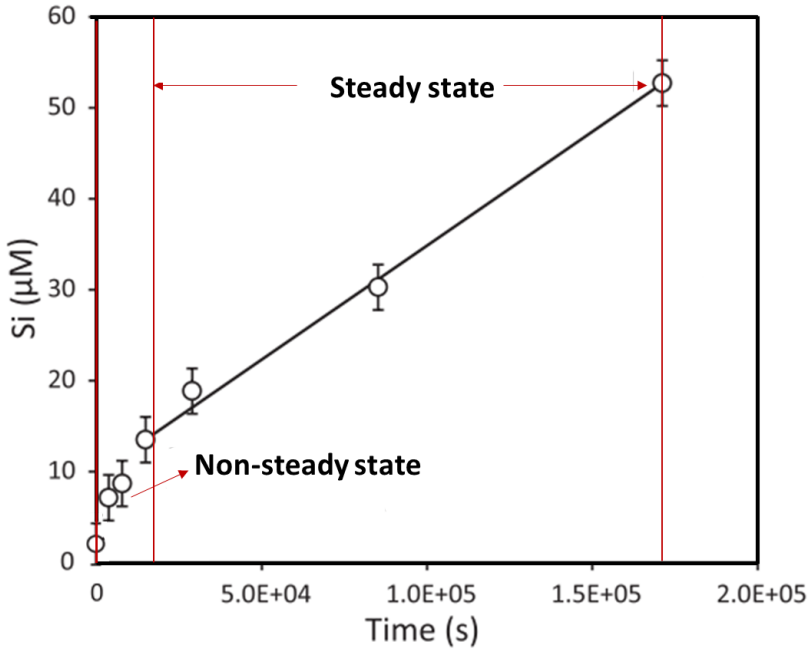

Figure 7.2 Concentration of Si for the dissolution of glass. A fast "non-steady state" dissolution stage is followed by a linear increase in Si concentration in a "steady state" dissolution stage. Redraw from [59].

The logarithmic forward dissolution rates of SiO_2 and CaO in the steady state were derived experimentally through the dissolution of slag in NaOH solutions at different pH values:

$$log\ r_{+,Si} = 0.0155pH\frac{NBO}{T} + 0.0727pH + 0.6199\frac{NBO}{T} - 9.0309 \tag{7.7}$$

$$log\ r_{+,Ca} = 0.1868pH - 8.7729 \tag{7.8}$$

where $\frac{NBO}{T}$ denotes the ratio of the non-bridging oxygen atoms to oxygen atoms in tetragonal coordination. The detailed derivation of Equations 7.7 and 7.8 can be found in [223].

According to the stoichiometric dissolution of Al and Si in aluminosilicate materials [223,224], the log forward dissolution rate of Al_2O_3 can be calculated using Equation 7.9:

$$log\ r_{+,Al} = log\left(\frac{v_{Al}}{v_{Si}}r_{+,Si}\right) = log\left(\frac{v_{Al}}{v_{Si}}\right) + logr_{+,Si} \tag{7.9}$$

where v_{Al} and v_{Si} are the molar fractions of Al and Si in the slag, respectively.

As for the minor constituents like Mg, Na, and K, the dissolution rates of these modifying elements (X) were obtained based on the dissolution rate of Ca:

$$r_X = f_X\frac{v_X}{v_{Ca}}r_{Ca} \tag{7.10}$$

where f_X is the ratio of the dissolution rate of element X relative to the dissolution rate of Ca.

Since the total surface area of precursors, affected by the digitization resolution, can be different from the experimental data, the function of dissolution rate was modified to take this into account:

$$r'_{+,X} = \frac{V_{model}/S_{model}}{V_{exp}/S_{exp}}r_{+,X} \tag{7.11}$$

where $r'_{+,X}$ and $r_{+,X}$ are the forward dissolution rates of element X before and after considering the effect of the solution-volume/surface-area ratio. V_{model} and V_{exp} denote the solution volume in simulation and experiment, respectively, while S_{model} and S_{exp} represent the surface area of the precursor in simulation and experiment, respectively.

The forward dissolution rate of element X in the non-steady state was described using the following equations:

$$r_{+,X,non-steady} = F_{X,non-steady}r'_{+,X} \tag{7.12}$$

$$F_{Si,non-steady} = 2.88 * \frac{V_{model}/S_{model}}{V_{exp}/S_{exp}} + 2.89 \tag{7.13}$$

$$F_{Ca,non-steady} = 8.81 * \frac{V_{model}/S_{model}}{V_{exp}/S_{exp}} + 7.26 \quad (7.14)$$

where $r_{+,X,non-steady}$ and $r'_{+,X}$ are the forward dissolution rates in the non-steady state and steady state, respectively. The derivation of factor $F_{X,non-steady}$ can be found in [223].

In addition, the effect of temperature on the dissolution rate was also considered based on the Arrhenius equation:

$$r_{new} = r_{ref} \exp\left[\frac{E_a}{R}\left(\frac{1}{T_{ref}} - \frac{1}{T_{new}}\right)\right] \quad (7.15)$$

where r_{new} and r_{ref} are the dissolution rates at the Kelvin temperatures T_{new} and T_{ref}(293.15 K), respectively. E_a is the activation energy of the dissolving element. R is the gas constant.

The amounts of dissolved elements from the precursor can be calculated based on the corresponding dissolution rate. Each precursor voxel has six neighboring cubes, creating six interfaces where dissolution can happen. The amounts of elements dissolved at each interface and at six interfaces can be calculated using Equation 7.16 and Equation 7.17, respectively.

$$\Delta n_{X,i} = (1 - V_i)^{1.1} r_{X,i} t_0 l_0^2 \quad (7.16)$$

$$\Delta N_X = \sum_{i=1}^{6} \Delta n_{X,i} \quad (7.17)$$

where $\Delta n_{X,i}$ and ΔN_X are the dissolved amounts of element X at interface i and six interfaces at one time step t_0, respectively. V_i is the volume fraction of solids in the voxel next to the interface area that is dissolving, $r_{X,i}$ is the dissolution rate of element X at the interface i, l_0 is the side length of a voxel.

(iii) Simulation of the diffusion of ions

The diffusion of ions was modeled using the lattice Boltzmann (LB) method [128,225], a powerful method widely applied for solving fluid dynamics and ionic transport problems. This method is rooted in a statistical interpretation of fluid dynamics at the microscopic level. The ions can move in all directions as a result of collisions between particles. The probability of particle positions in the physical space is dynamically described by the continuous Boltzmann equation. To streamline computational process and enhance efficiency, the LB method approximates the continuous Boltzmann equation through a discretization approach. This involves dividing physical space into uniformly spaced lattice nodes and discretizing velocity space into a finite set of microscopic velocity vectors. These discrete velocity vectors represent the propagation of particles between lattice nodes. The microscopic movements of particles at each lattice node are described by particle distribution functions, which define the probability of finding a particle around a lattice node at a specific time. This meticulous discretization and representation empower the LB method to simulate the crucial kinetics of a fluid system, with a specific emphasis on non-equilibrium processes and subsequent

relaxation to an equilibrium state. In GeoMicro3D, a cubic lattice model D3Q7[2] was employed to simulate the ion transport during the dissolution of slag in the alkaline solution. The evolution of particle distribution functions satisfies the following lattice Boltzmann equation:

$$f_j\left(x + e_j\delta t, t + \delta t\right) = f_j(x,t) - \frac{\delta t}{\tau}\left[f_j(x,t) - f_j^{eq}(x,t)\right] + w_j\delta t S \tag{7.18}$$

where f_j and f_j^{eq} represent the non-equilibrium and equilibrium particle distribution functions at location x and time t in the direction of the velocity j, respectively. e_j stands for the discrete velocity at location x and time t. w_j is the weighting factor in the velocity direction j (w_j=1/7 for all directions). δt is the LB time step and S signifies the source term, accounting for the amounts of dissolved elements and the amounts of elements consumed during the precipitation of the products at one LB time step. τ denotes the relaxation time. The relationship between the relaxation time and the ion diffusivity D_p should follow the Equation 7.19:

$$T_0 = L_0^2 e_s^2(\tau - \delta t/2)/D_p \tag{7.19}$$

where T_0 and L_0 are the time and length factors for conversion between the lattice unit and the real physical unit, respectively. e_s is the lattice speed of sound ($e_s = 0.53$).

Excluding the convection term, f_j^{eq} can be determined using the following equation, where F is the ion concentration in the lattice node:

$$f_j^{eq}(x,t) = \omega_j F(x,t) \tag{7.20}$$

$$F(x,t) = \sum_{j=0}^{6} f_j(x,t) \tag{7.21}$$

(iv) Simulation of the nucleation of reaction products

After a specific duration of slag dissolution, the pore solution may reach a state of saturation or oversaturation. In this state, solid reaction products can form if there are nuclei present or if new nucleation sites are likely to form. The probability $P(\Delta t)$ of at least one critical nucleus existing in the solution can be calculated using Equation 7.22 [129]:

$$P(\Delta t) = 1 - \exp\left(-JV\Delta t\right) \tag{7.22}$$

where V is the solution volume within which the nucleus forms, Δt is the time interval, while J is the nucleation rate that can be determined using the following equation:

$$J(S) = AS_s exp\left(-\frac{B}{ln^2 S_s}\right) \tag{7.23}$$

[2] In the term D3Q7, D3 refers to three dimensions, Q7 refers to seven discrete velocity directions.

where A is the kinetic parameter, S_s is the supersaturation index of the reaction products, and B is the thermodynamic parameter. The calculations for these parameters can be found in [40].

For a lattice node without reaction products, the thermodynamic modeling module is invoked only when there is a probability of nucleation of at least one primary gel and at least one of secondary reaction products according to Equation 7.22. In the case of a lattice cell with existing reaction products, the thermodynamic modeling module is called directly without calling the nucleation probability module. A schematic representation of the dissolution of the precursor and formation of reaction products are shown in Figure 7.3.

(v) Thermodynamic modeling

The function of this module was to model the chemical reactions and calculate the amounts of reaction products through thermodynamic modeling, which was performed via GEMS program. The thermodynamic database used in GeoMicro3D incorporated CEMDATA07 database [123], the thermodynamic data for C-(N-)A-S-H gel [182] and secondary reaction products [40] of AAS. Following the calculation, the compositions of solid phases and pore solution within the lattice cell were updated. The simulation then returned to the dissolution module iteratively until the simulation target time was achieved. The overall flowchart of GeoMicro3D is shown in Figure 7.4.

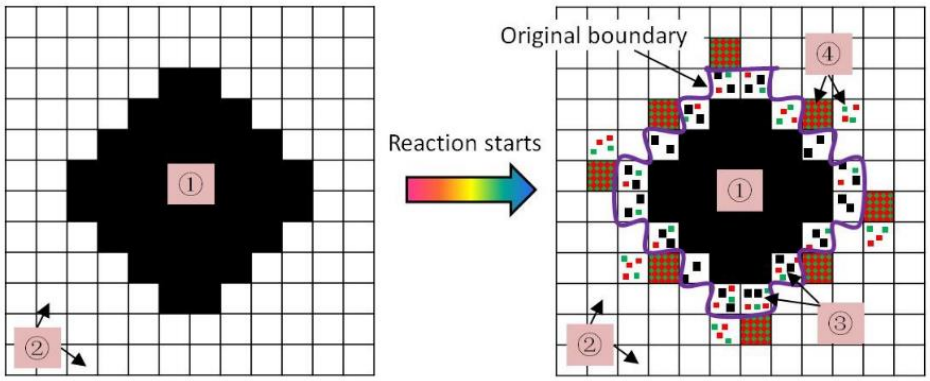

Figure 7.3 Schematic representation of the formation of the reaction products. ① represents the unreached precursor cells. ② represents the solution cells. ③ represents cells where precursor may dissolve and reaction products may precipitate. ④ represents cells that are completely or partially filled with reaction products [40].

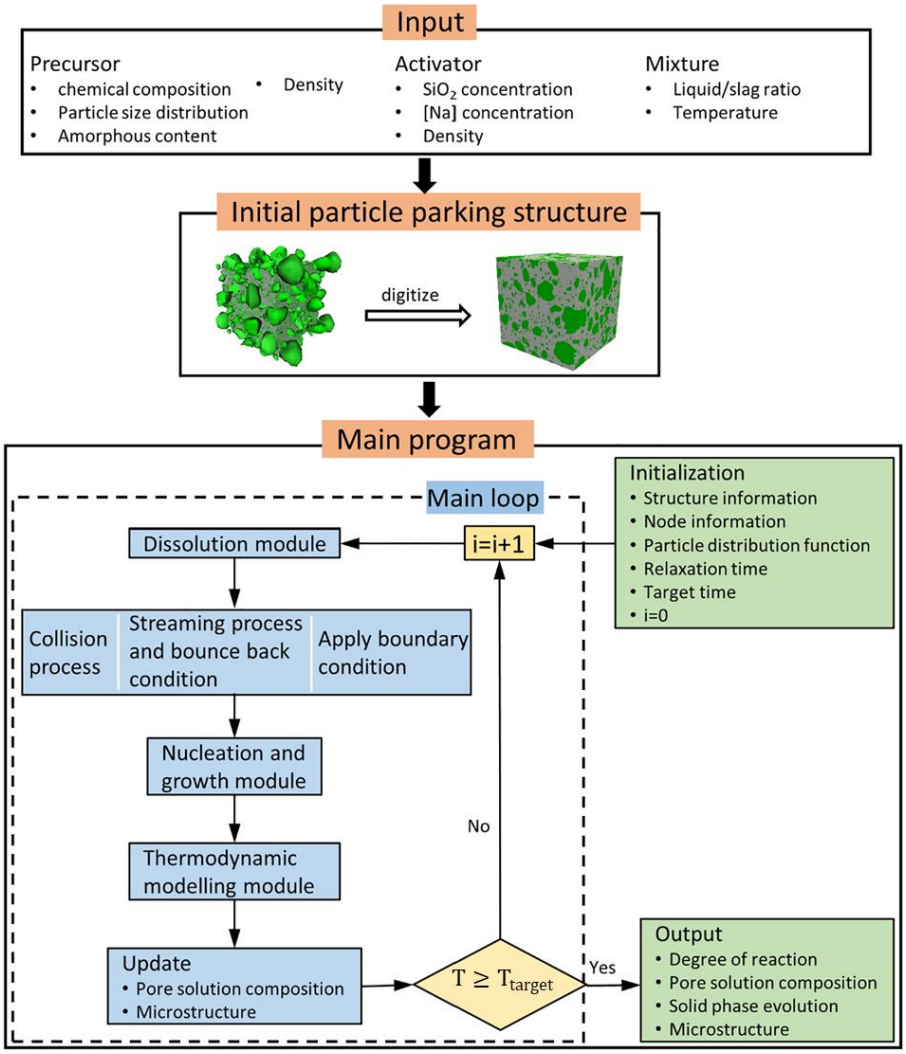

Figure 7.4 The overall flowchart of the GeoMicro3D model [40].

7.2.2 Limitation of GeoMicro3D

As GeoMicro3D was initially designed for AAS material, its adaptation to AAFA material is currently unavailable. The primary distinction between AAS and AAFA lies in their precursors. Consequently, the dissolution kinetics and chemical reactions differ between these two systems. Among the five modules in GeoMicro3D, the simulation of the initial structure, diffusion of ions, and nucleation of reaction products are universally applicable to any precursor, while the dissolution module and thermodynamic modeling module are specific to slag. To enhance GeoMicro3D's applicability to AAFA, two key steps are necessary. First, the dissolution kinetics of fly ash should be understood. More specifically, a function of the dissolution rate of fly ash should be established and incorporated into GeoMicro3D. Second, for the thermodynamic modeling of AAFA, the reaction products of AAFA and their corresponding thermodynamic data must be integrated into GeoMicro3D. In summary, it is feasible and meaningful to expand the functionality of GeoMicro3D for its use in AAFA.

7.3 Methodology

7.3.1 Dissolution of fly ash

7.3.1.1 Forward dissolution rate of fly ash

Experiments on the dissolution of fly ash were carried out to determine the forward dissolution rate of fly ash. As mentioned in Chapter2, the forward dissolution rate of fly ash can be described using the following equation [19,65,69]:

$$r_+ = k_0 10^{\pm \eta \cdot pH} \exp\left(\frac{-E_a}{RT}\right) \tag{7.24}$$

where k_0 is the intrinsic rate constant, η is the pH power law coefficient, E_a is the apparent activation energy (J/mol). R is the universal gas constant (R =8.31 J/mol/K).

To determine the parameters (k_0, η, E_a) in Equation 7.24, the dissolution experiment was conducted with the following procedure: 0.1 gram of fly ash was mixed with 100 ml of NaOH solution with different concentrations in a sealed container. The high solution-to-ash ratio of 1000 was adopted to avoid the formation of reaction products. The mixture was then placed in a temperature-controlled shaker operating at 250 rpm. The tests were performed at different temperatures. Detailed dissolution conditions are listed in Table 7.1. Subsequently, the sample was filtrated through a 0.2 μm filter at certain time intervals up to 48 hours. Note that individual samples were created for each testing time rather than sampling from the same solution over time. The concentrations of Si, Al and Ca in the solution were measured on duplicate samples using ICP-OES with the same procedures in Section 4.2.3.

Based on the elemental concentrations over time, the forward dissolution rate (mol/m^2/s) of the specific element (X) can be computed with the following equation:

$$r_{+,X} = \frac{\Delta(X)}{\Delta t} \frac{V}{m * SSA} \tag{7.25}$$

where $\Delta(X)$ denotes the change in elemental concentration (mol/L) over the time increment Δt (s), V is the solution volume (L), m is the mass of fly ash (g), SSA represents the specific surface area of fly ash, which was determined as 1.01 m^2/g using the Brunauer-Emmett-Teller (BET) method.

Table 7.1 Dissolution conditions.

Group	NaOH concentration	pH of NaOH solution	Temperature
1	1 M	14.00	20 °C
2	1.5 M	14.18	20 °C
3	3 M	14.48	20 °C
4	5 M	14.70	20 °C
5	5 M	14.70	40 °C
6	5 M	14.70	60 °C

7.3.1.2 Simulation of dissolution of fly ash in alkaline solution

The function developed to predict the forward dissolution rate of fly ash, based on the dissolution experiment, was then integrated into GeoMicro3D. A comprehensive description of the function derivation process will be shown in Sections 7.4.1 and 7.4.2.

To assess the accuracy of the function, the dissolution of fly ash in a 5M sodium hydroxide solution was simulated at different temperatures using the extended GeoMicro3D model. The initial structure consisted of fly ash particles with a maximum size of 10 μm, arranged within a cube of 125 μm×125 μm×125 μm. The solution to fly ash mass ratio was 1000, mirroring the conditions of the dissolution experiment. In the simulation, fly ash also contains three parts: amorphous particles, crystalline particles and voids. The relationship between the apparent volume of fly ash (V_a) and the volume of hollow voids (V_v) in fly ash can be determined using the following equation:

$$V_a\rho_a = (V_a - V_v)\rho_r \tag{7.26}$$

where ρ_a (g/cm^3) and ρ_r (g/cm^3) are the apparent density and the real density of fly ash, respectively. In this work, they are determined as 2.13 g/cm^3 and 2.65 g/cm^3, respectively.

The digitized simulation cube was initialized in terms of element compositions for liquid voxels and fly ash voxels. The model considered oxides including SiO_2, Al_2O_3, CaO, Fe_2O_3, MgO, K_2O and Na_2O for fly ash representation. The amounts of chemical compositions in the amorphous fly ash and crystalline fly ash were aligned with the chemical composition determined in Table 6.4 in Chapter 6. Only amorphous fly ash was considered reactive, having the capacity to dissolve.

The solubility products of SiO_2, Al_2O_3 and CaO, used in Equation 7.6, were set as 1.23×10^2, 3.55 and 2.1×10^{-1}, respectively [223]. The parameter f_X in Equation 7.10 was set as 0.8, 1.2 and 1.2 for Mg, K and Na, respectively [223]. Fe_2O_3 is a newly incorporated oxide. Given the fact that it usually functions as a network former in glass, its dissolution rate was established by correlating it with the dissolution rate of Al, using the following equation:

$$r_{Fe} = f_{Fe}\frac{v_{Fe}}{v_{Al}}r_{Al} \tag{7.27}$$

where f_{Fe} was set as 0.2, considering the low solubility of Fe_2O_3.

According to the experimental results shown in Section 7.4.1, the dissolution rate of Si in the non-steady state was set as three times ($F_{Si,non-steady}$=3) as that in the steady state, instead of using the original equation (Equation 7.13). In addition, the activation energy of CaO for dissolution, as employed in Equation 7.15, was taken as 13.6 kJ/mol [223]. It is worth noting that Equation 7.15 was exclusively applied to the dissolution of CaO to correct the effect of temperature. However, this correction was deemed unnecessary for SiO_2, as the newly formulated function (refer to Equation 7.29) for SiO_2 inherently accounts for temperature effects, eliminating the need for the additional temperature correction applied to CaO. The diffusivities of various ions used in Equation 7.19 are listed in Table 7.2.

Table 7.2 Diffusivities of aqueous ions in solution at 25 °C [40].

Ions	SiO_3^{2-}	AlO_2^-	Ca^{2+}	Mg^{2+}	FeO_2^-	K^+	Na^+	OH^-
D_p($\times 10^{-9}$ m^2/s)	0.7	0.6	0.72	0.71	0.6	1.96	1.33	5.28

7.3.2 Implementation of the extended GeoMicro3D model

In addition to adding the function for predicting the dissolution rate of fly ash, the reaction products of AAFA, based on the results of the thermodynamic modeling in Chapter 6, were also integrated into the extended GeoMicro3D model to simulate the reaction process and 3D microstructural evolution of AAFA. The physically adsorbed water in C-(N-)A-S-H gel and N-(C-)A-S-H gel, as discussed in Chapter 6 (see Section 6.3.5.1), were also incorporated in GeoMicro3D. Considering the limitation of thermodynamic modeling applied to the silicate-activated fly ash as shown in Chapter 6, the extended GeoMicro3D model was only applied to simulate the sodium hydroxide-activated system (sample NH-40˚C) in this work. According to its mixture (see Table 6.2), the initial structure was generated in a cube of 125 µm × 125 µm × 125 µm, as shown in Figure 7.5. The resolution was set at 1 µm × 1 µm × 1 µm per voxel. More specifically, the simulation box contains 125 × 125 × 125 voxels, with each voxel occupied by fly ash or alkaline solution. As recommended in [226], the size of the simulation box should be at least 2.5 times larger than the largest particle. Hence, the minimum and maximum particle size of fly ash was set at 1 µm and 50 µm, respectively. The model parameters outlined in Section 7.3.1.2 for the dissolution module were also adopted here. In addition, C-(N-)A-S-H gel and N-(C-)A-S-H gel were considered as diffusive phases for ions, while the other reaction products were treated as non-diffusive for ions. The diffusivities of ions through the C-(N-)A-S-H gel and N-(C-)A-S-H gel were set to be 0.0025 times those in the solution (see Table 7.2) [33]. A detailed description of diffusivity of ions through lattice nodes can be found in [33]. The simulation input and parameters used in the extended GeoMicro3D to model the reaction and microstructure of AAFA are summarized in Table 7.3.

Table 7.3 Simulation input and parameters.

Input	Mixture	Sample NH in Table 6.2
	Temperature	40 ˚C
	Simulation size	125 μm × 125 μm × 125 μm
Dissolution module	Dissolution rate of fly ash	Equations 7.8, 7.9, 7.10, 7.27, 7.29
	Relative dissolution rate f_X for Mg in Equation 7.10	0.8
	Relative dissolution rate f_X for K in Equation 7.10	1.2
	Relative dissolution rate f_X for Na in Equation 7.10	1.2
	Relative dissolution rate f_{Fe} in Equation 7.10	0.2
	$F_{Si,non-steady}$	3
	K_{sp} of SiO_2 (in Equation 7.6)	1.23×10^{2}
	$K_{sp}$of CaO (in Equation 7.6)	3.55
	K_{sp} of Al_2O_3 (in Equation 7.6)	2.1×10^{-1}
	Activation energy of CaO (in Equation 7.15)	13.6 kJ/mol
Transportation module	Diffusivity of aqueous ions in solution (D_p)	Table 7.2
	Diffusivities of aqueous ions in gels	0.0025× D_p
Nucleation and growth module	Parameters A and B (in Equation 7.23)	Same in [40]
Thermodynamic modeling module	Thermodynamic database of reaction products	N-(C-)A-S-H gel in Table 5.3, zeolites [124], Cemdata18 [32]
Others	Physically adsorbed water in C-(N-)A-S-H gel	Same in [40]
	Physically adsorbed water in N-(C-)A-S-H gel	11-15 wt. % of N-(C-)A-S-H gel*

*: The total fraction of physically adsorbed water in N-(C-)A-S-H gel in this work was determined based on the mass loss between 40-105 °C in TGA results (refer to Figure 4.6 and 4.10).

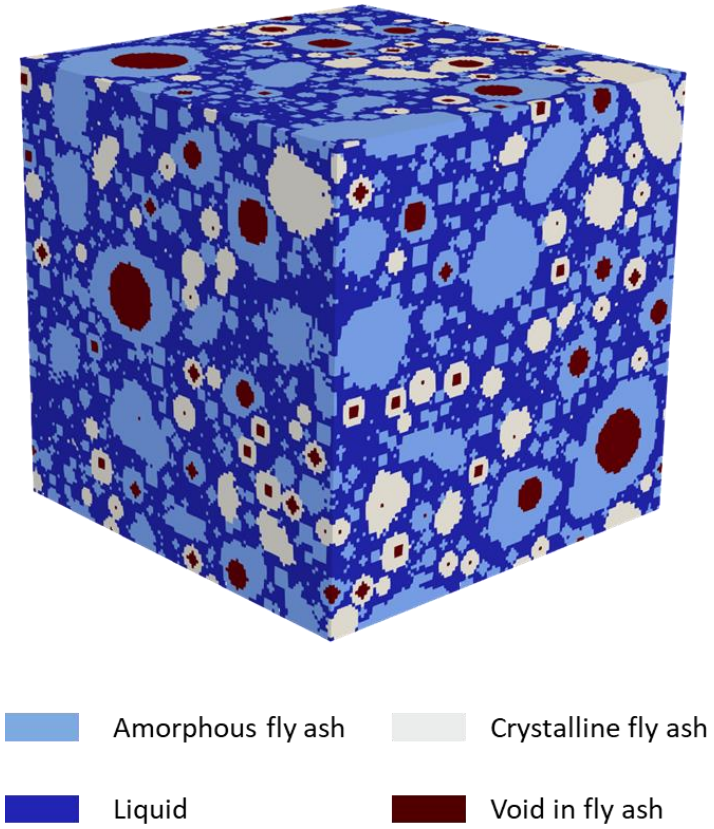

Figure 7.5 Initial structure of sample NH-40˚C with a size of 125 µm × 125 µm × 125 µm and a digitization resolution of 1 µm × 1 µm × 1 µm per voxel.

7.4 Experimental and simulated dissolution of fly ash

7.4.1 Experimental dissolution of fly ash under different conditions

To gain an understanding of the dissolution behavior of fly ash in an alkaline solution, the concentrations of Si and Al were measured from the early stages (5 minutes) to long-term stages (48 hours) for dissolution of fly ash in a 1.5M NaOH solution at 20 ˚C, as illustrated in Figure 7.6. The data clearly show a non-linear increase in Si and Al concentrations within the initial 6 hours, followed by a subsequent linear rise from 6 to 48 hours. The dissolution behavior of silicate glass under a far-from-equilibrium condition commonly involves two stages: the non-steady state and the steady state [59,65,67]. In this work, the non-linear stage from 0-6 hours is referred to as the non-steady state, indicating a varying dissolution rate, while the subsequent linear stage is considered the steady state, indicating a constant dissolution rate. To investigate forward dissolution rate r_+ in the steady state, the elemental concentrations were specifically examined from 6 to 48 hours under various pH and temperatures, as detailed below.

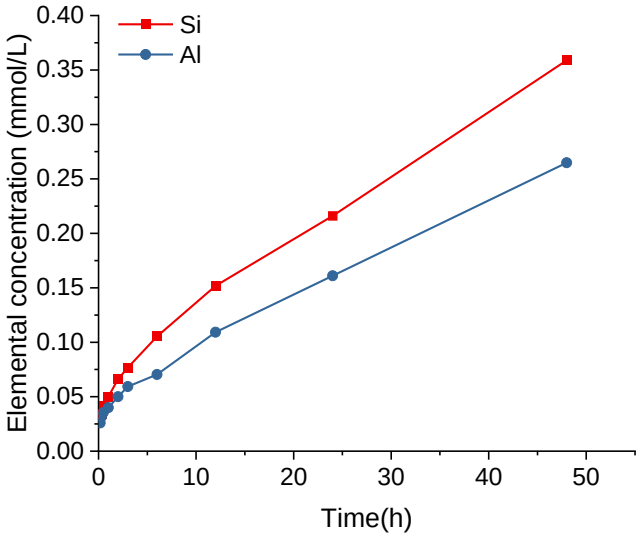

Figure 7.6 Measured concentrations of Si and Al for the dissolution of fly ash in a 1.5M NaOH solution at 20 ˚C.

The effects of the solution pH and the temperature on the dissolution of fly ash are shown in Figure 7.7. At 20 ˚C, the concentrations of Si and Al exhibited a linear correlation with time from 6 to 48 hours, albeit with a slight deviation from linearity observed at the 6-hour mark (see Figure 7.7(a) and (b)). This observation suggests that the transition from a non-steady state to a steady state occurs within the 6 to 12-hour range, irrespective of the solution's alkalinity. A similar observation was found in the dissolution at 40 ˚C. However, at 60 ˚C the dissolution rate for both Si and Al did not remain constant but dropped after 24 hours, as shown in Figure 7.7(c) and (d), indicating the end of the steady state. The decrease in the dissolution rate suggests that the dissolution had shifted away from a far-from-equilibrium state. This change is due to the dramatic increase in ion concentration, and thus the ion activity product, over time at 60 ˚C. As a result, after 24 hours of dissolution at 60 ˚C, the ion activity product became large enough to negatively impact the dissolution rate according to Equation 7.6, leading to a decrease in the dissolution rate. Overall, a steady state is consistently observed during dissolution, regardless of the solution pH and the temperature.

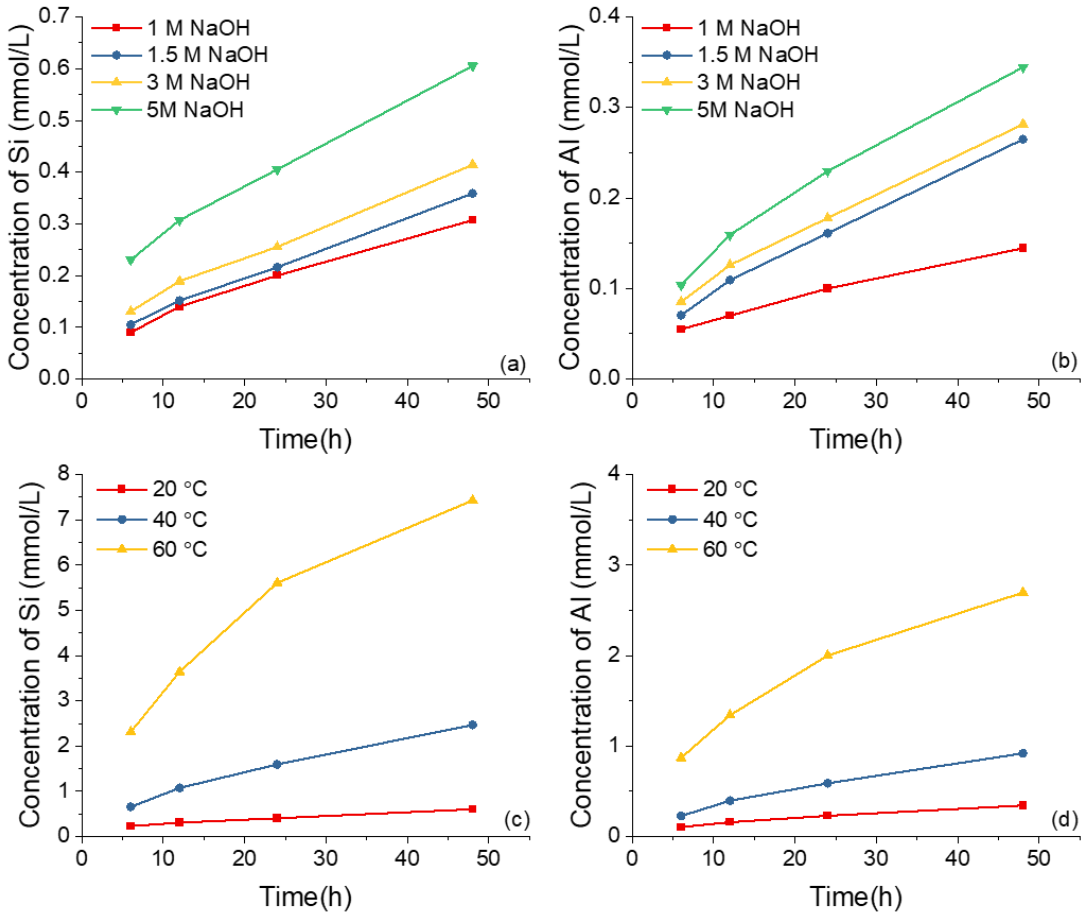

Figure 7.7 Measured concentrations of (a) Si and (b) Al for the dissolution of fly ash under different pH conditions at 20 ˚C; Measured concentrations of (c) Si and (d) Al for the dissolution of fly ash at different temperatures.

7.4.2 Forward dissolution rate of fly ash

According to the evolution of elemental concentrations in the steady state measured above, the forward dissolution rate of Si ($r_{+,Si}$) at different solution pH and temperatures can be calculated using Equation 7.25.

To fit η, E_a and k_0 in Equation 7.24, the equation was rearranged to a linear relationship as follows:

$$log\ r_+ = \eta * pH - E_a \frac{\log e}{R * T} + log\ k_0 \tag{7.28}$$

Figure 7.8 shows the fitting results for the parameters (η, E_a and k_0) in Equation 7.28. The relationship between pH of the solution and $log\ r_{+,Si}$ was plotted and fitted in Figure 7.8(a). The log forward dissolution rate of Si has a linear relationship with the pH values, with a fitting slope (η) of 0.4. For a constant pH of 14.7, the correlation between the log dissolution

rate of Si and temperature was fitted in Figure 7.8(b). According to the fitting results ($E_a \frac{\log e}{R}$=3157), the apparent activation energy E_a in Equation 7.28 was determined as 60.41 kJ/mol, which is in good agreement with the data obtained in [19]. The parameter k_0 is supposed to be linked to intrinsic properties of silicate glasses. With the determined $log\ r_{+,Si}$, η and E_a, $log\ k_0$ can be calculated using Equation 7.28. An index, Ca/(Si+Al) molar ratio, is proposed to represent glass reactivity. Since Ca acts as a network modifier, while Si and Al usually function as network formers, a higher Ca/(Si+Al) refers to a higher reactivity of an aluminosilicate glass. The correlation between $log\ k_0$ and Ca/(Si+Al) of glasses, including fly ash in this study and glasses from [59,223,227], are plotted in Figure 7.8(c). The dissolution conditions and forward dissolution rate of the glasses from [59,223,227] are provided in Table D.1 in Appendix D. A linear increase in $log\ k_0$ is observed with increasing Ca/(Si+Al), indicating more rapid dissolution in fly ash with higher reactivity.

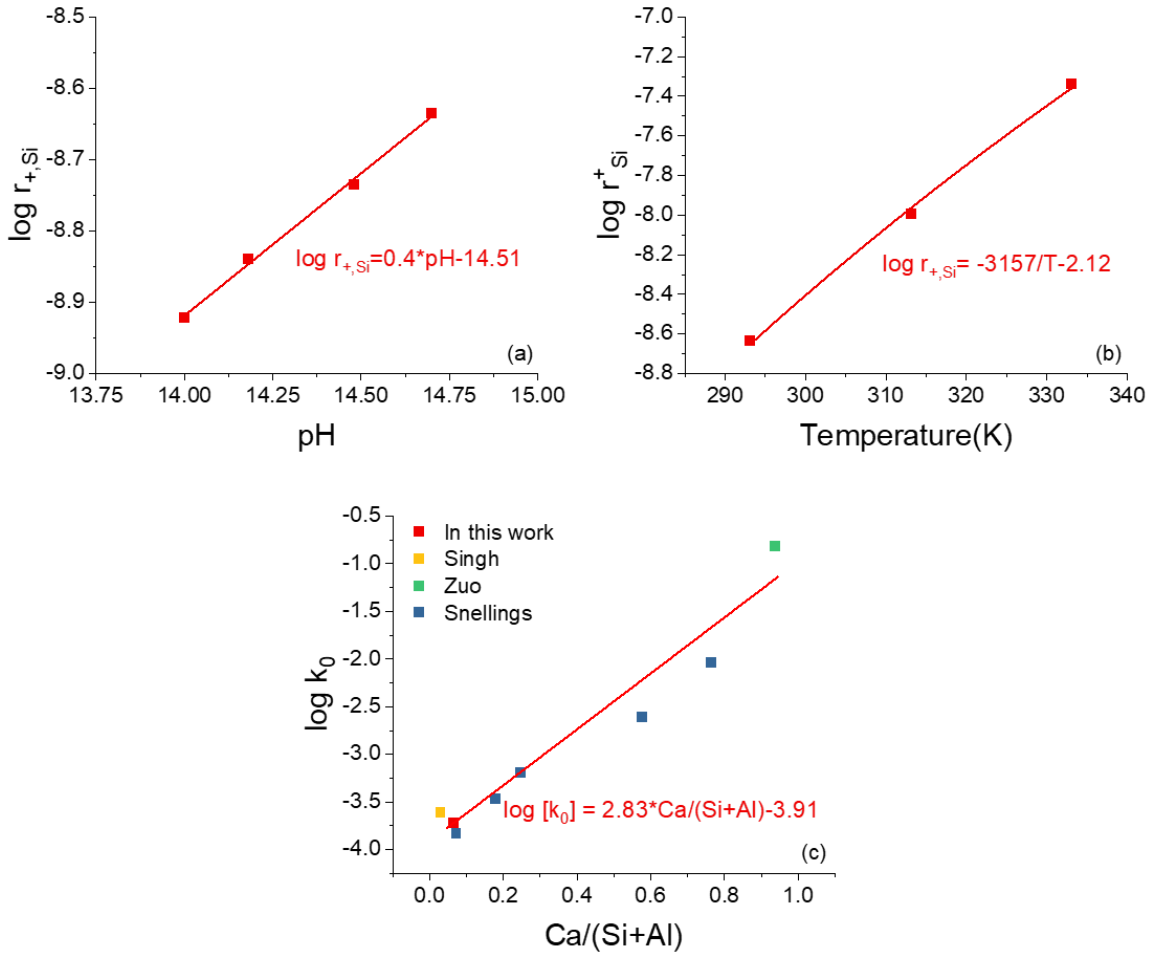

Figure 7.8 Forward dissolution rate of Si as a function of (a) pH and (b) temperature; (c) relationship between log k_0 and Ca/(Si+Al) molar ratio in glass. Part of data is obtained from Singh [227]*, Zuo* [223] *and Snellings [59].*

According to the fitting results shown in Figure 7.8, the general function describing the forward dissolution rate of Si (mol/m^2/s) can be expressed as follows:

$$log\ r_{+,Si} = 0.4 * pH - \frac{3157}{T} + 2.83 * \frac{Ca}{Si + Al} - 3.91 \quad (7.29)$$

Based on the theory of stoichiometric dissolution [59,68], the forward dissolution rate of Al was predicted by using Equation 7.9.

To evaluate the accuracy of these prediction functions, Figure 7.9 illustrates the correlation between the predicted and experimental log forward dissolution rates of Si and Al. Notably, in Figure 7.9(a), Equation 7.29 demonstrates a precise prediction of the forward dissolution rate of Si for the fly ash investigated in this work. Moreover, its applicability extends to well predicting the forward dissolution rate of Si for other aluminosilicate glasses documented in the literature [59,223,227]. The consistency between the predicted and experimental log forward dissolution rates of Al, as shown in Figure 7.9(b), affirms the rationality of predicting the dissolution rate of Al based on that of Si. In addition, the dissolution amount and dissolution rate of Ca for the dissolution of fly ash in this work are provided in Appendix D (Figure D.1 and Figure D.2). The result in Figure D.2 shows that the previously developed function (Equation 7.8) for the dissolution rate of Ca can effectively predict the dissolution rate of Ca. Consequently, the newly developed function for predicting the forward dissolution rates of Si will be seamlessly integrated into the GeoMicro3D model for its applicability in AAFA, while original functions of forward dissolution rate of Al and Ca remain unchanged.

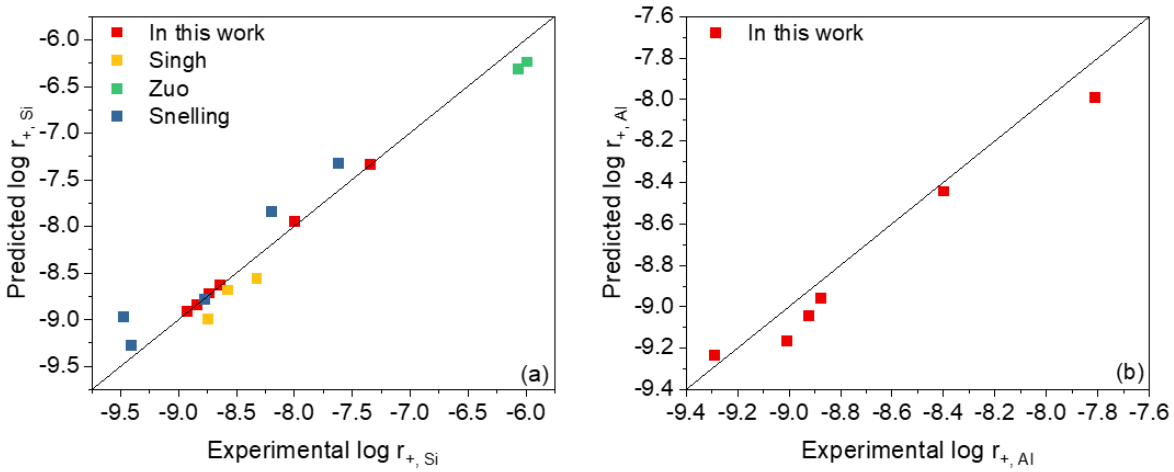

Figure 7.9 The correlation between predicted and experimental log forward dissolution rates of (a) Si, and (b) Al. Part of data is obtained from Singh [227]*, Zuo* [223] *and Snellings [59]. Note that the log forward dissolution rate from [59] has been recalculated according to Equation 7.25.*

7.4.3 Simulated dissolution of fly ash

The dissolution of fly ash in a 5M NaOH solution was simulated at different temperatures using the GeoMicro3D model modified with the developed dissolution rate functions. Figure 7.10 shows the simulated and measured concentrations of Si, Al, and Ca released from the fly ash. The simulated Si concentrations generally match the experimental results, except at 60 °C after 24 hours, where modeling concentrations are lower than the experimental ones. This discrepancy may be attributed to the slight dissolution of crystalline fly ash at high temperatures, which was considered completely inert in the simulation. Moreover, at 60 ˚C, a decrease in the dissolution rate of Si is observed after 24h in the modeling result, aligning with the experimental findings. In addition, the simulations capture well the evolution of Al and Ca concentrations, showing a good agreement with experimental data. The minor difference between the modeling and experimental Al concentrations can be attributed to slight discrepancies in the predicted and experimentally obtained dissolution rates of Al, as shown in Figure 7.9(b). Overall, the agreement between simulation and experimentally obtained results underscores the accuracy of the dissolution rate functions, affirming their capability to faithfully simulate the dissolution of fly ash in an alkaline solution.

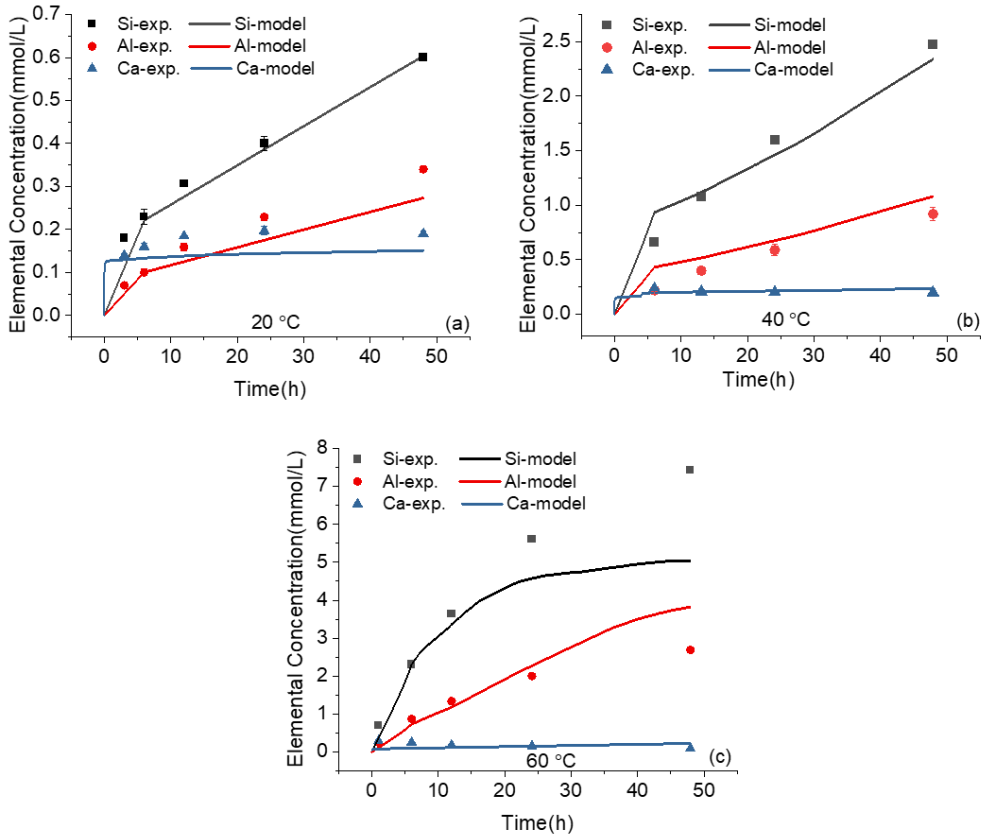

Figure 7.10 Comparison of elemental concentrations in fly ash dissolution: simulated and experimental results in a 5M NaOH solution at (a) 20 ˚C, (b) 40 ˚C and (c) 60 ˚C.

7.5 Application of extended GeoMicro3D to three-dimensional microstructure formation of AAFA

In this section, the dissolution module in the original GeoMicro3D model is equipped with the functions developed in Section 7.4 to describe the dissolution rate of fly ash, while the thermodynamic modeling module is upgraded with the thermodynamic database of reaction products of AAFA to simulate AAFA reactions. The simulation results of AAFA (for sample NH-40˚C) using the extended GeoMicro3D are presented below.

7.5.1 Simulated 3D microstructures

The simulated 3D microstructures of sample NH-40˚C at 10 mins, 3 hours, 7 days and 28 days are shown in Figure 7.11. The area in light blue and dark blue represents amorphous fly ash and alkaline activator, respectively. Upon contact with the alkaline activator, the amorphous fly ash particles underwent dissolution, forming a distinct reaction front zone (depicted in orange color). In contrast, the crystalline fly ash particles, represented by white, remained unreactive and undissolved, with no development of a reaction front zone around them. At 3 hours, a layer of reaction products, shown in red, began to form around the amorphous fly ash particles, with a few reaction products also forming on the surface of the crystalline fly ash particles due to ion transport. As the reaction proceeded, more reaction products emerged, connecting the fly ash particles to construct a solid microstructure. By 7 days, most liquid nodes were filled with reaction products as shown in Figure 7.11(c). The microstructure at 28 days, as shown in Figure 7.11(d), appeared similar to that at 7 days. One reason is that the reaction became very slow from 7 days to 28 days, which will be further discussed in Figure 7.13. Another reason is related to the way of visualization: any voxel containing partially or completely filled reaction products is marked in red, making it difficult to visualize the increase in reaction products after most liquid nodes are filled. For a more detailed understanding of the evolution of simulated microstructure, it is worthwhile to view the solid volume fraction of each voxel in the simulated box, as further shown below.

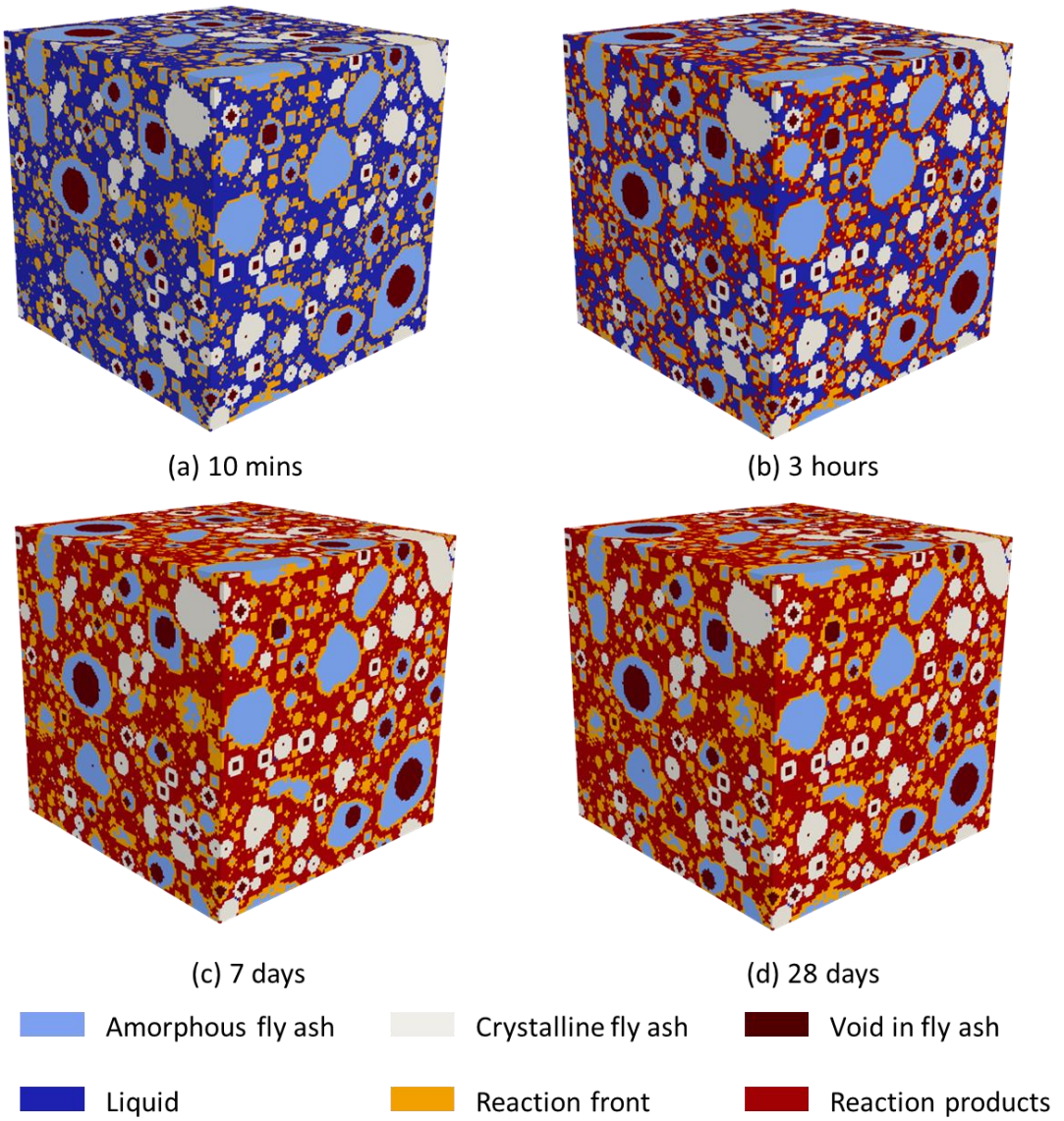

Figure 7.11 Simulated 3D microstructure of NH-40˚C at (a) 10mins, (b) 3 hours, (c) 7 days and (d) 28 days.

To help a better understanding, Figure 7.12 shows the simulated solid volume fraction of voxels in crosse-sections of sample NH-40˚C at 10 mins, 3 hours, 7 days and 28 days. In the beginning, each voxel was either occupied by fly ash (100 % solid) or liquid (0 % solid). As the reaction progressed, the solid volume fraction in the voxels around the surface of the amorphous fly ash particle decreased, indicating a dissolving fly ash. In contrast, the solid volume fraction in the voxels that were originally liquid increased, indicating the formation of reaction products. Over time, a more compact microstructure develops. Additionally, a higher fraction of reaction products accumulated around the amorphous fly ash particles, while a relatively porous structure developed within the spaces between the fly ash particles. This is in accordance with the observation from SEM images (see Figure 6.7).

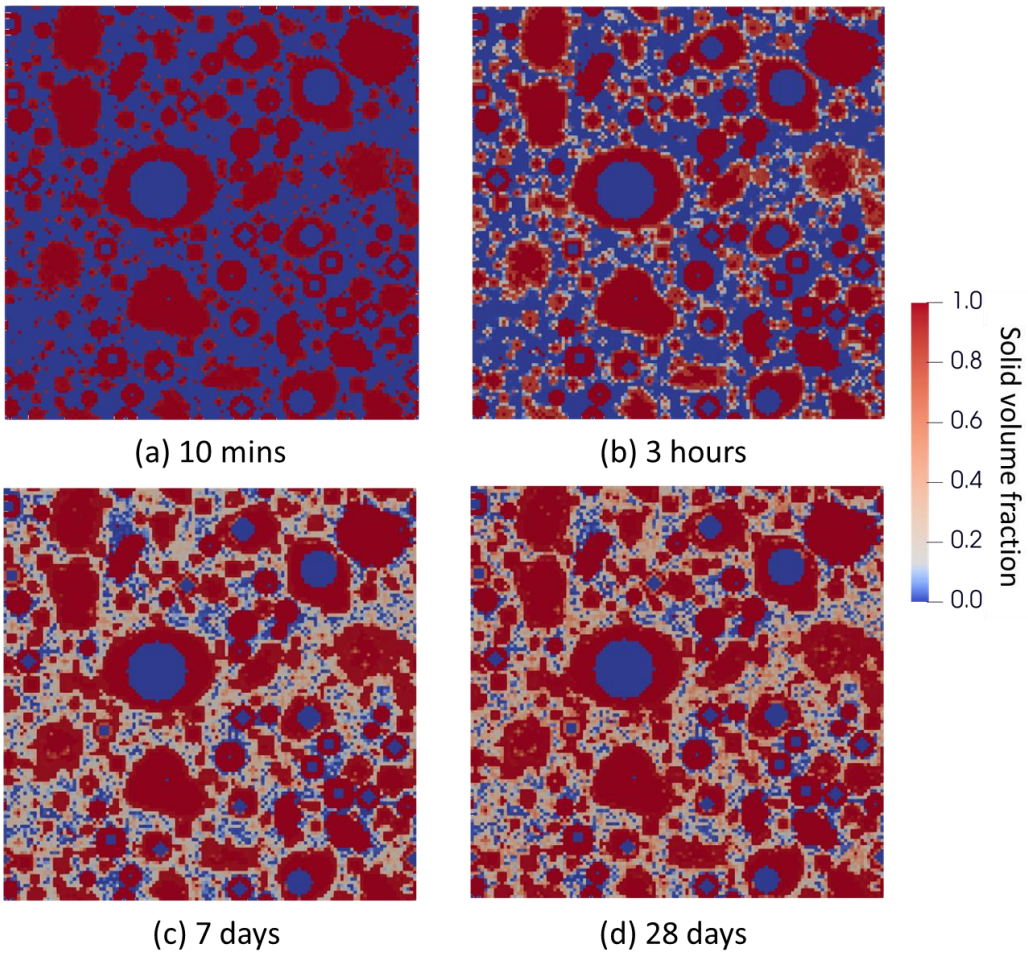

Figure 7.12 Solid volume fraction of voxels of cross sections of AAFA at (a) 10 mins, (b) 3 hours, (c) 7 days and (d) 28 days.

7.5.2 Degree of reaction

The simulated degree of reaction of fly ash as a function of time is shown in Figure 7.13, alongside the experimental data at 7 and 28 days (see Figure 6.13). The degree of reaction of fly ash increased significantly within the first day, followed by a gradual rise subsequently. This trend indicates an initial rapid dissolution of fly ash, which slowed down over time. Initially, fly ash dissolved quickly in the high-pH alkaline solution. However, the dissolution rate of fly ash decreased significantly over time due to two main reasons. First, the pH of the pore solution decreased a lot over time as a result of the reaction between the activator and fly ash, as confirmed in Figure 7.15. Second, the growth of reaction products on the surface of fly ash (see Figure 7.11) hindered further interaction between the activator and fly ash, thereby slowing down the dissolution process. The simulated degree of reaction reached 31 % and 34 % at 7 and 28 days, respectively, slightly lower than the experimental data. The consistency between the simulated and experimental degree of reaction implies that the simulation framework can effectively model the chemical reactions in AAFA.

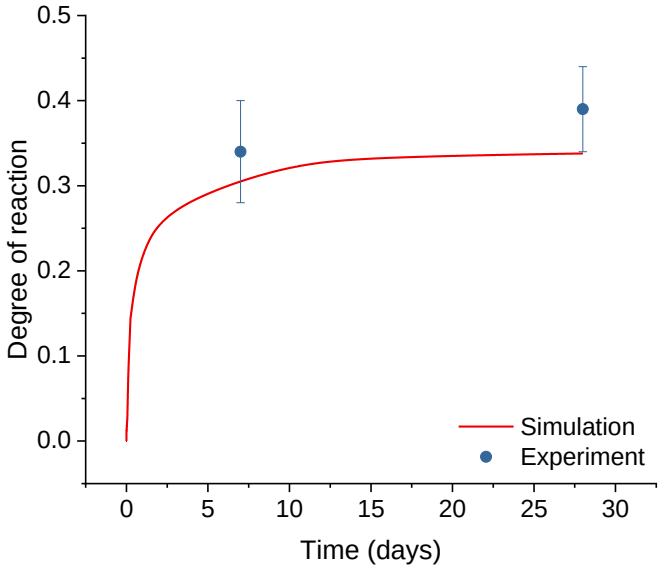

Figure 7.13 Simulated degree of reaction of fly ash at 40˚C.

7.5.3 Phases assemblage

The evolution of simulated phases in AAFA is presented in Figure 7.14. The main simulated reaction product of AAFA was N-(C-)A-S-H gel, which is consistent with both the experimental findings in this work and existing literature [21,89]. Minor amounts of C-(N-)A-S-H gel and hydroxysodalite (SOD(OH)) were observed, in accordance with the thermodynamic modeling results in Chapter 6. Besides, a trace amount of portlandite, hydrotalcite (MgAl-OH-LDH), magnesium silicates hydrate (M-S-H), Brucite ($Mg(OH)_2$) and Ferrihydrite-mc (FeOOH) were also formed, collectively presented as the 'other phases' in Figure 7.14. These reaction products align with the thermodynamic modeling results, except for portlandite and MgAl-OH-LDH. The variance in reaction products obtained by thermodynamic modeling and GeoMicro3D model can be attributed to the differences in reaction kinetics. More specifically, thermodynamic modeling was based on the congruent dissolution of various oxides in fly ash, whereas GeoMicro3D assigned a specific function of dissolution rate for each oxide. As a result, the chemistry in the pore solution may differ in these two cases, leading to the formation of distinct reaction products. Besides, the physically adsorbed water of C-(N-)A-S-H gel and N-(C-)A-S-H gel was considered in GeoMicro3D, which is another difference to the thermodynamic modeling results.

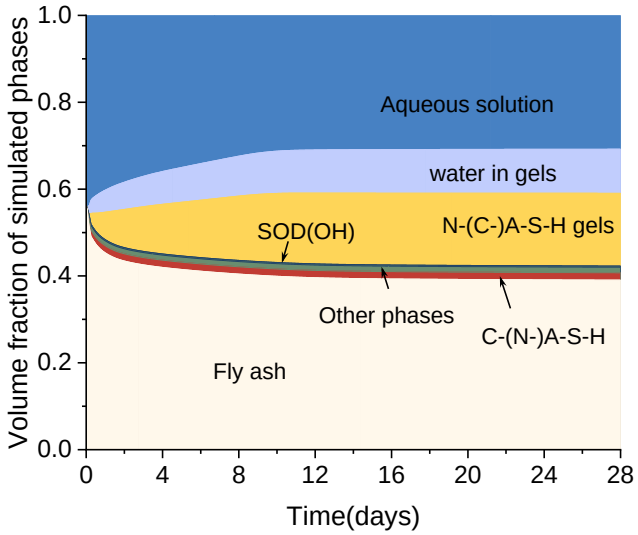

Figure 7.14 Phase evolution of simulated phases in AAFA at 40˚C. The label 'Other phases' refers to MgAl-OH-LDH (LDH denotes layered double hydroxide), M-S-H (magnesium silicates hydrate), Brucite ($Mg(OH)_2$), Portlandite ($Ca(OH)_2$) and Ferrihydrite-mc (FeOOH). The label 'water in gels' refers to the physically adsorbed water in C-(N-)A-S-H gel and N-(C-)A-S-H gel.

7.5.4 Pore solution chemistry

The evolution of simulated elemental concentrations is shown in Figure 7.15, alongside the experimental data at 7 and 28 days (see Figure 6.11). The concentration of Si initially increased with time, followed by a decrease after 2 days. This trend matches well with the experimental observations as shown in Figure 6.11. During the early simulation period, the reaction was dominated by the dissolution of fly ash, while the formation of reaction products prevailed once a sufficient quantity of ions dissolved in the pore solution. The competition between the dissolution and the formation of reaction products leads to the initial increase and subsequent decrease in the concentration of Si in the pore solution. However, the simulated Si concentration was underestimated compared to experimental data, especially at 28 days. This discrepancy may stem from the underestimated reaction degree (see Figure 7.13). Additionally, the GeoMicro3D model assumes that voids created by chemical shrinkage are automatically filled with water, which could further contribute to the underestimation of Si concentration in the pore solution.

Similarly, the concentration of Al initially paralleled the trend observed for Si but dropped much earlier, which occurred after a few hours, coinciding with the formation of N-(C-)A-S-H gel as can be seen in Figure 7.14. The simulated concentration of Al at 7 days is close to the experimental data. However, after 9 days, the concentration of Al increased slightly again while the concentration of Si started to decline. As a result, the simulated concentration of Al at 28 days is higher than the experimental result. It can be seen from Figure 7.15(a) that there were no sufficient Si ions in the pore solution. As a result, the formation of reaction

products, i.e. N-(C-)A-S-H gel, was limited, leading to the increase of Al concentration due to the ongoing dissolution of fly ash.

Apart from a slight initial increase due to the dissolution of fly ash, the Na concentration mainly decreased over time, resulting from the formation of C-(N-)A-S-H gel, SOD(OH) and N-(C-)A-S-H gel. The concentration of OH^- experienced a dramatic decrease and remained relatively stable after 2 days. The drop in the concentration of OH^- can be attributed to the consumption of OH^- during the dissolution of fly ash. Both simulated concentrations of Na and OH^- were close to the experimental results at 7 days and 28 days.

Both Ca and Mg concentrations rose sharply in the beginning due to their rapid dissolution rates, followed by a sudden drop due to the rapid formation of Ca- and Mg-containing phases. After that, their concentrations remained at an extremely low level, consistent with the thermodynamic modeling results shown in Figure 6.17. The trends observed in the concentrations of Fe and K are also similar to the thermodynamic modeling results shown in Figure 6.17. The overestimation of the simulated concentration of K is due to the absence of a solid K-containing phase in the model, as also discussed in Section 6.3.5.2. Consequently, all dissolved K remains in the aqueous phase, resulting in an overestimation of its concentration.

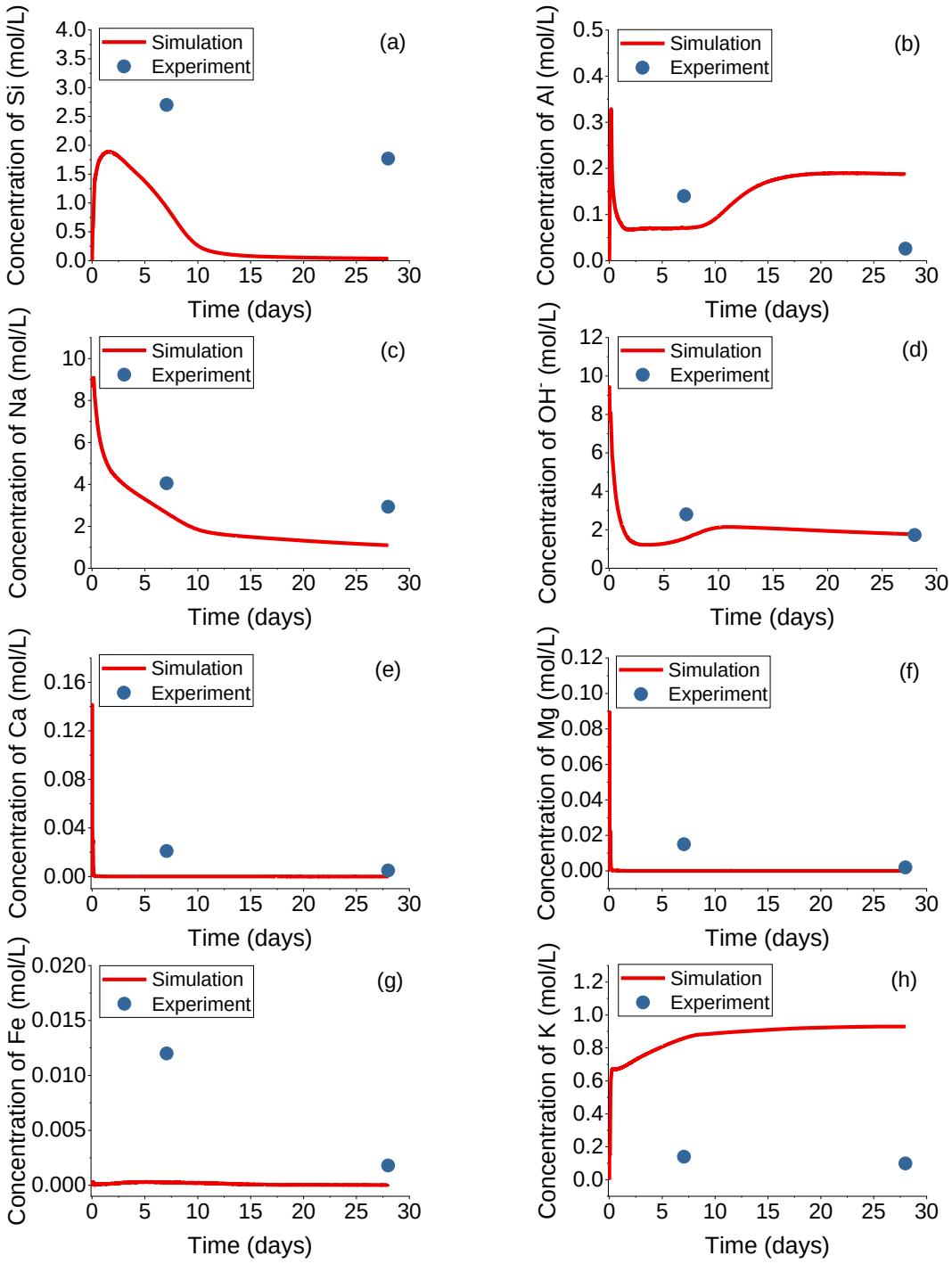

Figure 7.15 Simulated element concentrations in comparison with the experimental data.

Table 7.4 Comparison of the porosity of AAFA obtained from simulation and experiment.

Porosity	GeoMicro3D	Experiment*
NH-40°C at 7 days	38 %	37 %
NH-40°C at 28 days	35 %	34 %

* The porosity of AAFA paste in this work was measured by using mercury intrusion porosimetry (MIP) according to the procedure in [228].

7.5.5 Porosity of AAFA

Table 7.4 compares the porosity of sample NH-40°C obtained from simulation and experiment, i.e. mercury intrusion porosimetry (MIP). The porosity obtained by using MIP at 7 days and 28 days was 37 % and 34 %, respectively. These results were in good agreement with the porosity of the sample 'FA_N9.3S0T40' in [33], which employed an identical mixture. In the simulation, the porosity of the simulated structure was defined as the sum of the volume fraction of the aqueous phase (see Figure 7.14) and the hollow voids in fly ash. As shown in Table 7.4, there is a good agreement between the simulated porosity and experimental results.

7.6 Conclusions

This chapter developed a prediction function of dissolution rate for fly ash dissolving in alkaline solution. GeoMicro3D model was extended with the dissolution rate function and the thermodynamic database of N-(C-)A-S-H gel to simulate the reactions and microstructure of AAFA paste. From the results and discussion, the following remarks are made:

1. A dissolution rate prediction function, accounting for pH, temperature, and fly ash reactivity, was developed. This function demonstrates accurate predictions of the dissolution rates for various aluminosilicate glasses
2. Equipped with the newly developed prediction function, the updated GeoMicro3D model successfully simulated the dissolution behavior of fly ash in alkaline solution at different temperatures. The simulated evolution of the concentrations of Si, Al and Ca match well with the experimental data.
3. Integrated with the thermodynamic database of N-(C-)A-S-H gel, the GeoMicro3D model is expanded to simulate 3D microstructure of AAFA paste. For the first time, the distribution of different phases in the 3D microstructure of AAFA can be modeled as a function of time. The simulated degree of reaction and the porosity are consistent with the experimental results. Moreover, the simulated reaction products and pore solution chemistry were also in line with the experimental results. The reason for the minor differences between the simulation and experimental results were analyzed. Overall, the extended GeoMicro3D model is able to accurately simulate the chemical reactions and 3D microstructure of NaOH-based activated fly ash paste.

Chapter 8

Retrospection, conclusions, contributions and outlooks

8.1 Retrospection

Alkali-activated fly ash (AAFA) has stood out as a sustainable cement-free binder, appealing for its low carbon emissions and excellent engineering properties with proper mixtures. However, as pointed out in Chapter 1, the reactions of AAFA are governed by a series of factors, including the intrinsic properties of fly ash, the types of alkaline activators, the mixture and curing regime. As a result, the microstructure of AAFA displays considerable diversity, leading to a wide range of engineering properties. Prediction of the reactions and microstructure of AAFA is essential for designing AAFA with the desired performance. Therefore, this research aims to simulate the reaction process and development of the microstructure of AAFA.

In Chapter 3, the polymerization process of AAFA was modeled by reactive molecular dynamics simulation to construct the models of the main reaction product of AAFA, i.e. N-(C-)A-S-H gel. The Si/Al and Ca/Al ratios of N-(C-)A-S-H gels were investigated to explore the possible chemical compositions of N-(C-)A-S-H gels. The atomic structures of N-(C-)A-S-H gels were also characterized in terms of bond length, bond angle, XRD analysis, Q^n distribution.

In Chapter 4, N-(C-)A-S-H gels with various Si/Al and Ca/Al ratios, according to the findings in Chapter 3, were synthesized using the sol-gel method. Different mixtures and conditions were explored to achieve target ratios, and an optimal synthesis route for N-(C-)A-S-H gels was proposed. Characterization of the synthesized gels involved XRF, XRD, FTIR, and TGA techniques, with a comparative analysis against simulation results from Chapter 3.

In Chapter 5, the solubility of the N-(C-)A-S-H gels synthesized in chapter 4 was measured through a dissolution test. Other thermodynamic data of N-(C-)A-S-H gels, including the Gibbs free energy, heat capacity, entropy, enthalpy, and molar volume, was also determined to establish a thermodynamic database of N-(C-)A-S-H gels. The reliability of the thermodynamic data was confirmed by the good agreement between the experimentally derived solubilities of N-(C-)A-S-H gels and those estimated from thermodynamic data.

In Chapter 6, the reaction kinetics of AAFA was derived from results obtained from isothermal calorimetry and SEM-EDS analysis. With the thermodynamic database of N-(C-)A-S-H gels developed in Chapter 5, thermodynamic modeling of AAFA, in combination with the reaction kinetics, was performed to investigate the chemical reactions and the phase assemblage of AAFA over time. The reliability of the thermodynamic modeling is assessed by comparing results with experimental data obtained from AAFA paste.

In Chapter 7, the dissolution kinetics of fly ash was investigated through the dissolution of fly ash in sodium hydroxide solution with various concentrations at different temperatures. Prediction functions for the dissolution rate of Si and Al were developed to describe the dissolution of fly ash in alkaline solutions. The GeoMicro3D model, extended with these functions and the thermodynamic database of N-(C-)A-S-H gels, was employed to simulate the chemical reaction and 3D microstructure evolution of AAFA. The simulation results were analyzed and validated through comparisons with experimental findings.

8.2 Conclusions

The conclusions of this research are summarized as follows:

(1) Molecular dynamics simulation enables to explore the possible chemical compositions of the main reaction product of AAFA, i.e. N-(C-)A-S-H gels.

N-(C-)A-S-H model can be constructed by modeling the polymerization process using molecular dynamics simulation, thereby exploring its possible chemical composition. The Si/Al ratio in the N-A-S-H gel model mainly varied from 1 to 3, with a tendency for Ca incorporation into the N-A-S-H gel, resulting in the formation of N-(C-)A-S-H gel. This research suggests that a Si/Al ratio between 1 and 3 and a Ca/Al ratio ranging from 0 to 0.5 adequately represent the chemical compositions of N-(C-)A-S-H gel in a mature AAFA paste.

(2) When using the sol-gel method to synthesize N-(C-)A-S-H gel, three main factors influence the Si/Al ratio of the resulting gel: the initial Si/Al ratio, the concentration of the reactants, and the pH values.

It is found that higher concentrations of reactants, a higher initial Si/Al ratio, or a lower pH value can all contribute to the synthesis of N-(C-)A-S-H gels with a higher Si/Al ratio.

(3) Both molecular dynamic simulation results and experimental findings on AAFA pastes showed that the formation of N-A-S-H gel with a Si/Al ratio higher than 3 is unfavored.

Molecular dynamics simulation results showed that the Si/Al ratios in the constructed N-A-S-H model consistently remained below 3, regardless of employing an initial Si/Al ranging from 1-4. In addition, in the sodium hydroxide-activated fly ash paste, the average Si/Al ratio of the reaction products was consistently less than 3. In the sodium silicate-activated system, although initially slightly higher than 3, the Si/Al ratio decreased over time. Thermodynamic modeling results also observed a trace amount of N-A-S-H gel with a Si/Al of 3 formed in AAFA paste. On an atomic scale, this phenomenon can be ascribed to the lower formation energy of Si-O-Al compared to Si-O-Si bonds. From a thermodynamic perspective, N-A-S-H gel with a higher Si/Al ratio has a higher solubility, indicating its formation is thermodynamically less favored.

(4) The established thermodynamics database of N-(C-)A-S-H gel enable to perform thermodynamics modeling of AAFA.

A thermodynamics database of N-(C-)A-S-H gel with various Si/Al and Ca/Al ratios was developed. The evolution of phase assemblage and chemical compositions in the pore solution of AAFA can be simulated via thermodynamics modeling of AAFA. The simulation results were in good agreement with the experimental data, especially for the sodium hydroxide-activated system.

(5) The dissolution rate of fly ash can be calculated if the Ca/(Si+Al) ratio in amorphous fly ash, pH of the solution and temperature are available.

A universal prediction function has been developed to describe the dissolution rate of Si in fly ash, taking into account the intrinsic characteristics of fly ash, solution pH, and temperature. The dissolution rate of Al exhibited a stoichiometric proportionality to that of Si. A comparison between experimental data and prediction results affirmed the accuracy of the proposed prediction functions in describing the dissolution behavior of most aluminosilicate glass, especially those with low Ca content.

(6) The extended GeoMicro3D model can simulate the reaction and 3D microstructure evolution of sodium hydroxide-activated fly ash accurately.

Through integration of the dissolution rate function of fly ash and thermodynamics database of N-(C-)A-S-H gel, the functionality of GeoMicro3D model was expanded to simulate the reaction and 3D microstructure evolution of sodium hydroxide activated fly ash. This model is able to simulate the distribution of phases in a 3D microstructure, reaction degree of fly ash, pore solution chemistry and porosity as a function of time. A case study showed that the simulation results of the sodium hydroxide-activated system matched well with the corresponding experimental data.

8.3 Contributions of this research

The contributions of this research to science and the engineering application of AAFA are summarized as follows:

(1) In the constructed N-(C-)A-S-H gel model, both pentacoordinated Al and six-coordinated Al were identified. This discovery significantly reinforces the revised perspective that Al^5 and Al^6 present in AAFA paste originate not only from raw materials but also from the reaction product. This finding contributes to a deeper understanding of the atomic structure of N-(C-)A-S-H gel.

(2) A procedure for synthesizing N-(C-)A-S-H gel with target chemical composition was proposed based on sol-gel method. The effects of the initial Si/Al ratio, concentration and pH of the reactants on the resulting Si/Al ratio in the obtained N-(C-)A-S-H gel were clarified. The successful synthesis of N-(C-)A-S-H gel with a Si/Al ratio up to 3 addresses a notable gap in the existing literature.

(3) A thermodynamic dataset of N-(C-)A-S-H gel with various Si/Al and Ca/Al ratios was developed, enriching the current thermodynamic database of alkali-activated materials. Incorporating this thermodynamic dataset to existing thermodynamic softwares, like GEMS, could help the potential user to simulate the chemical reaction of AAFA and analogous low-Ca alkali-activated materials.

(4) A dissolution rate function (developed in Chapter 7) was formulated to describe the dissolution behavior of fly ash in an alkaline solution across various temperatures. Notably, this function demonstrates universality by effectively predicting the dissolution rates of numerous aluminosilicate glasses.

(5) The GeoMicro3D model was expanded to simulate the reaction process and 3D microstructural development of AAFA. As the sole available tool for simulating the 3D microstructure of AAFA, this model lays the groundwork for further simulating the engineering properties of AAFA, contributing to the computation material science of AAFA-based concrete.

(6) The developed numerical model can help industries to deal with fly ashes of various qualities and tailor AAFA to meet specific engineering requirements. This capability promotes the use of fly ash and the application of AAFA. Consequently, it broadens the range of usable materials and enhances the sustainability of construction materials.

8.4 Outlooks – Recommendations for future research

The key aspects that are worth further study are outlined as follows:

(1) Improvement of the thermodynamic database of N-(C-)A-S-H gel

The current solubility data for N-(C-)A-S-H gel is based on samples synthesized for just 1 day. The impact of synthesis time on the solubility of N-(C-)A-S-H gel needs to be thoroughly investigated. Additionally, the existing thermodynamic database for N-(C-)A-S-H gel includes Si/Al ratios ranging from 1 to 3. This range is based on findings that the formation of N-A-S-H gel with a Si/Al ratio above 3 is unfavorable. However, the incorporation of Ca may enhance the stability of N-C-A-S-H gel, potentially leading to the formation of gels with higher Si/Al ratios. Therefore, it is recommended to study the solubility of N-C-A-S-H gel with Si/Al ratios greater than 3. Expanding the thermodynamic database in this way would improve the accuracy of thermodynamic modeling for silicate-activated fly ash.

(2) Selection of a suitable equation for describing the activity coefficients of the aqueous species in AAFA

The accurate description of activity coefficients for aqueous species plays a pivotal role in thermodynamic modeling. In GEMS, the extended Debye-Huckel equation is typically employed to address ionic strengths up to 1-2 molar. However, the pore solution in AAFA often exhibits significantly higher ionic strengths, ranging from 5 to 10 molar as observed in this research. The impact of this disparity on the

thermodynamic modeling results warrants further investigation. Exploring alternative equations, such as the Pitzer equation, may offer insights into enhancing the precision of thermodynamic modeling for AAFA.

(3) The dissolution rate of fly ash in the non-steady state

The dissolution of fly ash experiences a short period of a non-steady state before it reaches a steady state. The dissolution rate in the steady state can be well predicted by the functions established in this research. However, the dissolution kinetics during the non-steady state needs to be further investigated.

(4) Physically adsorbed water in N-(C-)A-S-H gel

The amounts of physically adsorbed water in N-(C-)A-S-H gel are not reported in the literature. These values can affect the volume of the liquid phase and thus the pore solution chemistry. Therefore, a quantitative investigation of physically adsorbed water in N-(C-)A-S-H gel is necessary to validate the findings presented in this study.

(5) Transportation and precipitation in the hollow voids in fly ash

Hollow voids may exist inside a fly ash particle. These voids become exposed once the particle breaks apart due to dissolution. As a result, reaction products can form inside the voids once they come into contact with an alkaline solution. However, the transportation of the aqueous species in the voids of fly ash has not been considered in GeoMicro3D. As a result, there is no formation of reaction products within these voids, highlighting a worthwhile area for future research.

(6) Simulation of silicate-activated fly ash using GeoMicro3D

While GeoMicro3D was successfully applied to sodium hydroxide-activated fly ash in this research, its application to silicate-activated fly ash still needs unexplored. After improving the thermodynamic database of N-(C-)A-S-H gel and utilizing an optimal equation for accurately describing the activity coefficients of the aqueous species (corresponding to the 1^{st} and 2^{nd} recommendations in Section 8.4), it is also worth simulating the silicate-activated fly ash using GeoMicro3D in future work.

Appendix A for Chapter 3

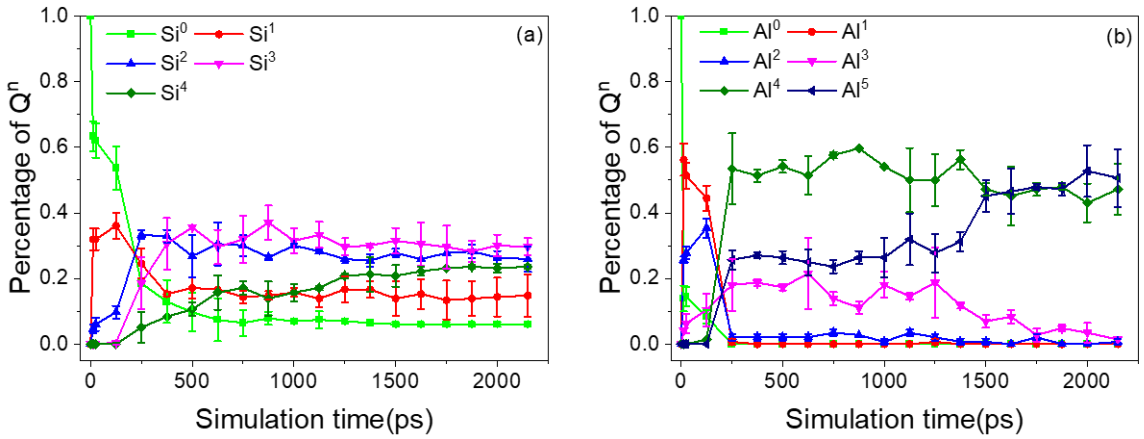

Figure A.1 Evolution of Q^n sites of Si/Al=1.5 for (a) Si sites and (b) Al sites.

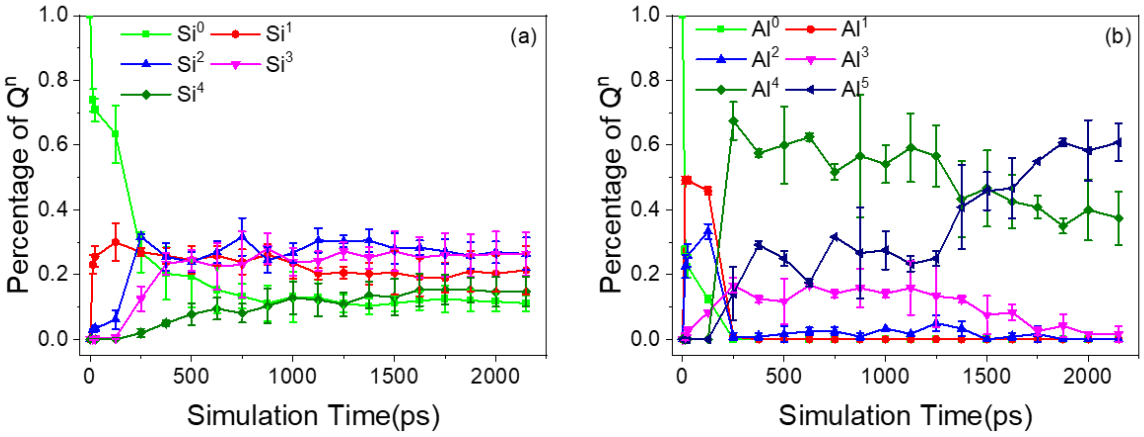

Figure A.2 Evolution of Q^n sites of Si/Al=2.0 for (a) Si sites and (b) Al sites.

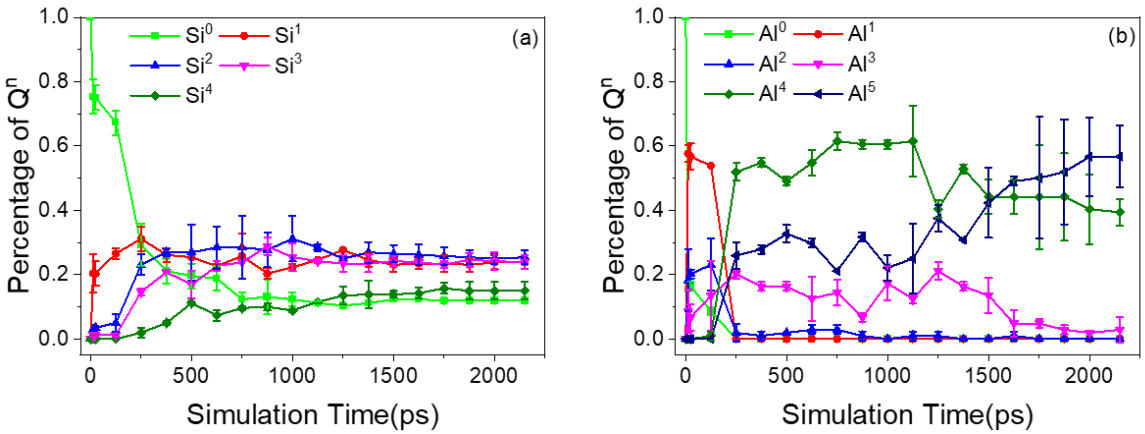

Figure A.3 Evolution of Q^n sites of Si/Al=2.5 for (a) Si sites and (b) Al sites.

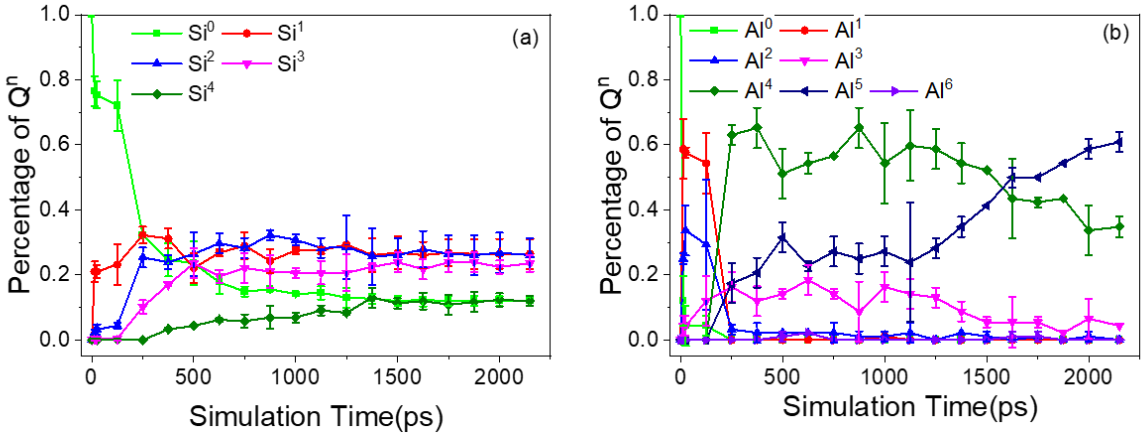

Figure A.4 Evolution of Q^n sites of Si/Al=3.0 for (a) Si sites and (b) Al sites.

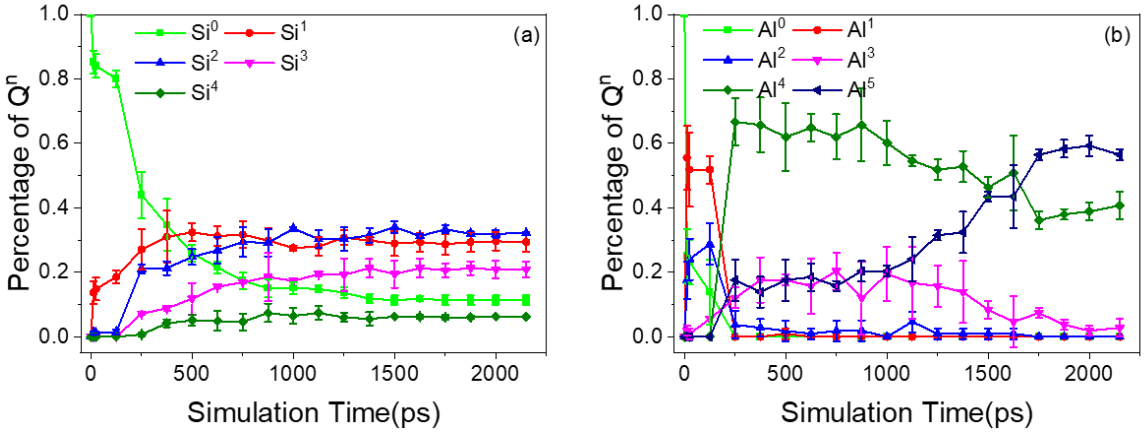

Figure A.5 Evolution of Q^n sites of Si/Al=4.0 for (a) Si sites and (b) Al sites.

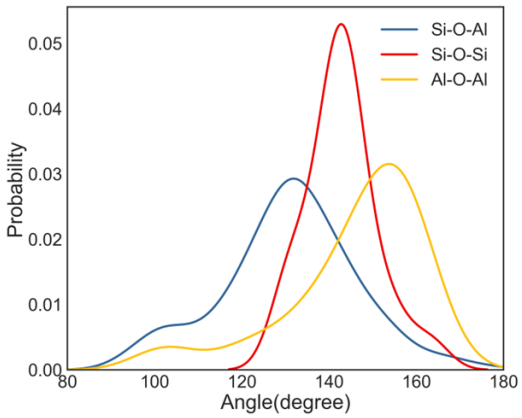

(a) Si/Al=1.5

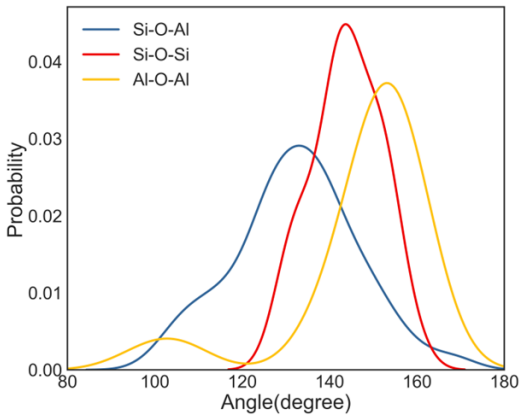

(b) Si/Al=2.0

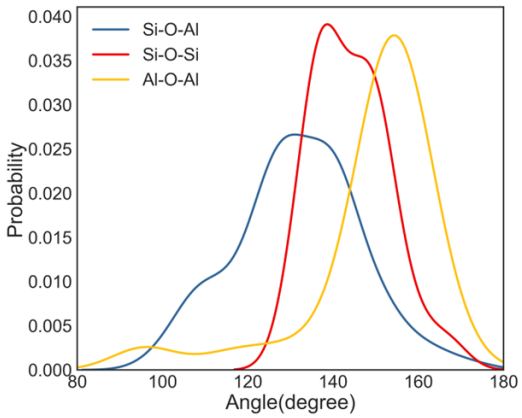

(c) Si/Al=2.5

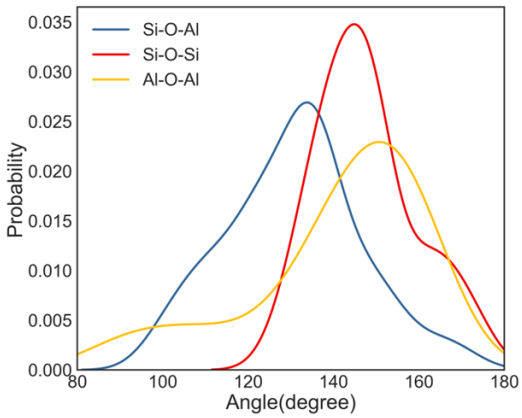

(d) Si/Al=3.0

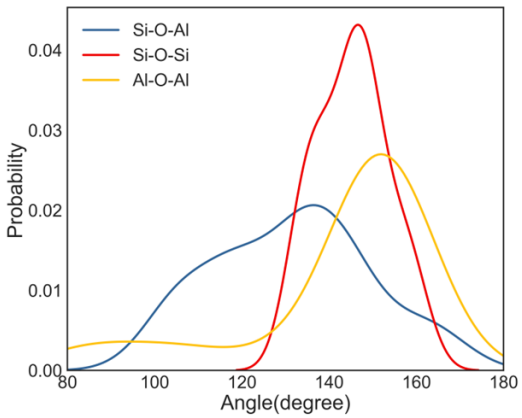

(e) Si/Al=4.0

Figure A.6 Bond angle distribution of Al-O-Al, Si-O-Al and Si-O-Si for N-A-S-H gel with a Si/Al ratio of (a) 1.5, (b) 2.0, (c) 2.5, (d) 3.0 and (e) 4.0.

Appendix B for Chapter 5

Table B.1 Thermodynamic properties of the components at 298.15 K for the additivity method.

Phase	S^0 (J/mol/K)	C_p^0 (J/mol/K)	V^0 (cm^3/mol)	ref
Faujasite(Y) $Na_2Al_2Si_4O_{12}{\cdot}8H_2O$	734	739	282.94	[124]
NaOH	64.4	59.5	18.78	[229,230]
SiO_2	41.3	44.5	7.76	[121,230]
CaO	39.7	42.8	18.41	[121,230]
Zeolitic H_2O	59	47.7	15.18	[121,230]

Table B.2 pH in the filtrated solution after immersion of the N-(C-)A-S-H gel in water.

Samples/Temperature	25 ℃	40 ℃	60 ℃
N1	11.02±0.05	10.42±0.01	9.90±0.12
N2	11.12±0.05	10.47±0.03	10.03±0.03
N3	10.78±0.08	10.07±0.03	9.72±0.01
NC2_0.25	11.71±0.03	11.08±0.01	10.75±0.01
NC2_0.5	11.86±0.01	11.18±0.03	10.89±0.01
NC3_0.25	11.49±0.00	10.84±0.03	10.50±0.02
NC3_0.5	11.52±0.01	10.85±0.04	10.53±0.00

Note: pH values shown refer to the values after temperature correction.

Appendix C for Chapter 6

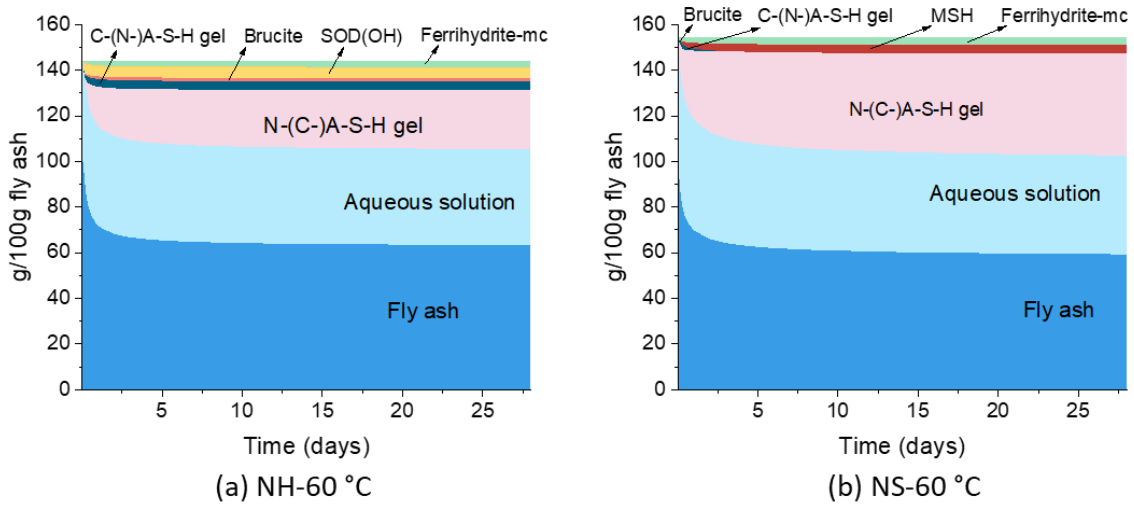

Figure C.1 Simulated phase assemblages of AAFA pastes cured at 60 °C as a function of time. (a) sodium hydroxide-activated system, (b) sodium silicate-activated system.

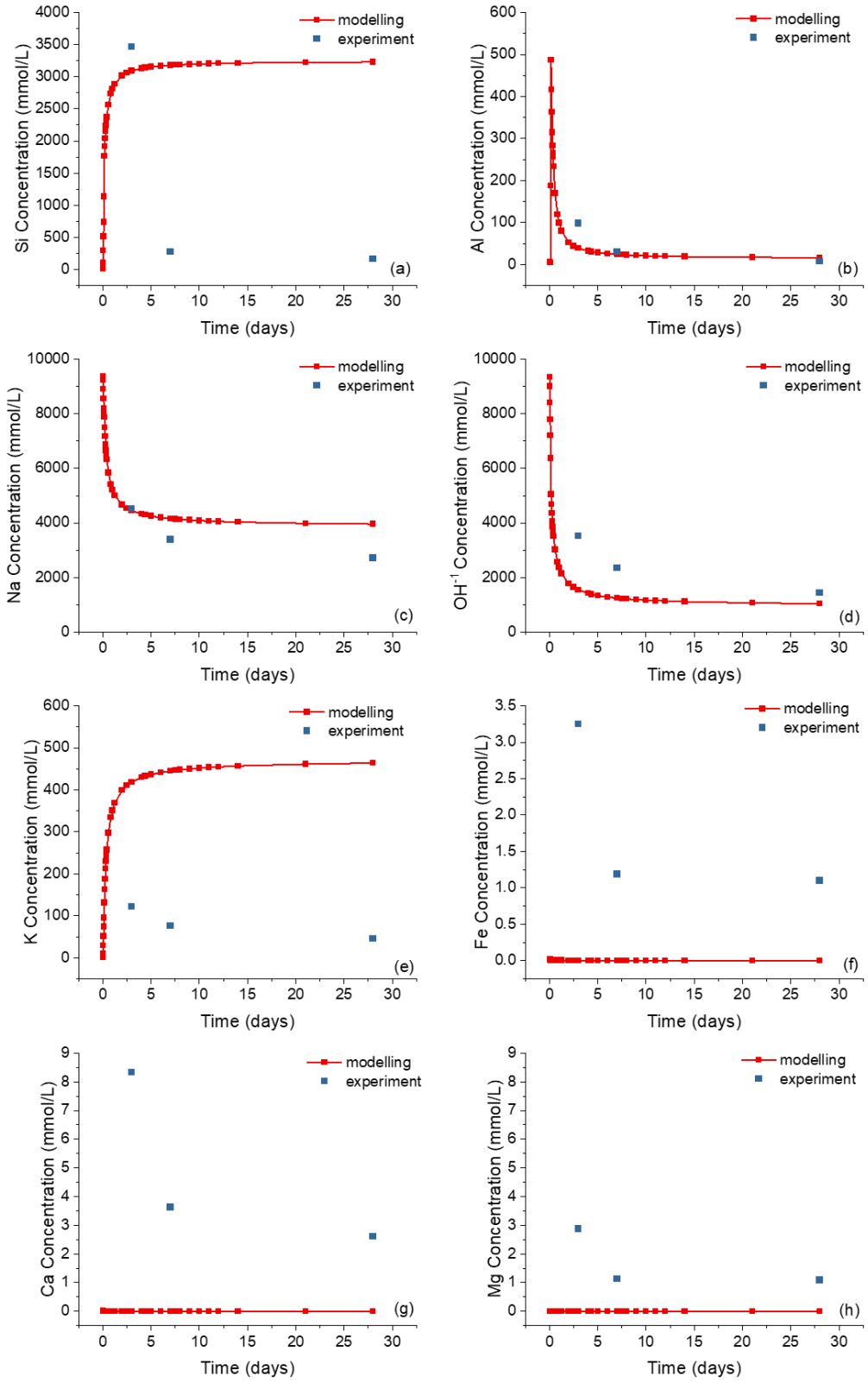

Figure C.2 Experimental and modeling element concentrations in the pore solutions of sodium hydroxide-activated fly ash cured at 60 °C.

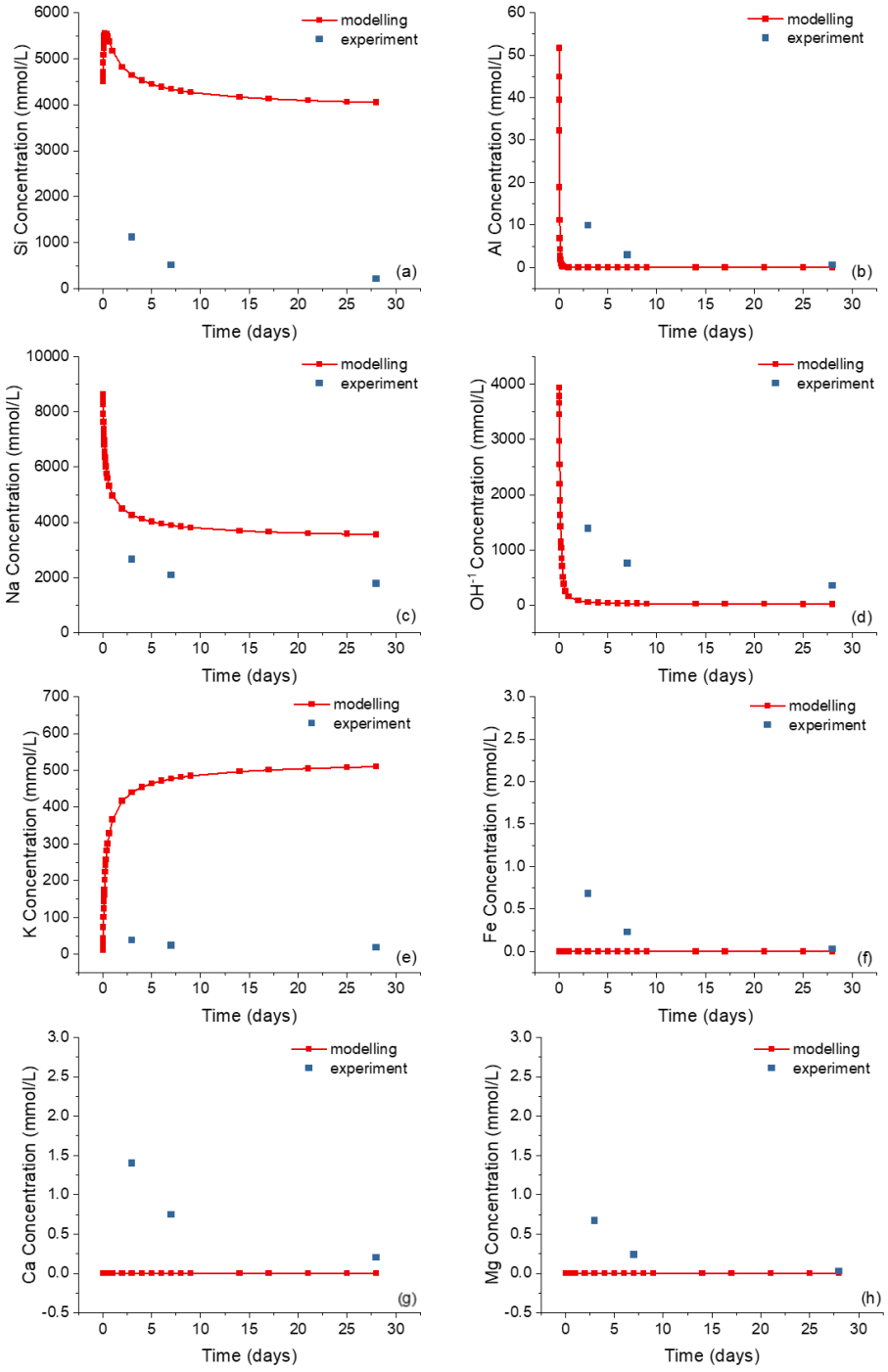

Figure C.3 Experimental and modeling element concentrations in the pore solutions of sodium silicate-activated fly ash cured at 60 °C.

Appendix D for Chapter 7

Table D.1 log forward dissolution rate of Si for the dissolution of different types of aluminosilicate glasses at room temperature.

Samples	Type	Ca/(Si+Al)	Concentration of NaOH	log $r_{+,Si}$ (mol/m^2/s)	Ref
A	fly ash	0.03	1 M	-8.74[a]	[227]
A	fly ash	0.03	6 M	-8.57[a]	[227]
A	fly ash	0.03	12 M	-8.32[a]	[227]
2.0 mol/L	slag	0.97	2 M	-6.06	[223]
3.0 mol/L	slag	0.97	3 M	-5.99	[223]
G1	slag	0.76	0.1 M	-7.62[b]	[59]
G2	slag	0.58	0.1 M	-8.19[b]	[59]
G3	fly ash	0.25	0.1 M	-8.77[b]	[59]
G4	fly ash	0.18	0.1 M	-9.47[b]	[59]
G5	Natural pozzolans	0.07	0.1 M	-9.41[b]	[59]

[a] Calculated from the differences in Si concentrations from 24 to 48 hours.

[b] Recalculated using Equation 7.25.

The evolution of Ca concentration over time during the dissolution of fly ash is illustrated in Figure D.1. Across all dissolution conditions, Ca concentration shows a rapid initial increase within a few hours, followed by a stable phase. However, at 60 °C, a notable decrease in Ca concentration is observed before the initial rise. The presence of a plateau suggests that saturation of the solution occurred around 6 hours, or earlier at higher temperatures, indicating a short far-from-equilibrium stage in Ca dissolution. As the steady-state (linear increase in concentration) was not observed, the forward dissolution rate of Ca was simply calculated based on concentration changes between 0-3 hours in this study.

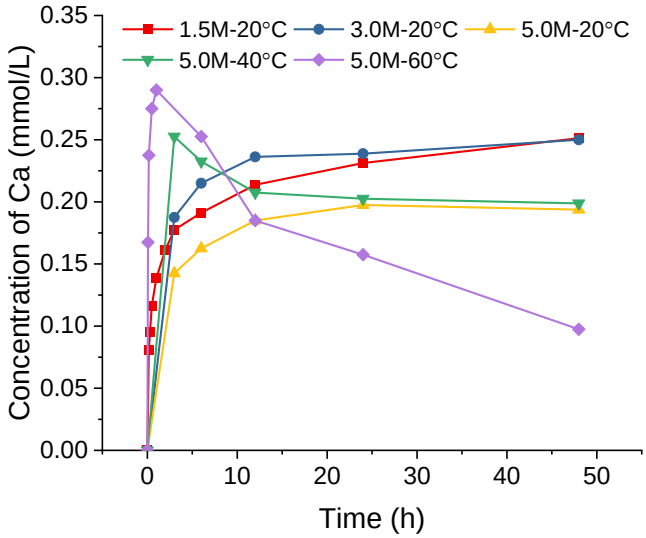

Figure D.1 Concentration of Ca for the dissolution of fly ash in sodium hydroxide solutions at various temperatures. The first value in the legend indicates the concentration of NaOH solution. For instance, 1.5M-20°C indicates the dissolution of ash in a 1.5M NaOH solution at 20 °C.

The forward dissolution rate of Ca was determined using the original equations developed in GeoMicro3D (Equations 7.8). Figure D.2 illustrates the correlation between the predicted and experimental logarithmic forward dissolution rates of Ca. The agreement between predicted and experimental results suggests that the original equations can effectively describe the dissolution of Ca from fly ash in this work.

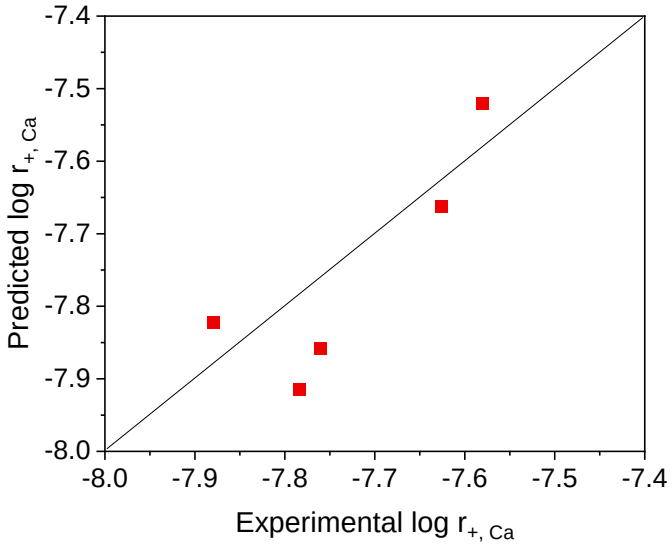

Figure D.2 The correlation between predicted and experimental log forward dissolution rate of Ca for the dissolution of fly ash in this work.

References

[1] J.L. Provis, J.S.J. van Deventer, Alkali Activated Materials, Springer, 2014. https://doi.org/10.1007/978-94-007-7672-2.

[2] K. Gao, M.C. Iliuta, Trends and advances in the development of coal fly ash-based materials for application in hydrogen-rich gas production: A review, J. Energy Chem. 73 (2022) 485–512. https://doi.org/10.1016/j.jechem.2022.05.016.

[3] J. Davidovits, Geopolymers:Inorganic polymeric new materials, J. Therm. Anal. 37 (1991) 1633–1656. https://doi.org/10.1533/9781845696382.

[4] D.M. Roy, Alkali activated cements opportunities and challenges, Cem. Concr. Res. 29 (1999) 249–254.

[5] G. Habert, C. Ouellet-Plamondon, Recent update on the environmental impact of geopolymers, RILEM Tech. Lett. 1 (2016) 17. https://doi.org/10.21809/rilemtechlett.v1.6.

[6] G. Kovalchuk, A. Fernández-Jiménez, A. Palomo, Alkali-activated fly ash: Effect of thermal curing conditions on mechanical and microstructural development - Part II, Fuel. 86 (2007) 315–322. https://doi.org/10.1016/j.fuel.2006.07.010.

[7] Y. Ding, J.G. Dai, C.J. Shi, Mechanical properties of alkali-activated concrete: A state-of-the-art review, Constr. Build. Mater. 127 (2016) 68–79. https://doi.org/10.1016/j.conbuildmat.2016.09.121.

[8] K. Arbi, M. Nedeljković, Y. Zuo, G. Ye, A Review on the Durability of Alkali-Activated Fly Ash/Slag Systems: Advances, Issues, and Perspectives, Ind. Eng. Chem. Res. 55 (2016) 5439–5453. https://doi.org/10.1021/acs.iecr.6b00559.

[9] J. Zhang, C. Shi, Z. Zhang, Z. Ou, Durability of alkali-activated materials in aggressive environments: A review on recent studies, Constr. Build. Mater. 152 (2017) 598–613. https://doi.org/10.1016/j.conbuildmat.2017.07.027.

[10] A. Fernández-Jiménez, A. Palomo, C. López-Hombrados, Engineering Properties of Compacted Fly Ash, ACI Mater. J. 3 (2006) 106–112. https://doi.org/10.1061/jsfeaq.0001744.

[11] A. Fernández-Jiménez, A. Palomo, New Cementitious Materials Based on Alkali-Activated Fly Ash: Performance at High Temperatures, J. Am. Ceram. Soc. 91 (2008) 3308–3314.

[12] M.T. Junaid, A. Khennane, O. Kayali, A. Sadaoui, D. Picard, M. Fafard, Aspects of the deformational behaviour of alkali activated fly ash concrete at elevated temperatures, Cem. Concr. Res. 60 (2014) 24–29. https://doi.org/10.1016/j.cemconres.2014.01.026.

[13] P. Duxson, A. Fernández-Jiménez, J.L. Provis, G.C. Lukey, A. Palomo, J.S.J. Van Deventer, Geopolymer technology: The current state of the art, J. Mater. Sci. 42 (2007) 2917–2933. https://doi.org/10.1007/s10853-006-0637-z.

[14] C. Ruiz-Santaquiteria, J. Skibsted, A. Fernández-Jiménez, A. Palomo, Alkaline

solution/binder ratio as a determining factor in the alkaline activation of aluminosilicates, Cem. Concr. Res. 42 (2012) 1242–1251. https://doi.org/10.1016/j.cemconres.2012.05.019.

[15] J.L. Provis, S.A. Bernal, Geopolymers and related alkali-activated materials, Annu. Rev. Mater. Res. 44 (2014) 299–327. https://doi.org/10.1146/annurev-matsci-070813-113515.

[16] I. Ismail, S.A. Bernal, J.L. Provis, R. San Nicolas, S. Hamdan, J.S.J. Van Deventer, Modification of phase evolution in alkali-activated blast furnace slag by the incorporation of fly ash, Cem. Concr. Compos. 45 (2014) 125–135. https://doi.org/10.1016/j.cemconcomp.2013.09.006.

[17] J. Shekhovtsova, I. Zhernovsky, M. Kovtun, N. Kozhukhova, I. Zhernovskaya, E. Kearsley, Estimation of fly ash reactivity for use in alkali-activated cements - A step towards sustainable building material and waste utilization, J. Clean. Prod. 178 (2018) 22–33. https://doi.org/10.1016/j.jclepro.2017.12.270.

[18] O.K. Wattimena, Antoni, D. Hardjito, A review on the effect of fly ash characteristics and their variations on the synthesis of fly ash based geopolymer, in: AIP Conf. Proc., 2017. https://doi.org/10.1063/1.5003524.

[19] J.D. Vienna, J.J. Neeway, J. V. Ryan, S.N. Kerisit, Impacts of glass composition, pH, and temperature on glass forward dissolution rate, Mater. Degrad. 2 (2018) 1–12. https://doi.org/10.1038/s41529-018-0042-5.

[20] C. Chen, W. Gong, W. Lutze, I.L. Pegg, Kinetics of fly ash geopolymerization, J. Mater. Sci. 46 (2011) 3073–3083. https://doi.org/10.1007/s10853-010-5186-9.

[21] A. Fernández-Jiménez, A. Palomo, Composition and microstructure of alkali activated fly ash binder: Effect of the activator, Cem. Concr. Res. 35 (2005) 1984–1992. https://doi.org/10.1016/j.cemconres.2005.03.003.

[22] M. Criado, A. Fernández-Jiménez, A. Palomo, Alkali activation of fly ash. Part III: Effect of curing conditions on reaction and its graphical description, Fuel. 89 (2010) 3185–3192. https://doi.org/10.1016/j.fuel.2010.03.051.

[23] A. Fernández-Jiménez, A. Palomo, M. Criado, Microstructure development of alkali-activated fly ash cement: A descriptive model, Cem. Concr. Res. 35 (2005) 1204–1209. https://doi.org/10.1016/j.cemconres.2004.08.021.

[24] B. Walkley, R. San Nicolas, M.A. Sani, J.D. Gehman, J.S.J. Van Deventer, J.L. Provis, Phase evolution of Na2O-Al2O3-SiO2-H2O gels in synthetic aluminosilicate binders, Dalt. Trans. 45 (2016) 5521–5535. https://doi.org/10.1039/c5dt04878h.

[25] P. Duxson, J.L. Provis, G.C. Lukey, S.W. Mallicoat, W.M. Kriven, J.S.J. Van Deventer, Understanding the relationship between geopolymer composition, microstructure and mechanical properties, Colloids Surfaces A Physicochem. Eng. Asp. 269 (2005) 47–58. https://doi.org/10.1016/j.colsurfa.2005.06.060.

[26] Z. Zhang, L. Li, X. Ma, H. Wang, Compositional, microstructural and mechanical properties of ambient condition cured alkali-activated cement, Constr. Build. Mater.

113 (2016) 237–245. https://doi.org/10.1016/j.conbuildmat.2016.03.043.

[27] Y. Ma, G. Ye, The shrinkage of alkali activated fly ash, Cem. Concr. Res. 68 (2015) 75–82. https://doi.org/10.1016/j.cemconres.2014.10.024.

[28] S.A. Bernal, J.L. Provis, Durability of Alkali-Activated Materials: Progress and Perspectives, J. Am. Ceram. Soc. 97 (2014) 997–1008.

[29] R.J. Myers, B. Lothenbach, S.A. Bernal, J.L. Provis, Thermodynamic modelling of alkali-activated slag cements, Appl. Geochemistry. 61 (2015) 233–247. https://doi.org/10.1016/j.apgeochem.2015.06.006.

[30] R.J. Myers, S.A. Bernal, J.L. Provis, Phase diagrams for alkali-activated slag binders, Cem. Concr. Res. 95 (2017) 30–38. https://doi.org/10.1016/j.cemconres.2017.02.006.

[31] B. Lothenbach, M. Zajac, Application of thermodynamic modelling to hydrated cements, Cem. Concr. Res. 123 (2019) 105779. https://doi.org/10.1016/j.cemconres.2019.105779.

[32] B. Lothenbach, D.A. Kulik, T. Matschei, M. Balonis, L. Baquerizo, B.Z. Dilnesa, G.D. Miron, M. R., Cemdata18: A chemical thermodynamic database for hydrated Portland cements and alkali-activated materials., Cem. Concr. Res. (2019) 472–506. https://doi.org/10.1109/ICCPS.2014.6843714.

[33] Y. Zuo, Experimental Study and Numerical Simulation of the Reaction Process and Microstructure Formation of Alkali-Activated Materials, 2019. https://doi.org/10.4233/uuid.

[34] B. Walkley, X. Ke, O. Hussein, J.L. Provis, Thermodynamic properties of sodium aluminosilicate hydrate (N-A-S-H), Dalt. Trans. (2021). https://doi.org/10.1039/d1dt02202d.

[35] L. Gomez-Zamorano, M. Balonis, B. Erdemli, N. Neithalath, G. Sant, C–(N)–S–H and N–A–S–H gels: Compositions and solubility data at 25°C and 50°C, J. Am. Ceram. Soc. 100 (2017) 2700–2711. https://doi.org/10.1111/jace.14715.

[36] T. Williamson, L.E. Katz, J. Han, H.A. Dobbs, B.F. Chmelka, G. Sant, M.C.G. Juenger, Relationship between aqueous chemistry and composition, structure, and solubility of sodium aluminosilicate hydrates, J. Am. Ceram. Soc. 103 (2020) 2160–2172. https://doi.org/10.1111/jace.16868.

[37] P. Gao, Simulation of hydration and microstructure development of blended cements, 2018. https://doi.org/10.4233/uuid.

[38] D.P. Bentz, CEMHYD3D: A Three-Dimensional Cement Hydration and Microstructure Development Modeling Package. Version 3.0., 2005.

[39] S. Bishnoi, K.L. Scrivener, μic: A new platform for modelling the hydration of cements, Cem. Concr. Res. 39 (2009) 266–274. https://doi.org/10.1016/j.cemconres.2008.12.002.

[40] Y. Zuo, G. Ye, GeoMicro3D: A novel numerical model for simulating the reaction

process and microstructure formation of alkali-activated slag, Cem. Concr. Res. 141 (2021). https://doi.org/10.1016/j.cemconres.2020.106328.

[41] D.A. Kulik, T. Wagner, S. V. Dmytrieva, G. Kosakowski, F.F. Hingerl, K. V. Chudnenko, U.R. Berner, GEM-Selektor geochemical modeling package: revised algorithm and GEMS3K numerical kernel for coupled simulation codes, Comput. Geosci. 17 (2013) 1–24. https://doi.org/10.1007/s10596-012-9310-6.

[42] J. Wastiels, X. Wu, S. Faignet, G. Patfoort, Mineral polymer based on fly ash, J. Resour. Manag. Technol. 22 (1994) 135–141.

[43] J.G.S. Van Jaarsveld, J.S.J. Van Deventer, G.C. Lukey, The characterisation of source materials in fly ash-based geopolymers, Mater. Lett. 57 (2003) 1272–1280. https://doi.org/10.1016/S0167-577X(02)00971-0.

[44] R.R. Lloyd, J.L. Provis, J.S.J. Van Deventer, Microscopy and microanalysis of inorganic polymer cements. 2: the gel binder, J. Mater. Sci. 44 (2009) 620–631. https://doi.org/10.1007/s10853-008-3077-0.

[45] M. Sofi, J.S.J. van Deventer, P.A. Mendis, G.C. Lukey, Engineering properties of inorganic polymer concretes (IPCs), Cem. Concr. Res. 37 (2007) 251–257. https://doi.org/10.1016/j.cemconres.2006.10.008.

[46] C. Shi, A. Fernández-Jiménez, Stabilization/solidification of hazardous and radioactive wastes with alkali-activated cements, J. Hazard. Mater. 137 (2006) 1656–1663. https://doi.org/10.1016/j.jhazmat.2006.05.008.

[47] J. Temuujin, A. Minjigmaa, W. Rickard, M. Lee, I. Williams, A. van Riessen, Fly ash based geopolymer thin coatings on metal substrates and its thermal evaluation, J. Hazard. Mater. 180 (2010) 748–752. https://doi.org/10.1016/j.jhazmat.2010.04.121.

[48] P. V. Krivenko, G.Y. Kovalchuk, Directed synthesis of alkaline aluminosilicate minerals in a geocement matrix, J. Mater. Sci. 42 (2007) 2944–2952. https://doi.org/10.1007/s10853-006-0528-3.

[49] Á. Palomo, A. Fernández-Jiménez, C. López Hombrados, J.L. Lleyda, Railway sleepers made of alkali activated fly ash concrete, (2007).

[50] R.T. Chancey, P. Stutzman, M.C.G. Juenger, D.W. Fowler, Comprehensive phase characterization of crystalline and amorphous phases of a Class F fly ash, Cem. Concr. Res. 40 (2010) 146–156. https://doi.org/10.1016/J.CEMCONRES.2009.08.029.

[51] ASTM C618-12a, Standard Specification for Coal Fly Ash and Raw or Calcined Natural Pozzolan for Use in Concrete, ASTM International, West Conshohocken, PA, 2012. https://doi.org/10.1520/C0618.

[52] C.L. Nicholson, B.J. Murray, R.A. Fletcher, D.R.M. Brew, K.J.D. Mackenzie, M. Schmücker, Novel geopolymer materials containing borate structural units, in: World Congr. Geopolymer, 2005: pp. 31–33.

[53] W. Rakngan, T. Williamson, R.D. Ferron, G. Sant, M.C.G. Juenger, Controlling workability in alkali-activated Class C fly ash, Constr. Build. Mater. 183 (2018) 226–

233. https://doi.org/10.1016/j.conbuildmat.2018.06.174.

[54] G. Xu, X. Shi, Characteristics and applications of fly ash as a sustainable construction material: A state-of-the-art review, Resour. Conserv. Recycl. 136 (2018) 95–109. https://doi.org/10.1016/j.resconrec.2018.04.010.

[55] C. Kuenzel, N. Ranjbar, Dissolution mechanism of fly ash to quantify the reactive aluminosilicates in geopolymerisation, Resour. Conserv. Recycl. 150 (2019) 104421. https://doi.org/10.1016/j.resconrec.2019.104421.

[56] P. Duxson, J.L. Provis, Designing precursors for geopolymer cements, J. Am. Ceram. Soc. 91 (2008) 3864–3869. https://doi.org/10.1111/j.1551-2916.2008.02787.x.

[57] E.H. Oelkers, S.R. Gislason, The mechanism, rates and consequences of basaltic glass dissolution: I. An experimental study of the dissolution rates of basaltic glass as a function of aqueous Al, Si and oxalic acid concentration at 25°C and pH = 3 and 11, Geochim. Cosmochim. Acta. 65 (2001) 3671–3681.

[58] E.M. Gartner, D.E. MacPhee, A physico-chemical basis for novel cementitious binders, Cem. Concr. Res. 41 (2011) 736–749. https://doi.org/10.1016/j.cemconres.2011.03.006.

[59] R. Snellings, Solution-controlled dissolution of supplementary cementitious material glasses at pH 13: The effect of solution composition on glass dissolution rates, J. Am. Ceram. Soc. 96 (2013) 2467–2475. https://doi.org/10.1111/jace.12480.

[60] K.C. Newlands, M. Foss, T. Matschei, J. Skibsted, D.E. Macphee, Early stage dissolution characteristics of aluminosilicate glasses with blast furnace slag- and fly-ash-like compositions, J. Am. Ceram. Soc. 100 (2017) 1941–1955. https://doi.org/10.1111/jace.14716.

[61] T. Oey, A. Kumar, I. Pignatelli, Y. Yu, N. Neithalath, J.W. Bullard, M. Bauchy, G. Sant, Topological controls on the dissolution kinetics of glassy aluminosilicates, J. Am. Ceram. Soc. 100 (2017) 5521–5527. https://doi.org/10.1111/jace.15122.

[62] L. Koech, R. Everson, H. Neomagus, H. Rutto, DISSOLUTION KINETICS OF SOUTH AFRICAN COAL FLY ASH AND THE DEVELOPMENT OF A SEMI-EMPIRICAL MODEL TO PREDICT DISSOLUTION, Chem. Ind. Chem. Eng. Q. 21 (2015) 319–330. https://doi.org/10.2298/CICEQ140423032K.

[63] C. Chen, W. Gong, W. Lutze, I.L. Pegg, J. Zhai, Kinetics of fly ash leaching in strongly alkaline solutions, J. Mater. Sci. 46 (2011) 590–597. https://doi.org/10.1007/s10853-010-4997-z.

[64] J.P. Icenhower, S. Samson, A. Lüttge, B.P. McGrail, Towards a consistent rate law: Glass corrosion kinetics near saturation, Geol. Soc. Spec. Publ. 236 (2004) 579–594. https://doi.org/10.1144/GSL.SP.2004.236.01.32.

[65] E.M. Pierce, E.A. Rodriguez, L.J. Calligan, W.J. Shaw, B. Pete McGrail, An experimental study of the dissolution rates of simulated aluminoborosilicate waste glasses as a function of pH and temperature under dilute conditions, Appl. Geochemistry. 23

(2008) 2559–2573. https://doi.org/10.1016/j.apgeochem.2008.05.006.

[66] D.G. Truhlar, B.C. Garrett, B.B. V, M.S. K-, S.J. Klippenstein, Current Status of Transition-State Theory, J. Phys. Chem. 3654 (1996) 12771–12800.

[67] E.H. Oelkers, General kinetic description of multioxide silicate mineral and glass dissolution, Geochim. Cosmochim. Acta. 65 (2001) 3703–3719. https://doi.org/10.1016/S0016-7037(01)00710-4.

[68] T.M. Iwalewa, T. Qu, I. Farnan, Investigation of the maximum dissolution rates and temperature dependence of a simulated UK nuclear waste glass in circum-neutral media at 40 and 90°C in a dynamic system, Appl. Geochemistry. 82 (2017) 177–190. https://doi.org/10.1016/j.apgeochem.2017.05.018.

[69] P. Aagaard, H.C. Helgeson, Thermodynamic and kinetic constraints on reaction rates among minerals and aqueous solutions: I, Theoretical considerations, Am. J. Sci. 282 (1982) 237–285.

[70] A. Palomo, S. Alonso, A. Fernández-Jiménez, Alkaline Activation of Fly Ashes: NMR Study of the Reaction Products, J. Am. Ceram. Soc. 87 (2004) 1141–1145. https://ceramics.onlinelibrary.wiley.com/doi/pdf/10.1111/j.1551-2916.2004.01141.x (accessed May 10, 2019).

[71] C. Shi, A.F. Jiménez, A. Palomo, New cements for the 21st century: The pursuit of an alternative to Portland cement, Cem. Concr. Res. 41 (2011) 750–763. https://doi.org/10.1016/j.cemconres.2011.03.016.

[72] J.L. Provis, J.S.J. van Deventer, Geopolymerisation kinetics. 1. In situ energy-dispersive X-ray diffractometry, Chem. Eng. Sci. 62 (2007) 2309–2317. https://doi.org/10.1016/j.ces.2007.01.027.

[73] C.A. Rees, J.L. Provis, G.C. Lukey, J.S.J. Van Deventer, In situ ATR-FTIR study of the early stages of fly ash geopolymer gel formation, Langmuir. 23 (2007) 9076–9082. https://doi.org/10.1021/la701185g.

[74] C.A. Rees, J.L. Provis, G.C. Lukey, J.S.J. van Deventer, The mechanism of geopolymer gel formation investigated through seeded nucleation, Colloids Surfaces A Physicochem. Eng. Asp. 318 (2008) 97–105. https://doi.org/10.1016/j.colsurfa.2007.12.019.

[75] C.A. Rees, J.L. Provis, G.C. Lukey, J.S.J. Van Deventer, Attenuated total reflectance fourier transform infrared analysis of fly ash geopolymer gel aging, Langmuir. 23 (2007) 8170–8179. https://doi.org/10.1021/la700713g.

[76] Z. Sun, A. Vollpracht, Isothermal calorimetry and in-situ XRD study of the NaOH activated fly ash, metakaolin and slag, Cem. Concr. Res. 103 (2018) 110–122. https://doi.org/10.1016/j.cemconres.2017.10.004.

[77] E. Deir, B.S. Gebregziabiher, S. Peethamparan, Influence of starting material on the early age hydration kinetics, microstructure and composition of binding gel in alkali activated binder systems, Cem. Concr. Compos. 48 (2014) 108–117. https://doi.org/10.1016/j.cemconcomp.2013.11.010.

[78] S. Chithiraputhiran, N. Neithalath, Isothermal reaction kinetics and temperature dependence of alkali activation of slag, fly ash and their blends, Constr. Build. Mater. 45 (2013) 233–242. https://doi.org/10.1016/j.conbuildmat.2013.03.061.

[79] S.K. Nath, S. Kumar, Role of alkali concentration on reaction kinetics of fly ash geopolymerization, J. Non. Cryst. Solids. 505 (2019) 241–251. https://doi.org/10.1016/J.JNONCRYSOL.2018.11.007.

[80] A. Palomo, M.W. Grutzeck, M.T. Blanco, Alkali-activated fly ashes: A cement for the future, Cem. Concr. Res. 29 (1999) 1323–1329. https://doi.org/10.1016/S0008-8846(98)00243-9.

[81] J.L. Provis, A. Palomo, Advances in understanding alkali-activated materials, Cem. Concr. Res. 78 (2015) 110–125. https://doi.org/10.1016/J.CEMCONRES.2015.04.013.

[82] P. Duxson, J.L. Provis, G.C. Lukey, F. Separovic, J.S.J. Van Deventer, 29Si NMR study of structural ordering in aluminosilicate geopolymer gels, Langmuir. 21 (2005) 3028–3036. https://doi.org/10.1021/la047336x.

[83] J.L. Provis, P. Duxson, G.C. Lukey, J.S.J. Van Deventer, Statistical thermodynamic model for Si/Al ordering in amorphous aluminosilicates, Chem. Mater. 17 (2005) 2976–2986. https://doi.org/10.1021/cm050219i.

[84] X. Gao, Q.L. Yu, H.J.H. Brouwers, Apply 29Si, 27Al MAS NMR and selective dissolution in identifying the reaction degree of alkali activated slag-fly ash composites, Ceram. Int. 43 (2017) 12408–12419. https://doi.org/10.1016/j.ceramint.2017.06.108.

[85] A. Fernández-Jiménez, A. Palomo, I. Sobrados, J. Sanz, The role played by the reactive alumina content in the alkaline activation of fly ashes, Microporous Mesoporous Mater. 91 (2006) 111–119. https://doi.org/10.1016/j.micromeso.2005.11.015.

[86] B. Walkley, G.J. Rees, R. San Nicolas, J.S.J. Van Deventer, J. V. Hanna, J.L. Provis, New Structural Model of Hydrous Sodium Aluminosilicate Gels and the Role of Charge-Balancing Extra-Framework Al, J. Phys. Chem. C. 122 (2018) 5673–5685. https://doi.org/10.1021/acs.jpcc.8b00259.

[87] I. García-Lodeiro, A. Fernández-Jiménez, A. Palomo, D.E. MacPhee, Effect of calcium additions on N-A-S-H cementitious gels, J. Am. Ceram. Soc. 93 (2010) 1934–1940. https://doi.org/10.1111/j.1551-2916.2010.03668.x.

[88] M.R. Rowles, B.H. O'Connor, Chemical and structural microanalysis of aluminosilicate geopolymers synthesized by sodium silicate activation of metakaolinite, J. Am. Ceram. Soc. 92 (2009) 2354–2361. https://doi.org/10.1111/j.1551-2916.2009.03191.x.

[89] G.V.P. Bhagath Singh, K.V.L. Subramaniam, Influence of processing temperature on the reaction product and strength gain in alkali-activated fly ash, Cem. Concr. Compos. 95 (2019) 10–18. https://doi.org/10.1016/j.cemconcomp.2018.10.010.

[90] T. Bakharev, Geopolymeric materials prepared using Class F fly ash and elevated temperature curing, Cem. Concr. Res. 35 (2005) 1224–1232. https://doi.org/10.1016/j.cemconres.2004.06.031.

[91] F. Winnefeld, A. Leemann, M. Lucuk, P. Svoboda, M. Neuroth, Assessment of phase formation in alkali activated low and high calcium fly ashes in building materials, Constr. Build. Mater. 24 (2010) 1086–1093. https://doi.org/10.1016/j.conbuildmat.2009.11.007.

[92] H. Rahier, B. Van Mele, M. Biesemans, J. Wastiels, X. Wu, Low-temperature synthesized aluminosilicate glasses: Part I. Low-temperature reaction stoichiometry and structure of a model compound, J. Mater. Sci. 31 (1996) 71–79. https://doi.org/10.1007/BF00355128.

[93] M.C.G. Juenger, F. Winnefeld, J.L. Provis, J.H. Ideker, Advances in alternative cementitious binders, Cem. Concr. Res. 41 (2011) 1232–1243. https://doi.org/10.1016/j.cemconres.2010.11.012.

[94] I. García-Lodeiro, A. Fernández-Jiménez, A. Palomo, Variation in hybrid cements over time. Alkaline activation of fly ash-portland cement blends, Cem. Concr. Res. 52 (2013) 112–122. https://doi.org/10.1016/j.cemconres.2013.03.022.

[95] N.K. Lee, H.K. Lee, Reactivity and reaction products of alkali-activated, fly ash/slag paste, Constr. Build. Mater. 81 (2015) 303–312. https://doi.org/10.1016/j.conbuildmat.2015.02.022.

[96] Y. Ma, J. Hu, G. Ye, The effect of activating solution on the mechanical strength, reaction rate, mineralogy, and microstructure of alkali-activated fly ash, J. Mater. Sci. 47 (2012) 4568–4578. https://doi.org/10.1007/s10853-012-6316-3.

[97] M. Criado, A. Fernández-Jiménez, A.G. de la Torre, M.A.G. Aranda, A. Palomo, An XRD study of the effect of the SiO2/Na2O ratio on the alkali activation of fly ash, Cem. Concr. Res. 37 (2007) 671–679. https://doi.org/10.1016/j.cemconres.2007.01.013.

[98] P. Rożek, M. Król, W. Mozgawa, Spectroscopic studies of fly ash-based geopolymers, Spectrochim. Acta - Part A Mol. Biomol. Spectrosc. 198 (2018) 283–289. https://doi.org/10.1016/j.saa.2018.03.034.

[99] J.E. Oh, P.J.M. Monteiro, S.S. Jun, S. Choi, S.M. Clark, The evolution of strength and crystalline phases for alkali-activated ground blast furnace slag and fly ash-based geopolymers, Cem. Concr. Res. 40 (2010) 189–196. https://doi.org/10.1016/j.cemconres.2009.10.010.

[100] G.V.P. Bhagath Singh, K.V.L. Subramaniam, Quantitative XRD study of amorphous phase in alkali activated low calcium siliceous fly ash, Constr. Build. Mater. 124 (2016) 139–147. https://doi.org/10.1016/j.conbuildmat.2016.07.081.

[101] M. Criado, M. Vicent, F.J. García-Ten, Reactivation of alkali-activated materials made up of fly ashes from a coal power plant, Clean. Mater. 3 (2022) 100043. https://doi.org/10.1016/j.clema.2022.100043.

[102] J.L. Provis, G.C. Lukey, J.S.J. Van Deventer, Do geopolymers actually contain nanocrystalline zeolites? A reexamination of existing results, Chem. Mater. 17 (2005) 3075–3085. https://doi.org/10.1021/cm050230i.

[103] S.R. Paudel, M. Yang, Z. Gao, pH Level of Pore Solution in Alkali-Activated Fly-Ash

Geopolymer Concrete and Its Effect on ASR of Aggregates with Different Silicate Contents, J. Mater. Civ. Eng. 32 (2020) 04020257. https://doi.org/10.1061/(asce)mt.1943-5533.0003344.

[104] T. Williamson, M.C.G. Juenger, The role of activating solution concentration on alkali-silica reaction in alkali-activated fly ash concrete, Cem. Concr. Res. 83 (2016) 124–130. https://doi.org/10.1016/j.cemconres.2016.02.008.

[105] Y. Zuo, M. Nedeljković, G. Ye, Pore solution composition of alkali-activated slag/fly ash pastes, Cem. Concr. Res. 115 (2019) 230–250. https://doi.org/10.1016/j.cemconres.2018.10.010.

[106] H. Manzano, Atomistic Simulation studies of the Cement Paste Components, University of the Basque Country, 2009.

[107] S.H. Hahn, J. Rimsza, L. Criscenti, W. Sun, L. Deng, J. Du, T. Liang, S.B. Sinnott, A.C.T. Van Duin, Development of a ReaxFF Reactive Force Field for NaSiO x /Water Systems and Its Application to Sodium and Proton Self-Diffusion, J. Phys. Chem. C. 122 (2018) 19613–19624. https://doi.org/10.1021/acs.jpcc.8b05852.

[108] L.Y. Xu, Y. Alrefaei, Y.S. Wang, J.G. Dai, Recent advances in molecular dynamics simulation of the N-A-S-H geopolymer system: modeling, structural analysis, and dynamics, Constr. Build. Mater. 276 (2021) 122196. https://doi.org/10.1016/j.conbuildmat.2020.122196.

[109] D.C. RAPAPORT, The art of molecular dynamics simulaiton, Cambridge University Press, 2004.

[110] M.R. Sadat, S. Bringuier, K. Muralidharan, K. Runge, A. Asaduzzaman, L. Zhang, An atomistic characterization of the interplay between composition, structure and mechanical properties of amorphous geopolymer binders, J. Non. Cryst. Solids. 434 (2016) 53–61. https://doi.org/10.1016/J.JNONCRYSOL.2015.11.022.

[111] Y. Zhang, J. Zhang, J. Jiang, D. Hou, J. Zhang, The effect of water molecules on the structure, dynamics, and mechanical properties of sodium aluminosilicate hydrate (NASH) gel: A molecular dynamics study, Constr. Build. Mater. 193 (2018) 491–500. https://doi.org/10.1016/J.CONBUILDMAT.2018.10.221.

[112] F. Lolli, H. Manzano, J.L. Provis, M.C. Bignozzi, E. Masoero, Atomistic Simulations of Geopolymer Models: The Impact of Disorder on Structure and Mechanics, ACS Appl. Mater. Interfaces. 10 (2018) 22809–22820. https://doi.org/10.1021/acsami.8b03873.

[113] R. Wang, J. Wang, T. Dong, G. Ouyang, Structural and mechanical properties of geopolymers made of aluminosilicate powder with different SiO2/Al2O3 ratio: Molecular dynamics simulation and microstructural experimental study, Constr. Build. Mater. 240 (2020) 117935. https://doi.org/10.1016/j.conbuildmat.2019.117935.

[114] M. Zhang, N.A. Deskins, G. Zhang, R.T. Cygan, M. Tao, Modeling the Polymerization Process for Geopolymer Synthesis through Reactive Molecular Dynamics Simulations, J. Phys. Chem. C. 122 (2018) 6760–6773. https://doi.org/10.1021/acs.jpcc.8b00697.

[115] X. Guan, L. Jiang, D. Fan, A. Garcia Hernandez, B. Li, H. Do, Molecular simulations of the structure-property relationships of N-A-S-H gels, Constr. Build. Mater. 329 (2022). https://doi.org/10.1016/j.conbuildmat.2022.127166.

[116] B. Lothenbach, Thermodynamic equilibrium calculations in cementitious systems, Mater. Struct. 43 (2010) 1413–1433. https://doi.org/10.1617/s11527-010-9592-x.

[117] J. Yang, D. Li, Y. Fang, Synthesis of nanoscale CaO-Al2O3-SiO2-H2O and Na2O-Al2O3-SiO2-H2O using the hydrothermal method and their characterization, Materials (Basel). 10 (2017). https://doi.org/10.3390/ma10070695.

[118] H. Ye, L. Huang, Degradation mechanisms of alkali-activated binders in sulfuric acid: The role of calcium and aluminum availability, Constr. Build. Mater. 246 (2020) 118477. https://doi.org/10.1016/j.conbuildmat.2020.118477.

[119] I. Garcia-Lodeiro, A. Palomo, A. Fernández-Jiménez, D.E. MacPhee, Compatibility studies between N-A-S-H and C-A-S-H gels. Study in the ternary diagram Na2O-CaO-Al2O3-SiO2-H2O, Cem. Concr. Res. 41 (2011) 923–931. https://doi.org/10.1016/j.cemconres.2011.05.006.

[120] T. Williamson, J. Han, L. Katz, G. Sant, M. Juenger, Method for experimentally determining N-A-S-(H) solubility, RILEM Tech. Lett. 3 (2019) 104–113. https://doi.org/10.21809/rilemtechlett.2018.63.

[121] H.C. Helgeson, J.M. Delany, H.W. Nesbitt, D.K. Bird, Summary and critique of the thermodynamic properties of rock-forming minerals, Am. J. Sci. 278 (1978) 1–229.

[122] D.A. Kulik, Aqueous Solubility Diagrams for Cementitious Waste Stabilization Systems: II, End-Member Stoichiometries of Ideal Calcium Silicate Hydrate Solid Solutions, J. Am. Ceram. Soc. 84 (2001) 3017–3026. http://scholar.google.com/scholar?hl=en&btnG=Search&q=intitle:Aqueous+Solubility+Diagrams+for+Cementitious+Waste#7.

[123] B. Lothenbach, T. Matschei, G. Möschner, F.P. Glasser, Thermodynamic modelling of the effect of temperature on the hydration and porosity of Portland cement, Cem. Concr. Res. 38 (2008) 1–18. https://doi.org/10.1016/j.cemconres.2007.08.017.

[124] B. Ma, B. Lothenbach, Synthesis, characterization, and thermodynamic study of selected Na-based zeolites, Cem. Concr. Res. 135 (2020) 106111. https://doi.org/10.1016/j.cemconres.2020.106111.

[125] B. Ma, B. Lothenbach, Synthesis, characterization, and thermodynamic study of selected K-based zeolites, Cem. Concr. Res. 148 (2021) 106537. https://doi.org/10.1016/j.cemconres.2021.106537.

[126] Z. Qian, E.J. Garboczi, G. Ye, E. Schlangen, Anm: a geometrical model for the composite structure of mortar and concrete using real-shape particles, Mater. Struct. 49 (2016) 149–158. https://doi.org/10.1617/s11527-014-0482-5.

[127] N.S. Martys, Diffusion in partially-saturated porous materials, Mater. Struct. Constr. 32 (1999) 555–562. https://doi.org/10.1007/bf02480489.

[128] M. Zhang, G. Ye, K. Van Breugel, Modeling of ionic diffusivity in non-saturated cement-based materials using lattice Boltzmann method, Cem. Concr. Res. 42 (2012) 1524–1533. https://doi.org/10.1016/j.cemconres.2012.08.005.

[129] S. Jiang, J.H. Ter Horst, Crystal nucleation rates from probability distributions of induction times, Cryst. Growth Des. 11 (2010) 256–261. https://doi.org/10.1021/cg101213q.

[130] B.P. Feuston, S.H. Garofalini, Onset of polymerization in silica sols, Chem. Phys. Lett. 170 (1990) 264–270. https://doi.org/10.1016/0009-2614(90)87126-C.

[131] J.S. Dolado, M. Griebel, J. Hamaekers, A molecular dynamic study of cementitious calcium silicate hydrate (C-S-H) gels, J. Am. Ceram. Soc. 90 (2007) 3938–3942. https://doi.org/10.1111/j.1551-2916.2007.01984.x.

[132] A. Allouche, Software News and Updates Gabedit — A Graphical User Interface for Computational Chemistry Softwares, J. Comput. Chem. 32 (2012) 174–182. https://doi.org/10.1002/jcc.

[133] A. Bhatt, S. Priyadarshini, A. Acharath Mohanakrishnan, A. Abri, M. Sattler, S. Techapaphawit, Physical, chemical, and geotechnical properties of coal fly ash: A global review, Case Stud. Constr. Mater. 11 (2019) e00263. https://doi.org/10.1016/j.cscm.2019.e00263.

[134] M.R. Sadat, S. Bringuier, A. Asaduzzaman, K. Muralidharan, L. Zhang, A molecular dynamics study of the role of molecular water on the structure and mechanics of amorphous geopolymer binders, J. Chem. Phys. 145 (2016). https://doi.org/10.1063/1.4964301.

[135] S. Chitsaz, A. Tarighat, Molecular dynamics simulation of N-A-S-H geopolymer macro molecule model for prediction of its modulus of elasticity, Constr. Build. Mater. 243 (2020) 118176. https://doi.org/10.1016/j.conbuildmat.2020.118176.

[136] S.Plimpton, Fast Parallel Algorithms for Short-Range Molecular Dynamics, J. Comput. Phys. 117 (1995) 1–19. https://doi.org/10.1006/jcph.1995.1039.

[137] A.C.T. Van Duin, A. Strachan, S. Stewman, Q. Zhang, X. Xu, W.A. Goddard, ReaxFFSiO reactive force field for silicon and silicon oxide systems, J. Phys. Chem. A. 107 (2003) 3803–3811. https://doi.org/10.1021/jp0276303.

[138] K.L. Joshi, A.C.T. Van Duin, Molecular Dynamics Study on the Influence of Additives on the High-Temperature Structural and Acidic Properties of ZSM-5 Zeolite, Energy Fuels. 27 (2013) 4481−4488. https://doi.org/10.1021/ef3020124.

[139] J.C. Fogarty, M. Aktulga, A.Y. Grama, A.C.T. Van Duin, S.A. Pandit, A reactive molecular dynamics simulation of the silica-water interface, J. Phys. Chem. 132 (2010) 174704. https://doi.org/10.1063/1.3407433.

[140] K.L. Joshi, G. Psofogiannakis, A.C.T. Van Duin, S. Raman, Reactive molecular simulations of protonation of water clusters and depletion of acidity in H-ZSM-5 zeolite †, Phys. Chem. Chem. Phys. 16 (2014) 18433--18441.

https://doi.org/10.1039/c4cp02612h.

[141] W. Humphrey, A. Dalke, K. Schulten, others, VMD: visual molecular dynamics, J. Mol. Graph. 14 (1996) 33–38.

[142] A. Stukowski, Visualization and analysis of atomistic simulation data with OVITO--the Open Visualization Tool, Model. Simul. Mater. Sci. Eng. 18 (2009) 15012.

[143] S.P. Coleman, D.E. Spearot, L. Capolungo, Virtual diffraction analysis of Ni [0 1 0] symmetric tilt grain boundaries, Model. Simul. Mater. Sci. Eng. 21 (2013) 0–16. https://doi.org/10.1088/0965-0393/21/5/055020.

[144] F. Brunet, B. Cabane, M. Dubois, B. Perly, Sol-gel polymerization studied through 29Si NMR with polarization transfer, J. Phys. Chem. 95 (1991) 945–951. https://doi.org/10.1021/j100155a082.

[145] P.S. Singh, T. Bastow, M. Trigg, Structural studies of geopolymers by 29Si and 27Al MAS-NMR, J. Mater. Sci. 40 (2005) 3951–3961. https://doi.org/10.1007/s10853-005-1915-x.

[146] J.L. Provis, J.S.J. van Deventer, Geopolymerisation kinetics. 2. Reaction kinetic modelling, Chem. Eng. Sci. 62 (2007) 2318–2329. https://doi.org/10.1016/j.ces.2007.01.028.

[147] W. Gordy, Dependence of bond order and of bond energy upon bond length, J. Chem. Phys. 15 (1947) 305–310. https://doi.org/10.1063/1.1746501.

[148] M.R. Sadat, K. Muralidharan, L. Zhang, Reactive molecular dynamics simulation of the mechanical behavior of sodium aluminosilicate geopolymer and calcium silicate hydrate composites, Comput. Mater. Sci. 150 (2018) 500–509. https://doi.org/10.1016/j.commatsci.2018.04.041.

[149] C.E. White, J.L. Provis, T. Proffen, J.S.J. Van Deventerz, The effects of temperature on the local structure of metakaolin-based geopolymer binder: A neutron pair distribution function investigation, J. Am. Ceram. Soc. 93 (2010) 3486–3492. https://doi.org/10.1111/j.1551-2916.2010.03906.x.

[150] S.K. Lee, J.F. Stebbins, Al-O-Al and Si-O-Si sites in framework aluminosilicate glasses with Si/Al= 1: quantification of framework disorder, J. Non. Cryst. Solids. 270 (2000) 260–264.

[151] J.F. Stebbins, S.K. Lee, J. V. Oglesby, Al-O-Al oxygen sites in crystalline aluminates and aluminosilicate glasses: High-resolution oxygen-17 NMR results, Am. Mineral. 84 (1999) 983–986. https://doi.org/10.2138/am-1999-5-635.

[152] R. Dongol, L. Wang, A.N. Cormack, S.K. Sundaram, Molecular dynamics simulation of sodium aluminosilicate glass structures and glass surface-water reactions using the reactive force field (ReaxFF), Appl. Surf. Sci. 439 (2018) 1103–1110. https://doi.org/10.1016/j.apsusc.2017.12.180.

[153] A. Pedone, E. Gambuzzi, M.C. Menziani, Unambiguous Description of the Oxygen Environment in Multicomponent Aluminosilicate Glasses from 17O Solid State NMR

Computational Spectroscopy, J. Phys. Chem. C. 116 (2012) 14599–14609. https://doi.org/10.1201/b12066-172.

[154] M. Ren, L. Deng, J. Du, Bulk, surface structures and properties of sodium borosilicate and boroaluminosilicate nuclear waste glasses from molecular dynamics simulations, J. Non. Cryst. Solids. 476 (2017) 87–94. https://doi.org/10.1016/j.jnoncrysol.2017.09.030.

[155] X. Lu, J.T. Reiser, B. Parruzot, L. Deng, I.M. Gussev, J.C. Neuefeind, T.R. Graham, H. Liu, J. V. Ryan, S.H. Kim, N. Washton, M. Lang, J. Du, J.D. Vienna, Effects of Al:Si and (Al + Na):Si ratios on the properties of the international simple glass, part II: Structure, J. Am. Ceram. Soc. 104 (2021) 183–207. https://doi.org/10.1111/jace.17447.

[156] B. Lee, G. Kim, R. Kim, B. Cho, S. Lee, C.M. Chon, Strength development properties of geopolymer paste and mortar with respect to amorphous Si/Al ratio of fly ash, Constr. Build. Mater. 151 (2017) 512–519. https://doi.org/10.1016/j.conbuildmat.2017.06.078.

[157] C. Mundus, W. Müller-Warmuth, 27Al magic-angle spinning nuclear magnetic resonance satellite transition spectroscopy of glasses in the system K2O-Al2O3-SiO2, Solid State Nucl. Magn. Reson. 5 (1995) 79–88.

[158] J.F. Stebbins, S. Kroeker, S.K. Lee, T.J. Kiczenski, Quantification of five- and six-coordinated aluminum ions in aluminosilicate and fluoride-containing glasses by high-field, high-resolution 27Al NMR, J. Non. Cryst. Solids. 275 (2000) 4–9.

[159] T.K. Bechgaard, A. Goel, R.E. Youngman, J.C. Mauro, S.J. Rzoska, M. Bockowski, L.R. Jensen, M.M. Smedskjaer, Structure and mechanical properties of compressed sodium aluminosilicate glasses: Role of non-bridging oxygens, J. Non. Cryst. Solids. 441 (2016) 49–57. https://doi.org/10.1016/j.jnoncrysol.2016.03.011.

[160] H. Wan, L. Yuan, Y. Zhang, Insight Into the Leaching of Sodium Alumino-Silicate Hydrate (N-A-S-H) Gel: A Molecular Dynamics Study, Front. Mater. 7 (2020) 1–11. https://doi.org/10.3389/fmats.2020.00056.

[161] J. Davidovits, 30 Years of Successes and Failures in Geopolymer Applications . Market Trends and Potential Breakthroughs ., in: Geopolymer 2002 Conf., 2002: pp. 1–16. https://doi.org/10.1017/CBO9781107415324.004.

[162] S. Lyu, T. Wang, T. Cheng, T. Ueng, Main factors affecting mechanical characteristics of geopolymer revealed by experimental design and associated statistical analysis, Constr. Build. Mater. 43 (2013) 589–597. https://doi.org/10.1016/j.conbuildmat.2013.02.033.

[163] M.T. Melchior, D.E.W. Vaughan, A.J. Jacobson, Characterization of the Silicon-Aluminum Distribution in Synthetic Faujasites by High-Resolution Solid-State 29Si NMR, J. Am. Chem. Soc. 104 (1982) 4859–4864.

[164] E. Lippmaa, M. Mági, A. Samoson, M. Tarmak, G. Engelhardt, Investigation of the Structure of Zeolites by Solid-State High-Resolution 29Si NMR Spectroscopy, J. Am.

Chem. Soc. 103 (1981) 4992–4996. https://doi.org/10.1021/ja00407a002.

[165] A. Fernández-Jiménez, A.G. de la Torre, A. Palomo, G. López-Olmo, M.M. Alonso, M.A.G. Aranda, Quantitative determination of phases in the alkaline activation of fly ash. Part II: Degree of reaction, Fuel. 85 (2006) 1960–1969. https://doi.org/10.1016/j.fuel.2006.04.006.

[166] H.F.W.Taylor, Cement chemistry, 1998. https://doi.org/10.1016/S0958-9465(98)00023-7.

[167] H.J.H. Brouwers, The work of Powers and Brownyard revisited: Part 1, Cem. Concr. Res. 34 (2004) 1697–1716. https://doi.org/10.1016/j.cemconres.2004.05.031.

[168] W.K.W. Lee, J.S.J. Van Deventer, The effects of inorganic salt contamination on the strength and durability of geopolymers, Colloids Surfaces A Physicochem. Eng. Asp. 211 (2002) 115–126. https://doi.org/10.1016/S0927-7757(02)00239-X.

[169] A. Fernández-Jiménez, A. Palomo, Mid-infrared spectroscopic studies of alkali-activated fly ash structure, Microporous Mesoporous Mater. 86 (2005) 207–214. https://doi.org/10.1016/j.micromeso.2005.05.057.

[170] I. García-Lodeiro, A. Fernández-Jiménez, M.T. Blanco, A. Palomo, FTIR study of the sol-gel synthesis of cementitious gels: C-S-H and N-A-S-H, J. Sol-Gel Sci. Technol. 45 (2008) 63–72. https://doi.org/10.1007/s10971-007-1643-6.

[171] T. Thoenen, W. Hummel, U. Berner, E. Curti, The PSI/Nagra Chemical Thermodynamic Database 12/07, 2014.

[172] Y. Yan, B. Ma, G.D. Miron, D.A. Kulik, K. Scrivener, B. Lothenbach, Al uptake in calcium silicate hydrate and the effect of alkali hydroxide, Cem. Concr. Res. 162 (2022) 106957. https://doi.org/10.1016/j.cemconres.2022.106957.

[173] M. Criado, A. Fernández-Jiménez, A. Palomo, Alkali activation of fly ash: Effect of the SiO2/Na2O ratio. Part I: FTIR study, Microporous Mesoporous Mater. 106 (2007) 180–191. https://doi.org/10.1016/j.micromeso.2007.02.055.

[174] Z. Zhang, H. Wang, J.L. Provis, Quantitative study of the reactivity of fly ash in geopolymerization by FTIR, J. Sustain. Cem. Mater. 1 (2012) 154–166. https://doi.org/10.1080/21650373.2012.752620.

[175] A. Hajimohammadi, J.L. Provis, J.S.J. Van Deventer, Effect of alumina release rate on the mechanism of geopolymer gel formation, Chem. Mater. 22 (2010) 5199–5208. https://doi.org/10.1021/cm101151n.

[176] S.A. Bernal, J.L. Provis, V. Rose, R. Mejía De Gutierrez, Evolution of binder structure in sodium silicate-activated slag-metakaolin blends, Cem. Concr. Compos. 33 (2011) 46–54. https://doi.org/10.1016/j.cemconcomp.2010.09.004.

[177] D. Dimas, I. Giannopoulou, D. Panias, Polymerization in sodium silicate solutions: A fundamental process in geopolymerization technology, J. Mater. Sci. 44 (2009) 3719–3730. https://doi.org/10.1007/s10853-009-3497-5.

[178] W.R. Taylor, Application of infrared spectroscopy to studies of silicate glass structure:

Examples from the melilite glasses and the systems Na2O-SiO2 and Na2O-Al2O3-SiO2, Proc. Indian Acad. Sci. - Earth Planet. Sci. 99 (1990) 99–117. https://doi.org/10.1007/BF02871899.

[179] H.C. Helgeson, D.H. Kirkham, G.C. Flowers, Theoretical prediction of the thermodynamic behavior of aqueous electrolytes by high pressures and temperatures; IV, Calculation of activity coefficients, osmotic coefficients, and apparent molal and standard and relative partial molal properties to 600 d, Am. J. Sci. 281 (1981) 1249–1516. https://doi.org/10.2475/ajs.281.10.1249.

[180] G.M. Anderson, D.A. Crerar, Thermodynamics in geochemistry: the equilibrium model, Oxford University Press, Oxford, 1993.

[181] B. Lothenbach, E. Bernard, U. Mäder, Zeolite formation in the presence of cement hydrates and albite, Phys. Chem. Earth. 99 (2017) 77–94. https://doi.org/10.1016/j.pce.2017.02.006.

[182] R.J. Myers, S.A. Bernal, J.L. Provis, A thermodynamic model for C-(N-)A-S-H gel: CNASH-ss. Derivation and validation, Cem. Concr. Res. 66 (2014) 27–47. https://doi.org/10.1016/j.cemconres.2014.07.005.

[183] C.F. Maitland, C.E. Buckley, B.H. O'Connor, P.D. Butler, R.D. Hart, Characterization of the pore structure of metakaolin-derived geopolymers by neutron scattering and electron microscopy, J. Appl. Crystallogr. 44 (2011) 697–707. https://doi.org/10.1107/S0021889811021078.

[184] F.P. Glasser, J. Pedersen, K. Goldthorpe, M. Atkins, Solubility reactions of cement components with NaCl solutions: I. Ca(OH)2 and C-S-H, Adv. Cem. Res. 17 (2005) 57–64. https://doi.org/10.1680/adcr.2005.17.2.57.

[185] Rupert Jacob Myers, Thermodynamic modelling of CaO-Al2O3-SiO2-H2O-Based Cements, 2015. https://doi.org/10.1016/j.jallcom.2015.01.199.

[186] B. Lothenbach, D. Jansen, Y. Yan, J. Schreiner, Solubility and characterization of synthesized 11 Å Al-tobermorite, Cem. Concr. Res. 159 (2022) 106871. https://doi.org/10.1016/j.cemconres.2022.106871.

[187] E.P. Partridge, A.H. White, The solubility of calcium sulfate from 1 to 200°, J. Am. Chem. Soc. 51 (1929) 360–370.

[188] Y. Zuo, M. Nedeljković, G. Ye, Coupled thermodynamic modelling and experimental study of sodium hydroxide activated slag, Constr. Build. Mater. 188 (2018) 262–279. https://doi.org/10.1016/j.conbuildmat.2018.08.087.

[189] ASTM C618-19, Standard specification for coal fly ash and raw or calcined natural pozzolan for use in concrete, ASTM International: West Conshohocken, 2019.

[190] J.L. Provis, S.A. Bernal, Geopolymers and Related Alkali-Activated Materials, Annu. Rev. Mater. Res. 44 (2014) 299–327. https://doi.org/10.1146/annurev-matsci-070813-113515.

[191] R. Snellings, J. Chwast, Ö. Cizer, N. De Belie, Y. Dhandapani, P. Durdzinski, J. Elsen, J. Haufe, D. Hooton, C. Patapy, M. Santhanam, K. Scrivener, D. Snoeck, L. Steger, S. Tongbo, A. Vollpracht, F. Winnefeld, B. Lothenbach, RILEM TC-238 SCM recommendation on hydration stoppage by solvent exchange for the study of hydrate assemblages, Mater. Struct. Constr. 51 (2018). https://doi.org/10.1617/s11527-018-1298-5.

[192] N. Doebelin, R. Kleeberg, Profex: a graphical user interface for the Rietveld refinement program BGMN, J. Appl. Crystallogr. 48 (2015) 1573–1580.

[193] K. Scrivener, R. Snellings, B. Lothenbach, A Practical Guide to Microstructural Analysis of Cementitious Materials, 2018. https://doi.org/10.1201/b19074.

[194] M. Ben Haha, K. De Weerdt, B. Lothenbach, Quantification of the degree of reaction of fly ash, Cem. Concr. Res. 40 (2010) 1620–1629. https://doi.org/10.1016/j.cemconres.2010.07.004.

[195] T. Wang, T. Ishida, R. Gu, A study of the influence of crystal component on the reactivity of low-calcium fly ash in alkaline conditions based on SEM-EDS, Constr. Build. Mater. 243 (2020) 118227. https://doi.org/10.1016/j.conbuildmat.2020.118227.

[196] W. Wilson, L. Sorelli, A. Tagnit-Hamou, Automated coupling of NanoIndentation and Quantitative Energy-Dispersive Spectroscopy (NI-QEDS): A comprehensive method to disclose the micro-chemo-mechanical properties of cement pastes, Cem. Concr. Res. 103 (2018) 49–65. https://doi.org/10.1016/j.cemconres.2017.08.016.

[197] J.E. Rossen, K.L. Scrivener, Optimization of SEM-EDS to determine the C–A–S–H composition in matured cement paste samples, Mater. Charact. 123 (2017) 294–306. https://doi.org/10.1016/j.matchar.2016.11.041.

[198] Y. Ma, Microstructure and Engineering Properties of Alkali Activated Fly Ash - as an environment friendly alternative to Portland cement, 2013. https://doi.org/10.4233/uuid:dc26be48-b007-4c17-973f-e386e4dcf821.

[199] N. Otsu, A Threshold Selection Method from Gray-Level Histograms, IEEE Trans. Syst. Man. Cybern. 9 (1979) 62–66. https://doi.org/10.1109/TSMC.1979.4310076.

[200] J. Kempl, O. Çopuroğlu, EH-pH- and main element analyses of Blast Furnace Slag Cement paste pore solutions activated with sodium monofluorophosphate - Implications for carbonation and self-healing, Cem. Concr. Compos. 71 (2016) 63–76. https://doi.org/10.1016/j.cemconcomp.2016.05.004.

[201] J. Duchesne, M.A. Bérubé, Evaluation of the validity of the pore solution expression method from hardened cement pastes and mortars, Cem. Concr. Res. 24 (1994) 456–462. https://doi.org/https://doi.org/10.1016/0008-8846(94)90132-5.

[202] F. Chayes, Petrographic modal analysis: an elementary statistical appraisal, (No Title). (1956).

[203] G. Fang, Q. Wang, M. Zhang, In-situ X-ray tomographic imaging of microstructure evolution of fly ash and slag particles in alkali-activated fly ash-slag paste, Compos.

Part B Eng. 224 (2021) 109221. https://doi.org/10.1016/j.compositesb.2021.109221.

[204] R. Caron, R.A. Patel, G.D. Miron, C. Le Galliard, B. Lothenbach, F. Dehn, Microstructure development of slag activated with sodium silicate solution: Experimental characterization and thermodynamic modeling, J. Build. Eng. 71 (2023) 106398. https://doi.org/10.1016/j.jobe.2023.106398.

[205] D. Ravikumar, N. Neithalath, Reaction kinetics in sodium silicate powder and liquid activated slag binders evaluated using isothermal calorimetry, Thermochim. Acta. 546 (2012) 32–43. https://doi.org/10.1016/j.tca.2012.07.010.

[206] V. Kocaba, E. Gallucci, K.L. Scrivener, Methods for determination of degree of reaction of slag in blended cement pastes, Cem. Concr. Res. 42 (2012) 511–525. https://doi.org/10.1016/j.cemconres.2011.11.010.

[207] B.J. Merkel, B. Planer-Friedrich, D.K. Nordstrom, Groundwater geochemistry: A practical guide to modeling of natural and contaminated aquatic systems, Springer, 2005.

[208] Y. Chen, L.M. de Lima, Z. Li, B. Ma, B. Lothenbach, Synthesis , solubility and thermodynamic properties of N-A-S-H gels with various target Si / Al ratios, Cem. Concr. Res. 180 (2024) 107484. https://doi.org/10.1016/j.cemconres.2024.107484.

[209] Z. Qing, F. Basquiroto, D. Souza, R.J. Mulder, W. Duan, Multistep nucleation and growth mechanism of aluminosilicate gel observed by cryo-electron microscopy, Cem. Concr. Res. 159 (2022) 106873. https://doi.org/10.1016/j.cemconres.2022.106873.

[210] V. Bocullo, L. Vitola, D. Vaiciukyniene, A. Kantautas, D. Bajare, The influence of the SiO2/Na2O ratio on the low calcium alkali activated binder based on fly ash, Mater. Chem. Phys. 258 (2021) 123846. https://doi.org/10.1016/j.matchemphys.2020.123846.

[211] A.R. Brough, M. Holloway, J. Sykes, A. Atkinson, Sodium silicate-based alkali-activated slag mortars. Part II. The retarding effect of additions of sodium chloride or malic acid, Cem. Concr. Res. 30 (2000) 1375–1379. https://doi.org/10.1016/S0008-8846(00)00356-2.

[212] J.A. Gadsden, Infrared spectra of minerals and related inorganic compounds, 1975.

[213] Y. Yan, S.Y. Yang, G.D. Miron, I.E. Collings, E. L'Hôpital, J. Skibsted, F. Winnefeld, K. Scrivener, B. Lothenbach, Effect of alkali hydroxide on calcium silicate hydrate (C-S-H), Cem. Concr. Res. 151 (2022). https://doi.org/10.1016/j.cemconres.2021.106636.

[214] C. Liu, X. Liang, Y. Chen, Z. Li, G. Ye, Degradation of alkali-activated slag subjected to water immersion, Cem. Concr. Compos. 142 (2023) 105157. https://doi.org/10.1016/j.cemconcomp.2023.105157.

[215] C. Liu, Z. Li, S. Nie, J. Skibsted, G. Ye, Structural evolution of calcium sodium aluminosilicate hydrate (C-(N-)A-S-H) gels induced by water exposure: The impact of Na leaching, Cem. Concr. Res. 178 (2024). https://doi.org/10.1016/j.cemconres.2024.107432.

[216] M. Criado, A. Palomo, A. Fernández-Jiménez, Alkali activation of fly ashes. Part 1: Effect of curing conditions on the carbonation of the reaction products, Fuel. 84 (2005) 2048–2054. https://doi.org/10.1016/J.FUEL.2005.03.030.

[217] E. Ul Haq, S.K. Padmanabhan, A. Licciulli, In-situ carbonation of alkali activated fly ash geopolymer, Constr. Build. Mater. 66 (2014) 781–786. https://doi.org/10.1016/j.conbuildmat.2014.06.012.

[218] H. Xu, J.S.J. Van Deventer, The effect of alkali metals on the formation of geopolymeric gels from alkali-feldspars, Colloids Surfaces A Physicochem. Eng. Asp. 216 (2003) 27–44. https://doi.org/10.1016/S0927-7757(02)00499-5.

[219] E. Ul Haq, S.K. Padmanabhan, A. Licciulli, In-situ carbonation of alkali activated fly ash geopolymer, Constr. Build. Mater. 66 (2014) 781–786. https://doi.org/10.1016/j.conbuildmat.2014.06.012.

[220] S.A. Bernal, J.L. Provis, B. Walkley, R. San Nicolas, J.D. Gehman, D.G. Brice, A.R. Kilcullen, P. Duxson, J.S.J. Van Deventer, Gel nanostructure in alkali-activated binders based on slag and fly ash, and effects of accelerated carbonation, Cem. Concr. Res. 53 (2013) 127–144. https://doi.org/10.1016/j.cemconres.2013.06.007.

[221] M.M. Kumar, H. Jena, Direct single-step synthesis of phase pure zeolite Na–P1, hydroxy sodalite and analcime from coal fly ash and assessment of their Cs+ and Sr2+ removal efficiencies, Microporous Mesoporous Mater. 333 (2022) 111738. https://doi.org/10.1016/j.micromeso.2022.111738.

[222] Y. Zuo, Z. Qian, E.J. Garboczi, G. Ye, Numerical simulation of the initial particle parking structure of cement/geopolymer paste and the dissolution of amorphous silica using real-shape particles, Constr. Build. Mater. 185 (2018) 206–219. https://doi.org/10.1016/j.conbuildmat.2018.07.063.

[223] Y. Zuo, G. Ye, Lattice Boltzmann simulation of the dissolution of slag in alkaline solution using real-shape particles, Cem. Concr. Res. 140 (2021). https://doi.org/10.1016/j.cemconres.2020.106313.

[224] D. Wolff-Boenisch, S.R. Gislason, E.H. Oelkers, C. V. Putnis, The dissolution rates of natural glasses as a function of their composition at pH 4 and 10.6, and temperatures from 25 to 74°C, Geochim. Cosmochim. Acta. 68 (2004) 4843–4858. https://doi.org/10.1016/j.gca.2004.05.027.

[225] Q. Kang, S. Chen, Lattice Boltzmann simulation of chemical dissolution in porous media, Phys. Rev. E. 65 (2002) 1–8. https://doi.org/10.1103/PhysRevE.65.036318.

[226] Z. Qian, E. Schlangen, G. Ye, K. van Breugel, Modeling framework for fracture in multiscale cement-based material structures, Materials (Basel). 10 (2017). https://doi.org/10.3390/ma10060587.

[227] G.V.P.B. Singh, C. Subrahmanyam, K.V.L. Subramaniam, Dissolution of the glassy phase in low-calcium fly ash during alkaline activation, Adv. Cem. Res. 30 (2018) 313–322. https://doi.org/10.1680/jadcr.17.00170.

[228] Y. Zuo, G. Ye, Pore structure characterization of sodium hydroxide activated slag using

mercury intrusion porosimetry, nitrogen adsorption, and image analysis, Materials (Basel). 11 (2018). https://doi.org/10.3390/ma11061035.

[229] R.A. Robie, B.S. Hemingway, Thermodynamic properties of minerals and related substances at 298.15 K and 1 bar (105 Pascals) pressure and at higher temperatures, US Government Printing Office, 1995.

[230] L. Glasser, The effective volumes of waters of crystallization & the thermodynamics of cementitious materials, Cement. 3 (2021) 100004. https://doi.org/10.1016/j.cement.2021.100004.

Acknowledgments

Year after year, I have watched the cycles of flowers blooming and fading across the campus, wondering when my own journey would reach its culmination. Now, my own chapter at TU Delft gently draws to a close. When looking back, I am always fully grateful for so many nice people who have shaped this experience.

First and foremost, I extend my deepest gratitude to my promotor, Prof. Guang Ye, for offering me this opportunity to pursue my PhD research. Your steadfast support over the years has been invaluable, and our discussions have profoundly influenced my work, especially your insightful comments on my writing. Meanwhile, I deeply admire your relentless pursuit of perfection in every detail and your unwavering commitment to integrity in research, which has profoundly shaped my own approach.

My boundless gratitude also goes to my promotor Prof. Qijun Yu. I am heartily grateful for your meticulous care and colossal support. Beyond that, your attitude toward research and your treatment of others have been a lasting inspiration. I feel fortunate to have had the chance for such meaningful interactions with you during your visiting to Delft last year: a time rich with countless lessons that words can hardly capture.

My wholehearted gratitude extends to Prof. Suhong Yin as well. You are the one who inspired me to embark on the academic path. I am deeply appreciative of your steadfast support and care over the years. Our conversations, whether about research or broader aspects of life, have been a source of insight and joy. I am truly grateful for your understanding and patience with my shortcomings.

I am deeply indebted to Dr. Jorge S. Dolado for his unwavering guidance and support. I am grateful for the time you dedicated to our discussions, even amidst your busy schedule, including during your business trips. Your generous affirmation and compliment have given me confidence and motivation to move forward.

I would also like to express my heartfelt gratitude to Prof. Barbara Lothenbach. This endeavor would not have been possible without your selfless help and guidance. I am moved by your willingness to assist young researchers, even those you may not know personally. Your fresh insights into research questions and practical advice on data analysis and presentation have been invaluable to me.

I feel fortunate to have Prof. Klaas van Breugel as one of my committee members of my defense. I am truly grateful for your thorough review of my thesis and for taking the time to discuss it with me. I really enjoyed our inspiring conversation.

I acknowledge the other committee members, Prof. Erik Schlangen and Dr. Ruben Snellings. Thank you for the time and effort you devoted to reviewing my thesis and for your valuable feedback.

The greatest acknowledgement goes to China Scholarship Council and South China University of Technology (SCUT) for funding this research.

Many thanks to Prof. Jiangxiong Wei, Prof. Jie Hu, Assoc. Prof. Haoliang Huang, Prof. Tongsheng Zhang, Assoc. Prof. Fangxian Li, Dr. Weiting Xu, Assoc. Prof. Yuwei Ma, Prof. Peng Gao. Assoc. Prof. Xiaowei Ouyang. Thank you for your support and guidance.

Special thanks go to Dr. Bin Ma. You are really nice. I am full of gratitude for your kind help and guidance with my research.

I would like to express my sincere thanks to my friends and colleagues in Microlab. My first thanks go to my officemates: Dr. Zhenming Li (Na Yu). I fondly remember the times we shared our thoughts on various topics, and I really enjoyed your crosstalk show. I also appreciate your help with my scientific writing. Jiayi Chen (Dr. Wenqin Shi). I cannot count how many times you have helped me with my research. You always offer unconditional help, without asking for rewards. Dr. Tianshi Lu, so much joy you have brought to our office. I often miss the days when you were here. Xuliang Hou (Dr. Ying Yang), I like the nickname you created for me. It is really warm. Dr. Bei Wu, your kindness and generosity have not gone unnoticed. Dr. Mayank Gupta, it is great to have you as an officemate. Our many discussions on research have been incredibly helpful, and I have enjoyed our cultural exchange. Big thanks also to Xuhui Liang, Chen Liu and Shi Hu for your comforting presence and cherished friendship. I wish you all a life filled with your heart's desires. Additionally, I would like to extend my sincere appreciation to my esteemed colleagues and dear friends: Dr. Branko Šavija, Prof. Henk Jonkers, Dr. Oğuzhan Çopuroğlu, Dr. Mohammad Fotouhi, Dr. Gozde Ozerkan, Dr. Dessi Koleva, Dr. Zhiwei Qian, Dr. Hua Dong, Dr. Yong Zhang, Dr. Hongzhi Zhang, Dr. Shi Xu, Dr. Marija Nedeljković, Dr. Yibing Zuo, Dr. Wenjuan Lyu, Dr. Yu Chen, Dr. Yidong Gan, Dr. Yading Xu, Dr. Yu Zhang, Dr. Xingliang Yao, Dr. Shizhe Zhang, Dr. Hao Huang, Dr. Ze Chang, Dr. Wan Zhi (Jing Chen), Dr. Minfei Liang, Dr. Boyu Chen, Dr. Albina Kostiuchenko, Dr. Ameya Kamat, Luiz Miranda de Lima Junior, Zhiyuan Xu, Irving Alfredo Flores Beltran, Guilherme da Silva Munhoz, Yu Zeng, Farnaz Aghabeyk, Anne Linde van Overmeir, Shan He, Jinbao Xie, Ali Ghaderiaram, Rowin Bol, Dr. Wen Zhou, Zhaozheng Meng, Max Veeger, Patrick Holthuizen, Burcu Aytekin Turkoglu, Eyuphan Kucukkalfa, Sebastian Kuniewski. It is my honor to have you on this journey.

I will not forget the support of our dedicated technicians in Microlab. Thank you, John, for assisting with my chemical experiments. Thank you, Ton, for helping with the tough and dangerous task of pore solution extraction! Thank you, Arjan, for your patience with all the EDX measurements. And thank you, Maiko, for your warm and kind assistance every time.

My research journey started at SCUT. My warmest acknowledgement goes to Dr. Jing Li. I am deeply grateful for your continuous care and support, both in my personal life and in my research road. It is so good to have you as a friend in my life. I would also like to thank many wonderful members of Prof. Yin’s group: Yongfeng Yang, Rong Li, Kunxue Zhu, Rongyong Lin, Haiyu Guan, Kang Wang, Jian Ma, Dr. Guogang Li, and Zhanqiang Zhang. Your friendship and kindness have been invaluable, both in supporting my experiments and in helping with

personal matters. I would like to acknowledge the assistance of Dr. Yiqun Guo, Dr. Shaolong Liu, Dr. Wenhao Guo, Dr. Yangyang Wang, and Dr. Hao Liu, with special thanks to Dr. Zhangmin Zhang. I am also grateful to Dr. Bin Li, Dr. Mengmeng Ren, Dr. Shunjie Luo, Xiaogeng Xie, Yanzhi Hu, Zhenguo Yang, Yinwei Wu, Wen Jin, and Liang Shi for the joyful moments we shared along the way. A big thank you also goes to the laboratory technicians: Datong Zhang, Jianqin Lin, Manman Fang, Qian Sun, and Jieru Zheng, for your steady support and dedication.

Gratitude is due to all the colleagues at Lychee restaurant. Working here has been a special experience, and I have learned so much. I appreciate the support of Bo and Lily, without you, I cannot imagine how hard it would be for me to manage life here. I am also very grateful for Yao. I will keep your valuable suggestions in mind. My gratitude extends to all the chefs for taking such good care of me. My appreciation goes to Demi as well. It is really pleasant and relaxing when I am with you.

I would also like to thank my roommates: Keer Zhang, Xiangjun Chen, Dr. Haohui Xin, Hao Cheng for the joyful moments we spent together. Nice to meet you too, Xinyi Wang. Your handwritten letter is one of the best gifts I received here. My warm appreciation also goes to Li Sun for your kindness and consideration.

I am also deeply thankful for Yun Chen(陈云). You are the one who introduced me to my fitness journey, transforming me not only from the outside, but more importantly, within.

Special thanks go to Lexie. I was swept away by the opening line of our story, high up and deep down as it upfolded. In time, I learned to accept things as they are with calm, like the peace that settles after a storm.

I would like to extend my immense gratitude to my dearest friend Xiaoyan. We are more than just friends in each other's life. I have reserved this special position in my acknowledgment for you, just as you always hold a special space in my heart.

Last but certainly not least, words cannot express my unlimited gratitude to my family. 亲爱的爸爸妈妈，这么多年来，是你们无私的爱，无条件的支持，以及默默的付出，我才能全身心地投入到学业和工作中。感谢你们顶着四面八方的压力，支持我漂洋过海，长年离家，尊重我的每一个决定。恁个全潮汕尚好的父母。Dear Mom and Dad, without your steadfast love, support and sacrifice, I would not have been able to fully dedicate myself to my research career. Mom, I deeply appreciate, from the bottom of my heart, that you always try to understand me and stand by my side, even when my decisions go against your own beliefs and wishes. And to my beloved younger sister, Qi Chen, I cannot count how much happiness you have brought into my life. If I may make an analogy, it's as though you have placed a star on my thesis cover, yet to my life, you are truly the sun. I love you with all my heart, always.

Yun Chen

Delft, Nov. 2024